Thermodynamic Properties for Pre-Combustion CO_2 Capture and Pipeline Transportation

Lorena Fernanda dos Santos de Souza

A thesis submitted in partial fulfilment of the requirements for the degree of Doctor of Philosophy in Chemical Engineering of Imperial College London and the Diploma of Imperial College London

Department of Chemical Engineering

Imperial College London

London SW7 2AZ, United Kingdom

October 2018

Originality Declaration

I herewith certify that all material in this dissertation which is not my own work has been properly acknowledged.

Lorena Fernanda dos Santos de Souza

Copyright Declaration

"The copyright of this thesis rests with the author and is made available under a Creative Commons Attribution Non-Commercial No Derivatives licence. Researchers are free to copy, distribute or transmit the thesis on the condition that they attribute it, that they do not use it for commercial purposes and that they do not alter, transform or build upon it. For any reuse or redistribution, researchers must make clear to others the licence terms of this work"

“And, when you want something, all the universe conspires in helping you to achieve it.”

Paulo Coelho, The Alchemist

Acknowledgements

It has passed only four years but it seems I have lived a decade in London. I have visited new places and met so many nice people from all around the world. But I am mainly proud of having the opportunity to contribute to an area of research that is making the world a better place.

Firstly, I would like to immensely thank my academic supervisor, Professor J P Martin Trusler, for not only his excellent guidance during this last four years but also for his knowledge and patience. I have to thank Martin for believing I was capable of great things during my PhD even when I did not believe it myself. I am grateful to have the opportunity to work with Dr Saif Z Al Ghafri, my unofficial co-supervisor, for all his help in the laboratory and meaningful discussions about the project, especially in my first months at Imperial College London.

To all the amazing friends I have got in the Thermophysics group, my most sincere gratitude for all the time we have spent together. I have collected so many good memories during this past four years. Thanks including to Hao Bian, Florence Chow, Malami Mohammed, Jiafei Zhang, Christine Seifried, Cheng Peng, Rayane Hoballah, Shane Cadogan, Claudio Calabrese, Theodor Videnberg, Sultan Al-Habsi, Benaiah Anabaraonye, Mihaela Stevar, Chidi Efika, Ines da Graca, Ruien Hu, Geraldine Ollarves, Clemens Patzschke, Caroline Jones, Malyanah Taib, Humera Ansari and many others. Thank you all for making this chapter of my life enjoyable. I am grateful to Dr Yolanda Sanchez-Vicente and Dr Weparn Julian Tay not only for their friendship but for all the help with the experimental density measurements.

I am also grateful to all the help and supported received from Fennell's group, which I shared not only the space in the laboratory but also an amazing time together.

I am thankful to Professor Roland Span, Dr Markus Richter and Dr Monika Thol for kindly organising my staying in Bochum, where I spent almost three months with the lovely RUB group. I am thankful to all of you to welcome me in your group and make me feel at home. I had a wonderful time. I would like to especially thank Stefan Herrig for all his time and patience; life has presented me with a lovely friend disguised as collaborator.

I would like to thank the electrical and mechanical workshop staff, especially, Gavin Barnes, Richard Wallington, and Chin Lang for your professional help and support throughout this four years.

Lastly, but not less important, I would like to thank my husband. It is hard to express in words the immense gratitude I have for your love and support. Thank you for sharing with me the joy of my victories and sadness of the defeats in this last 10 years. Thank you for supporting this idea (some would say crazy) of crossing the Atlantic Ocean to become a PhD. I also grateful for my mum, dad, grandma and brother who always supported all my decisions without any judgment. I have always felt I am the most blessed person on earth.

L F S Souza

October 2018

Abstract

Carbon capture and storage is a key technology to achieve the goal of ensuring that the global temperature rise is maintained below 1.5 °C, in accordance with the 2015 Paris agreement. One possibility is to produce hydrogen through the gasification of carbonaceous fuels, such as coal, combined with the pre-combustion carbon capture process. In these process, a syngas comprised of CO and H_2 is generated. In order to both facilitate carbon capture and increase the hydrogen production, the syngas is shifted in a water-gas-shift reaction. Then, CO_2 is separated from the resulting stream, and subsequently transported and stored in appropriated geological formations. The gas separation processes, namely air separation and syngas separation, along with the compression of CO_2 for storage, are the most expensive and challenge stages. For the design, optimisation and safe operation of these processes, accurate equations of state (EOS) are required to describe thermodynamic properties of the various mixtures of CO_2 with relevant substances, including H_2, N_2, CH_4, CO, Ar, O_2 and H_2S. A popular and potentially very accurate approach is to use empirical multi-fluid multi-parameter EOS. In order to adjust the interaction parameters in those models, reliable and accurate experimental thermodynamic data of (CO_2 + diluent) mixtures are indispensable, in which the diluents of interest are H_2, N_2, CH_4, CO, Ar, O_2 and H_2S.

In this PhD project, new vapour liquid equilibrium (VLE) measurements have been made on two relevant binary systems: (CO_2 + CH_4) and (CO_2 + CO). Additionally, measurements were made of the distribution of trace levels of H_2S between the liquid and vapour phases in these two systems. The measurements were carried out at temperatures ranging from just above the triple-point to just below the critical point of CO_2, and at pressures from the vapor pressure of pure CO_2 up to approximately 15 MPa or, if lower, the mixture critical pressure. Furthermore, homogenous density measurements of the (CO_2 + CO) system were carried out using a vibrating-tube densimeter over a temperature range of (283.15 to 373.15) K and pressures up to 48 MPa.

The new VLE and homogenous density data have been compared with the predictions of available thermodynamic models, including the GERG-2008 model of Kunz and Wagner, the EOS-CG model of Gernert and Span and the SAFT-γ Mie approach.

Additionally, the data have been correlated with the Peng-Robinson EOS, generally incorporating a single temperature-dependent binary interaction parameter.

Finally, an improved Helmholtz-energy-explicit mixture model for the (CO_2 + CO) system was developed within the framework of GERG-2008 in collaboration with the Ruhr-Universität Bochum. The development of the new mixture model was only possible due to the accurate density and VLE measurements carried out in this work.

In summary, new VLE and homogeneous density data are reported that help to fill important knowledge gaps relating to the thermodynamic properties of mixtures of CO_2 with substances relevant to pre-combustion CO_2 capture and pipeline transportation.

Contents

Chapter 1 Introduction 1

1.1 Introduction 1
1.2 Scope and Objectives 2
1.3 Thesis Outline 4

Chapter 2 Context of CO_2 Capture, Transportation and Storage 5

2.1 Overview 5
2.2 CO_2 Capture 5
2.2.1 Pre-Combustion Carbon Capture Technology 6
2.2.2 Gas Separation Processes 7
2.2.3 Pre-Combustion Carbon Capture by Low-Temperature Separation 9
2.3 CO_2 Transportation 9
2.4 CO_2 Storage 10
2.5 Evaluation of Impurities 10

Chapter 3 Equations of State for Mixture 14

3.1 Overview 14
3.2 Phase Behaviour of Pure Substances and Binary Systems 14
3.3 Cubic Equations of State 16
3.3.1 PR-EOS with Van der Waals Mixing Rules 19
3.3.2 Fitting Procedure of the PR-EOS 20
3.4 Helmholtz-Energy Explicit Mixture Model 21
3.4.1 Mathematical Structure 22
3.4.2 Fitting Procedure of the New Mixture Model 24
3.5 Statistical Associating Fluid Theory (SAFT) 27
3.5.1 SAFT-γ Mie Group Contribution Approach 28
3.5.2 Fitting Procedure of the SAFT-γ Mie 30

Chapter 4 Vapour Liquid Equilibrium Apparatus and Experimental Methodology 33

4.1 Apparatus Design 33
4.2 Material 36
4.3 Toxicity of Materials / Safety Procedures 36
4.4 GC Calibration 39
4.4.1 Calibration Procedure 39

4.4.2 Validation of the GC Calibration 45
4.5 Experimental Procedures 45
4.6 Uncertainty Analysis 47
Chapter 5 Density Apparatus Design and Experimental Methodology 51
5.1 Material 51
5.2 Apparatus Description 51
5.3 Toxicity of Materials / Safety Procedures 53
5.4 Densimeter Calibration and Validation 53
5.5 Experimental Procedure 55
5.6 Uncertainty Analysis 57
Chapter 6 The (CO_2 + CO) System 59
6.1 Literature Review on Vapour-Liquid Equilibrium and Density 59
6.2 Vapour-Liquid Equilibrium Results 62
6.2.1 Critical Point Estimation 68
6.2.2 Comparison of VLE Data with Literature Data 71
6.2.3 Comparison of VLE Data with Equations of State 74
6.3 Homogeneous Density Results 79
6.3.1 Comparison of Homogeneous Density Data with Literature Data 88
6.3.2 Comparison of Homogeneous Density Data with Equations of State 90
6.4 Extrapolation Behaviour of the New Mixture Model 91
6.5 Estimated Uncertainty of Calculated Properties for the New Mixture Model ..94
6.6 Conclusions 94
Chapter 7 The (CO_2 + CH_4) System 96
7.1 Literature Review on Vapour-Liquid Equilibrium and Density 96
7.2 Vapour-Liquid Equilibrium Results 100
7.2.1 Critical Point Estimation 105
7.2.2 Comparison of VLE Literature Data 107
7.2.3 Comparison of VLE Data with Equations of State 111
7.3 Conclusions 114
Chapter 8 H_2S Trace Analysis: (CO_2 + CH_4 + H_2S) and (CO_2 + CO + H_2S) Systems 116
8.1 Literature Review on Vapour-Liquid Equilibrium 116
8.1.1 Binary Systems Relevant to the H_2S Trace Analysis 116

8.1.2 (CO_2 + CH_4 + H_2S) Ternary System 118
8.1.3 (CO_2 + CO + H_2S) Ternary System 118
8.2 The Partition Coefficient of H_2S 119
8.3 Comparison with Thermodynamic Models 122
8.4 Conclusions 129
Chapter 9 Conclusions and Recommendations for Future Work 130
9.1 Conclusions 130
9.2 Contribution of This Work 131
9.3 Recommendation for Future Work 133
9.3.1 Further Experimental Investigations 133
9.3.2 Further Apparatus Improvements 134
References 136
Appendices 151

List of Publications

I. Lorena FS Souza, Saif ZS Al Ghafri and JP Martin Trusler - Measurement and modelling of the vapour-liquid equilibrium of (CO_2 + CO) at temperatures between (218.15 and 302.93) K at pressures up to 15 MPa, J. Chem. Thermodynamics 126 63–73, 2018

II. Lorena FS Souza, Stefan Herrig, Roland Span and JP Martin Trusler - Experimental density and Helmholtz-energy explicit mixture model for (CO_2 + CO) (Expect to be submitted to Applied Energy by the end of December/2018)

III. Lorena FS Souza, Saif ZS Al Ghafri and JP Martin Trusler - Measurement and modelling of the vapour-liquid equilibrium of (CO_2 + CH_4) at temperatures between (218.15 and 303) K at pressures up to 9 MPa (In preparation)

IV. Lorena FS Souza and JP Martin Trusler - H_2S Trace Analysis: Measurement of the vapour-liquid equilibrium of (CO_2 + CH_4 + H_2S) and (CO_2 + CO + H_2S) systems (In preparation)

V. Sven Fürstenberg, Lorena FS Souza and JP Martin Trusler - Measurement and modelling of the vapor-liquid equilibrium of (CO_2 + CO + H_2) and (CO_2 + CO + H_2 + CH_4 + N_2) between (223 and 273) K and at pressures up to 14 MPa (In preparation)

List of Figures

Figure 2.1 Three main types of technologies developed for electric-power generation combined with CO_2 capture methods for CO_2 capture processes [33]. 6

Figure 2.2 Basic technologies for separation of gases: separation with sorbents/solvents, separation with membrane, and separation by cryogenic distillation [5]. 7

Figure 2.3 Process of power generation with pre-combustion CO_2 separation. Adapted from Jackson et al. [32]. 9

Figure 2.4 Typical temperatures and pressures in carbon capture and storage [47] processes and the phase diagram of CO_2 [33]. 11

Figure 3.1 - (p , T) projections showing behaviour diagrams for binary mixtures according to Scott and van Konynenburg [57] classification. 15

Figure 3.2 – Saturated densities and vapour pressures of pure CO: ●, VLE data calculated from the short industrial EOS of Lemmon and Span [72]; ___, SAFT-γ Mie approach fitted with like parameters from Table 3.6. 31

Figure 3.3 - Single-phase densities and isobaric heat capacities of pure CO. Data calculated from the short industrial EOS of Lemmon and Span [72] at pressures: ●, p = 10 MPa; ●, p = 20 MPa; ●, p = 40 MPa; ●, p = 50 MPa; ___, SAFT-γ Mie approach fitted with like parameters from Table 3.6. 31

Figure 4.1 Schematic diagram of the experimental apparatus used to measure low-temperature VLE. V1 to V7: inlet and outlet valves; V8 and V9: sampling valve (ROLSI Evolution IV™); T1: external platinum resistance thermometer; T2: Type K thermocouple; P1 to P3: pressure transducer; E-1: equilibrium cell; E-2: reservoir; E-3: thermostat bath (Lauda Proline model RP890). 34

Figure 4.2 Picture of the VLE apparatus as built in the Laboratory. 38

Figure 4.3 Thermal-conductivity detector (TCD) calibration data for CO (a and c) and CO_2 (b and d) with He carrier gas: (a) and (b), gas molar density ρ under filling-loop conditions against area response A; (c) and (d), deviations $\Delta\rho$ of gas molar density from Eq. (32) against area response A. O, experimental data; ——, Eq. (32). 43

Figure 4.4 Thermal-conductivity detector (TCD) calibration data for CH_4 (a and c) and CO_2 (b and d) with He carrier gas: (a) and (b), gas molar density ρ under filling-loop conditions against area response A; (c) and (d), deviations $\Delta\rho$ of gas molar density from Eq. (32) against area response A. □, experimental data; ——, Eq. (32). 44

Figure 4.5 Flame Photometric Detector (FPD) calibration data for H_2S with He carrier gas: (a), gas molar density ρ under filling-loop conditions against area response A; (b), deviations $\Delta\rho$ of gas molar density from Eq. (32) against area response A. ◇, experimental data; ——, Eq. (32). 44

Figure 4.6 Deviation $\Delta p = (p_{exp} - p_{EoS})$ between the experimental vapor pressure of pure CO_2 and the reference values p_{EoS} calculated from the equation of state of Span and Wagner [70] as a function of temperature T: ◇, this work. Error bars show the standard uncertainty of the experimental data, while the dashed lines indicate the uncertainty of the calculated vapor pressures as specified in reference [70]. 46

Figure 5.1 Schematic diagram of the experimental apparatus used to measure density. V1 and V3: inlet and outlet valves; V2: isolation and pressure relief valve; T: external platinum resistance thermometer; P: pressure transducer. 52

Figure 5.2 Picture of the density apparatus. 53

Figure 5.3 Relative deviation $\Delta\rho/\rho = (\rho_{exp} - \rho_{calc})/\rho_{exp}$ between the experimental density ρ_{exp} of pure CO_2 and the reference values ρ_{calc} calculated from the EOS of Span and Wagner [70] as a function of pressure p at T = 293.15 K. Error bars show the combined expanded uncertainty of the experimental data, while the horizontal dashed lines indicate the uncertainty of the calculated density as specified in reference [30] and the vertical dashed line indicates the vapor pressure of pure CO_2. 55

Figure 5.4 Temperature-pressure diagram of the (CO_2 + CO) system at different compositions: ___, vapor pressure of pure CO_2 calculated from the EOS of Span and Wagner [70]; ___, 0.0625 CO; ___, 0.125 CO; ___, 0.25 CO; ___, 0.5 CO all calculated from the Peng-Robinson EOS fitted with recommended binary parameters Table 3.3; **.....**, isotherms measured. 56

Figure 6.1 Temperature-pressure diagram of the (CO_2 + CO) system: x, available literature data; O, this work; – ·– ·, critical locus calculated from new mixture model; ----, vapor pressure of CO_2 from Span and Wagner EOS [70]. 60

Figure 6.2 Pressure-composition diagrams of the (CO_2 + CO) system: (■ and □), 218.15 K; (◆ and ◇), 233.15 K; (● and ○), 243.15 K; (▲ and △), 258.15 K; (■ and □), 273.15 K; (◆ and ◇), 288.15 K; (■ and □), 302.95 K, and ----, trend line. 67

Figure 6.3 Optimized parameters from asymptotic behaviour approaching the critical point applied to the binary system (CO_2 + CO): λ_1 (a), λ_2 (b), μ (c), z_c (d) and p_c (e) against temperature. ——, Eq. (49).....69

Figure 6.4 Critical point estimation by regression analysis of asymptotic behaviour approaching the critical point in Eq. (47). Pressure p vs. mole fraction z of CO divided by critical mole fraction z_c for the (CO_2 + CO) system: ◇, T = 218.15 K; X, T = 233.15 K; △, T = 243.15 K; □, T = 258.15 K; ∗, T = 273.15 K; ○, T = 288.15 K, ——, asymptotic behaviour approaching the critical point Eq. (47) at each temperature. 70

Figure 6.5 Critical loci for (CO_2 + CO) system predicted by Eq. (47). Critical temperature T_c (left) and critical pressure p_c (right) plotted against the critical mole fraction z_c of CO. 70

Figure 6.6 Relative deviations $\Delta p/p = (p_{exp} - p_{calc})/p_{exp}$ between the experimental bubble and dew pressures p_{exp} of (CO_2 + CO) [21, 75, 76, 81-83] and values p_{calc} calculated from the new mixture model as a function of pressure. ◁, Blanco et al., 2014; ¬, Christiansen et al., 1974; + Huamin, 1991; ⋎ ,Kaminishi et al., 1968; ○, this work, published by Souza et al.,2018; □, Westman et al., 2018. 71

Figure 6.7 Deviations $\Delta x = x_{exp} - x_{calc}$ and $\Delta y = y_{,exp} - y_{,calc}$ between experimental mole fractions ($x_{,exp}$, $y_{,exp}$) and the values ($x_{,calc}$, $y_{,calc}$) calculated from the Peng-Robinson EOS with recommended binary parameters for the (CO_2 + CO) system. ●, this work; □, Huamin, 1991; △, Kaminishi et al., 1968; ×, Christiansen et al., 1974; ◇, Blanco et al., 2014. (a) and (c): blue, T/K ≤ 223.15; purple, 223.15 < T/K ≤ 233.15; green, 233.15 < T/K ≤ 253.15; (b) and (d): orange, 253.15 < T/K ≤ 263.15; red, 263.15 < T/K ≤ 273.15; brown, 273.15 < T/K ≤ 288.15; dark grey, 288.15 < T/K ≤ 300. Outliers are plotted on the upper or lower horizontal axes. [76] 72

Figure 6.8 Pressure-composition diagrams of the (CO_2 + CO) system as calculated from the new mixture model. Experimental VLE data from different sources [21, 75, 76, 81-83] and models are shown for comparisons. ◁, Blanco et al., 2014; ⊣, Christiansen et al., 1974; ⅄ Huamin, 1991; ⅄ ,Kaminishi et al., 1968; ○, this work, published by Souza et al.,2018; □, Westman et al., 2018. – – –, EOS-CG; – ·– ·, GERG-2008 ——, New model. 74

Figure 6.9 Pressure-composition diagrams of the (CO_2 + CO) system: ○, this work, published by Souza et al. [76] and models: – – –, EOS-CG; – ·– ·, GERG-2008 ——, New model and ……, Peng-Robinson EOS fitted with recommended binary parameters. 75

Figure 6.10 Pressure-composition diagram of the (CO_2 + CO) system at T = 302.94 K: ○, this work; ——, new mixture model. 76

Figure 6.11 Relative volatility diagrams of the (CO_2 + CO) system at T = (233.15, 243.15, 273.15 and 288.15) K: ○, this work; ——, new mixture model.....77

Figure 6.12 Pressure-composition diagrams of the (CO_2 + CO) system: ○, this work; ——, SAFT-γ Mie with original parameters values; - - -, SAFT-γ Mie fitted. 78

Figure 6.13 Relative percentage deviations $\Delta\rho/\rho$ = (ρ_{exp} − ρ_{calc})/ρ_{exp} between the experimental density ρ_{exp} of (CO_2 + CO) and values ρ_{calc} calculated from the new mixture model as a function of the measured density. ⊽, x_{CO} = 0.05031; ⊽, x_{CO} = 0.10107; ⊽, x_{CO} = 0.25254; and ⊽, x_{CO} = 0.50183. 87

Figure 6.14 Relative percentage deviations $\Delta\rho/\rho$ = (ρ_{exp} − ρ_{calc})/ρ_{exp} between the experimental density ρ_{exp} of (CO_2 + CO) and values ρ_{calc} calculated from the new mixture model as a function of the measured density. ▽, Blanco et al., 2014; ⅄, Mallu et al., 1987; ⅄, Mallu et al., 1989; □, Cipollina et al., 2007; ○, this work.....89

Figure 6.15 Relative percentage deviations $\Delta\rho/\rho$ = (ρ_{exp} − ρ_{calc})/ρ_{exp} between the experimental density ρ_{exp} of (CO_2 + CO) and values ρ_{calc} calculated from the new mixture model as a function of the measured density, ⅄, Mallu et al., 1987; □, Cipollina et al., 2007; ⅄, Tsankova et al., 2018; ○, this work. For further comparisons, deviations from values calculated with the – – –, EOS-CG; – ·– ·, GERG-2008. 91

Figure 6.16 Compressibility factor as a function of pressure of the (CO_2 + CO) mixture with mole fraction equal to 0.5. Temperatures ranging from (283.15 to 383.15) K.: symbols, this work; ——, new mixture model. 91

Figure 6.17 Top to bottom: p,h-, p,□-, and p,T-diagrams calculated with the new mixture model for three different compositions (10, 50, 75) mol% CO at extreme conditions. Isotherms up to 2000 K and 6000 K were included in the p,h-diagram and the p,ρ-diagram, respectively, while the p,T-diagram includes isochors up to 26 mol·dm^{-3}. 93

Figure 7.1 Temperature-pressure diagram of the (CO_2 + CH_4) system: x or x, available literature data; O, SVLE data from our group (unpublished); O, this work; – ·– ·, critical locus calculated from GERG-2008; ____, vapor pressure of CO_2 from Span and Wagner EOS [70]; ____, vapor pressure of CH_4 from Setzmann and Wagner EOS [71], ____, trend line of available solid-liquid-vapor equilibrium (SLVE) data and ____, trend line of solid-liquid-vapor equilibrium (SLVE) data from our group [120]. 97

Figure 7.2 Pressure-composition diagrams for (CO_2 + CH_4) : (▲ and △), 218.15 K; (■ and □), 233.15 K; (● and ○), 243.15 K; (◆ and ◇), 258.15 K; (▲ and △), 273.15 K; (✳ and ✳); 288.15 K, (■ and □) 303.15 K, and ----, trend line. 104

Figure 7.3 Critical point estimation by regression analysis of asymptotic behaviour approaching the critical point in Eq. (47). Pressure p vs. mole fraction z of CH_4 divided by critical mole fraction z_c for the (CO_2 + CH_4) system: ◇, T = 218.15 K; x, T = 233.15 K; △, T = 243.15 K; ○, T = 258.15 K; □, T = 273.15 K; ✳, T = 288.15 K, ——, asymptotic behaviour approaching the critical point in Eq. (47) at each temperature.....105

Figure 7.4 Optimized parameters from asymptotic behaviour approaching the critical point applied to the binary system (CO_2 + CH_4): λ_1 (a), λ_2 (b), μ (c), z_c (d) and p_c (e) against temperature. ——, Eq. (49).....106

Figure 7.5 Critical loci for (CO_2 + CH_4) system predicted by Eq. (47). Critical temperature T_c (left) and critical pressure p_c (right) plotted against the critical mole fraction z_c of CH_4. 107

Figure 7.6 Pressure-composition diagrams of the (CO_2 + CH_4) system at 220 K as calculated from the GERG-2008. Experimental VLE data from different sources: ○, Donnelly et al. [117]; ◇, Neumann and Walch [130]; ✳, Mraw et al. [129]; △, Hwang et al. [126]; x, Joffe et al. [127]; –, Al-Sahhaf et al. [121]; +, Knapp et al. [128]; and – ·– ·, GERG-2008. 108

Figure 7.7 Pressure-composition diagrams of the (CO_2 + CH_4) system at 220 K as calculated from the GERG-2008. Experimental VLE data from different sources: ○, Webster and Kidnay [119]; ◇, Davalos et al. [124]; △, Wei et al. [133]; and – ·– ·, GERG-2008. 108

Figure 7.8 Pressure-composition diagrams of the (CO_2 + CH_4) system at 270 K as calculated from the GERG-2008. Experimental VLE data from different sources: ○, Webster and Kidnay[119]; ◇, Davalos et al. [124]; △, Wei et al. [133]; ✳, Somait and Kidnay[118]; –, Al-Sahhaf et al. [121]; and – ·– ·, GERG-2008. 109

Figure 7.9 Pressure-composition diagrams of the (CO_2 + CH_4) system. Experimental VLE data from different sources: ✳, Knapp et al. [128]; ✳, Arai et al. [122]; x, Xu et al. [145]; O, this work; and model: ……, Peng-Robinson EOS fitted with recommended binary parameters from Table 3.4; – ·– ·, GERG-2008 ____, SAFT-γ Mie. 111

Figure 7.10 Pressure-composition diagrams of the (CO_2 + CH_4) system: O, this work; ……, Peng-Robinson EOS fitted with recommended binary parameters from Table 3.4; – ·– ·, GERG-2008; ____, SAFT-γ Mie. 112

Figure 7.11 Relative volatility diagrams of the (CO_2 + CO) system at T = (233.15, 243.15, 273.15 and 288.15) K: ○, this work; – ·– ·, GERG-2008. 114

Figure 8.1 Pressure-composition diagrams of the (CO_2 + H_2S) system: ●, literature data; ----, Peng-Robinson EOS fitted with recommended binary parameters from Table 8.5. 123

Figure 8.2 Pressure-composition diagrams of the (CH_4 + H_2S) system: ●, literature data; ----, Peng-Robinson EOS fitted with recommended binary parameters from Table 8.5. 124

Figure 8.3 Pressure-composition diagrams of the (CO + H_2S) system: ●, literature data; ----, Peng-Robinson EOS fitted with recommended binary parameters from Table 8.5. 125

Figure 8.4 k-factor for H_2S: k = (y_{H_2S}/x_{H_2S}) measured for x_{H_2S} ≤ 200 ppm (CO_2 + CH_4 + H_2S) system: ○, 218.15 K; ○, 243.15 K; ○, 273.15 K; ○, 288.15 K; ____, Peng-

Robinson EOS fitted with recommended binary parameters from Table 3.4 and Table 3.3. 126

Figure 8.5 Relative deviations $\Delta k/k = (k_{exp} - k_{calc})/k_{exp}$ between the experimental H_2S distribution k_{exp} of (CO_2 + CH_4 + H_2S) and values k_{calc} calculated from the PR-EOS with the optimized binary parameters were presented as a function of pressure (top) and temperature (bottom). O, 218.15 K; O, 243.15 K; O, 273.15 K; O, 288.15 K; ___, PR-EOS fitted with recommended binary parameters from Table 3.4 and Table 3.3. 127

Figure 8.6 *K*-factor for H_2S: $k = (y_{H_2S}/x_{H_2S})$ measured for $x_{H_2S} \leq 200$ ppm (CO_2 + CO + H_2S) system: O, 218.15 K; O, 243.15 K; O, 273.15 K; O, 288.15 K; ____, Peng-Robinson EOS fitted with recommended binary parameters from Table 3.3 and Table 3.3. 128

Figure 8.7 Relative deviations $\Delta k/k = (k_{exp} - k_{calc})/k_{exp}$ between the experimental H_2S distribution k_{exp} of (CO_2 + CO + H_2S) and values k_{calc} calculated from the PR-EOS with the optimized binary parameters were presented as a function of pressure (top) and temperature (bottom). O, 218.15 K; O, 243.15 K; O, 273.15 K; O, 288.15 K; ____, PR-EOS fitted with recommended binary parameters from Table 3.3 and Table 3.3. 129

List of Tables

Table 2.1 - Possible impurities associated with different CO_2 capture technologies. Source: IPCC 2005 [48]. 11

Table 2.2 - Average compositions of CO_2-rich stream captured by the briefly described capture technologies: oxy-fuel, pre-combustion and post-combustion [17]. 12

Table 3.1 Examples of Cubic EOS rooted in the van der Waals theory. 17

Table 3.2 Critical temperature T_c, critical pressure p_c and acentric factor ω used in the thermodynamic models calculations.....19

Table 3.3 Coefficients $k_{12,1}$ and $k_{12,2}$ and objective function S for the (CO_2 + CO) system fitted in this work. 20

Table 3.4 Coefficients $k_{12,1}$ and $k_{12,2}$ and objective function S for the (CO_2 + CH_4) system fitted in this work. 20

Table 3.5 Available experimental data of the mixture (CO_2 + CO) for VLE and homogeneous densities from the present equation of state. * represent the data used for fitting the new mixture model. 25

Table 3.6 Parameters of the new equation of state. 27

Table 3.7 Like parameters for use within the SAFT-γ Mie group-contribution approach: the number of spherical segments v^*_k, the shape factor S_k, the segment diameter σ_{kk}, the dispersive energy ε_{kk}, k_B is the Boltzmann constant and the repulsive and attractive exponents λ^r_{kk} and λ^a_{kk}. 32

Table 3.8 Unlike parameters for use within the SAFT-γ Mie group-contribution approach: the dispersion interaction energy ε_{kl} and repulsive exponent λ^r_{kl}. 32

Table 4.1 Description of chemical sample, where x is mole fraction. 36

Table 4.2 – Determination of the overall risk level of each chemical substances used in the experimental procedure with ABC method. 37

Table 4.3 Optimized gas chromatograph conditions for separation of CO_2 from CO. .40

Table 4.4 Optimized gas chromatograph conditions for separation of CO_2 from CH_4. 41

Table 4.5 Optimized gas chromatograph conditions for separation of the ternaries....41

Table 4.6 Optimized Calibration Parameters for CO_2 and CO. 45

Table 4.7 Optimized Calibration Parameters for CO_2, CH_4 and H_2S. 45

Table 4.8 Description of samples, where z is the mole-fraction purity specified by the supplier, and x is the mole fraction of either CO or CH_4 and $u(x)$ is the standard uncertainty of x in the mixtures.....45

Table 5.1 Description of samples, where z is the mole-fraction purity specified by the supplier, and x is the mole fraction of CO and $u(x)$ is the standard uncertainty of x in the mixtures of CO_2 and CO.....51

Table 5.2 Coefficients of the polynomial calibration model, Eq. (43) for the vibrating-tube densimeter. 54

Table 5.3 Uncertainty budget for density ρ at pressure p = 28 MPa and temperature T = 313.15 K, where τ is period of oscillation and subscripts 1 and 2 refer to the calibration fluids helium and water, respectively. Sensitivity factors associated with temperature and pressure were estimated from the new mixture model for the (CO_2 + CO) system developed in this work (see Section 4). 58

Table 6.1 Summary of the literature data available for the vapor-liquid equilibria of the (CO_2 + CO) system. 60

Table 6.2 Summary of the literature data available for the density of the (CO_2 + CO) system. 61

Table 6.3 Experimental VLE data for the (CO_2 + CO) system at temperature T, pressure p, vapor mole fraction of CO y, and liquid mole fraction of CO x.[a] 62

Table 6.4 Coefficients of Eqs. (47) and (49) for the critical locus. 69

Table 6.5 Density ρ for (CO_2 + CO) mixture x of 0.05031 at temperatures T and pressure p.[a] 79

Table 6.6 Density ρ for (CO_2 + CO) mixture x of 0.101073 at temperatures T and pressure p.[a] 81

Table 6.7 Density ρ for (CO_2 + CO) mixture x of 0.25254 at temperatures T and pressure p.[a] 83

Table 6.8 Density ρ for (CO_2 + CO) mixture x of 0.50183 at temperatures T and pressure p.[a] 85

Table 7.1 Summary of the literature data available for the vapor-liquid equilibria and solid-liquid-vapor equilibria of the (CO_2 + CH_4) system. 98

Table 7.2 Summary of the literature data available for the density of the (CO_2 + CH_4) system. 99

Table 7.3 Experimental VLE data for the (CO_2 + CH_4) system at temperature T, pressure p, vapor mole fraction of CH_4 y, and liquid mole fraction of CH_4 x.[a] 101

Table 7.4 Coefficients of Eqs. (47) and (49) for the critical locus. 106

Table 8.1 - Summary of the literature data available for the vapor-liquid equilibria of (CO_2 + H_2S), (CH_4 + H_2S) and (CO + H_2S) systems. 117

Table 8.2 - VLE data of the (CO_2 + CH_4 + H_2S) system. 118

Table 8.3 - Experimental partition coefficient of H_2S k of the (CO_2 + CH_4 + H_2S) system at temperature T, pressure p.[a] 119

Table 8.4 - Experimental partition coefficient of H_2S k of the (CO_2 + CO + H_2S) system at temperature T, pressure p.[a] 120

Table 8.5 Coefficients $k_{12,1}$ and $k_{12,2}$ and objective function S for the (CO_2 + CO) system fitted in this work. 125

Chapter 1 **Introduction**

1.1 Introduction

Climate change is one of the biggest challenges of the 21st century. It is certainly influencing the planet with many observable effects [1, 2]. The consensus among the vast majority of scientists is that the main cause of the current climate change effects stem from anthropogenic emissions of greenhouse gases. Since the Industrial Revolution, the burning of fossil fuels like coal and oil has drastically increased the atmospheric concentration of greenhouse gases (GHGs), of which the most predominant is carbon dioxide (CO_2). This year, atmospheric CO_2 levels have reached 410 ppm [3] and this represents an increase of 30% since 1960. It is undeniable that major reductions of global CO_2 emissions are necessary to mitigate climate change. A crucial response to tackle this problem came at the COP21 meeting in December 2015, where 195 countries committed to limit warming to less than 2°C, with a stated aim of limiting the increase to 1.5°C if possible [4].

Currently, the global energy and industrial sectors combined represent almost half of the CO_2 emissions [1]. Further, energy demand is projected to keep increasing as a consequence of the growth on global population and economic development of fast emerging economies [5, 6]. In fact, the global energy demand is expect to double by 2050 [7]. It is not a surprise that there is an urgent need for the decarbonisation of the energy and industrial sectors. This can be achieved through a combination of actions such as demand reduction, increased efficiency in the utilisation of energy, switching to low- or zero-carbon fuels, improvements in the collection, storage and transmission of energy from renewable sources, and carbon capture and storage [8]. CCS is recognised as a key technology for delivering low-carbon heat and power production and decarbonising industries such as cement and iron/steel production [9]. The major technical and economic challenges are in the carbon capture stage, with the gas separation processes, typically both air separation and syngas processing [10-12]. If and when CCS is deployed on the scale understood to be required, the aforementioned challenges involved on this process should be addressed over the course of the next decade.

1.2 Scope and Objectives

For the design, optimization and safe operation of all CCS processes, including pre-combustion carbon capture, the accurate description of thermodynamic properties is crucial. In particular, processes such as separation of gas mixtures and pipeline transportation of CO_2 in CCS processes require a detailed thermodynamic analysis [13]. In addition, the capture, transport and storage of CO_2 does not involve pure CO_2 streams, but CO_2-rich mixtures containing various impurities. The particular impurities and their concentration can vary significantly depending on the type of fuel, capture process (post-combustion, pre-combustion, and oxy-combustion), and separation technology (absorption, adsorption, membranes, cryogenic distillation, gas hydrates, and chemical looping) used [14-17]. There are many studies regarding the different separation technologies and the associated spectrum of impurities [15, 18-20]. One promising approach is to use a pre-combustion capture process incorporating low-temperature elevated-pressure flash separation, which allows significant savings on the compression work required for pipeline transportation and storage of CO_2. In this type of process, the most likely impurities are non-condensable gases, such as H_2, N_2, O_2, Ar, CH_4 and CO, and trace levels of acid gases such as H_2S and COS [15, 20]. Such impurities can considerably alter the phase equilibria and other thermophysical properties of the CO_2-rich stream as shown in, for example, the work of Blanco et al. [21], Ahmad et al. [22] and Chapoy et al. [23].

A wide range of models are available to calculate thermodynamic properties of CO_2-rich mixtures. The most commonly used models are cubic equations of state (EOS) and derivative thereof, such as the Peng and Robinson EOS [24] and the Cubic Plus Association EOS [25]. However, while cubic EOS generally offer a reliable description of phase equilibria, these models typically show quite poor accuracy in the description of other thermodynamic properties especially densities [26]. In contrast, multi-fluid Helmholtz-energy models can, when fully parameterised, describe accurately both phase behaviour and phase properties [27, 28].

A common approach to predict the thermodynamic properties of mixtures is to use multi-fluid Helmholtz-energy models incorporating highly-accurate pure-fluid EOS [27]. In order to adjust the binary parameters that appear in those models, reliable and accurate experimental data on phase equilibria are indispensable. In fact, combining

experimental phase-equilibrium data with multi-parameter Helmholtz-energy models is a highly successful way to reduce the amount of experimental data needed to describe a system, while at the same time improving the predictive capability of the EOS.

More recently, the use of the Statistical Associating Fluid Theory (SAFT), such as the SAFT-γ Mie group contribution approach [29, 30], to describe fluids of interest in CCS applications have attracted some attention. Again, experimental data are needed in order to fit parameters in the model.

The main objectives of this research can, therefore, be summarised as follows:

I. To carry out comprehensive reviews of the available data on phase equilibria and thermophysical properties of binary, ternary and multi-component systems relevant to CCS processes, with focus on pre-combustion carbon capture and pipeline transportation. Specifically, to: (a) identify gaps and discrepancies among different data in the literature; and (b) assess the capability of available apparatus in the Thermophysics group to measure the data required to fill these gaps.

II. To study phase equilibria of the selected binary systems: (CO_2 + CH_4) and (CO_2 + CO), over wide ranges of temperature and pressure. Additionally, to investigate the distribution of trace levels of H_2S between the liquid and vapour phases for the same systems at similar temperature and pressure conditions.

III. To study the homogenous density of the selected binary system: the (CO_2 + CO), over a wide range of temperature and pressure.

IV. To select appropriate thermodynamic models to describe the thermodynamic properties of CO_2-rich mixtures in relevant CCS processes, pre-combustion carbon capture and pipeline transportation. Optimization and further development of thermodynamic models where necessary and possible. This includes the assessment of the performance of the models compared to the new data and to the available data in the literature.

1.3 Thesis Outline

Chapter 2: A literature review of carbon capture technologies, phase behaviour and density of CO_2 mixture relevant to CO_2 capture and transportation processes is presented in this chapter. Different techniques used to measure VLE and density are also discussed therein.

Chapter 3: A overview of EOS for mixtures is briefly described in this section. Cubic equations of state, which are the most commonly used models to calculate thermodynamic properties, are introduced with its conventional and non-conventional mixing rules. Here, the mathematical development of empirical multi-fluid Helmholtz-energy models: GERG-2008, EOS-CG and the new mixture model for the (CO_2 + CO) system developed in this work are presented. Finally, a brief introduction on the SAFT-γ Mie group contribution approach is provided. Most importantly, this chapter includes the fitting procedure of PR-EOS, the new mixture model and SAFT-γ Mie with preliminaries results.

Chapter 4: The VLE apparatus design and related experimental methodology are described in this chapter. It includes discussion of the safety procedures implemented, validation and calibration, and uncertainty analysis.

Chapter 5: The density apparatus design and related experimental methodology are described in this chapter. It includes validation, calibration and uncertainty analysis.

Chapter 6: Experimental VLE and homogeneous density results for the (CO_2 + CO) system can be found in this chapter. Comparisons among models, including the new mixture model, literature data and results from this work are also presented.

Chapter 7: Experimental VLE results for the (CO_2 + CH_4) system can be found in this chapter. Comparisons among models, literature data and results from this work are also presented.

Chapter 8: The distribution of trace levels of H_2S between the two phases from the two relevant binary systems: (CO_2 + CH_4) and (CO_2 + CO) are presented in this chapter.

Chapter 9: Conclusions from this work, identifying the key contributions, are summarised, in addition to the discussion on relevant areas of this research to be usefully extended.

Chapter 2 Context of CO_2 Capture, Transportation and Storage

2.1 Overview

In order to tackle climate change, the ideal solution would be to completely switch to a new way to generate electricity that produced little or no GHGs. However, it is unlikely that the increased demand of electricity would be met without the continued use of fossil-fuel power stations to some extent [9, 31]. If the COP21 meeting's target for reduction on GHGs emissions is to be achieved, therefore, some additional strategy must be employed. As mentioned before, this can be achieved through a combination of actions including CCS [8].

CCS is recognised as a key technology for delivering low-carbon heat and power production and decarbonising industries such as cement and iron/steel production [9]. It starts with the CO_2 capture, which can occur through different separation processes. Then, this process is followed by secure transportation and finally storage of CO_2 in underground geological formations.

2.2 CO_2 Capture

Figure 2.1 shows the three main types of technologies developed for electric-power generation combined with CO_2 capture: post-combustion, pre-combustion and oxy-fuel combustion.

In the post-combustion capture process, the CO_2 produced by the conventional combustion of fuel, such as coal, is captured from the exhaust flue gases before they are vented into the atmosphere. As the fuel is burnt in air, these flue gases include around 78% nitrogen, which makes the recovery of the CO_2 more difficult [32]. One way to overcome this problem is to use the oxy-combustion capture process instead, which burns the coal in pure oxygen rather than air. However, the large-scale separation of oxygen from air for this purpose is costly and energy-intensive to

operate. An advanced alternative technology is the pre-combustion capture, explained in detailed below.

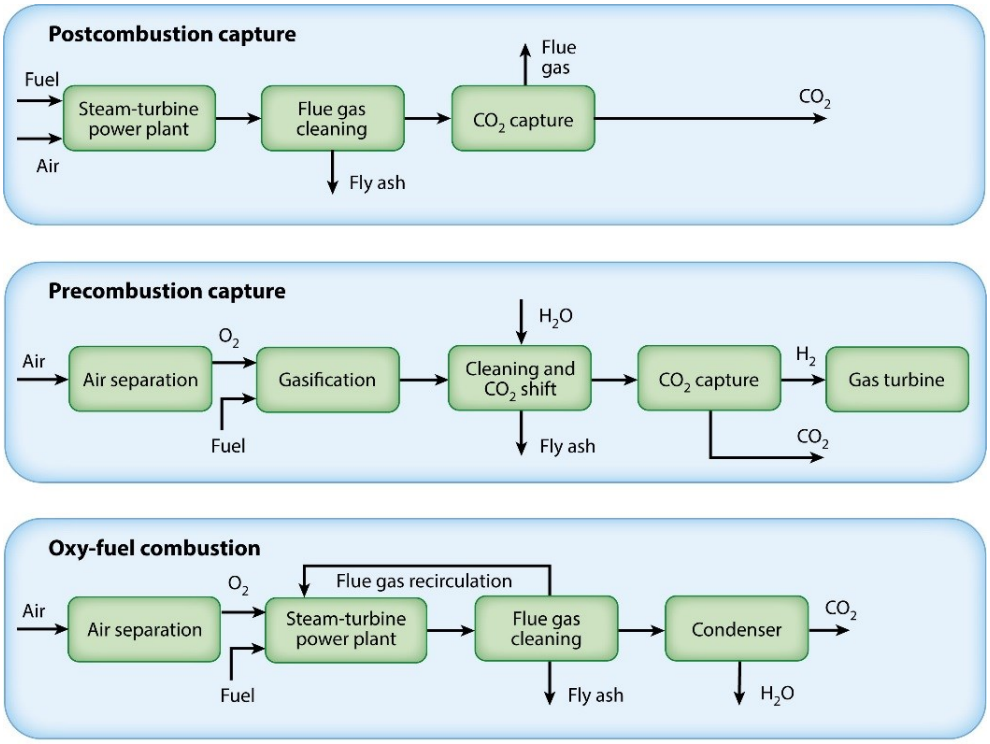


Figure 2.1 Three main types of technologies developed for electric-power generation combined with CO_2 capture methods for CO_2 capture processes [33].

2.2.1 Pre-Combustion Carbon Capture Technology

Pre-combustion capture process has been the focus of number of studies recently [22, 34-37] and has the potential to permit the continued use of fossil fuels such as coal or natural gas for energy generation while, at the same time, reduces CO_2 emissions. The process starts with the gasification of the fuel to produce a mixture of mainly CO and H_2, known as syngas (see Figure 2.1). Following the gasification process, steam is added to the syngas to increase the production of H_2 and convert CO into CO_2 in the process called water-gas shift reaction as following

$$CO + H_2O \Leftrightarrow CO_2 + H_2 .$$

Typically, H_2S is removed from the syngas rich in CO_2 by means of a solvent absorption unit. The H_2S is commonly sent to a gas treatment side plant, where it can be turned into re-usable by-products such as sulphur by utilizing the modified Claus

process. The main stream, rich in CO_2 and H_2, is directed to a separation process. The conditions for CO_2 separation in pre-combustion capture processes will be quite different from those in post-combustion capture. For example, the CO_2-H_2 main stream from a pre-combustion capture process is comprised of 35-40% CO_2 and at pressure of 2 MPa or more, while the similar stream from post-combustion capture process would be significantly more diluted by the presence of N_2 [5].

Pre-combustion capture technology offers an attractive route to the decarbonising of industries such as cement and iron/steel production as it is comparatively easier to capture CO_2, owing to its higher concentration in the exhaust flue gas stream. Additionally, this process removes pollutants generated in the gasification process more efficiently and economically [38].

2.2.2 Gas Separation Processes

It is known that the major technical and economic challenges are in the carbon capture stage, with the gas separation processes, typically both air separation and syngas processing [10-12]. The main technologies for the syngas separation can be divided in three groups: separation with sorbents/solvents, separation with membrane, and separation by cryogenic distillation. A schematic is shown on Figure 2.2.

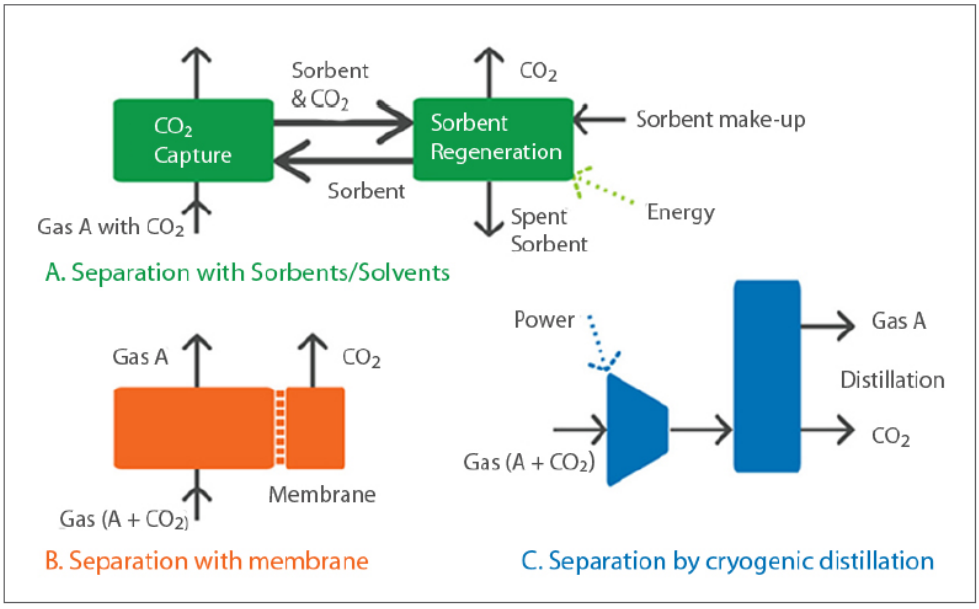


Figure 2.2 Basic technologies for separation of gases: separation with sorbents/solvents, separation with membrane, and separation by cryogenic distillation [5].

Separation with amine (solvent), is the bets established of the methods available for CO_2 capture, with monoethanolamide the most used solvent [39]. It presents the advantage of achieving high rates of CO_2 recovery, up to 98%, and also high purity product, over 99%. However, the amount of energy required for the regeneration and the degradation rate of most solvents used in oxidising environment are limitations to be concerned. Studies suggested that improved solvents could reduce energy requirements by as much as 40% compared to conventional MEA solvents [40]. CO_2 can also be separated from the syngas by solid adsorbents, such as zeolites and activated carbon, in either pressure swing adsorption (PSA) or temperature swing adsorption [41] process. Adsorption is not yet considered attractive for large-scale separation of CO_2 from flue gas because the capacity and CO_2 selectivity of available adsorbents are still low. However, it may be considered in combination with another CO_2 capture technology.

Membranes are another means by which CO_2 can be separated from syngas. As membranes cannot usually achieve high degrees of separation, it is generally used in multiple stages and/or with recycling of one of the streams. Gas separation by membranes requires elevate energy consumption and significant maintaining costs. and much development is required. Even thought, membranes are prospective mean for pre-combustion carbon capture, those remaining issues need to be resolved before before membranes could be efficiently and economically used on a large scale for CO_2 capture [37, 42].

Cryogenic separation is widely used for streams that have high CO_2 concentrations (typically >90%) [37]. One of the most important advantages of this physical separation process is that it enables direct production of liquid CO_2, which means significant cost saving on energy to compress the CO_2 stream for transportation [32]. However, this process has not yet been commercially developed for more dilute CO_2 streams. Cryogenic separation could be more efficiently applied to gas separation processes of streams with high pressure, such as in pre-combustion capture, with considerably decreasing on energy consumption.

2.2.3 Pre-Combustion Carbon Capture by Low-Temperature Separation

A new solution to the challenge of reducing cost while improving efficiency of the CO_2 capture stage was proposed by Costain: the Next Generation Capture Technology (NGCT) [32]. The new process is based on a patented low temperature physical separation technology involving a sequence of compressions to remove the CO_2 from the syngas [32]. A power-generation process based on this approach is illustrated in Figure 2.3.

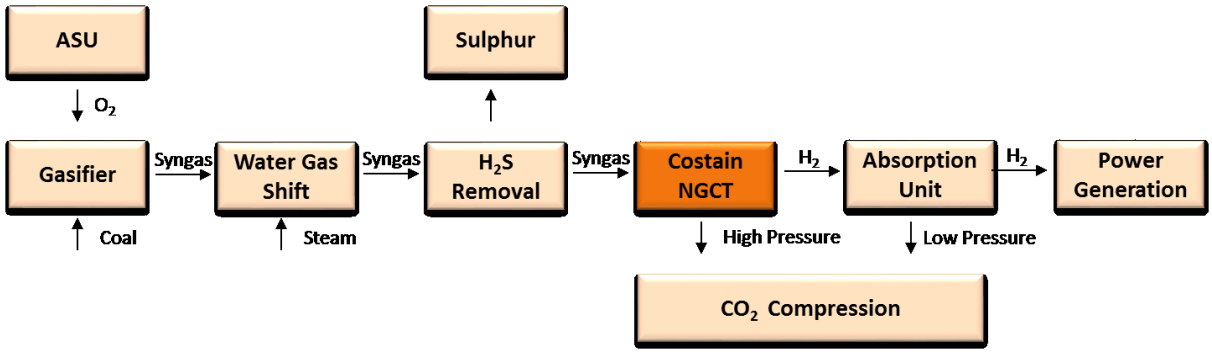


Figure 2.3 Process of power generation with pre-combustion CO_2 separation. Adapted from Jackson et al. [32].

The low temperature separation technology can remove up to 75% of CO_2; which can increased to around 95% or higher if a solvent absorption unit is introduced as a secondary CO_2 capture process. NGCT significantly reduces the size of the CO_2 compressors needed to prepare the CO_2 stream to transportation, offering significant cost savings compared with traditional amine based absorption processes. Another alternative is the use of physical solvents, such as Selexol®, as a secondary CO_2 capture process. Selexol® has the advantage of being regenerated by depressurisation, thereby avoiding the high heat consumption of amine processes. [8]

2.3 CO_2 Transportation

The CO_2 transportation is considered to be the most technologically mature stage of the CCS processes. Following the CO_2 capture, CO_2-rich stream is compressed and generally transported through pipeline network in liquid or supercritical conditions in a

similar process already used for the transportation of oil and gas. CO_2 has been transported by pipeline network with the purpose of enhanced oil recovery (EOR) in some countries, including the USA and Brazil.

The transport of CO_2 does not involve pure CO_2 streams, but CO_2-rich mixtures containing various impurities, which significantly affect the thermophysical properties [15, 16, 23, 43, 44]. Therefore, the development of accurate modelling tools is fundamental to the safe and economical design and operation of CO_2 transportation in pipelines.

2.4 CO_2 Storage

The final stage of the CCS processes is the safe storage of the CO_2-rich mixtures into deep porous reservoir. This work are not considering the temperature, pressure and components conditions of this stage. A number of reviews approach the challenges and recent developments of this stage, such as Bui et al. and Trusler [9, 33].

2.5 Evaluation of Impurities

Figure 2.4 shows the typical ranges of temperature and pressure encountered in CCS processes, which can significant vary depending of the process. The conditions for CO_2 capture vary mainly depending on the technology used for the separation, which also directly influence the composition and quantity of impurities in the main streams [15, 45]. The conditions for pipeline transportation vary from liquid or supercritical conditions in a CO_2 pipeline network to gas phase for local distribution. Finally, the storage conditions, high temperature and pressure, reflect the reservoir operational conditions [46].

Analysis and assessment of impurities in the H_2 + CO_2 stream before the separation process and the CO_2-rich stream after separation are fundamental to understand the way impurities interfere in stream behaviour of the studied process. For instance, the presence of non-condensable components such as oxygen, argon and nitrogen increases the amount of energy required to compress the CO_2-rich stream.

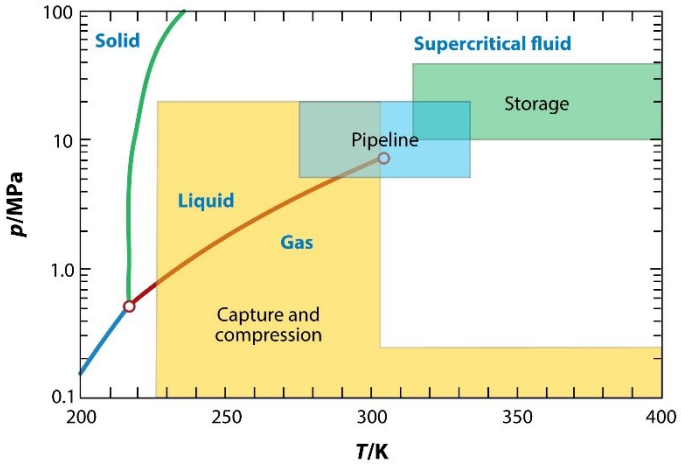


Figure 2.4 Typical temperatures and pressures in carbon capture and storage [47] processes and the phase diagram of CO_2 [33].

Concentration and type of impurities vary depending on a number of factors, including the type of CO_2 capture technology, the quality of the fuel source and the efficiency of the separation process. Review on different CO_2 capture technologies from Li et al. [15] presents the most common impurities for each of the most used CO_2 capture technologies (see Table 2.1).

Table 2.1 - Possible impurities associated with different CO_2 capture technologies. Source: IPCC 2005 [48].

CO_2 capture technologies description	Possible impurities
CO_2 capture from natural gas sweetening	CH_4, amines, H_2O
CO_2 capture from heavy oil production and upgrading	H_2S, N_2, O_2, H_2O, H_2, COS, Ar, SO_X, NO_X
CO_2 capture from power plants using post-combustion capture	Amines, H_2S, N_2, O_2, NH_3, SO_X, NO_X
CO_2 capture from power plants using oxy-combustion capture	H_2S, N_2, O_2, Ar
CO_2 capture from power plants using pre-combustion capture	H_2S, N_2, H_2, CO, CH_4

A number of reviews approach the composition of CO_2-rich stream associated with the different CO_2 capture technologies, such as Porter et al., Martynov et al., and Najafi-Marghmaleki et al. [17, 49, 50].

Table 2.2 presents an average compositions of CO_2-rich stream captured by the briefly described capture technologies: oxy-fuel, pre-combustion and post-combustion [17]. IT can been seen that the presence or not of components such as O_2, H_2S, NOx, CO, H_2 and CH_4 are directed related with the different CO_2 capture technologies.

Table 2.2 - Average compositions of CO_2-rich stream captured by the briefly described capture technologies: oxy-fuel, pre-combustion and post-combustion [17].

	Oxy-fuel[a]	Pre-combustion[b]	Post-combustion[c]
CO_2 (% v/v)	96.78	98.07	99.8
O_2 (% v/v)	1.2	–	0.015
N_2 (% v/v)	1.6	0.02	0.045
Ar (% v/v)	0.4	0.018	–
NOx (ppmv)	150	–	20
SO_2 (ppmv)	36	700	10
H_2O (ppmv)	–	150	100
CO (ppmv)	–	1300	10
H_2S (ppmv)	–	1700	–
H_2 (ppmv)	–	15000	–
CH_4 (ppmv)	–	110	–

[a] Pipitone et al. [51]; [b] Geological Storage of Carbon Dioxide Guidance Document [52]; [c] Kather et al. [53].

The challenge of the prediction of the thermophysical properties and phase behavior in the CCS processes is a direct reflection of the wide ranges of composition, temperature and pressure. This work focuses on mixtures rich in CO_2 with compositions typical of either pipeline transportation or pre-combustion synthesis-gas processing. The major components are considered as those present in high concentrations before the separation stage (at least 10% of the stream concentration). In pre-combustion CO_2 capture, they are CO_2, H_2 and N_2. Similarly, the minor

components in the mentioned process are considered as those existing in considerably low concentration before the separation stage, such as CO, CH_4 and H_2S.

Thus, relevant VLE data of binaries systems containing CO_2 are: (CO_2 + N_2), (CO_2 + H_2), (CO_2 + CH_4), (CO_2 + CO). The VLE measurement and thermodynamic modelling of (CO_2 + N_2) and (CO_2 + H_2) was published by our group in Fandiño et al. [54] and the remaining systems: (CO_2 + CH_4) and (CO_2 + CO) are measured in this work. Besides, this work includes the measurement of homogeneous density of the (CO_2 + CO) system and assessment and development of thermodynamic models for both systems. Finally, the distribution of trace levels of H_2S between the two phases from the two relevant binary systems: (CO_2 + CH_4) and (CO_2 + CO) were measured.

Chapter 3 **Equations of State for Mixture**

3.1 Overview

Equations of State (EOS) allow the calculation of thermodynamic properties and are extremely useful in various industries [28]. EOS relate the properties pressure *p*, volume *v* and temperature *T* of a fluid in the state of thermodynamic equilibrium. While all thermodynamic properties can be obtained from a fundamental EOS, a PVT EOS needs an additional expression for the ideal-gas heat capacity before all thermodynamic properties can be obtained. Desired characteristics of a successful EOS include accuracy, consistency, computational speed, robustness, and predictive ability outside of the domain where they have been fitted [55, 56].

This chapter presents a brief description of the types of phase behaviour as classified by Scott and van Konynenburg [57] and a summary of some of the most commonly used EOS in the context of CCS processes, mainly in the gas separation processes and pipeline transportation of CO_2-rich mixtures. The models used for comparisons with the data measured in this work are: Peng-Robinson equation of state (PR-EOS) [24], GERG-2008 [26], EOS-CG [58] and SAFT-γ Mie [29]. Furthermore, new data were used to fit three of the mentioned models: PR-EOS with classical mixing rule; a Helmholtz-free-energy explicit EOS (new mixture model as it will be called throughout this thesis); and finally SAFT-γ Mie, a group-contribution version of the Statistical Associating Fluid Theory (SAFT) which was implemented with the generalized Mie potential to represent segment-segment interactions. Here, new like and unlike parameters are presented for the pure CO, and the CO_2-CO cross interaction.

3.2 Phase Behaviour of Pure Substances and Binary Systems

The phase behaviour of pure components can be described by *T*-*v*, *p*-*v* and *p*-*T* diagrams. The diagram shows all conditions at which phases can coexist at equilibrium. It also represents the critical point, defined as the point at which the saturated liquid and vapour phases become indistinguishable. The temperature and pressure at these conditions are known as critical temperature and critical pressure, respectively.

In general, the complexity of phase behaviour increases with the number of components, as well as their molecular structure and size. The phase behaviour of a binary system is more complex than that a pure component. Thus, to describe binary systems, three independent variables are necessary instead of the two that are required for pure component systems. Instead of being graphically represented with three dimensional diagrams, they are generally represented with two dimensional projections such as *T-x, T-v*, *p-v* and *p-T* diagrams for simplicity. The diagram of the binary systems also shows all conditions under which phases can coexist at equilibrium.

According to Scott and van Konynenburg [57], the phase behaviour of fluids can be classified into six main types (shown in Figure 3.1). All of these, except for type VI, can be predicted with a simple EOS such as the van der Waals.

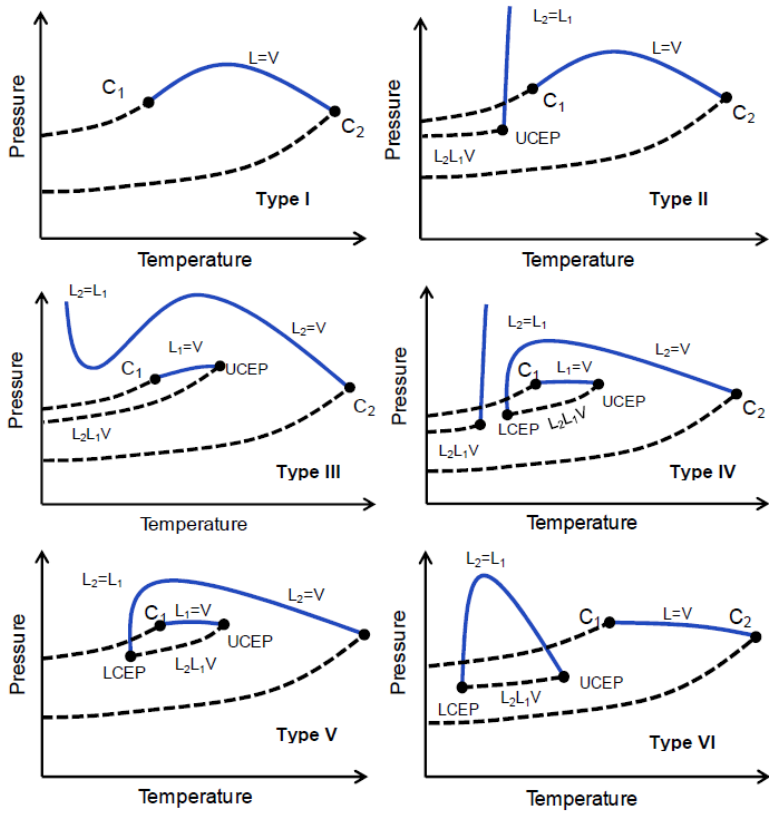


Figure 3.1 - (*p* , *T*) projections showing behaviour diagrams for binary mixtures according to Scott and van Konynenburg [57] classification.

3.3 Cubic Equations of State

Cubic EOS rooted in the van der Waals theory [59], such as the PR-EOS [24], Soave-Redlich-Kwong equation of state (SRK-EOS) [60] and the Cubic Plus Association EOS [25] have been widely and successfully applied for the past 40 years in process engineering calculations. They benefit from simplicity, low-computational requirements and straightforward implementation.

Cubic EOS was first suggested for fluid phase equilibria calculations by van der Waals in 1873. It comprises two terms: a repulsive term, incorporating the effects of repulsive intermolecular forces, and a second term which incorporates attractive intermolecular iterations. The pressure p is related to the temperature T, universal gas constant R, and molar volume v as follows:

$$p = \frac{RT}{v-b} - \frac{a}{v^2}. \tag{1}$$

Here, the pure component parameters a and b represent a measure of attractive forces between the molecules and the size of the molecules, respectively. At a particular temperature, Eq. (1) yields p-v curves that exhibit a maximum and a minimum at two points where $(\partial p/\partial v)_T = 0$. As temperature increases the maximum and minimum coalesce into a single inflection point where $(\partial p/\partial v)_T = 0$ and $(\partial^2 p/\partial v^2)_T = 0$. If required that the EOS has a horizontal point of inflexion at the critical temperature and pressure, T_c and p_c respectively, then a and b are given by the following expression

$$a = 0.421875\,(RT_c)^2 / p_c \tag{2}$$

$$b = 0.125 RT_c / p_c \tag{3}$$

Over the years, many modifications at the van der Waals EOS have been proposed to address deficiencies such as inaccuracy on the prediction of properties of compressed gases and liquids [61]. Some examples of Cubic EOS rooted in the van der Waals theory are listed in Table 3.1.

Table 3.1 Examples of Cubic EOS rooted in the van der Waals theory.

Reference	Cubic EOS	Ref.	Eq.
Redlich-Kwong (1949)	$p = \frac{RT}{v-b} - \frac{a}{v(v+b)T^{0.5}}$	[62]	(4)
Soave-Redlich-Kwong [60]	$p = \frac{RT}{v-b} - \frac{a(T)}{v(v+b)}$	[60]	(5)
Peng-Robinson (1976)	$p = \frac{RT}{v-b} - \frac{a(T)}{v(v+b)+b(v-b)}$	[24]	(6)
Patel-Teja (1982)	$p = \frac{RT}{v-b} - \frac{a(T)}{v(v+b)+c(v-b)}$	[63]	(7)

For PR-EOS, Eq. (6), $a(T)$ is a temperature-dependent energy parameter given for a single-component fluid by

$$a(T) = 0.457235\,(RT_c)^2\,\alpha(T)\,/\,p_c \tag{8}$$

b is a co-volume parameter given for a single-component fluid by

$$b = 0.077796\,RT_c\,/\,p_c \tag{9}$$

The alpha function $\alpha(T)$ is given in terms of the acentric factor of the pure component ω in the following expression:

$$\alpha(T) = \left[1 + \left(0.37464 + 1.54226\,\omega - 0.26992\,\omega^2\right)\left(1 - \sqrt{T/T_c}\right)\right]^2 \tag{10}$$

In order to improve the description of the saturation pressure curve $p_{sat}(T)$ for pure component and mixtures, many studies have presented modified alpha functions [64]. For example, the modified alpha function proposed by Mathias and Copeman [65] for polar compounds is given by

$$\alpha(T) = \left[1 + c_1\left(1 - \sqrt{T/T_c}\right) + c_2\left(1 - \sqrt{T/T_c}\right)^2 + c_3\left(1 - \sqrt{T/T_c}\right)^3\right]^2, \tag{11}$$

where c_1, c_2 and c_3 are adjustable parameters.

This modification has been proven to provide a reasonable correlation of $p_{sat}(T)$ in a number of works, including the description of the phase equilibria of the (H_2S + CH_4) system by Coquelet et al. [66]. Recommendations concerning the alpha functions can be found in the literature, including the recent reviews of Valderrama [61] and Lopez-Echeverry et al. [64].

In this work, the modified alpha function proposed by Mathias and Copeman from Eq. (11) was not used because, for the fluids studied, the standard PR-EOS with the standard alpha function from Eq. (10) gives an adequate description of the vapour pressures curves.

Cubic EOS are most commonly extended to mixtures by means of mixing rules, which relate the properties of pure components to the properties of the mixture. Over the years, many mixing rules were developed to replace parameters *a* and *b* with a composition-dependent expression. The most commonly used mixing rules are the classical van der Waals one-fluid rules [67], given as follows:

$$a = \sum_i \sum_j x_i x_j a_{ij} \tag{12}$$

$$b = \sum_i \sum_j x_i x_j b_{ij} \,. \tag{13}$$

Here, a_{ii} and b_{ii} are the equation of state parameters for pure components and cross parameters a_{ij} and b_{ij} ($i \neq j$) are determined by an appropriate combining rules, such as the combining rule proposed by van der Waals:

$$a_{ij} = (1 - k_{ij}) \sqrt{a_i a_j} \tag{14}$$

$$b_{ij} = (b_i + b_j) / 2 \tag{15}$$

Here k_{ij} is an adjustable parameter so called binary interaction parameter, which is commonly obtained by fitting experimental VLE data. It's worth noting that, with the combining rule from Eq. (15), the Eq. (13) reduces to a linear rule.

Although k_{ij} can be merely represented as a constant, a variety of empirical models were developed to improve the representation of different systems, generally by a function of temperature. As for alpha functions, recommendations on k_{ij} estimations can also be found widespread in the literature [64].

Further modifications of the conventional combining rules are generally required for systems of strongly polar and hydrogen-bonded fluids, or natural gas mixtures. For example, the b_{ij} term can be calculated from the following, instead of Eq. (15),

$$b_{ij} = (1 - l_{ij})(b_i + b_j) / 2 \tag{16}$$

where l_{ij} is an adjustable binary interaction parameter, set to either zero or constant. A temperature-dependent correlation for l_{ij} was not considered because this can lead to unphysical behavior such as *p*-*v* isotherms crossing [68]. Others non-conventional

mixing rules used in the description of strongly polar and hydrogen-bonded fluids can be found in the literature [64].

More recent modifications of PR-EOS include the Predictive Peng-Robinson 1978 (PPR78) EOS by Jaubert and Mutelet [69]. PPR78 incorporates its own group contribution method for estimating k_{ij}.

3.3.1 PR-EOS with Van der Waals Mixing Rules

In this work, the PR-EOS with van der Waals mixing rules is fitted to the new VLE data measured of both (CO_2 + CH_4) and (CO_2 + CO) systems. While k_{ij} from Eq. (14) is represented as a linear function of inverse temperature: $k_{ij} = k_{ij,0} + k_{ij,1}/T$, l_{ij} from Eq. (16) is either zero or constant, leading to up to three adjustable parameters per binary mixture. As explained in the work of Fandiño et al. [54], a temperature-dependency for l_{ij} was not considered because this can lead to unphysical behavior. The optimum values of the binary interaction parameters $k_{ij,0}$, $k_{ij,1}$ and l_{ij} were found by minimization of the objective function S defined as follows:

$$S^2 = \frac{1}{N}\sum_{i=1}^{N}\left[(x_{2,i} - x_{2,i,\mathrm{calc}})^2 + (y_{2,i} - y_{2,i,\mathrm{calc}})^2\right]. \tag{17}$$

Here N is the total number of equilibrium state points used in the regression and subscript ‘calc’ indicates values calculated from the PR-EOS. This objective function recognises that the dominant experimental uncertainties are those in the phase compositions, while the experimental temperature and pressure were determined with small uncertainties.

The values of the pure-fluid properties used in this work, including the critical temperature $T_{c,i}$, critical pressure $p_{c,i}$ and acentric factor ω_i are given in Table 3.2.

Table 3.2 Critical temperature T_c, critical pressure p_c and acentric factor ω used in the thermodynamic models calculations.

Components	T_c/K	p_c/MPa	ω	Ref.
CO_2	304.13	7.3773	0.22394	[70]
CH_4	190.56	4.5992	0.01142	[71]
CO	132.86	3.494	0.0497	[72]
H_2S	373.1	9.0	0.1005	[72]

Even thought, PR-EOS and its modifications are widely used for oil, gas and petrochemical applications, there remains a need for the development of more accurate EOS to address the shortcomings of cubic EOS, especially for the prediction of thermodynamic properties at high pressure and in the critical region.

3.3.2 Fitting Procedure of the PR-EOS

When fitting the binary interaction parameters in the PR-EOS, experimental data close to the critical point on each isotherm were not considered as the model fails to follow experiment in this region. Initially, $k_{ij,1}$ was set to zero, and $k_{ij,0}$ was optimized as a constant across all isotherms. Next, both $k_{ij,0}$ and $k_{ij,1}$ were optimized, again across all six isotherms. Finally, the optimization of the model was considered in two sub-ranges: a low-temperature range, from (218.15 to 243.15) K, and an upper-temperature range, from (273.15 to 288.15) K. The fitting of sub-intervals in temperature may be helpful when the model is applied in specific process simulations. For example, gas separations by flash processes would typically fall into the low-temperature range, while pipeline transportation falls into the upper-temperature range [14, 15]. The coefficients for all different cases are summarized in Table 3.3 for the (CO_2 + CO) system and in Table 3.4 for the (CO_2 + CH_4) system, together with the values of the objective function S.

Table 3.3 Coefficients $k_{12,1}$ and $k_{12,2}$ and objective function S for the (CO_2 + CO) system fitted in this work.

System	Fitted range		$k_{12,0}$	$k_{12,1}$/K	l_{12}	S	Note
	T_{min}/K	T_{max}/K					
CO_2 + CO	218.15	288.15	-0.0643	0.0000	0.0000	0.010	(a)
	218.15	288.15	-0.0689	1.06485	0.0000	0.010	
	218.15	243.15	-0.0646	0.0000	0.0000	0.011	
	218.15	243.15	-0.0875	5.23082	0.0000	0.011	
	273.15	288.15	-0.0524	0.0000	0.0000	0.007	
	273.15	288.15	-0.0551	0.01645	0.0000	0.007	

[a] recommended parameters.

Table 3.4 Coefficients $k_{12,1}$ and $k_{12,2}$ and objective function S for the (CO_2 + CH_4) system fitted in this work.

System	Fitted range		$k_{12,0}$	$k_{12,1}$/K	l_{12}	S	Note
	T_{min}/K	T_{max}/K					
CO_2 + CH_4	218.15	303.15	0.0909	0	0	0.0085	(a)
	218.15	303.15	0.1115	-4.75635	0	0.0084	
	218.15	303.15	0.0737	2.04029	-0.02009	0.0064	
	218.15	243.15	0.0901	0	0	0.0084	
	218.15	243.15	0.0766	3.07645	0	0.0084	
	273.15	303.15	0.1068	0	0	0.0015	(b)

[a] recommended parameters. [b] optimized for $x_1 > 0.93$

As can be seen in Tables 3.3 and 3.4, little improvement in the correlation of the data is gained when fitting both coefficients $k_{ij,0}$ *and* $k_{ij,1}$ as little or no decrease in the objective function S is obtained.

3.4 Helmholtz-Energy Explicit Mixture Model

Over recent years, facilitated by advances in computing performance and improved algorithms for determining the structure of complex empirical EOS, the development of empirical multi-parameter Helmholtz-energy models has attracted widespread interest in the field [26, 58, 73, 74]. For the description of binary and multi-component mixtures relevant to CCS processes there are two commonly used EOS based on the multi-fluid Helmholtz-energy approach: the GERG-2008 of Kunz and Wagner [26] and the EOS-CG of Gernert and Span [58]. While GERG-2008 was developed to calculate the thermodynamic properties of natural gas and similar mixtures, EOS-CG was developed with the same framework as GERG-2008 to describe binary and multi-component CO_2-rich mixtures typically present in CCS processes. EOS-CG presents new parameters for mixtures of CO_2, H_2O, N_2, O_2, Ar and CO. As a result, it improved the calculation of phase boundaries and phase properties of CO_2-rich mixtures. However, since the development of EOS-CG, additional data for the (CO_2 + CO) system have become available including VLE data from Westman et al. [75] and the present work available in Souza et al. [76], and density data from Blanco et al. [21], Tsankova et al. [77] and the present work. The VLE data span temperatures from just above the triple point of CO_2 to just below the critical point of CO_2, whereas the measured densities cover temperatures from (253 to 423) K and pressures up to 48

MPa for different mixture compositions ranging from (1 to 50) mol% CO. The availability of these additional data presented an opportunity for a further substantial improvement of the description of the (CO_2 + CO) system. The (CO_2 + CH_4) system is compared with the GERG-2008 and further improvement on the description of this binary was not attempted due to the lack of new experimental density data.

3.4.1 Mathematical Structure

The new mixture model for (CO_2 + CO) conforms to the mathematical approach introduced with GERG-2008 [26] and also adopted in EOS-CG [58]. This model is based on a fundamental EOS for the Helmholtz-energy; as a consequence, all thermodynamic properties can be calculated by combinations of its derivatives.

The EOS explicit in the Helmholtz energy a used for mixtures has temperature T, density ρ and the vector of mole fractions $\mathbf{x}$ as independent state variables. It is commonly split into two parts: a^o, which represents the hypothetical ideal-gas contribution, and a^r, which represents the residual part of the Helmholtz energy of the mixture. The basic mathematical structure of the mixture model can therefore be expressed as follows:

$$\frac{a(\rho,T,\mathbf{x})}{RT} = \alpha(\delta,\tau,\mathbf{x}) = \alpha^o(\rho,T,\mathbf{x}) + \alpha^r(\delta,\tau,\mathbf{x}). \tag{18}$$

Here, $\alpha = a/RT$ is the dimensionless reduced Helmholtz energy, R is the molar gas constant, $\delta = \rho/\rho_r(\mathbf{x})$ is the reduced density and $\tau = T_r(\mathbf{x})/T$ is the inverse reduced temperature, where $\rho_r(\mathbf{x})$ and $T_r(\mathbf{x})$ are the reducing functions discussed further below.

The ideal-gas term α^o is given by

$$\alpha^o(\rho,T,\mathbf{x}) = \sum_{i=1}^{N} x_i \left[\alpha^o_{0,i}(\delta_{0,i},\tau_{0,i}) + \ln x_i \right], \tag{19}$$

where N is the number of components in the mixture, x_i is the mole fraction of component i, and $\alpha^o_{0,i}$ is the dimensionless ideal-gas part of the Helmholtz energy of the pure component i in the mixture, which is calculated from the corresponding EOS for each pure component at the reduced density $\delta_{0,i}$ and the inverse reduced temperature $\tau_{0,i}$. For the ideal-gas part, the reduced input variables for the pure fluids are obtained by their fluid-specific critical parameters as $\delta_{0,i} = \rho/\rho_{c,i}$ and $\tau_{0,i} = T_{c,i}/T$.

The residual part of the Helmholtz energy of the mixture α^r is given by

$$\alpha^r(\rho,T,\mathbf{x}) = \sum_{i=1}^{N} x_i \alpha_{0,i}^r(\delta,\tau) + \Delta\alpha^r(\delta,\tau,\mathbf{x}), \tag{20}$$

where $\alpha_{0,i}^r$ is the residual part of the reduced Helmholtz energy of the pure component i and $\Delta\alpha^r(\delta, \tau, \mathbf{x})$ is the so-called departure function. The reducing functions ρ_r and T_r are given by

$$\frac{1}{\rho_r(\mathbf{x})} = \sum_{i=1}^{N} x_i^2 \frac{1}{\rho_{c,i}} + \sum_{i=1}^{N-1}\sum_{j=i+1}^{N} 2x_i x_j \beta_{\upsilon,ij}\gamma_{\upsilon,ij} \frac{x_i + x_j}{\beta_{\upsilon,ij}^2 x_i + x_j} \frac{1}{8}\left(\frac{1}{\rho_{c,i}^{1/3}} + \frac{1}{\rho_{c,j}^{1/3}}\right)^3 \tag{21}$$

$$T_r(\mathbf{x}) = \sum_{i=1}^{N} x_i^2 T_{c,i} + \sum_{i=1}^{N-1}\sum_{j=i+1}^{N} 2x_i x_j \beta_{T,ij}\gamma_{T,ij} \frac{x_i + x_j}{\beta_{T,ij}^2 x_i + x_j}\left(T_{c,i}T_{c,j}\right)^{0.5}, \tag{22}$$

where $\beta_{T,ij}$, $\beta_{v,ij}$, $\gamma_{T,ij}$ and $\gamma_{v,ij}$ are adjustable binary parameters which can be fitted to experimental data. The binary parameters β and γ consider the deviation between the behaviour of the real mixture and the one resulting from the combining rules for the critical parameters of the pure components. The reducing functions can be adjusted as a quadratic mixing rule when the binary parameters β and γ are set to unity and respective combining rules for the critical parameters of the pure components are used according to Lorentz and Berthelot [13].

The general structure of the departure function introduced by described by Kunz and Wagner [26] is given by

$$\Delta\alpha^r(\delta,\tau,\mathbf{x}) = \sum_{i=1}^{N-1}\sum_{j=i+1}^{N} x_i x_j F_{ij} \alpha_{ij}^r(\delta,\tau), \tag{23}$$

where α^r_{ij} and F_{ij} are the binary-specific departure function and a weighting factor, respectively, for the binary mixture of the components i and j. The binary function α^r_{ij} is an empirical model that depends only on the reduced mixture variables δ and τ. Its mathematical structure typically combines different types of term, such as polynomials, exponential or so-called special exponential terms [26, 58]. Recently, the additional use of Gaussian-bell shaped terms was successfully tested for the description of the thermodynamic properties of (H_2O + NH_3) [78]. The number of terms in the departure function as well as the combination of term types is assessed while fitting the model to the available experimental data for a specific binary mixture.

With the amount of experimental data of (CO_2 + CH_4) available at the development of GERG-2008, it was possible to develop a binary-specific departure function. It comprises of 6 terms: 3 polynomial and 3 exponential terms. Nevertheless, Kunz and Wagner highlighted that there is still a need for further development on this model. Compared to the (CH_4 + N_2) and (CH_4 + C_2H_6) systems, the extent and quality of the data of (CO_2 + CH_4) cover a narrow temperature and pressure ranges, which make the development of an accurate, wide-ranging equation of state difficult. New data, especially densities at pressure above 20 MPa are needed to further improve this model.

During the development of GERG-2008, most binary systems containing CO_2 were considered as of minor relevance. In view of the lack of reliable experimental data for (CO_2 + CO), no binary parameters or binary-specific departure function were fitted for this system. Instead, in the GERG-2008 formulation, the binary parameters β and γ for (CO_2 + CO) were set to unity. In EOS-CG, the reducing function for (CO_2 + CO) were adjusted by fitting the binary parameters β and γ to the available experimental data published up until 2012. As a result, EOS-CG is significantly more accurate than GERG-2008 in describing the thermodynamic properties of (CO_2 + CO). Nevertheless, the limited amount of available data meant that no binary-specific departure function could be developed.

With the availability of new data, an improved mixture model for the (CO_2 + CO) system comprising both a binary-specific departure function and re-optimised values of the binary parameters β and γ were developed.

3.4.2 Fitting Procedure of the New Mixture Model

A nonlinear fitting algorithm developed by Dr. Eric W. Lemmon at the National Institute of Standards and Technology [56] was used to adjust the parameters of the new mixture model [79]. This algorithm has the capability of simultaneously adjusting all parameters in a binary-specific departure function and the parameters $\beta_{T,ij}$, $\beta_{V,ij}$, $\gamma_{T,ij}$, $\gamma_{V,ij}$ in Eqs. (3.22) and (3.23) in order to minimise the overall sum of squares of the deviations between the experimental data points and their equivalents calculated from the new model. A subset of the available data is selected to be representative of the

most accurate values measured. Each experimental datum is individually weighted according to the property type, state region and the experimental uncertainty. The residual sum of square is given as

$$S = \sum w_{\mathrm{p},i} F_{\mathrm{p},i}^2 + \sum w_{\mathrm{c},i} F_{\mathrm{c},i}^2 \tag{24}$$

where w_i and F_i are the individual weight and the relative deviation function for a specific property p or constraints c [80]. Constrains are complex to define but are a powerful way to improve the representation of the physical behaviour of the fluid/mixture [80]. Table 3.5 presents the available density and VLE experimental data on the (CO_2 + CO) system and reference for the data used on fitting the new mixture model. The new mixture model was almost exclusively fitted to the VLE data from this work, available at Souza et al. [76], and density data from this work. The use of thermodynamic constraints in fitting process is powerful way to improve the representation of the physical behaviour of the fluids investigated [56].

Table 3.5 Available experimental data of the mixture (CO_2 + CO) for VLE and homogeneous densities from the present equation of state. * represent the data used for fitting the new mixture model.

VLE data							
Reference	Year	N_x	N_v	T/K	p/MPa	x_{liq}	x_{vap}
Blanco et al. [21]	2014	25	25	253.15 - 293.15	1.977 - 7.465	0.010 - 0.100	0.002 - 0.020
Christiansen et al.[81]	1974	34	34	223.16 - 283.16	0.827 - 14.15	0.003 - 0.463	0.015 - 0.800
Huamin [82]	1991	10	10	223.15 - 261.15	1.572 - 6.960	0.008 - 0.155	0.170 - 0.791
Kaminishi et al. [83]	1968	19	19	223.16 - 283.15	2.360 - 12.91	0.043 - 0.369	0.173 - 0.787
*Souza et al. [76]	2018	103	103	218.15 - 302.94	0.766 - 14.63	0.003 - 0.512	0.005 - 0.477
Westman et al. [75]	2018	24	24	253.15 - 298.16	6.033 - 12.55	0.018 - 0.374	0.041 - 0.574

pvT data					
Reference	Year	N	T/K	p/MPa	x
*This work	2019	169	283.15 - 373.15	1.96 - 48.65	0.050
		176	283.14 - 373.15	1.90 - 48.20	0.101
		188	283.15 - 373.16	2.06 - 48.06	0.253
		187	283.15 - 373.15	2.03 - 48.17	0.502
Overall		*720*	*283.15 - 373.16*	*1.96 - 48.64*	*0.050 - 0.502*
Blanco et al. [21] [a]	2014	197	253.15 - 343.15	0.10 - 20.00	0.004
		197	253.15 - 343.15	0.10 - 20.00	0.007
		197	253.15 - 343.15	0.10 - 23.85	0.010
		197	253.15 - 343.15	0.10 - 20.00	0.019

		197	253.15 - 343.15	0.02 - 20.17	0.030
Overall		*985*	*253.15 - 343.15*	*0.02 - 23.85*	*0.004 - 0.030*
Cipollina et al. [84]	2007	8	308.00 - 343.00	22.50 - 42.20	0.046
		8	308.00 - 343.00	26.50 - 47.00	0.065
		8	308.00 - 343.00	24.70 - 43.00	0.089
		8	308.00 - 343.00	25.40 - 43.30	0.115
		8	308.00 - 343.00	25.50 - 44.40	0.117
		8	308.00 - 343.00	26.60 - 44.10	0.134
		8	308.00 - 343.00	26.00 - 42.30	0.138
Overall		*56*	*308.00 - 343.00*	*22.50 - 47.00*	*0.046 - 0.138*
*Mallu et al. [85]	1987	75	323.14-423.11	0.10 - 6.50	0.427
		15	273.20-313.27	1.45 - 6.54	0.497
Overall		*90*	*273.20-423.11*	*0.10 - 6.54*	*0.427 - 0.497*
*Mallu et al. [86]	1989	75	323.15-423.15	0.10 - 6.50	0.202
		75	323.15-423.15	0.10 - 6.50	0.701
Overall		*150*	*323.15-423.15*	*0.10 - 6.50*	*0.202 - 0.701*
Tsankova et al. [77]	2019	21	255.05 - 313.27	1.45 - 6.54	0.496
		26	255.04 - 313.29	1.96 - 8.00	0.752
Overall		*47*	*255.04 - 313.29*	*1.45 - 8.00*	*0.496 - 0.752*

Numerous combinations of terms were investigated for the optimal representation of the binary-specific departure function. Throughout the fitting process, the behaviour of the EOS was assessed by means of the software packages REFPROP (version 10) [87] and TREND (version 3.1) [88]. Finally, a combination of two polynomials, two exponential and two Gaussian-bell shaped terms, which was first introduced for mixtures in the work Bell et al. [78], was adopted as follows:

$$\alpha^{r}(\delta,\tau)=\sum_{k=1}^{2}n_{ij,k}\delta^{d_{ij,k}}\tau^{t_{ij,k}}+\sum_{k=3}^{4}n_{ij,k}\delta^{d_{ij,k}}\tau^{t_{ij,k}}\exp(-\delta^{pi})+ \\ \sum_{k=5}^{6}n_{ij,k}\delta^{d_{ij,k}}\tau^{t_{ij,k}}\exp\left[-n_{ij,k}(\delta-\varepsilon_{ij,k})^{2}-\beta_{ij,k}(\delta-\gamma_{ij,k})^{2}\right] \tag{25}$$

Here, coefficients $n_{ij,k}$ and the exponents $d_{ij,k}$, $t_{ij,k}$, $\eta_{ij,k}$, $\varepsilon_{ij,k}$, $\beta_{ij,k}$, and $\gamma_{ij,k}$ are adjustable parameters fitted to the selected data. The values of the coefficients of the new equation of state are listed in Table 3.6.

Table 3.6 Parameters of the new equation of state.

Parameters of the reducing functions							
$\beta_{T,12}$	$\gamma_{T,12}$	$\beta_{v,12}$	$\gamma_{v,12}$	F_{12}			
0.9897820	1.1621298	1.0338017	1.0001623	1			
Parameters of the binary specific departure function							
k	$n_{12,k}$	$t_{12,k}$	$d_{12,k}$	$\eta_{12,k}$	$\varepsilon_{12,k}$	$\beta_{12,k}$	$\gamma_{12,k}$
1	1.8610	2.820	1	-	-	-	-
2	-4.0170	3.260	1	-	-	-	-
3	0.2734	0.940	2	1	-	-	-
4	2.3930	3.944	4	1	-	-	-
5	26.4600	2.530	1	-0.385	-0.144	5.100	0.109
6	-1.2130	4.380	1	-0.295	-0.310	1.661	2.596

3.5 Statistical Associating Fluid Theory (SAFT)

The statistical associating fluid theory (SAFT) equation of state (EOS) have been successfully applied in a number of thermodynamic property studies, including challenging systems such as polymeric and reactive [89]. The SAFT EOS originated from the Wertheim's work [90-94], who introduced a first-order thermodynamic perturbation theory (TPT1) for the description of the Helmholtz free energy of associating fluids. The generalized SAFT formulation represents the Helmholtz free energy of the system a in terms of four separate contributions. It is expressed as following:

$$\frac{a}{Nk_{\mathrm{B}}T} = \frac{a^{ideal}}{Nk_{\mathrm{B}}T} + \frac{a^{mono}}{Nk_{\mathrm{B}}T} + \frac{a^{chain}}{Nk_{\mathrm{B}}T} + \frac{a^{assoc}}{Nk_{\mathrm{B}}T} \tag{26}$$

where N is the number of molecules (or chains), k_{B} is Boltzmann's constant and T is temperature. The a^{ideal} is the contribution to the Helmholtz free energy arising from the ideal gas system, while the residual terms: a^{mono}, a^{chain} and a^{assoc} correspond to the contribution to the Helmholtz free energy arising from the monomeric segment system, the contribution to the Helmholtz free energy arising from the formation of chains of segments and the contribution to the Helmholtz free energy due to short-range directional forces, respectively.

In the SAFT EOS molecules are modelled as associating chains formed of bonded *m* spherical monomeric segments molecule that interact via a intermolecular potential, such as the Lennard-Jones [29], square-well (SW) [95, 96] or Mie potential [29].

Since it first appeared, SAFT has been further developed by different groups, in which the reference fluids have been represented with the square-well, Lennard-Jones, and Sutherland potentials. This flexibility in the EOS formulation results in numerous versions of SAFT such as soft-SAFT [97], SAFT-VR [98] and SAFT-*γ* approaches [98]. Comprehensive and detailed reviews about SAFT approach and its many different versions can be found in references [99-101].

Coupling the group-contribution [102] approach [102] within the framework of SAFT has made possible a useful predictive tools. In GC methods the thermodynamic properties of the fluid, either a pure compound or a mixture, are described in terms of the distinct functional groups making up the molecules. Therefore, with the description of a small number of functional groups it is possible to obtain the thermodynamic properties and phase equilibria of a large number of pure compounds and mixtures without additional fitting to experimental data.

The comparisons between different versions of SAFT EOS are difficult because of the many factors to be assessed, such as type of thermodynamic data and the temperature and pressure ranges used in the parameters optimization. In this work, the capability of SAFT-*γ* Mie group contribution approach were assessed, described in detailed in the next section.

3.5.1 SAFT-*γ* Mie Group Contribution Approach

A model of fused monomeric Mie-segments is proposed in the SAFT-*γ* approach, which means each group is described by an integer number of segments v^*_k and the so-called shape factor S_k (a parameter reflecting the contribution of each group *k*). Here, the shape factor S_k, describes the contribution that a given segment *k* of diameter σ_{kk} makes to the overall molecular geometry, which include contributions to the mean radius of curvature, the surface area and the volume of the molecule. A given functional group *k* is characterized by the set of like parameters: the number of segments in the group v^*_k, the shape factor S_k, the segment diameter σ_{kk}, the dispersive energy ε_{kk}, and the range λ_{kk} (repulsive and attractive exponents λ^r_{kk} and

λ^a_{kk}). Two additional parameters are introduced in the case of associating groups, but that is not discussed here.

In SAFT-γ Mie group contribution approach [29, 30], the molecules are described as distinct functional groups and the force fields describing the interactions between the segments are represented with the Mie (generalized LJ) potential u^{Mie}, given by

$$u^{Mie} = C\varepsilon\left[\left(\frac{\sigma}{r}\right)^{\lambda_r} - \left(\frac{\sigma}{r}\right)^{\lambda_a}\right]. \tag{27}$$

Here, λ_r and λ_a are exponents of the repulsive and attractive contributions to the intermolecular potential, respectively; σ is the segment diameter, r is the center-to-center distance between segments, ε is the potential well depth (maximum energy of interaction between segments), and C is defined as

$$C = \frac{\lambda_r}{\lambda_r - \lambda_a}\left(\frac{\lambda_r}{\lambda_a}\right)^{\frac{\lambda_a}{\lambda_r - \lambda_a}}. \tag{28}$$

The cross (unlike) interaction parameters between distinct functional groups are usually obtained using simple combining rules. The unlike segment diameter σ_{kl} between groups k and l are calculated from the arithmetic mean of the two segment size parameters (Lorentz-Berthelot combining rule)[103] as

$$\sigma_{kl} = \frac{1}{2}\left(\sigma_{kk} + \sigma_{ll}\right). \tag{29}$$

The unlike energy of interaction (or cross potential well depth) ε_{kl} is obtained using a geometric mean as following

$$\varepsilon_{kl} = \frac{\sqrt{\sigma_{kk}^3 \sigma_{ll}^3}}{\sigma_{kl}^3}\sqrt{\varepsilon_{kk}\varepsilon_{ll}}. \tag{30}$$

Finally, the combining rule for the repulsive λ^r_{kl} and the attractive λ^a_{kl} exponents of the unlike interaction are calculated by

$$\lambda_{kl} = 3 + \sqrt{\left(\lambda_{kk} - 3\right)\left(\lambda_{ll} - 3\right)}. \tag{31}$$

However, the estimations obtained with these combining rules may not always be sufficiently accurate, especially if the functional groups differ widely in terms of size and shape. In practice, if enough experimental data are available, ε_{kl} and λ^r_{kl} can be treated as adjustable parameters. Some examples on the development of like and

unlike group parameters can be found in the work of Al Ghafri et al. [104], Papaioannou et al. [30], and Sanchez-Vicente et al. [105].

3.5.2 Fitting Procedure of the SAFT-*γ* Mie

In this work, the estimation of the like parameters of pure CO and unlike parameters of the CO_2-CO interaction were carried out following the work of Papaioannou et al. [29]. The individual functional group *k* is characterized by the set of like parameters: the number of segments v^*_k, the shape factor S_k, the segment diameter σ_{kk}, the dispersive energy ε_{kk}, and the repulsive and attractive exponents λ^r_{kk} and λ^a_{kk}. In practice, v^*_k, is generally assigned equal to a fixed values based on the chemical nature of the functional group and all other like parameters are fitted to experimental data. All molecules relevant for this work, which are CO_2, CH_4 and CO were represented by single groups and the like parameters of these groups were obtained by regression to pure component data. The like parameters of pure CO_2 and CH_4 were used as published in Papaioannou et al. [30] and can be found in Table 3.7. The CO molecule is modelled by means of the molecular group CO comprised of two fused Mie segments, (i.e. the number of segments v^*_k is equal to two). The attractive Mie potential exponent λ^a_{kk} is fixed to the value of 6. The remaining like parameters of CO were fitted to vapor pressure and saturated vapour and liquid densities data calculated from the short industrial EOS of Lemmon and Span [72], also found in Table 3.7. The data were selected at temperatures ranging from (70 to 110) K. In total, 9 points with 5 K step between them were used in the fitting. Points close to the critical temperature, 132.86 K, are avoid following the parameter estimation described by McCabe and Galindo [101]. The fit is usually restricted to subcritical conditions because there are more reliable experimental data, aside from the critical point typically be over predicted by the classical theories. The uncertainties in the short industrial EOS of Lemmon and Span are 0.3% in density, approaching 1% near the critical point, 0.2% in vapor pressure, valid from the triple point to 500K and pressures up to 100 MPa [72]. Figure 3.3 and 3.3 present the comparison between the resulting model and the VLE data calculated from the short industrial EOS of Lemmon and Span [72].

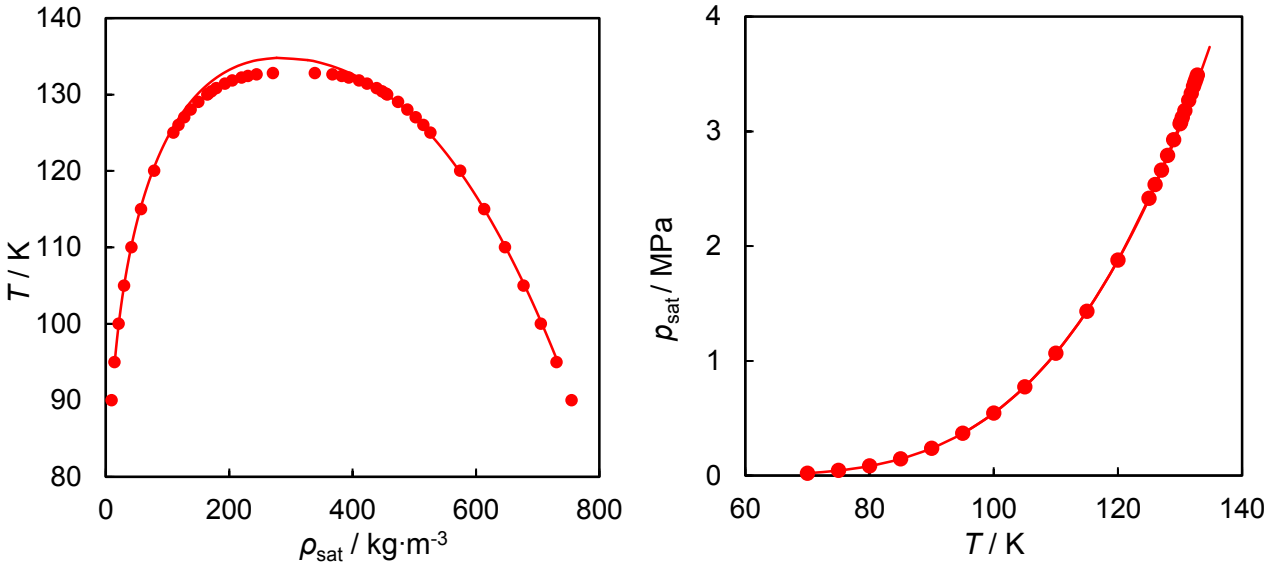


Figure 3.2 – Saturated densities and vapour pressures of pure CO: ●, VLE data calculated from the short industrial EOS of Lemmon and Span [72]; ___, SAFT-γ Mie approach fitted with like parameters from Table 3.7.

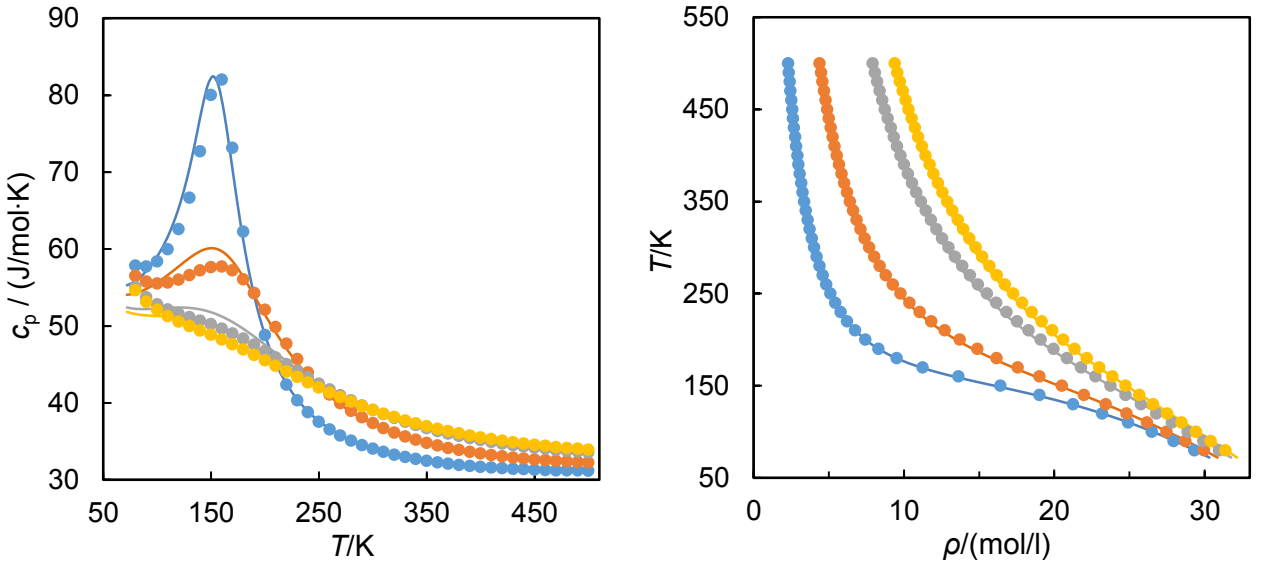


Figure 3.3 - Single-phase densities and isobaric heat capacities of pure CO. Data calculated from the short industrial EOS of Lemmon and Span [72] at pressures: ●, p = 10 MPa; ●, p = 20 MPa; ●, p = 40 MPa; ●, p = 50 MPa; ___, SAFT-γ Mie approach fitted with like parameters from Table 3.7.

In the present work, the CO_2-CO unlike interaction parameters ε_{kl} and λ^r_{kl} were obtained by fittings to data of the (CO_2 + CO) system of this work. VLE data at temperatures ranging from (218 to 288) K and pressures up to 15 MPa [76], while density data at temperature ranging from (283 to 373) K and pressure up to 48 MPa.

Here, 10 to 20 data points of bubble pressure and different 10 to 20 data points on dew pressure were selected from temperatures of 218, 243, 273 and 288 K. Besides, up to 20 data points on homogenous density were included from temperatures of 283, 303, 333 and 373 K. Note that the selected experimental data comprise of 4 out of the 7 isotherms for each property measured. The experimental data from the temperatures not used for the parameter estimation will help to validate the fitting procedure.

For both fitting procedures, the data subset selected are weighted mainly to the property type. The parameters are then adjusted to the data subset selected in order to minimise the overall sum of squares of the deviations of the experimental data from the model - Eq. (24). The minimizations are carried out using a numerical solver provided by the commercial software package gPROMS (version 5.1) [106]. All other unlike parameters were calculated by means of using combining rules, Eqs. (29), (30) and (31).

The resulting values of the like interaction parameters for pure CO are listed in Table 3.7 and unlike interaction parameters for CO_2-CO in Table 3.8.

Table 3.7 Like parameters for use within the SAFT-γ Mie group-contribution approach: the number of spherical segments v^*_k, the shape factor S_k, the segment diameter σ_{kk}, the dispersive energy ε_{kk}, k_B is the Boltzmann constant and the repulsive and attractive exponents λ^r_{kk} and λ^a_{kk}.

Group k	v^*_k	S_k	λ^r_{kk}	λ^a_{kk}	(ε_{kk}/k_B)/K	σ_{kki}/Å	Note
CO_2	2	0.84680	26.408	5.0550	207.89	3.0500	[30]
CH_4	1	1.0000	12.504	6.0000	152.58	3.7370	[30]
CO	2	0.75287	10.119	6.0000	75.48	3.1300	a

[a] current work

Table 3.8 Unlike parameters for use within the SAFT-γ Mie group-contribution approach: the dispersion interaction energy ε_{kl} and repulsive exponent λ^r_{kl}.

Group k	Group l	(ε_{kk}/k_B)/K	λ^r_{kk}	Note
CO_2	CH_4	144.72	11.950	[30]
CO_2	CO	144.18	15.764	a

[a] current work

Further discussion and results of the parameter estimation is presented in Section 6, in which SAFT-γ Mie description of the phase behaviour of the (CO_2 + CO) system.

Chapter 4 Vapour Liquid Equilibrium Apparatus and Experimental Methodology

4.1 Apparatus Design

The low-temperature VLE apparatus used in this study was previously described by Fandiño et al. [54] and Souza et al. [76]. The apparatus implemented the static-analytic method with online sampling and composition measurement by gas chromatography, and was designed for a maximum working pressure of 20 MPa at temperatures in the range from (183 to 473) K. Figure 4.1 shows the schematic of the apparatus, comprised of three main sub-systems: gas-handling, equilibrium cell, and quantitative compositional analysis.

The gas-handling system comprised valves V-1 to V-7, digital pressure sensors P1 to P3 and a N2 purge. Valves V-1, V-2 and V-3 are used to introduce an approximately-known quantity of CO_2 into the equilibrium cell E-1. Valves V-4 and V-5 are used to introduce up to four further gases, thereby permitting the study of binary and multicomponent systems. The system was also used to clean the lines, reservoir and equilibrium cell by means of the venting valve V-6 and the diaphragm vacuum valve V-7. The reservoir E-2, having an internal volume of 500 cm^3, was used as an intermediate CO_2 store between the supply cylinder and the equilibrium cell E-1. The amount of CO_2 introduced into the equilibrium cell was roughly determined from changes in the reading of the pressure sensor P-3 and temperature sensor T-2.

The high-pressure equilibrium cell E-1, fabricated from type 316L stainless steel, had an internal volume of approximately 143 cm^3 and was fitted with a PTFE-coated magnetic stirrer bar. It was housed in a thermostat bath E-3 (Lauda Proline model RP890) filled with ethanol. The external permanent magnet drive, coupled with a magnetic stirrer bar, was rotated by means of a motor and gear assembly. A N_2 purge gas was used to create an inert atmosphere inside the ethanol bath both to avoid condensation of humidity and to reduce the risk of explosion in the event of a leak.

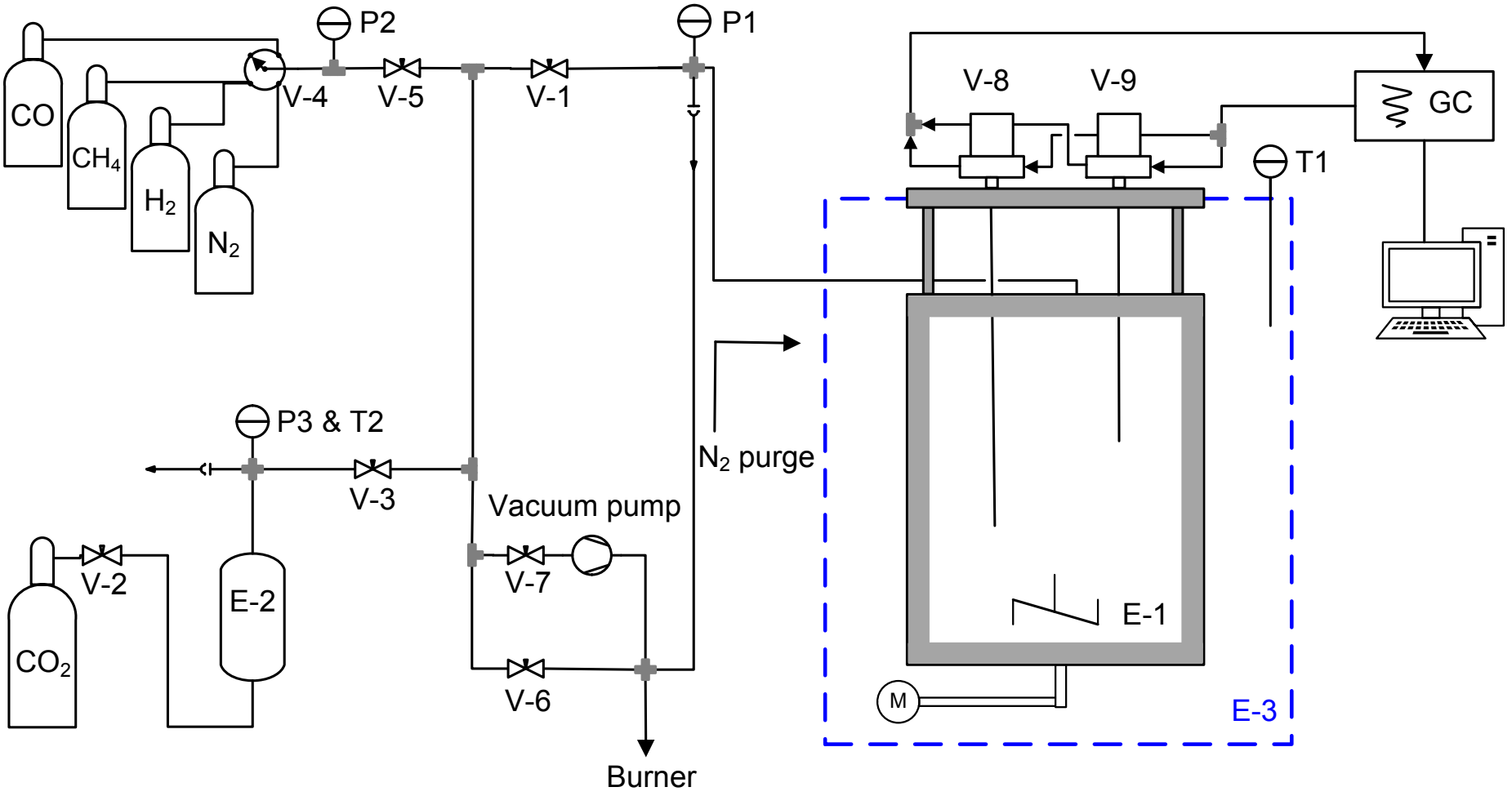


Figure 4.1 Schematic diagram of the experimental apparatus used to measure low-temperature VLE. V1 to V7: inlet and outlet valves; V8 and V9: sampling valve (ROLSI Evolution IV™); T1: external platinum resistance thermometer; T2: Type K thermocouple; P1 to P3: pressure transducer; E-1: equilibrium cell; E-2: reservoir; E-3: thermostat bath (Lauda Proline model RP890).

The experimental temperature was measured with a platinum resistance thermometer (Fluke model 5615) calibrated on the International Temperature Scale of 1990 at temperatures ranging between (77 and 693) K. This was inserted into a blind hole bored in the wall of the equilibrium cell. The resistance of the thermometer was measured and converted to a temperature reading by a digital readout unit (Fluke model 1502A). The experimental pressure was measured using a high-precision digital pressure transmitter (P-1, Keller model PA-33X, 30 MPa full scale) with manufacturer's stated maximum uncertainty of 0.05% of the full scale pressure (i.e. k = 1.73, corresponding to a standard uncertainty of 0.009 MPa). Since this measured gauge pressure, an additional absolute pressure sensor was used to obtain the atmospheric pressure (Keller model PAA-21Y, 0.2 MPa full scale) with manufacturer's stated maximum uncertainty of 1% of the full scale pressure (i.e. k = 1.73, corresponding to a standard uncertainty of 0.001 MPa).

Sampling of the liquid and vapor phases was made through a pair of electromagnetic sampling valves (ROLSI Evolution IV™, V-8 and V-9 in Figure 4.1), each coupled to the equilibrium cell E-1 by a capillary tube. This arrangement permitted the withdrawal of small amounts of either phase without significantly disturbing the equilibrium. The samples were transferred to the gas chromatograph [102] via a heated transfer line that was continuously swept by the carrier gas. The sampling valves and the transfer lines were heated to temperatures 323.15 K and 363.15 K, respectively, to prevent adsorption or condensation of the components. The configuration was to the carrier gas flows through the Rolsi valves in parallel. Dataflow programming software (implemented in Keysight VEE) was used to control the operation of the sampling valves and to collect temperature and pressure data, thereby permitting full automation of the measurements.

The quantitative compositional analysis was carried out by means of an on-line GC (Agilent 7890A) fitted with a ShinCarbon ST packed column (100/120 mesh, 2m, 1 mm ID) and a thermal conductivity detector (TCD) for the binaries (CO_2 + CO) and (CO_2 + CH_4); and Rt-sulfur packed column (Restek™, 2m, 2mm ID) and a flame photometric detector (FPD) for the ternaries (CO_2 + CO + H_2S) and (CO_2 + CH_4 + H_2S). The GC was also equipped with a gas sampling valve and a sample loop for the purpose of injecting calibration gases. Further details on the operational conditions of the GC are described in section 4.4.

4.2 Material

Details of the gases used for VLE measurements of (CO_2 + CO), (CO_2 + CH_4), (CO_2 + CO + H_2S) and (CO_2 + CH_4 + H_2S) are presented in Table 4.1. No further purification was attempted.

Table 4.1 Description of chemical sample, where *x* is mole fraction.

Sample	Source	Purity as supplied	Additional purification
CO_2	BOC	$x \geq 0.999\ 95$	None
1000ppm H_2S / CO_2 balance	BOC	$x \geq 0.999\ 95$	None
CO	BOC	$x \geq 0.999$	None
CH_4	BOC	$x \geq 0.999\ 5$	None
N_2	BOC	$x \geq 0.999\ 992$	None
He	BOC	$x \geq 0.999\ 99$	None

4.3 Toxicity of Materials / Safety Procedures

Prior to the start of any experimental procedure, a hazard evaluation and risk determination is crucial to learn which health hazards are present and determine how best to mitigate these hazards and prevent work-related illness or injury. The risk assessment for an activity involving the use of hazardous chemicals, which was the case with the present low-temperature high-pressure VLE measurements, includes listing each of the chemical substances used in the procedure and applying the risk matrix ABC method to determine the risk level for each one. In short, A, B and C represent different scales of frequency and consequence ranging from 1 to 3, that multiplied estimate the overall risk level (≤ 7 Low; 8-11 Medium; ≥ 12 High).

The results of this method is shown in Table 4.2. Supplementary information on risk assessment including the matrix guide to the risk matrix ABC method is included in the Appendix A, together with tables of CO and H_2S concentrations, effects, inhalation time and toxic symptoms developed .

Table 4.2 – Determination of the overall risk level of each chemical substances used in the experimental procedure with ABC method.

Substance	Route of Exposure					Risk Phrases	WEL*	A	B	C	A x B x C	
	Inhalation 	Ingestion 	Skin Contact 	Penetration 	Eye Splash 			Health Hazard Score	Dustiness, Volatility Score	Overall Quantity Score***	Risk Level	
											Score	L/M/H
Carbon Monoxide	X					R61 – May cause harm to the unborn child R23 – Toxic by inhalation R48/23 Toxic: danger of serious damage to health by prolonged exposure through inhalation R12 – Extremely flammable	30 ppm	3	3	3	27	H
Hydrogen Sulfide	X					R12 – Extremely flammable. R26 – Very toxic by inhalation. R50– Very toxic to aquatic organisms	Long Term (8 hours) 5 ppm Short Term (5 min.) 10 ppm	3	3	3	27	H
Hydrogen	X					R12 – Extremely flammable.	LEL: 4% V UEL: 74.2% V	1	3	3	9	M
Carbon Dioxide	X						TWA 5,000 ppm STEL 15,000 ppm	1	3	3	9	M
Methane	X					R12 – Extremely flammable.	LEL: 5% V UEL: 15 % V	1	3	3	9	M
Propane	X					R12 – Extremely flammable	LEL: 2.1% V UEL: 9.5 % V	1	3	3	9	M

*Workplace Exposure Limit (see safety data sheet of each component) – usually in ppm for vapours or mg/m^3 for particulates.

As can be seen from the list of chemical substances used in the VLE measurements, the risk level of using them are either medium or high. This is the result of not only the nature of the substances, but its combination with the quantity needed to carry out the experiment at low temperature and high pressure. From the risk assessment of our VLE set-up, areas that may result in the release of a hazardous chemical were modified to improve their safety and control measures were identified and applied. This included: placing the entire apparatus, apart from the GC, inside a fume cupboard to ensure safe containment of toxic gases in the event of a leak; the use of N_2 purge to avoid condensation of humidity and to create an inert atmosphere inside the ethanol bath, thereby reducing the risk of explosion in the event of a leak (see Figure 5.2). Additionally, CO, H_2 and H_2S alarms were fitted in the laboratory and portable CO and H_2S alarms were used within the fume cupboard to check for leaks.

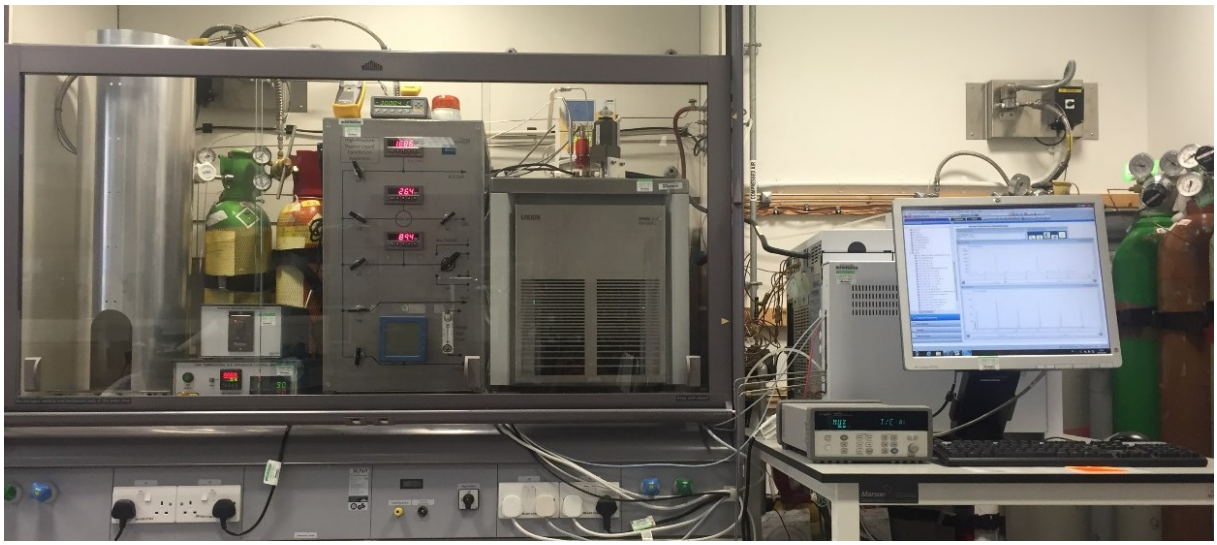


Figure 4.2 Picture of the VLE apparatus as built in the Laboratory.

Others important procedures put in place to help ensure safety are:

- Annual inspection of the fume cupboard and the fixed and portable leak detectors;
- Regular leakage tests on all lines, fittings, valves and regulators, besides relevant equipment;
- Storage of cylinders not in use outside the laboratory and of cylinder containing toxic substances inside the fume cupboard;

- Disposal of flammable substance carried out by venting to a Bunsen burner and releasing the combustion products into the fume cupboard;
- Oxygen depletion of the laboratory is also detected by a separated fixed detector;
- All users of the VLE apparatus were trained following the procedures of both the COSHH/DSEAR risk assessment and the activity risk assessment. This include instructions on the meaning of alarm signals from the gas detectors and the procedure to be adopted in the event of a release;
- Hot spots were confined and isolated within the fume cupboard, that was kept closed during the measurements. High temperatures hazard signs were put in place, where appropriate.

All mentioned control measures identified were applied to create a safe environment to carry out the VLE measurements of all binary and ternary systems.

4.4 GC Calibration

4.4.1 Calibration Procedure

A robust GC calibration method is fundamental for an accurate quantification of the components in both liquid and vapour phases. In this work, the area response of the TCD and FPD detector was calibrated for each component by an absolute method using two gas sampling loops, with nominal volumes of 0.05 and 0.25 cm^3. In order to permit calculation of the density of the calibration gas in the filling loop prior to injection, measurements of temperature and pressure were made. The temperature of the sample loop was measured with an uncertainty of 1 K by means of two K-type thermocouples, one located in the middle of the sample loop and the other at one end. The pressure was determined with a relative standard uncertainty of 0.3% by means of a pressure sensor (Keller model PAA-21Y, 0.6 MPa full scale) located in the tubing upstream of the sample loop.

The amount of the gas injected was adjusted by varying the filling pressure of the loop from (0.1 to 0.5) MPa. Prior to each injection, alternatively, each sample loop was flushed with the gas for around 30 s and then left to equilibrate before first measuring the temperature and pressure and then injecting the gas into the GC. The temperature of the sampling loops were kept constant at approximately 323.15 K throughout all

calibration measurements. The CO_2, CO and CH_4 density at the loop conditions were obtained from the EOSs by Span and Wagner [70], Lemmon and Span [72], and Setzmann and Wagner [71], respectively, with uncertainties of the equations ranging between (0.03 to 0.1)% at the relevant temperatures and pressures. The peak area response curves from CO_2, CO, and CH_4 were recorded using the TCD, while from H_2S using the FPD.

A ShinCarbon ST column was used to separate either CO_2 and CO or CO_2 and CH_4 with He as the carrier gas, while a Rt-sulfur to separate either CO_2, CO and H_2S or CO_2, CH_4 and H_2S. The GC conditions were optimized to provide adequate separation performance of the (CO_2 + CO), (CO_2 + CH_4) (CO_2 + CO + H_2S) or (CO_2 + CH_4 + H_2S) systems. The analytical runtime was kept as short as possible while assuring complete separation between the chromatographic peaks corresponding to the different components. Optimized GC conditions are summarized below. Table 4.3 presents the optimized GC conditions for separation of CO_2 from CO, Table 4.4 for separation of CO_2 from CH_4, and Table 4.5 for separation of the ternaries: (CO_2 + CO + H_2S) and (CO_2 + CH_4 + H_2S). Absolute calibrations was performed under identical GC detector conditions; the conditions of the column should not alter the area response of the detectors.

Table 4.3 Optimized gas chromatograph conditions for separation of CO_2 from CO.

Gas Chromatograph Parameter	Optimized Condition
Detector Conditions	
Detector	Thermal conductivity detector (TCD)
TCD temperature	473.15 K
Carrier gas	He
Carrier gas flow rate	15 mL/min
Makeup gas	N_2
Makeup gas flow rate	2 mL/min
Column Conditions	
Separation column	ShinCarbon ST, 100/120 mesh, 2m, 1.0 mm ID
Oven temperature	423.15 K [60]
CO retention time	1.165 min
CO_2 retention time	1.467 min

Table 4.4 Optimized gas chromatograph conditions for separation of CO_2 from CH_4.

Gas Chromatograph Parameter	Optimized Condition
Detector Conditions	
Detector	Thermal conductivity detector (TCD)
TCD temperature	473.15 K
Carrier gas	He
Carrier gas flow rate	20 mL/min
Makeup gas	N_2
Makeup gas flow rate	2 mL/min
Column Conditions	
Separation column	ShinCarbon ST, 100/120 mesh, 2m, 1.0 mm ID
Oven temperature	423.15 K [60]
CH_4 retention time	0.795 min
CO_2 retention time	1.467 min

Table 4.5 Optimized gas chromatograph conditions for separation of the ternaries.

Gas Chromatograph Parameter	Optimized Condition
Detector Conditions	
Detector	Thermal conductivity detector (TCD)
TCD temperature	473.15 K
Carrier gas	He
Carrier gas flow rate	15 mL/min
Makeup gas	N_2
Makeup gas flow rate	2 mL/min
FPD temperature	473.15 K
Carrier gas	He
Carrier gas flow rate	15 mL/min
Makeup gas	N_2
Makeup gas flow rate	2 mL/min
H_2 flow rate	
Column Conditions	
Separation column	Rt Sulfur 2m, 2mm ID
Oven temperature	323.15 K [60]
CH_4 retention time	0.967 min

Gas Chromatograph Parameter	Optimized Condition
CO retention time	1.264 min
CO_2 retention time	1.965 min
H_2S retention time	6.362 min

A slightly non-linear relationship between the amount of CO_2, CO or CH_4 and the corresponding TCD peak area was observed. In contrast, the relationship between H_2S and the corresponding FPD peak area is proportional to the square of the sulfur concentration in the flame. This happens because when sulfur containing compounds such as H_2S are introduced into the hydrogen flame, molecular band emission occurs because of the decay of S2 from an excited state. The calibration data were therefore fitted with the following function:

$$\rho = \frac{n_i}{V} = a_{i,1}A_i + a_{i,2}A_i^2 \tag{32}$$

where, n_i is the amount of pure substance i injected in the GC at a determined pressure, V is the volume of the sample loop, A_i is either the TCD or FPD peak area for component i and $a_{i,1}$ and $a_{i,2}$ are fitting parameters. The ratio (n_i/V) was set equal to the molar density of the gas at the loop filling conditions. The GC calibration results for CO_2 and CO, CO_2 and CH_4, and H_2S, together with respectively deviations of the data from Eq. (32), are shown in Figure 4.3, Figure 4.4 and Figure 4.5, respectively. The optimized calibration parameters are presented in Table 4.6 and Table 4.7.

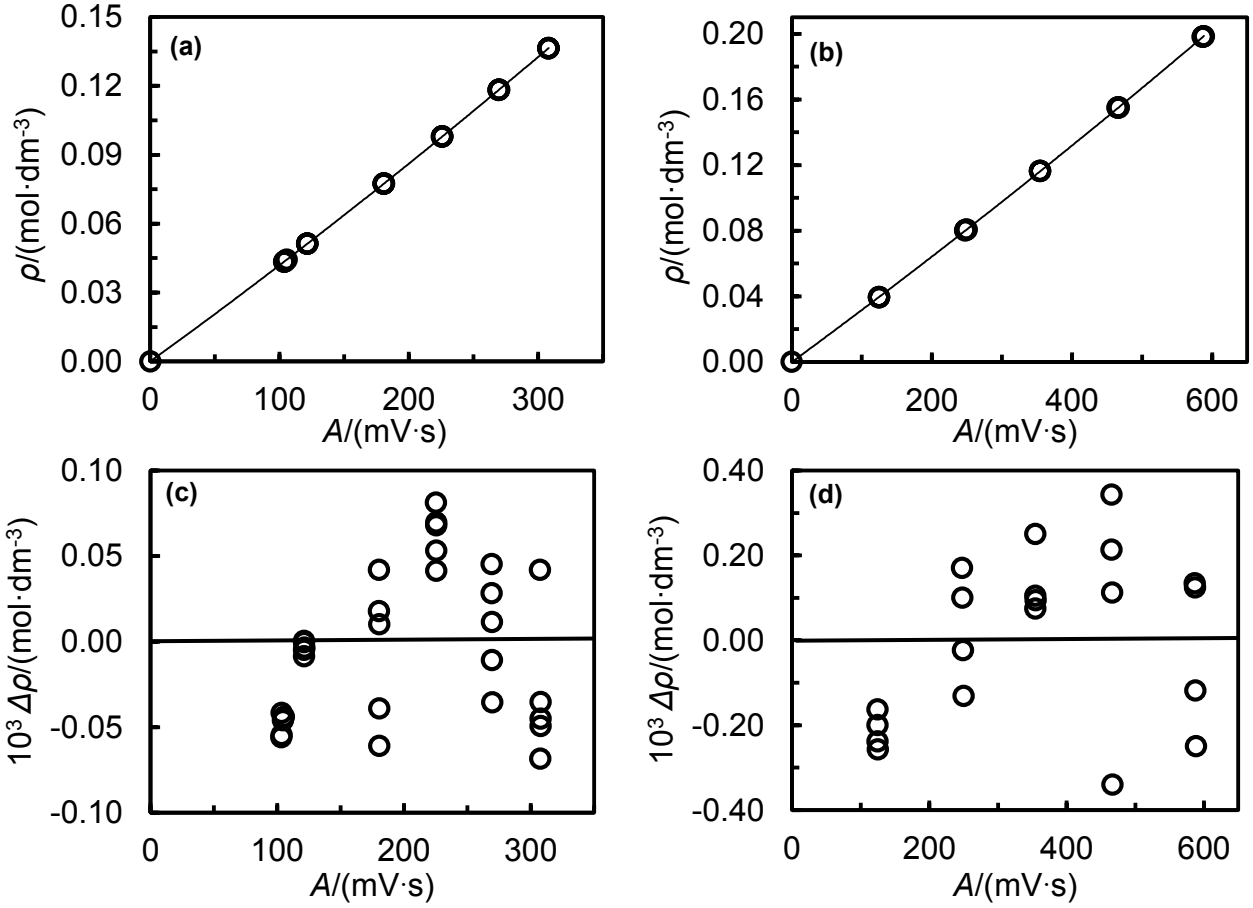


Figure 4.3 Thermal-conductivity detector (TCD) calibration data for CO (a and c) and CO_2 (b and d) with He carrier gas: (a) and (b), gas molar density ρ under filling-loop conditions against area response A; (c) and (d), deviations $\Delta\rho$ of gas molar density from Eq. (32) against area response A. O, experimental data; ——, Eq. (32).

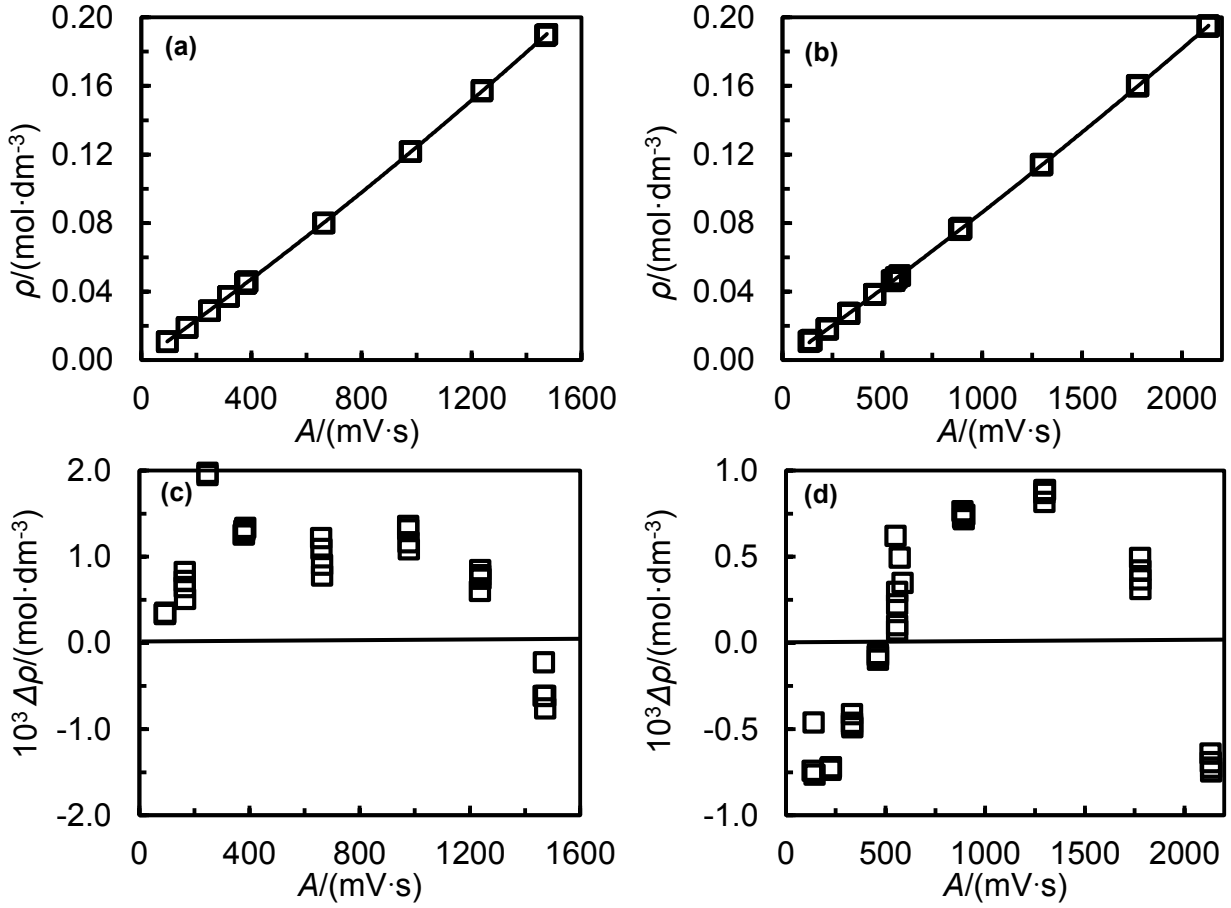


Figure 4.4 Thermal-conductivity detector (TCD) calibration data for CH_4 (a and c) and CO_2 (b and d) with He carrier gas: (a) and (b), gas molar density ρ under filling-loop conditions against area response A; (c) and (d), deviations $\Delta\rho$ of gas molar density from Eq. (32) against area response A. □, experimental data; ——, Eq. (32).

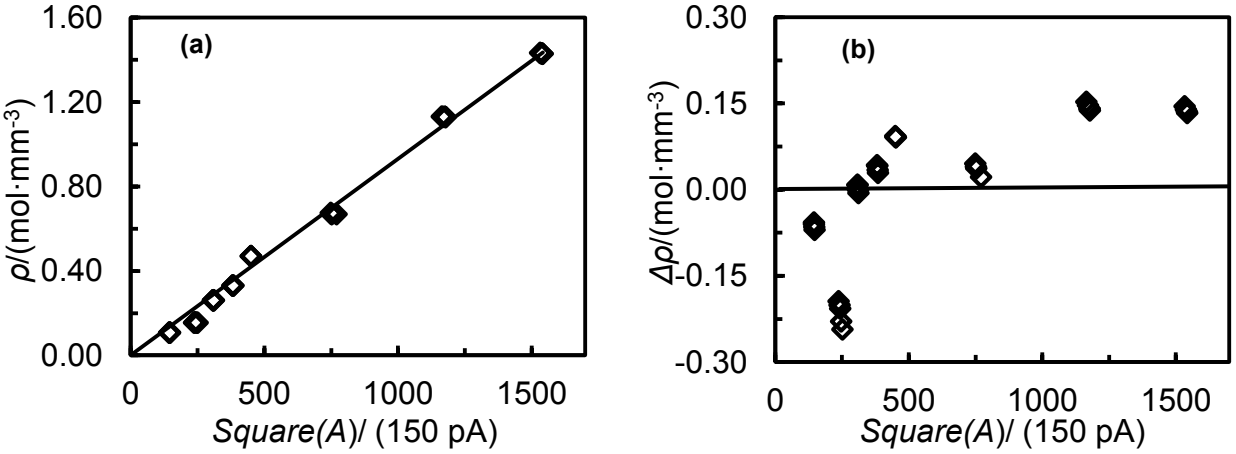


Figure 4.5 Flame Photometric Detector (FPD) calibration data for H_2S with He carrier gas: (a), gas molar density ρ under filling-loop conditions against area response A; (b), deviations $\Delta\rho$ of gas molar density from Eq. (32) against area response A. ◇, experimental data; ——, Eq. (32).

Table 4.6 Optimized Calibration Parameters for CO_2 and CO.

Parameters	CO_2	CO
$a_{i,1}$	4.131×10^{-10}	4.601×10^{-10}
$a_{i,2}$	2.534×10^{-16}	8.060×10^{-15}

Table 4.7 Optimized Calibration Parameters for CO_2, CH_4 and H_2S.

Parameters	CO_2	CH_4	H_2S
$a_{i,1}$	4.611×10^{-10}	6.910×10^{-10}	1.604×10^{-13}
$a_{i,2}$	7.850×10^{-16}	1.990×10^{-15}	0

4.4.2 Validation of the GC Calibration

Two binary mixtures of either $(1 - x)$ CO_2 + x CO or $(1 - x)$ CO_2 + x CH_4 were used to carry out the validation of the GC calibration. The mixtures were purchased from BOC or SIP who specified an expanded uncertainty in composition (k = 1.73) of 0.01x. The mole fraction of the mixtures are presented in Table 4.8.

Table 4.8 Description of samples, where z is the mole-fraction purity specified by the supplier, and x is the mole fraction of either CO or CH_4 and $u(x)$ is the standard uncertainty of x in the mixtures.

Sample	Source	z	x [a]	x [b]	$u(x)$ [b]
$(1 - x)$ CO_2 + x CO	BOC	> 0.99945	0.5000	0.50183	2.75×10^{-3}
$(1 - x)$ CO_2 + x CH_4	SIP	> 0.99990	0.0500	0.05031	2.39×10^{-3}

[a] Specified by the supplier

[b] Determined by GC analysis

4.5 Experimental Procedures

The low-temperature VLE apparatus was validated by means of comparing vapor pressures of pure CO_2 at temperatures ranging from (218 to 303) K with those predicted by the reference EoS of Span and Wagner [70]. Results are shown in Figure 4.6. In no case did the deviation exceeded the standard uncertainty of the experimental data.

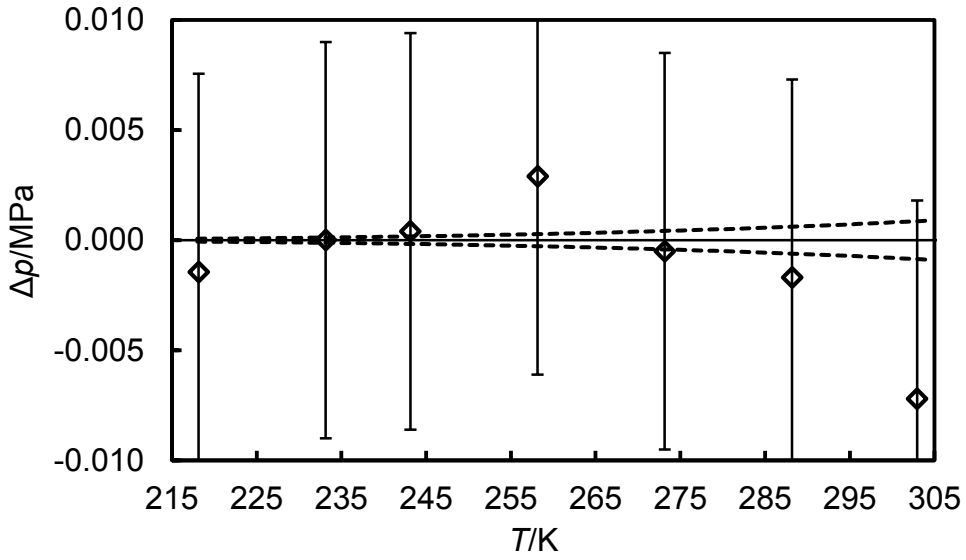


Figure 4.6 Deviation $\Delta p = (p_{exp} - p_{EoS})$ between the experimental vapor pressure of pure CO_2 and the reference values p_{EoS} calculated from the equation of state of Span and Wagner [70] as a function of temperature T: ◇, this work. Error bars show the standard uncertainty of the experimental data, while the dashed lines indicate the uncertainty of the calculated vapor pressures as specified in reference [70].

The experimental procedure was carried out in a series of steps including cleaning the VLE apparatus, filling the equilibrium cell with an approximately-known amount of CO_2, raising the pressure by introducing CO, equilibration, sampling from both phases and quantitative compositional analysis by GC.

Initially, any remaining gas in the apparatus was vented and evacuated through valves V-6 and V-7 (see Figure 4.1), discharging into a burner for safe disposal of toxic and flammable gases. The apparatus was then flushed a few times with pure CO_2 and evacuated for at least 30 minutes using the diaphragm vacuum pump to a pressure below 100 Pa. This procedure was repeated several times.

For the three lowest isotherms, T = (218.15, 233.15 and 243.15) K, the thermostat bath was set to the desired temperature from the start. For the remaining isotherms, T = (258.15, 273.15, 288.15 and 302.93) K, the thermostat bath was first set to temperature between (243.15 and 253.15) K to facilitate adequate filling with CO_2. For the binary mixtures, the reservoir was filled with CO_2 gas up to the CO_2 cylinder supply pressure of about 6 MPa. The equilibrium cell was then filled with CO_2 from the reservoir until the saturated vapor pressure was reached and approximately one-third of the cell volume was filled with liquid. The bath temperature was then set to the desired value for the isotherm.

Following initial filling, the vapor pressure of the CO_2 was measured as a check for system purity. The result was compared with the reference equation of state of Span and Wagner [70] and presented deviations in all cases within ±0.004 MPa. The secondary gas, either CO or CH_4, was then introduced slowly until the next desired pressure was reached. The content of the equilibrium cell was then left to equilibrate with stirring for (30 to 60) min. The system was considered to be in equilibrium if both temperature and pressure were constant within ± 0.01 K and 0.01 MPa, respectively, for at least ten minutes. About 10 min prior to sampling, the stirrer was turned off to ensure that there was no entrainment of one phase in the other. Between 5 and 10 samples where then withdrawn and analyzed. Additional CO or CH_4 was then introduced, and the measurement process was repeated for at least 10 different set pressures on each isotherm.

The experimental procedure slightly changed for ternary mixtures. The reservoir was initially filled with a gas mixture of 1000 ppm H_2S balance with CO_2 up to pressure of about 5 MPa. Pure CO_2 was then introduced to the reservoir until final concentration of H_2S of about 100ppm, besides approximately one-third of the cell volume was filled with liquid. Finally, the secondary gas, either CO or CH_4, was introduced until the next desired pressure was reached. The same equilibration and sampling procedure used for binaries was used.

4.6 Uncertainty Analysis

The uncertainty analysis of this work follows the “Evaluation of Measurement Data - Guide to the Expression of Uncertainty in Measurement (GUM)” [107] suggested by NIST.

In this work, the quantities being measured were the temperature, pressure and the compositions of the liquid and vapor phases in equilibrium. For the binary mixtures, only the mole fractions x and y of CO or CH_4 in the liquid and vapor phases, respectively, were considered. While for ternaries, only the mole fractions x and y of H_2S were considered. As explained in section 4.5, for each equilibrium condition of temperature and pressure, between 5 and 10 samples were withdrawn and send to the GC for quantitative compositional analysis. Thus, the quantities T, p, x and y are determined by the sample mean of N independent observations under almost identical

conditions of measurement. The combined standard uncertainty of the mole fraction z_i (equal to either x_i or y_i) designated by u_c[108] is given as following

$$u_c(z_i) = \sqrt{u^2(z_i) + \left[\left(\frac{\partial z_i}{\partial T}\right)u(T)\right]^2 + \left[\left(\frac{\partial z_i}{\partial p}\right)u(p)\right]^2} \quad . \tag{33}$$

Where $(\partial z_i/\partial T)$ and $(\partial z_i/\partial p)$ are sensitivity coefficients, $u(T)$ and $u(p)$ are the standard uncertainty of temperature and pressure, respectively. The standard uncertainty in mole fraction of each component in a given phase u[108], arising from both calibration and measurement, as given by

$$u^2(z_i) = \sum_{j=1}^{Nc}\left(\frac{\partial z_i}{\partial n_i}\right)^2 u^2(n_i) \tag{34}$$

Where n_i is the amount of the substance i in the sample calculated from Eq. (32). In this way, the impurity of each component (purity presented in Table 4.1) is indirectly included in the calibration. Following the uncertainty analysis presented by Al Ghafri et al. [104], the quadratic relationship of the calibration curves are assumed linear related to a chromatographic response factor f_i as in $n_i = f_i \cdot A_i$. As a result, the molar fraction is calculated as following

$$z_i = \frac{n_i}{\sum_{j=1}^{Nc} n_j} = \frac{A_i f_i}{\sum_{j=1}^{Nc} A_j f_j}. \tag{35}$$

Eq. (34) can be also expressed as

$$u^2(z_i) = \sum_{i=1}^{Nc}\left(\frac{\partial z_i}{\partial n_j}\frac{\partial n_j}{\partial f_i}\right)^2 u^2(f_i) + \sum_{i=1}^{Nc}\left(\frac{\partial z_i}{\partial n_j}\frac{\partial n_j}{\partial A_i}\right)^2 u^2(A_i) \tag{36}$$

where the partial derivatives $(\partial z_i/\partial n_i)$, $(\partial n_i/\partial f_i)$ and $(\partial n_i/\partial A_i)$ are given by

$$\begin{aligned} &\frac{\partial z_i}{\partial n_j} = -z_i z_j / n_j, \quad if \quad (i \neq j); \quad (1 - z_i) z_i / z_i \\ &\frac{\partial n_j}{\partial f_i} = A_i \\ &\frac{\partial n_j}{\partial A_i} = f_i \end{aligned} \tag{37}$$

Resulting in equation (36) is given by

$$u^2(z) = \sum_{i \neq j}(z_i z_j)^2\left[u_r^2(f_i) + u_r^2(A_i)\right] + \left[z(1-z)\right]^2\left[u_r^2(f_i) + u_r^2(A_i)\right] \tag{38}$$

Here, $u_r(A_i)$ is the relative standard uncertainty in the peak area associated with component i and $u_r(f_i)$ is the relative standard uncertainty of the corresponding response factor given by

$$u_r^2(f_i) = \left[u_r^2(n_i) + u_r^2(A_i) \right]_{cal}, \tag{39}$$

where $u_r(n_i)$ is the relative standard uncertainty of the amount of substance n introduced in the calibration measurement. Following the same assumptions of Fandiño et al. [54], $u_r(n_i)$ may be equated with the relative standard uncertainty of the gas density in the sample loop, in turn related mainly to the uncertainties of filling pressure and temperature, $0.001p$ and 1 K, respectively. Furthermore, $u_r(A_i)$ was obtained from the relative standard deviation of the N independent observations under the same filling conditions and found to be $<0.5\%$. This uncertainty analysis leads to $u_r(n_i) = 0.3\%$ and $u_r(f_i) \sim 0.6\%$ for both components.

In the case of a binary mixture, Eq. (38) are express as

$$u^2(z) = \left[z(1-z) \right]^2 \sum_{i=1}^{2} \left[u_r^2(A_i) + u_r^2(f_i) \right]. \tag{40}$$

Combining the above terms, the estimated standard uncertainty can be reduced to the following simple expression:

$$u(z_i) = 0.011\, z_i \left(1 - z_i\right) \tag{41}$$

The standard uncertainty of temperature $u(T)$ was estimated to be 0.006 K over the temperature range of the VLE measurements, while the standard uncertainty of pressure $u(p)$ was estimated according to the manufacture's specification to be 0.009 MPa. These uncertainties were verified in previous works [54, 76].

The partial derivatives of the mole fraction of z_i in Eq. (33) - $(\partial z_i/\partial T)$ and $(\partial z_i/\partial p)$, also known as sensitivity coefficients according to GUM [107], can be calculated from established EOS. In the work of Richter et al.[109] and Lentner et al. [110] the use of GERG-2008 is suggested in the case of natural gases and similar mixtures. In this work, except in the critical region, the sensitivity coefficients were calculated through a series numerically from the PR-EOS with the binary interaction parameters fitted to the measured data. However, in the critical region, the PR-EOS failed to follow the experimental data so, in that region, $(\partial z/\partial T)_p$ and $(\partial z/\partial p)_T$ were estimated from the asymptotic behaviour approaching the critical point discussed below in section 5.2.

The final overall combined standard uncertainty u_c[108] was then computed on a point-by-point basis. The results are shown in Section 6-2.

Chapter 5 **Density Apparatus Design and Experimental Methodology**

5.1 Material

Four mixtures of (1 – x) CO_2 + x CO, with x ranging from (0.05 to 0.50) were used in this study. The mixtures were purchased from BOC who specified an expanded uncertainty in composition (k = 1.73) of 0.01x. Further quantitative compositional analysis was carried out by means of a previously calibrated GC [76]. The mole fraction of the mixtures are presented in Table 5.1.

Table 5.1 Description of samples, where z is the mole-fraction purity specified by the supplier, and x is the mole fraction of CO and $u(x)$ is the standard uncertainty of x in the mixtures of CO_2 and CO.

Sample	Source	z	x [a]	x [b]	$u(x)$ [b]
CO_2	BOC	> 0.99995	-	-	-
(1 – x) CO_2 + x CO	BOC	> 0.99990	0.0500	0.05031	5.20×10^{-4}
(1 – x) CO_2 + x CO	BOC	> 0.99985	0.1000	0.10107	9.90×10^{-4}
(1 – x) CO_2 + x CO	BOC	> 0.99971	0.2500	0.25254	2.06×10^{-3}
(1 – x) CO_2 + x CO	BOC	> 0.99945	0.5000	0.50183	2.75×10^{-3}

[a] Specified by the supplier

[b] Determined by GC analysis

5.2 Apparatus Description

The apparatus used in this study to measure the density was a slightly modified version of that described in detail by Tay et al. [111]. The main components were a vibrating-tube densimeter (VTD, Anton-Paar model DMA HP), a piston-driven pump (Teledyne Isco Series D single-pump, 100DM), a vacuum pump, and pressure and temperature sensors. Figure 5.1 is a schematic diagram of the experimental apparatus.

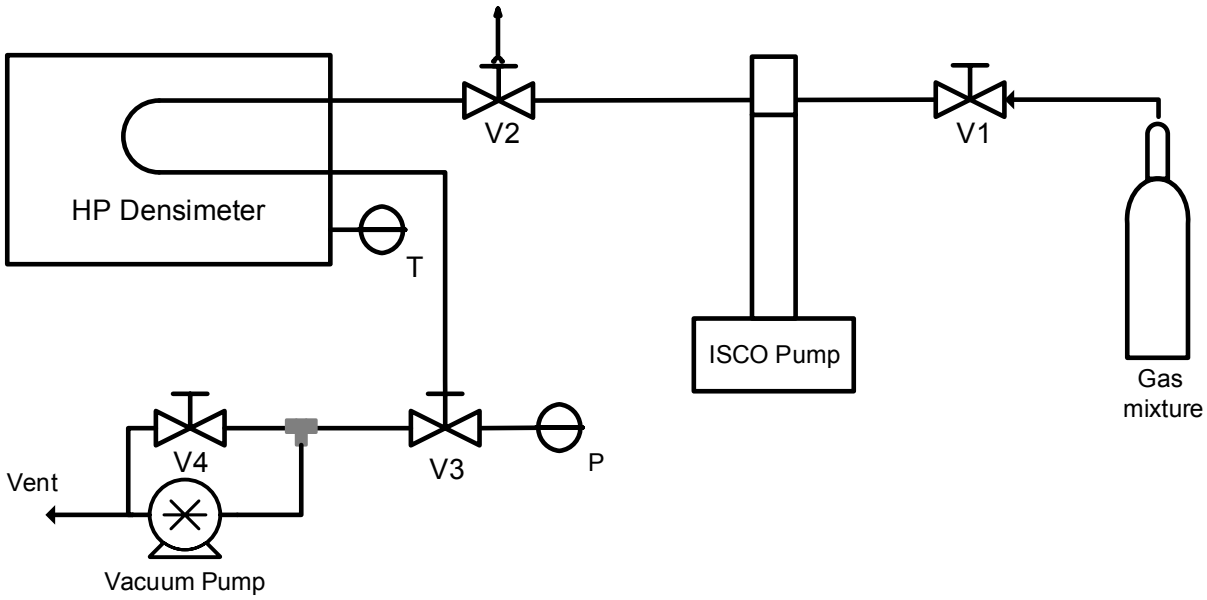


Figure 5.1 Schematic diagram of the experimental apparatus used to measure density. V1 and V3: inlet and outlet valves; V2: isolation and pressure relief valve; T: external platinum resistance thermometer; P: pressure transducer.

The piston-driven pump, valves 2 and 3, and all lines connecting them were constantly heated to temperatures above 313.15 K to avoid phase separation and a consequent shift in the composition of the mixture. Also, to ensure mixture homogeneity, the gas supply cylinder was constantly kept at a temperature of about 323 K by means of an electric heater.

The DMA HP model uses a U-shaped hastelloy vibrating tube with an internal volume of approximately 2 mL. It is suitable for the measurement of densities at temperatures from (283 to 473) K and pressures up to 70 MPa. The temperature was controlled by means of integrated Peltier elements with stability of ± 0.003 K. The DMA HP model was connected to a master instrument (Anton-Paar, DMA 5000 M), in which the temperature and period of oscillation were displayed.

The pressure was measured with a high-precision digital pressure sensor (Keller model PA-33X, 70 MPa full scale) with a manufacturer's stated expanded uncertainty (k = 1.73) of 0.02 MPa (0.05% of the full scale pressure). The VTD cell temperature was measured by an internal Pt100 sensor with an expanded (k = 1.73) uncertainty of 0.05 K at 95 % probability [111].

The piston-driven pump with a maximum working pressure of 70 MPa and maximum capacity of 100 mL was directly connected to the gas supply cylinder and used to fill the VTD to the desired pressure.

5.3 Toxicity of Materials / Safety Procedures

Figure 5.2 shows a picture of the apparatus, which was placed inside a fume cupboard to ensure safe containment of toxic gases in the event of a leak. The safety procedures carried out for the density measurements follow the procedures of the VLE measurements, which was already presented in section 4.3.

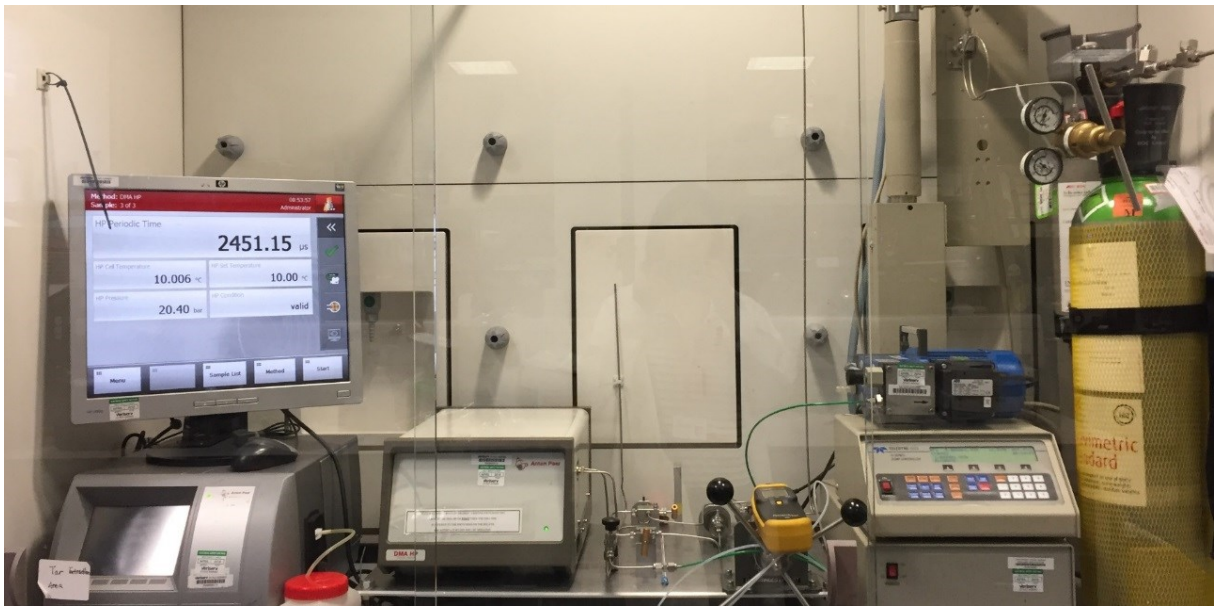


Figure 5.2 Picture of the density apparatus.

5.4 Densimeter Calibration and Validation

The density ρ is related to the period of oscillation τ in a VTD by the following relation:

$$\rho(T,p) = A(T,p)\tau^2 - B(T,p) \tag{42}$$

where A and B are the characteristic parameters, which are determined by calibration with reference fluids of known density in the ranges of temperature and pressure to be studied. The present densimeter was calibrated by Tay and Trusler [111] using helium and deionized water at temperatures between (283.15 and 473.15) K and at pressures

up to 65 MPa. Besides, the vacuum resonance period of oscillation was measured over the same temperature range. According to the VTD manufacturer, *A* and *B* can be approximated to a power series expansion in temperature *T* and pressure *p*, given as following

$$A / (\mathrm{kg \cdot m^{-3} \cdot \mu s^{-2}}) = \sum_{i=0}^{1} \sum_{j=0}^{2} a_{ij} p^i T^j \qquad B / (\mathrm{kg \cdot m^{-3}}) = \sum_{i=0}^{1} \sum_{j=0}^{2} b_{ij} p^i T^j \tag{43}$$

where *a* and *b* are coefficients of the polynomial calibration model determined by a regression against the calibration fluids densities. For both *A* and *B*, Tay and Trusler [111] obtained a linear dependency on pressure and cubic on temperature. Table 5.2 lists the parameters of Eq. (43).

Table 5.2 Coefficients of the polynomial calibration model, Eq. (43) for the vibrating-tube densimeter.

Parameter	Value	Parameter	Value
a_{00}	1.0398481×10^{-3}	b_{00}	-5.8224160×10^{3}
a_{01}	$-2.4886900 \times 10^{-5}$	b_{01}	3.2959073×10^{1}
a_{02}	$-8.0276216 \times 10^{-7}$	b_{02}	-3.0864669×10^{0}
a_{03}	4.7235209×10^{-8}	b_{03}	2.6061357×10^{-1}
a_{10}	$-2.9570996 \times 10^{-7}$	b_{10}	1.9604001×10^{0}
a_{11}	1.7434523×10^{-7}	b_{11}	-1.2527929×10^{0}
a_{12}	$-4.1738567 \times 10^{-8}$	b_{12}	3.0224710×10^{-1}
a_{13}	3.1901053×10^{-9}	b_{13}	$-2.3190075 \times 10^{-2}$

As a validation, the vacuum period was re-measured over the same temperature range and compared with the previous results; absolute deviations of not more than 0.03 μs were obtained, equivalent to a density change of < 0.15 $\mathrm{kg \cdot m^{-3}}$. As a further validation, the density of pure CO_2 was measured at T = 293.15 K and at pressures from (2 to 49) MPa. The measured densities of CO_2 are compared with values calculated from the EOS of Span and Wagner [70], as implemented in the software package REFPROP (version 10) [87], in Figure 5.3. The relative combined expanded uncertainty (k = 2) in density, discussed in detail below, was estimated to be between (0.06 and 1.4) %, while the uncertainty in the densities calculated from the EOS is

stated to be ≤ 0.05% at $p \leq 30$ MPa and ≤ 0.1% at higher pressures. The relative deviations shown in Figure 5.3 are therefore reasonable.

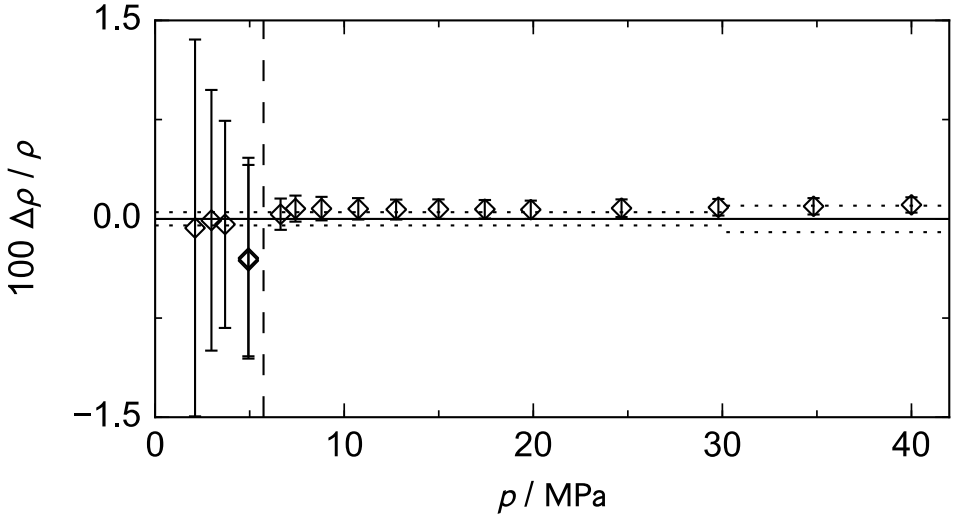


Figure 5.3 Relative deviation $\Delta\rho/\rho = (\rho_{exp} - \rho_{calc})/\rho_{exp}$ between the experimental density ρ_{exp} of pure CO_2 and the reference values ρ_{calc} calculated from the EOS of Span and Wagner [70] as a function of pressure p at $T = 293.15$ K. Error bars show the combined expanded uncertainty of the experimental data, while the horizontal dashed lines indicate the uncertainty of the calculated density as specified in reference [30] and the vertical dashed line indicates the vapor pressure of pure CO_2.

5.5 Experimental Procedure

Prior to the measurement of any isotherm, the VTD was set to the desired temperature and the apparatus was flushed with the gas mixture to be measured and evacuated for a period of at least 30 minutes. To check the stability of the apparatus, the period of oscillation under vacuum was measured before and after measuring each isotherm, absolute deviations of not more than 0.03 µs were obtained, equivalent to a density change of < 0.15 kg·m^{-3}.

The ISCO pump was filled with the mixture to be studied at the full supply cylinder pressure, which varied from (4 to 6) MPa, depending on the mixture. The pump was then placed in pressure control mode and used to regulate the pressure at values between (2 to 48) MPa. Measurements were made at temperatures from (283.15 to 313.15) K in increments of 10 K and at temperatures from (333.15 to 373.15) K in increments of 20 K. At least two measurements were made at each state point, and

the results were averaged, and at least 20 pressure points were measured on each isotherm. Check measurements were carried out with decreasing pressure and no hysteresis was observed. The repeatability of the period of oscillation measurements was within the resolution of 0.01 μs, equivalent to a density change of < 0.08 kg·m^{-3}.

Figure 5.4 illustrates the temperature-pressure diagram of the (CO_2 + CO) system at different compositions, from vapor pressure of CO_2 to equimolar composition. Besides, the temperature measured are shown.

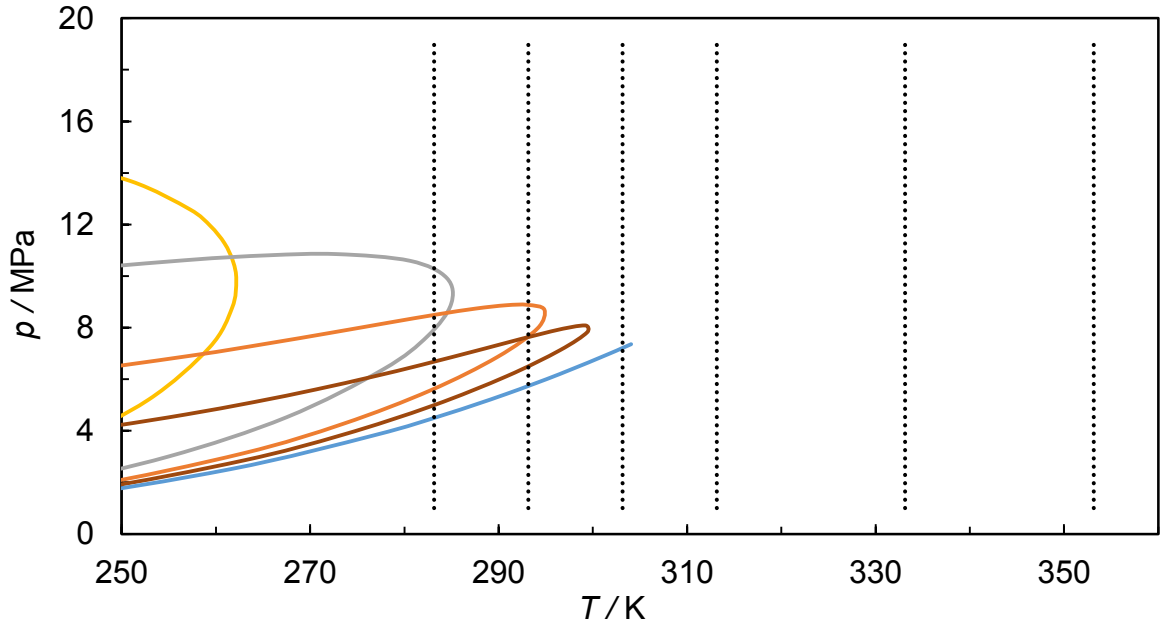


Figure 5.4 Temperature-pressure diagram of the (CO_2 + CO) system at different compositions: ___, vapor pressure of pure CO_2 calculated from the EOS of Span and Wagner [70]; ___, 0.0625 CO; ___, 0.125 CO; ___, 0.25 CO; ___, 0.5 CO all calculated from the Peng-Robinson EOS fitted with recommended binary parameters Table 3.3; **.....**, isotherms measured.

The room temperature was constantly measured at values varying from (292 to 295) K. Therefore, to avoid phase separation and a consequent shift in the composition of the mixture, the piston-driven pump, valves 2 and 3, and all lines connecting them were constantly heated to temperatures above 313.15 K (see Figure 5.1).

5.6 Uncertainty Analysis

The present uncertainty analysis follows that of Tay and Trusler [111], which was based on the ‘‘Evaluation of Measurement Data – Guide to the Expression of Uncertainty in Measurement (GUM)” [107] suggested by NIST. By rewriting Eq. (42) in terms of the densities ρ_1 and ρ_2, and the corresponding periods of oscillation τ_1 and τ_2, of the two calibration fluids measured at the same temperature and pressure conditions as the test fluid, one obtains the following:

$$\rho = \frac{\rho_1(\tau^2 - \tau_2^2) - \rho_2(\tau^2 - \tau_1^2)}{(\tau_1^2 - \tau_2^2)}. \tag{44}$$

Here, subscripts 1 and 2 refer to the calibration fluids, which were helium and water. From this, it follows that the standard uncertainty $u(\rho)$ of the test-fluid density obeys the following relation:

$$\begin{aligned} u^2(\rho) &= \left[\left(\frac{\partial\rho}{\partial\tau}\right)u(\tau)\right]^2 + \left[\left(\frac{\partial\rho}{\partial\tau_1}\right)u(\tau_1)\right]^2 + \left[\left(\frac{\partial\rho}{\partial\tau_2}\right)u(\tau_2)\right]^2 + \left[\left(\frac{\partial\rho}{\partial\rho_1}\right)u(\rho_1)\right]^2 + \left[\left(\frac{\partial\rho}{\partial\rho_2}\right)u(\rho_2)\right]^2 \\ &= \left[\frac{2\tau(\rho_1-\rho_2)}{\tau_1^2-\tau_2^2}u(\tau)\right]^2 + \left[\frac{2\tau_1(\rho_2-\rho)}{\tau_1^2-\tau_2^2}u(\tau_1)\right]^2 + \left[\frac{2\tau_2(\rho-\rho_1)}{\tau_1^2-\tau_2^2}u(\tau_2)\right]^2 \\ &\quad + \left[\frac{\tau^2-\tau_2^2}{\tau_1^2-\tau_2^2}u(\rho_1)\right]^2 + \left[\frac{\tau_1^2-\tau^2}{\tau_1^2-\tau_2^2}u(\rho_2)\right]^2 + u_B^2(\rho) \end{aligned} \tag{45}$$

This standard uncertainty includes contributions from the uncertainty in the measured period for the test fluid $u(\tau)$, the uncertainties in the measured period and the densities of the two calibration fluids $u(\tau_1)$, $u(\tau_2)$, $u(\rho_1)$ and $u(\rho_2)$, and an estimated of the systematic (type-B) uncertainty $u_B(\rho)$. Each of these terms have been discussed in detail by Tay and Trusler [111], who estimated the type-B term from test measurements carried out on methylbenzene under conditions in which highly-accurate independent measurements were available [112].

The overall combined uncertainty of the density of the (CO_2 + CO) mixtures is then given by

$$U_c(\rho) = k\left[u^2(\rho) + \left\{\left(\frac{\partial\rho}{\partial p}\right)_{T,x}u(p)\right\}^2 + \left\{\left(\frac{\partial\rho}{\partial T}\right)_{p,x}u(T)\right\}^2 + \left\{\left(\frac{\partial\rho}{\partial x}\right)_{T,p}u(x)\right\}^2\right]^{1/2} \tag{46}$$

where k is the coverage factor, and $u(p)$, $u(T)$ and $u(x)$ are the standard uncertainties in pressure, temperature and mole fraction of CO, respectively, which have been

discussed in section 5.2. The partial derivatives, or sensitivity factors, $(\partial\rho/\partial p)_T$, $(\partial\rho/\partial T)_p$, and $(\partial\rho/\partial x)_T$ were calculated from the new multi-parameter mixture model for the (CO_2 + CO) system developed in this work (see Section 3.3). The uncertainty budget is exemplified in Table 5.3 for the case of measurements at p = 28 MPa, T = 313.15 K and x = 0.1.

Table 5.3 Uncertainty budget for density ρ at pressure p = 28 MPa and temperature T = 313.15 K, where τ is period of oscillation and subscripts 1 and 2 refer to the calibration fluids helium and water, respectively. Sensitivity factors associated with temperature and pressure were estimated from the new mixture model for the (CO_2 + CO) system developed in this work (see Section 4).

Quantity	Value	Standard uncertainty	Sensitivity factor	Standard uncertainty
ρ_1	38.34 kg·m^{-3}	0.0194 kg·m^{-3}	0.21	0.004 kg·m^{-3}
ρ_2	1004.11 kg·m^{-3}	0.0191 kg·m^{-3}	0.80	0.015 kg·m^{-3}
τ_1	2459.96 µs	0.01 µs	0.98 kg·m^{-3}·µs^{-1}	0.010 kg·m^{-3}
τ_2	2657.81 µs	0.01 µs	4.01 kg·m^{-3}·µs^{-1}	0.040 kg·m^{-3}
τ	2617.87 µs	0.01 µs	4.99 kg·m^{-3}·µs^{-1}	0.050 kg·m^{-3}
p	28 MPa	0.0175 MPa	5.82 kg·m^{-3}·MPa^{-1}	0.102 kg·m^{-3}
T	313.15 K	0.025 K	4.21 kg·m^{-3}·K^{-1}	0.105 kg·m^{-3}
x	0.10107	0.00999	656.04 kg·m^{-3}	0.656 kg·m^{-3}
Type B				0.26 kg·m^{-3}
Expanded uncertainty (k = 2)			1.45 kg·m^{-3}	

The overall combined uncertainty of the density of the (CO_2 + CO) mixtures $U_c(\rho)$ is found to be ≤ 2.6 kg·m^{-3}, corresponding to relative expanded uncertainty of ≤ 1 % for most state points. The standard uncertainties in pressure $u(\rho)$ is found to be mostly about the same, except in the critical region. This means that the overall combined relative uncertainty becomes unfavourable at low densities; for a few state points at p = 2 MPa or close to the phase boundary, it approaches 2 %. On the other hand, the overall combined relative uncertainty is found to be ≤ 0.5% for all state points at p > 30 MPa. The dominant contribution to the overall uncertainty arises from the mixture composition, with an average relative contribution of 80% of $U_c(\rho)$.

Chapter 6 The (CO_2 + CO) System

This section presents the results and discussion of the measurements of VLE and homogeneous density for the (CO_2 + CO) system and comparison with literature data, in addition to result and performance of existing models and the new mixture model compared to VLE and homogenous density.

6.1 Literature Review on Vapour-Liquid Equilibrium and Density

VLE and density data for binary systems comprising CO_2 and toxic gases, such as CO, are still scarce. CO is formed in the first stage of a power-generation process based on gasification of coal [14, 113]. CO is a major component of the syngas and becomes a minor impurities, after the water-shift reaction. After that, CO is present in the pre-combustion CO_2 capture process in lower concentration, generally below 0.2% mol. Nevertheless, even small impurities on the CO_2 stream can drastically change the thermodynamic behaviour when compared to pure CO_2, as shown in the work of di Visser et al. [14].

Experimental VLE data for the (CO_2 + CO) system were first reported by Kaminishi et al. [83], who used an analytical method but reported only a few points covering the temperature range between (223.15 and 283.15) K, with no measurements close to the critical locus. Christiansen et al. [81] used an analytical method with vapor recirculation to measure VLE of the (CO_2 + CO) system over the same temperature range. Huamin [82] reported measurements at pressures of less than 7 MPa over a temperature range from (223.15 to 261.15) K and Blanco et al. [21], who used a synthetic method to study five different mixtures with CO_2 mole fractions ranging from 0.970 to 0.996 at temperatures between (253.15 and 293.15) K. The most-recent measurements for this system were reported by Westman et al. [75] almost at the same time as our work [76] were reported. Their measurement covers the temperature range between (253 and 298) K and pressures up to 13 MPa.

Figure 6.1 shows a graphic overview of the available literature VLE data of the (CO_2 + CO) system together with the present work, which range from temperatures just above the triple point of CO_2 to just below the critical point of CO_2. Table 6.1 summarises the literature data available for the vapor-liquid equilibria of the (CO_2 + CO) system.

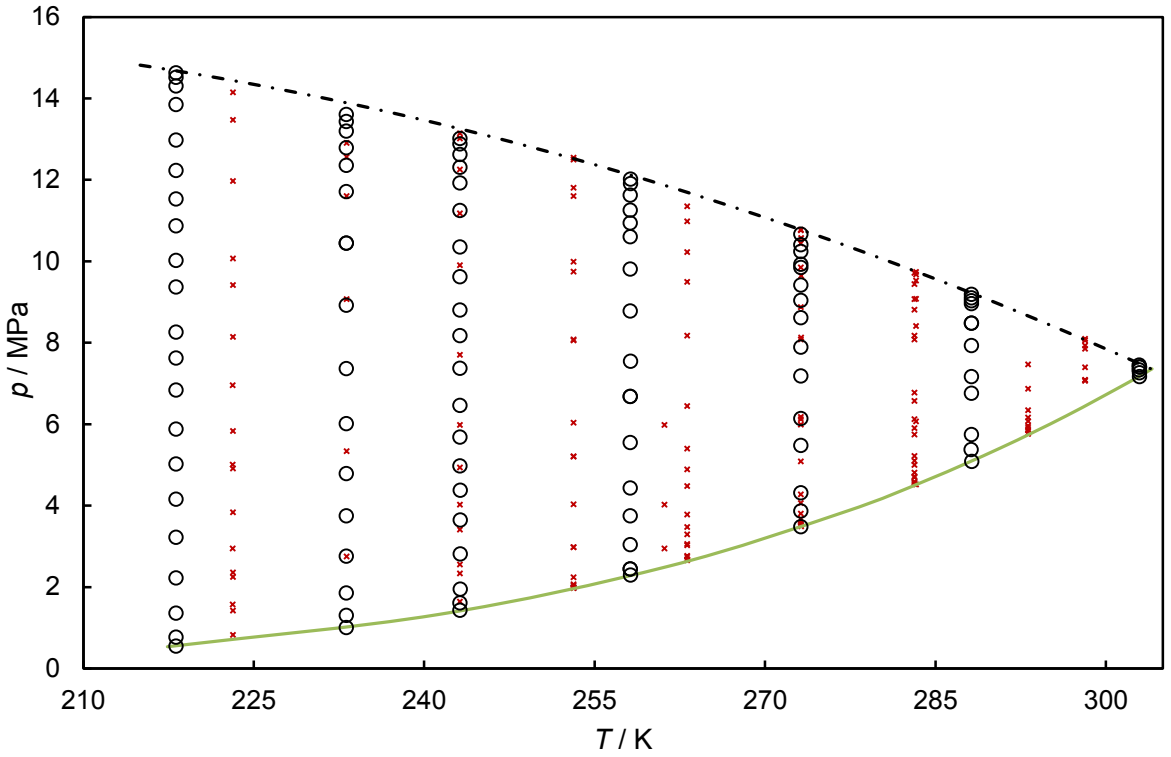


Figure 6.1 Temperature-pressure diagram of the (CO_2 + CO) system: x, available literature data; O, this work; – ·– ·, critical locus calculated from new mixture model; ----, vapor pressure of CO_2 from Span and Wagner EOS [70].

Table 6.1 Summary of the literature data available for the vapor-liquid equilibria of the (CO_2 + CO) system.

Authors	T_{min}/K	T_{max}/K	p_{max}/MPa	Reference
Kaminishi et al.	223.15	283.15	13	[83]
Christiansen et al.	223.15	283.15	14	[114]
Huamin	223.15	261.15	7	[82]
Blanco et al.	253.15	293.15	8	[21]
Westman et al.	253.15	298.15	13	[75]

In order to check the consistency and reliability of these reported measurements [83],[81],[82],[21],[75] experimental data available at similar conditions of mole fraction, pressure and temperature have been compared. Unfortunately, as detailed further below in section 6.2.2, the agreement between the five available data sources is poor, except for the dew-point data of Kaminishi et al. [83] and Christiansen et al.

[81] at 283.15 K. Significant inconsistencies between the measurements of all five authors occur even at low pressure.

The data situation can be misrepresented if just the number of data points and the ranges of temperature and pressure are assessed without considering the composition range. Compared to VLE, homogeneous density measurements are subject to an additional degree of freedom because the mixture composition can also be varied. Therefore, such measurements are a valuable addition to VLE data. One of the key binary systems for which density data are lacking is (CO_2 + CO). Most of the available data come from the work of Blanco et al. [21] which, despite the large number of data, covers only a limited composition range of (0.4 to 3) mol% CO. Other available data are those of Cipollina et al. [84], for mixtures containing (5 to 14) mol% CO at temperatures from (308 to 343) K and pressures up to 44 MPa, and Mallu et al. [85, 86] for composition of (20, 43 and 70) mol% CO at temperatures from (322 to 423) K and pressures up to 8 MPa. The most-recent measurement for this system were reported by Tsankova et al. [77] for composition of (50 and 75) mol% CO at temperatures from (255 to 313) K and pressures up to 8 MPa. Table 6.2 summarises the literature data available for the density of the (CO_2 + CO) system.

Table 6.2 Summary of the literature data available for the density of the (CO_2 + CO) system.

Authors	T_{min}/K	T_{max}/K	p_{max}/MPa	x_{CO} range	Reference
Mallu et al.	323.15	423.15	6.5	0.427	[85]
Mallu et al.	323.15	423.15	6.5	0.299 – 0.798	[86]
Cipollina et al.	308	338	44	0.050 – 0.140	[84]
Blanco et al.	253.15	298.15	13	0.004 – 0.030	[21]
Tsankova et al.	255	313	8	0.500 – 0.750	[115]

In summary, the (CO_2 + CO) system presents large regions without VLE and density data among the pressure, temperature and composition range relevant to CCS, besides discrepancies between different data sources. Clearly, there is a strong need for more data for certain properties, conditions, and mixtures, such as VLE and density measurements of the (CO_2 + CO) system.

6.2 Vapour-Liquid Equilibrium Results

The VLE of the (CO_2 + CO) system was measured along seven isotherms at temperatures varying from (218.15 to 302.93) K at pressures from the vapor pressure of pure CO_2 to just below the mixture critical pressure. The experimental results obtained for both the vapor and the liquid phases are given in Table 6.3, in which the temperature *T*, pressure *p* and compositions *x* and *y* represent the average of temperature, pressure and liquid or vapor mole fraction of CO at each state point, based on replicated measurements. The corresponding uncertainties for each series, which was obtain as described in Section 4.6, are also given in Table 6.3. The same set of measured data are shown in Figure 6.2 on a pressure-composition diagrams for all seven temperatures measured (218.15, 233.15, 243.15, 258.15, 273.15 and 288.15, 302.95) K. There is an slightly increase in the uncertainty in the mole fractions with increase in pressure. The highest values of uncertainty are on the proximity to the critical point of each isotherm as a consequence of the increase of contribution of the uncertainty in pressure in the total uncertainty in the mole fractions.

Table 6.3 Experimental VLE data for the (CO_2 + CO) system at temperature *T*, pressure *p*, vapor mole fraction of CO *y*, and liquid mole fraction of CO *x*.[a]

T/K	*p*/MPa	*x*	*y*	$u_c(y)$	$u_c(x)$
218.150[b]	0.5525	0.0000	0.0000	-	-
218.146	0.7663	0.0041	0.2352	2.15×10^{-3}	5.11×10^{-5}
218.147	1.3595	0.0169	0.5435	2.17×10^{-3}	3.03×10^{-4}
218.146	2.2203	0.0364	0.6975	1.83×10^{-3}	3.19×10^{-4}
218.147	3.2249	0.0595	0.7653	1.53×10^{-3}	4.88×10^{-4}
218.146	4.1612	0.0815	0.7988	1.37×10^{-3}	6.54×10^{-4}
218.149	5.0224	0.1024	0.8160	1.29×10^{-3}	7.83×10^{-4}
218.146	5.8773	0.1231	0.8248	1.24×10^{-3}	9.19×10^{-4}
218.145	6.8408	0.1461	0.8285	1.21×10^{-3}	1.06×10^{-3}
218.151	7.6271	0.1678	0.8291	1.21×10^{-3}	1.19×10^{-3}
218.146	8.2620	0.1858	0.8268	1.28×10^{-3}	1.29×10^{-3}
218.153	9.3705	0.2183	0.8194	1.48×10^{-3}	1.49×10^{-3}
218.150	10.0250	0.2394	0.8129	1.38×10^{-3}	1.65×10^{-3}

T/K	p/MPa	x	y	$u_c(y)$	$u_c(x)$
218.150	10.8735	0.2698	0.8020	1.38×10^{-3}	1.71×10^{-3}
218.153	11.5344	0.2953	0.7906	1.43×10^{-3}	1.79×10^{-3}
218.153	12.2332	0.3255	0.7752	1.49×10^{-3}	1.88×10^{-3}
218.156	12.9761	0.3606	0.7513	1.60×10^{-3}	1.98×10^{-3}
218.155	13.8475	0.4160	0.7112	1.76×10^{-3}	2.08×10^{-3}
218.153	14.3069	0.4588	0.6748	1.88×10^{-3}	2.13×10^{-3}
218.153	14.5194	0.4924	0.6460	2.11×10^{-3}	2.30×10^{-3}
218.153	14.6315	0.5117	0.6181	2.09×10^{-3}	2.21×10^{-3}
233.148[b]	1.0044	0.0000	0.0000	-	-
233.142	1.3063	0.0065	0.2089	1.65×10^{-3}	5.66×10^{-5}
233.142	1.8523	0.0184	0.4169	2.13×10^{-3}	1.55×10^{-4}
233.142	2.7598	0.0388	0.5782	2.16×10^{-3}	3.21×10^{-4}
233.139	3.7526	0.0617	0.6522	1.99×10^{-3}	5.22×10^{-4}
233.139	4.7869	0.0864	0.6964	1.84×10^{-3}	6.91×10^{-4}
233.139	6.0169	0.1167	0.7249	1.75×10^{-3}	8.84×10^{-4}
233.140	7.3685	0.1512	0.7383	1.68×10^{-3}	1.12×10^{-3}
233.140	8.9211	0.1961	0.7383	1.71×10^{-3}	1.39×10^{-3}
233.140	10.4460	0.2468	0.7220	1.91×10^{-3}	1.65×10^{-3}
233.140	10.4489	0.2471	0.7235	1.74×10^{-3}	1.63×10^{-3}
233.142	11.7145	0.2991	0.6996	1.87×10^{-3}	1.85×10^{-3}
233.140	12.3592	0.3295	0.6811	1.89×10^{-3}	1.97×10^{-3}
233.141	12.7913	0.3542	0.6641	1.95×10^{-3}	2.03×10^{-3}
233.140	13.1979	0.3824	0.6414	2.02×10^{-3}	2.11×10^{-3}
233.139	13.4335	0.4028	0.6233	2.11×10^{-3}	2.18×10^{-3}
233.140	13.6067	0.4218	0.6059	2.09×10^{-3}	2.19×10^{-3}
243.146[b]	1.4280	0.0000	0.0000	-	-
243.156	1.6086	0.0039	0.0966	1.03×10^{-3}	3.38×10^{-5}
243.160	1.9526	0.0114	0.2329	1.61×10^{-3}	9.72×10^{-5}
243.157	2.8150	0.0306	0.4309	2.22×10^{-3}	2.58×10^{-4}
243.157	3.6502	0.0500	0.5257	2.81×10^{-3}	4.74×10^{-4}
243.161	4.3809	0.0686	0.5750	2.40×10^{-3}	6.74×10^{-4}

T/K	p/MPa	x	y	$u_c(y)$	$u_c(x)$
243.151	4.9754	0.0784	0.6075	2.08×10^{-3}	7.79×10^{-4}
243.141	5.6865	0.0983	0.6298	2.04×10^{-3}	7.72×10^{-4}
243.136	6.4581	0.1183	0.6480	1.98×10^{-3}	9.15×10^{-4}
243.138	7.3727	0.1432	0.6607	1.94×10^{-3}	1.08×10^{-3}
243.137	8.1763	0.1665	0.6671	1.97×10^{-3}	1.21×10^{-3}
243.139	8.8071	0.1850	0.6669	1.96×10^{-3}	1.34×10^{-3}
243.140	9.6222	0.2120	0.6640	1.97×10^{-3}	1.50×10^{-3}
243.152	10.3503	0.2380	0.6570	1.95×10^{-3}	1.59×10^{-3}
243.152	11.2522	0.2744	0.6412	2.06×10^{-3}	1.77×10^{-3}
243.152	11.9288	0.3057	0.6217	2.13×10^{-3}	1.86×10^{-3}
243.143	12.3102	0.3278	0.6074	2.07×10^{-3}	1.91×10^{-3}
243.143	12.6259	0.3490	0.5901	2.44×10^{-3}	2.00×10^{-3}
243.141	12.8860	0.3706	0.5702	2.20×10^{-3}	2.14×10^{-3}
243.144	13.0151	0.3842	0.5558	2.27×10^{-3}	2.06×10^{-3}
258.150[b]	2.2937	0.0000	0.0000	-	-
258.130	2.4417	0.0032	0.0449	7.69×10^{-4}	2.71×10^{-5}
258.135	2.4420	0.0028	0.0406	7.55×10^{-4}	2.44×10^{-5}
258.141	3.0421	0.0163	0.1916	1.39×10^{-3}	1.40×10^{-4}
258.140	3.7519	0.0323	0.3025	1.84×10^{-3}	2.77×10^{-4}
258.133	4.4357	0.0479	0.3733	2.19×10^{-3}	4.09×10^{-4}
258.132	5.5498	0.0750	0.4499	2.38×10^{-3}	6.16×10^{-4}
258.132	6.6833	0.1044	0.4950	2.23×10^{-3}	8.40×10^{-4}
258.132	6.6842	0.1045	0.4952	2.12×10^{-3}	7.93×10^{-4}
258.146	7.5430	0.1289	0.5164	4.16×10^{-3}	1.20×10^{-3}
258.133	8.7832	0.1656	0.5299	2.11×10^{-3}	1.17×10^{-3}
258.130	9.8098	0.2007	0.5279	2.26×10^{-3}	1.46×10^{-3}
258.129	10.6078	0.2325	0.5173	2.39×10^{-3}	1.63×10^{-3}
258.127	10.9393	0.2419	0.5099	2.33×10^{-3}	1.74×10^{-3}
258.126	11.2542	0.2650	0.5004	2.17×10^{-3}	1.69×10^{-3}
258.126	11.6229	0.2888	0.4841	2.16×10^{-3}	1.85×10^{-3}
258.146	11.9075	0.3200	0.4690	2.50×10^{-3}	2.06×10^{-3}

T/K	p/MPa	x	y	$u_c(y)$	$u_c(x)$
258.149	12.0211	0.3349	0.4527	2.25×10^{-3}	2.09×10^{-3}
273.151[b]	3.4846	0.0000	0.0000	-	-
273.146	3.8678	0.0090	0.0710	6.20×10^{-4}	7.59×10^{-5}
273.144	4.3153	0.0195	0.1368	1.10×10^{-3}	1.69×10^{-4}
273.147	5.4789	0.0484	0.2562	1.74×10^{-3}	4.09×10^{-4}
273.148	6.1410	0.0658	0.3009	1.85×10^{-3}	5.46×10^{-4}
273.146	7.1824	0.0952	0.3500	2.05×10^{-3}	7.61×10^{-4}
273.149	7.8939	0.1170	0.3709	2.00×10^{-3}	8.83×10^{-4}
273.149	8.6173	0.1406	0.3830	2.18×10^{-3}	1.09×10^{-3}
273.140	9.0416	0.1550	0.3860	2.09×10^{-3}	1.20×10^{-3}
273.138	9.4148	0.1671	0.3855	2.12×10^{-3}	1.27×10^{-3}
273.145	9.8470	0.1830	0.3753	2.14×10^{-3}	1.35×10^{-3}
273.142	9.9318	0.1880	0.3780	2.15×10^{-3}	1.41×10^{-3}
273.144	10.2418	0.2037	0.3685	2.17×10^{-3}	1.55×10^{-3}
273.144	10.4118	0.2144	0.3605	2.10×10^{-3}	1.54×10^{-3}
273.146	10.6647	0.2362	0.3419	2.07×10^{-3}	1.64×10^{-3}
288.188[b]	5.0896	0.0000	0.0000	-	-
288.146	5.3739	0.0072	0.0316	3.16×10^{-4}	6.05×10^{-5}
288.156	5.7490	0.0164	0.0677	6.78×10^{-4}	1.48×10^{-4}
288.157	6.7619	0.0437	0.1396	1.13×10^{-3}	3.92×10^{-4}
288.161	7.1708	0.0556	0.1608	1.24×10^{-3}	4.78×10^{-4}
288.156	7.9308	0.0797	0.1881	1.44×10^{-3}	6.79×10^{-4}
288.161	8.4807	0.1001	0.1980	1.43×10^{-3}	8.58×10^{-4}
288.159	8.4809	0.1001	0.1980	1.48×10^{-3}	8.36×10^{-4}
288.164	8.9625	0.1271	0.1966	1.45×10^{-3}	1.05×10^{-3}
288.157	9.0304	0.1296	0.1954	2.20×10^{-3}	1.11×10^{-3}
288.163	9.0997	0.1380	0.1926	1.48×10^{-3}	1.13×10^{-3}
288.157	9.1867	0.1569	0.1861	1.50×10^{-3}	1.29×10^{-3}
302.940[b]	7.1712	0.0000	0.0000	-	-
302.938	7.2607	0.0028	0.0047	7.69×10^{-5}	3.08×10^{-5}

T/K	p/MPa	x	y	$u_c(y)$	$u_c(x)$
302.936	7.3326	0.0053	0.0082	1.07×10^{-4}	5.82×10^{-5}
302.937	7.4068	0.0080	0.0114	1.37×10^{-4}	8.77×10^{-5}
302.937	7.4068	0.0080	0.0114	1.37×10^{-4}	8.77×10^{-5}
302.936	7.4519	0.0097	0.0131	1.43×10^{-4}	1.06×10^{-4}

[a] Standard uncertainties (k = 1.73) are $u(T)$ = 0.006 K, $u(p)$ = 0.009 MPa.

[b] CO_2 vapor pressure measurement.

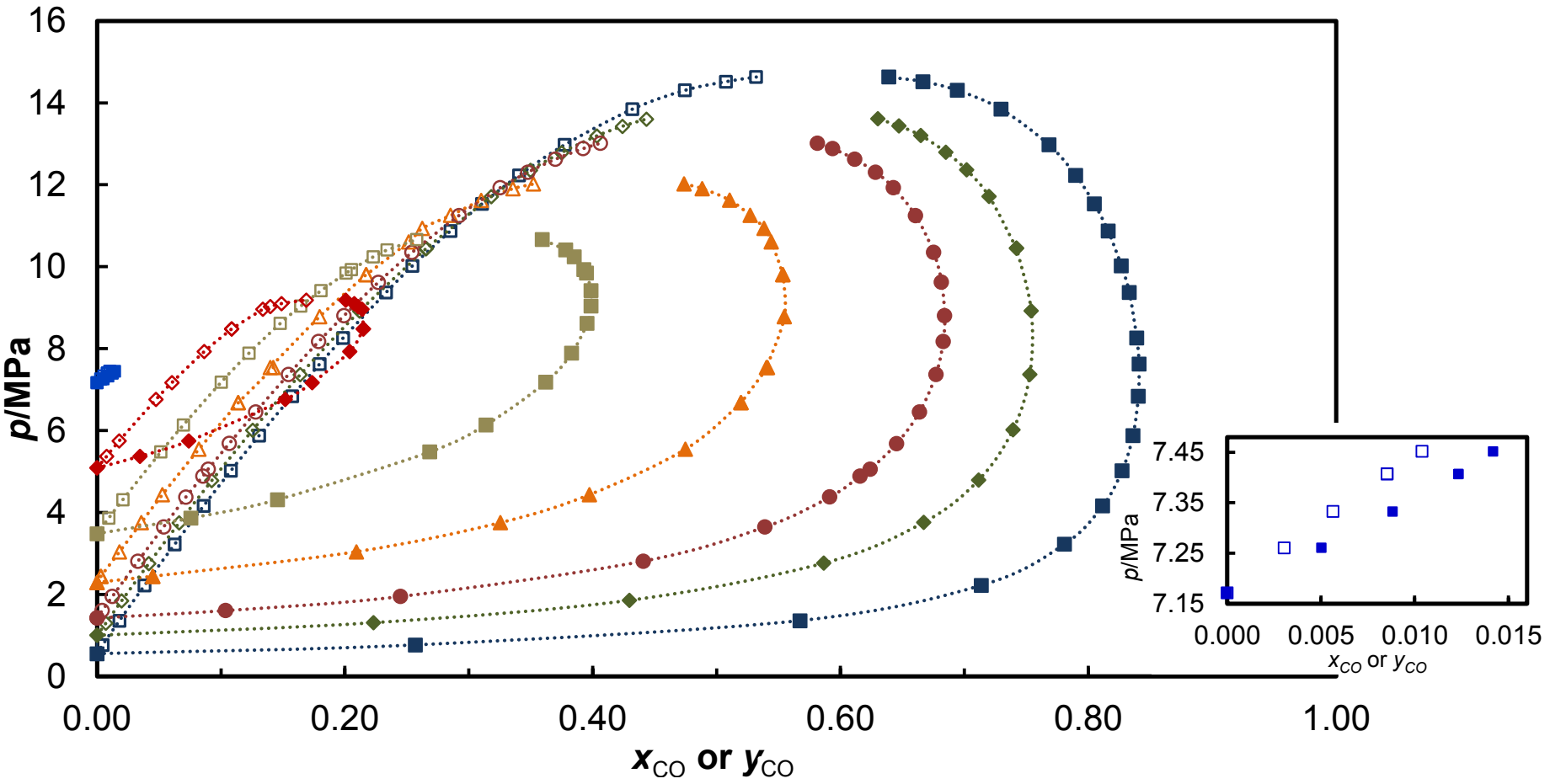


Figure 6.2 Pressure-composition diagrams of the (CO_2 + CO) system: (■ and □), 218.15 K; (◆ and ◇), 233.15 K; (● and ○), 243.15 K; (▲ and △), 258.15 K; (■ and □), 273.15 K; (◆ and ◇), 288.15 K; (■ and □), 302.95 K, and ----, trend line.

6.2.1 Critical Point Estimation

Accurate and direct experimental determination of mixture critical points is a challenge that typically requires a windowed equilibrium cell to permit visual observation. In this work, all VLE measurements were carried out without visual observation. Nevertheless, the critical point can be determined by analysing near-critical data in terms of the asymptotic behaviour approaching the critical point [116] which, applied to a binary system, can be expressed as follows:

$$z = z_c + \left(\lambda_1 + \varepsilon\frac{\lambda_2}{2}\right)(p_c - p) + \varepsilon\frac{\mu}{2}(p_c - p)^{\beta} \tag{47}$$

Here, ε is 1 for bubble points or -1 for dew points; z represents either x or y at pressure p; z_c is the critical composition, p_c is the critical pressure, and β = 0.325. Between four and seven pairs of VLE tie lines close to the critical point on each isotherm up to 288.15 K were considered. Initially for each isotherm individually, z_c was set as the medium between the last bubble and dew points measured, and p_c was set at least 0.01 MPa bigger than the last pressure point measured. The parameters λ_1, λ_2 and μ of Eq. (47) were optimized so as to minimise the normalised objective function S defined as:

$$S^2 = (1/N)\sum_{i=1}^{N}(z_i - z_{i,\mathrm{calc}})^2 \ . \tag{48}$$

Here, N is the total number of state points used in the regression and subscript 'calc' indicates values calculated from the asymptotic behaviour approaching the critical point as shown in Eq. (47). Then, the parameters λ_1, λ_2 and μ of Eq. (47) were re-optimized together with z_c and p_c as to minimise Eq. (49).

In order to extend Eq. (47) to cover a range of temperatures, each parameter M (*i.e.* λ_1, λ_2, μ, z_c and p_c) was represented as a polynomial in temperature as follows:

$$M(T) = a_1 + a_2(T/\mathrm{K}) + a_3(T/\mathrm{K})^2 \ . \tag{49}$$

The optimized parameters are given in Table 6.4 and shown in Figure 6.3. The parameters were found to result in a good description of the critical region. Parameter λ_1 and λ_2 were found to be represented adequately as linear function, so that a_3 was zero in those cases. The high quality of the fit in the critical region is illustrated in Figure 6.4, where the bubble and dew pressures against z/z_c are plotted.

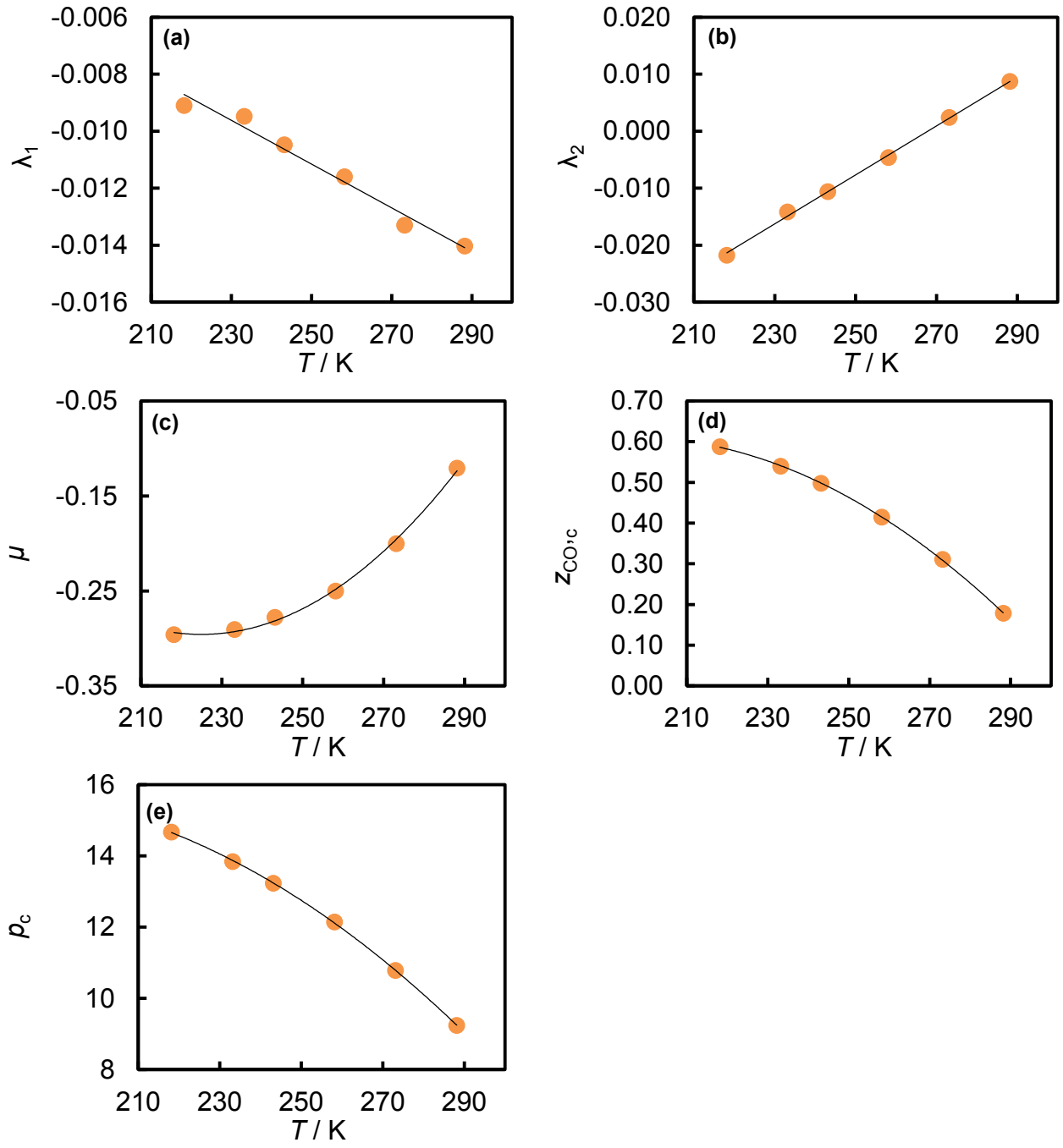


Figure 6.3 Optimized parameters from asymptotic behaviour approaching the critical point applied to the binary system (CO_2 + CO): λ_1 (a), λ_2 (b), μ (c), z_c (d) and p_c (e) against temperature. ——, Eq. (49).

Table 6.4 Coefficients of Eqs. (47) and (49) for the critical locus.

Parameter	a_1	a_2	a_3
$\lambda_1(T)$/MPa^{-1}	7.74×10^{-3}	-7.65×10^{-5}	-
$\lambda_2(T)$/MPa^{-1}	-1.08×10^{-1}	3.87×10^{-4}	-
$\mu(T)$/MPa$^{-\beta}$	1.58×10^{0}	-1.69×10^{-2}	3.76×10^{-5}
$z_{CO,c}(T)$	-1.35×10^{0}	2.00×10^{-2}	-5.11×10^{-5}
$p_c(T)$/MPa	2.47×10^{0}	1.57×10^{-1}	-4.65×10^{-4}

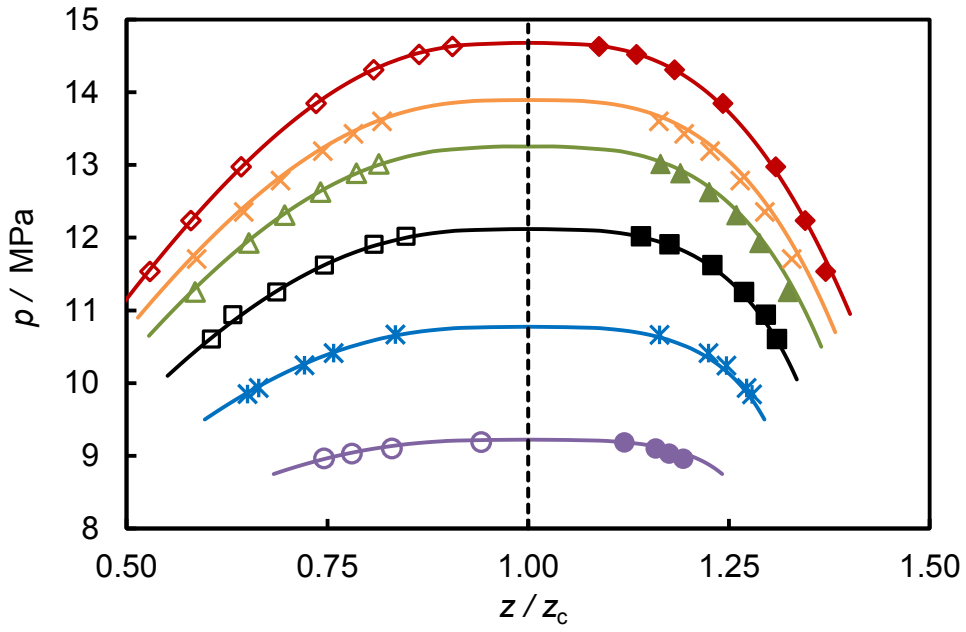


Figure 6.4 Critical point estimation by regression analysis of asymptotic behaviour approaching the critical point in Eq. (47). Pressure p vs. mole fraction z of CO divided by critical mole fraction z_c for the (CO_2 + CO) system: ◇, T = 218.15 K; X, T = 233.15 K; △, T = 243.15 K; □, T = 258.15 K; ✳, T = 273.15 K; ○, T = 288.15 K, ——, asymptotic behaviour approaching the critical point Eq. (47) at each temperature.

The critical loci are plotted in Figure 6.5 over the range of critical compositions investigated; also shown is the critical point of CO_2 [70].

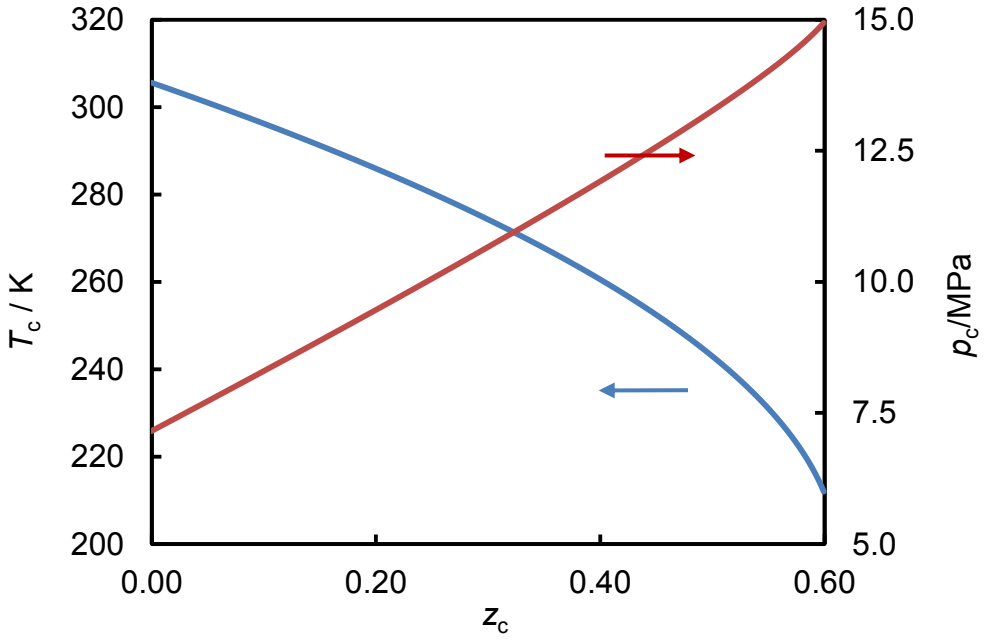


Figure 6.5 Critical loci for (CO_2 + CO) system predicted by Eq. (47). Critical temperature T_c (left) and critical pressure p_c (right) plotted against the critical mole fraction z_c of CO.

6.2.2 Comparison of VLE Data with Literature Data

Figure 6.6 presents comparisons between the available VLE data in the literature [21, 75, 76, 81-83] and the new mixture model. The available data cover almost the full temperature range possible from just above the triple-point temperature of CO_2 to just below the critical temperature of CO_2. The plot presents relative deviations of pressure at specified temperature and liquid composition from the mixture model as a function of pressure. The majority of the VLE data are represented within ±5% or better; however, most of the off-scale points come from Blanco et al. [21]. The most reliable data as judged in our assessment, those of Kaminishi et al. [83], Souza et al. [76] and Westman at al. [75], show mutual agreement in $p(x,T)$ to within about ±1% and are described by the model to within about ±2%. Nevertheless, these small deviations exceed typical experimental uncertainties which, in the work of Souza et al. [76], were estimated to be < 1%.

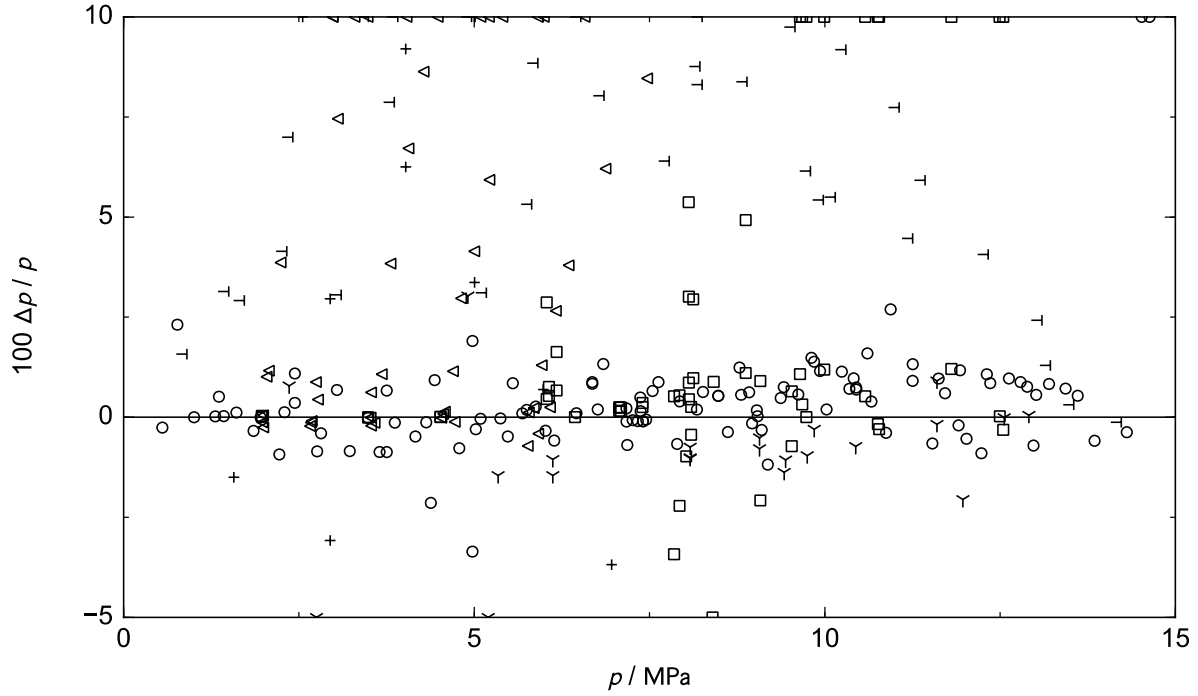


Figure 6.6 Relative deviations $\Delta p/p = (p_{exp} - p_{calc})/p_{exp}$ between the experimental bubble and dew pressures p_{exp} of (CO_2 + CO) [21, 75, 76, 81-83] and values p_{calc} calculated from the new mixture model as a function of pressure. ◁, Blanco et al., 2014; ⊣, Christiansen et al., 1974; + Huamin, 1991; ⋎ ,Kaminishi et al., 1968; ○, this work, published by Souza et al.,2018; □, Westman et al., 2018.

Figure 6.7 illustrates the deviations of the experimental mole fractions (x_{exp}, y_{exp}) obtained in this work and in the literature [21, 81-83] from the values (x_{calc}, y_{calc}) calculated from the PR-EOS with the recommended binary parameters from Table 3.3, section 3.2.2. The plots are divided into two sub-intervals of temperature: Figure 6.7(a) and (c) represent temperatures below 253 K and Figure 6.7(b) and (d) temperatures above 253 K. For both sub-intervals, it can be seen that the experimental data obtained in this work present systematic deviations from the PR-EOS, considerably greater than the uncertainties reported in Section 4.

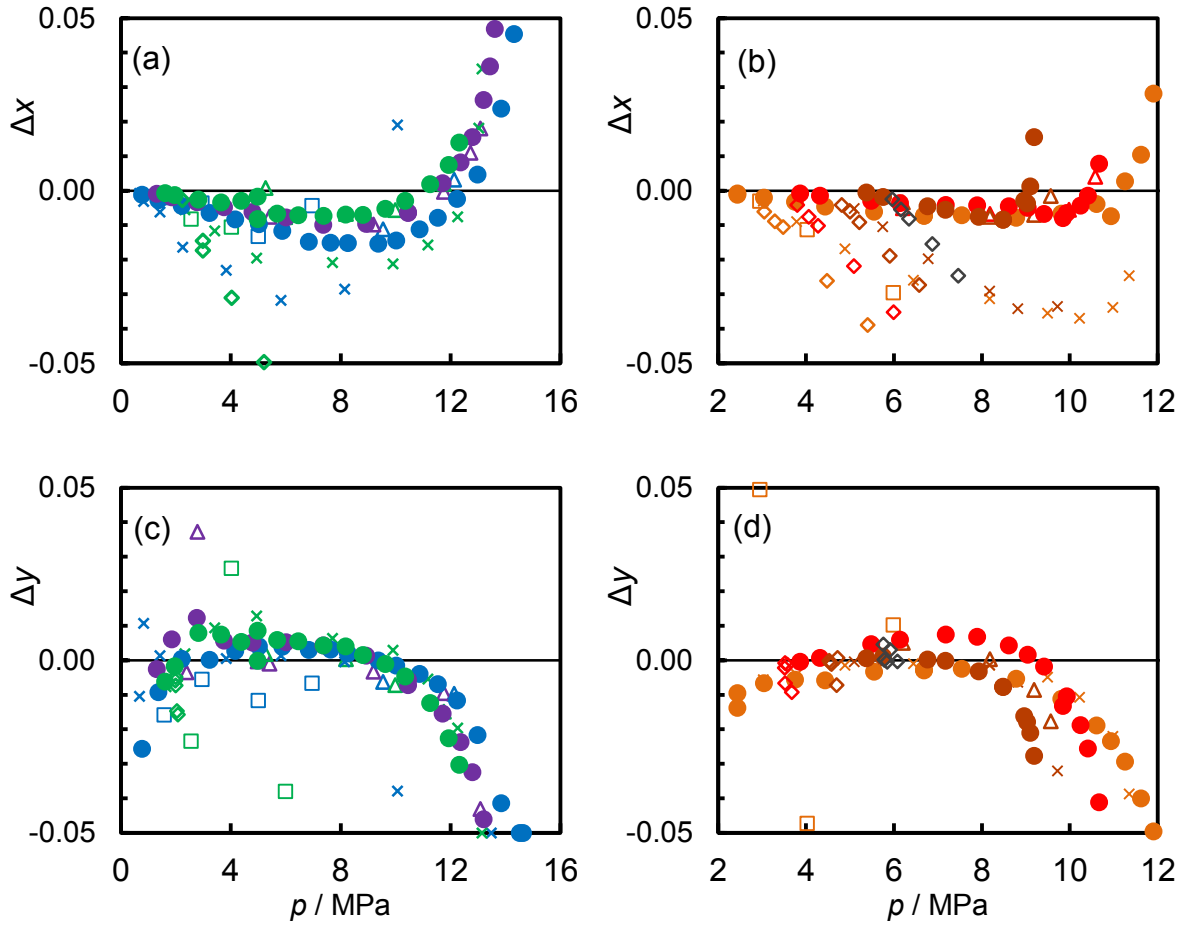


Figure 6.7 Deviations $\Delta x = x_{exp} - x_{calc}$ and $\Delta y = y_{,exp} - y_{,calc}$ between experimental mole fractions ($x_{,exp}$, $y_{,exp}$) and the values ($x_{,calc}$, $y_{,calc}$) calculated from the Peng-Robinson EOS with recommended binary parameters for the (CO_2 + CO) system. ●, this work; ☐, Huamin, 1991; △, Kaminishi et al., 1968; ×, Christiansen et al., 1974; ◇, Blanco et al., 2014. (a) and (c): blue, T/K ≤ 223.15; purple, 223.15 < T/K ≤ 233.15; green, 233.15 < T/K ≤ 253.15; (b) and (d): orange, 253.15 < T/K ≤ 263.15; red, 263.15 < T/K ≤ 273.15; brown, 273.15 < T/K ≤ 288.15; dark grey, 288.15 < T/K ≤ 300. Outliers are plotted on the upper or lower horizontal axes. [76]

It is evident that the mole fractions in the liquid phase are considerably better represented by the PR-EOS than the mole fractions in the vapor phase. If the near-critical state points are not considered, the greatest absolute deviation between the mole fractions in the liquid phase is 0.008 (excluding the results of the 218.15 K isotherm), while the corresponding in the vapor phase is 0.022. The experimental data reported by Blanco et al. [21], Christiansen et al. [81] and Huamin et al. [82] present generally worse deviations from the PR-EOS model than the experimental data presented in this work, even at low pressures. In contrast, there is generally good agreement between the few experimental data reported by Kaminishi et al. [83], Westman et al. [75] and our experimental data in the upper sub-interval of temperature for both liquid and vapor phases.

The deviations among different authors are more evident when assessing pressure-composition diagrams, as shown in Figure 6.8. The plots represent selected isotherms with VLE data from Kaminishi et al. [83], Christiansen et al. [81], Huamin et al. [82], Blanco et al. [21], Souza et al. [76] and Westman et al. [75]. Data from different sources deviate among one another on average less than 5% in pressure at similar conditions of temperature and composition, even at lower pressures. The largest deviation from the new mixture model are observed for the dew points of Blanco et al. [21], as can be seen in Figure 6.8 at T = 273.15 K. In general, the VLE data of Blanco et al. [21] deviate from all others sources [75, 76, 83] by between 2% and 15% in pressure at similar composition; surprisingly, they are in close agreement with the GERG-2008 model. Some disagreement between different sources is also observed in the retrograde regions of most isotherms, as evident at temperatures of 243.15 K and 273.15 K.

In the critical region, the new mixture model agrees well with the different data sources [21, 75, 76, 81-83]. In particular, the model agrees with the measurements of Souza et al. [76] in the critical region to within about 2% in $p(x,T)$.

Figure 6.8 also includes values calculated from GERG-2008 and EOS-CG and further comparisons with those models are discussed at section 6.2.3.

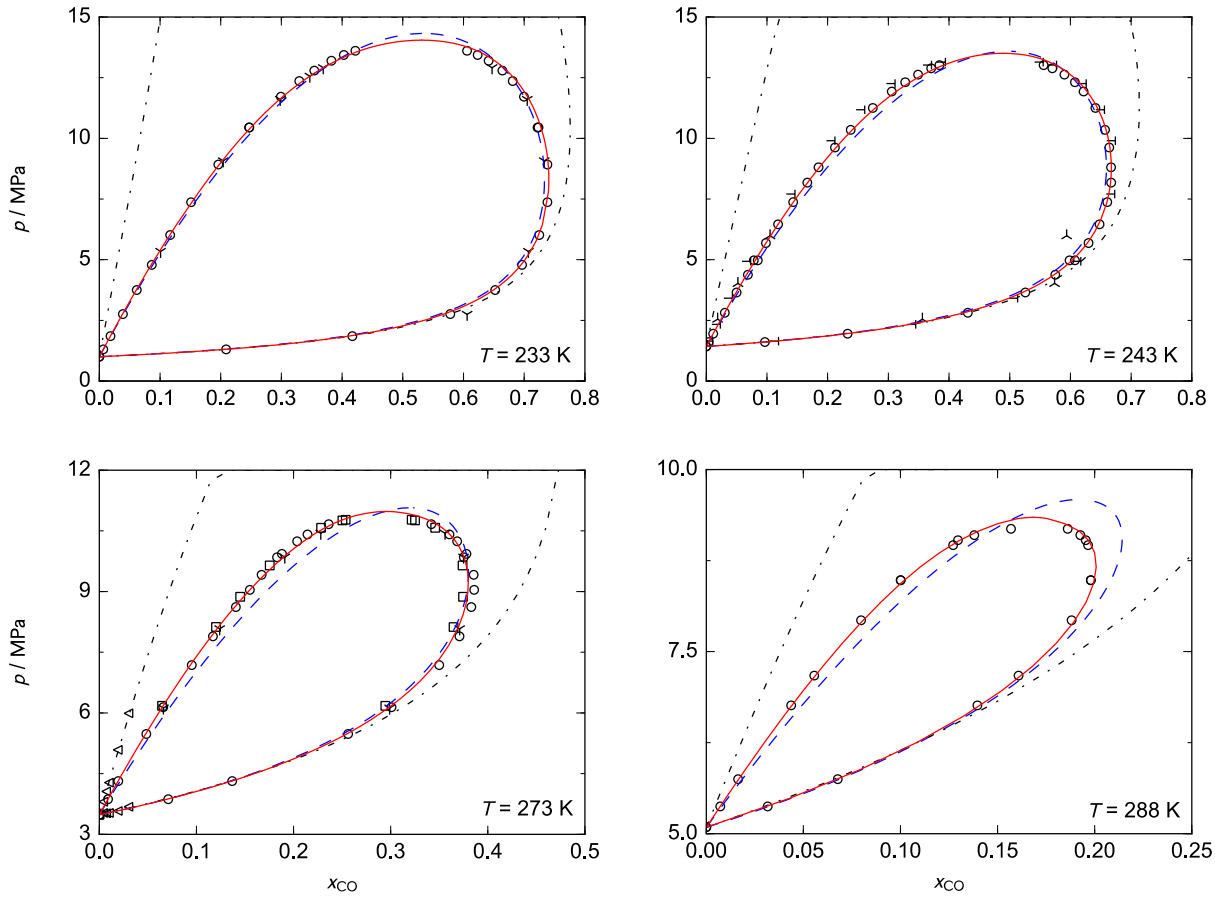


Figure 6.8 Pressure-composition diagrams of the (CO_2 + CO) system as calculated from the new mixture model. Experimental VLE data from different sources [21, 75, 76, 81-83] and models are shown for comparisons. ◁, Blanco et al., 2014; ⊣, Christiansen et al., 1974; ⅄ Huamin, 1991; ⅄ ,Kaminishi et al., 1968; ○, this work, published by Souza et al.,2018; □, Westman et al., 2018. – – –, EOS-CG; – ·– ·, GERG-2008 ——, New model.

6.2.3 Comparison of VLE Data with Equations of State

Figure 6.9 and 6.10 present the experimental pressure-composition data on each of the seven isotherms studied. Also plotted are the values calculated from the PR-EOS, with the optimized binary parameters presented in Table 3.3, section 3.2.2; GERG-2008 [26] and EOS-CG with original parameters values and the new mixture model from this work.

The PR-EOS gives a reasonably-good representation of our data at low and medium pressures and presents significantly better agreement for the liquid-phase composition than for the vapor-phase composition. As expected, without exception, the PR-EOS

overestimates the mole fractions in both liquid and vapor phases at pressures close to the critical point of all isotherms of the (CO_2 + CO) system.

It is obvious that EOS-CG presents a significant improvement in the estimation of mole fractions in both liquid and vapor phases at pressures close to the critical point of all isotherms of the (CO_2 + CO) system except the lower temperature of 218.15 K when compared with PR-EOS.

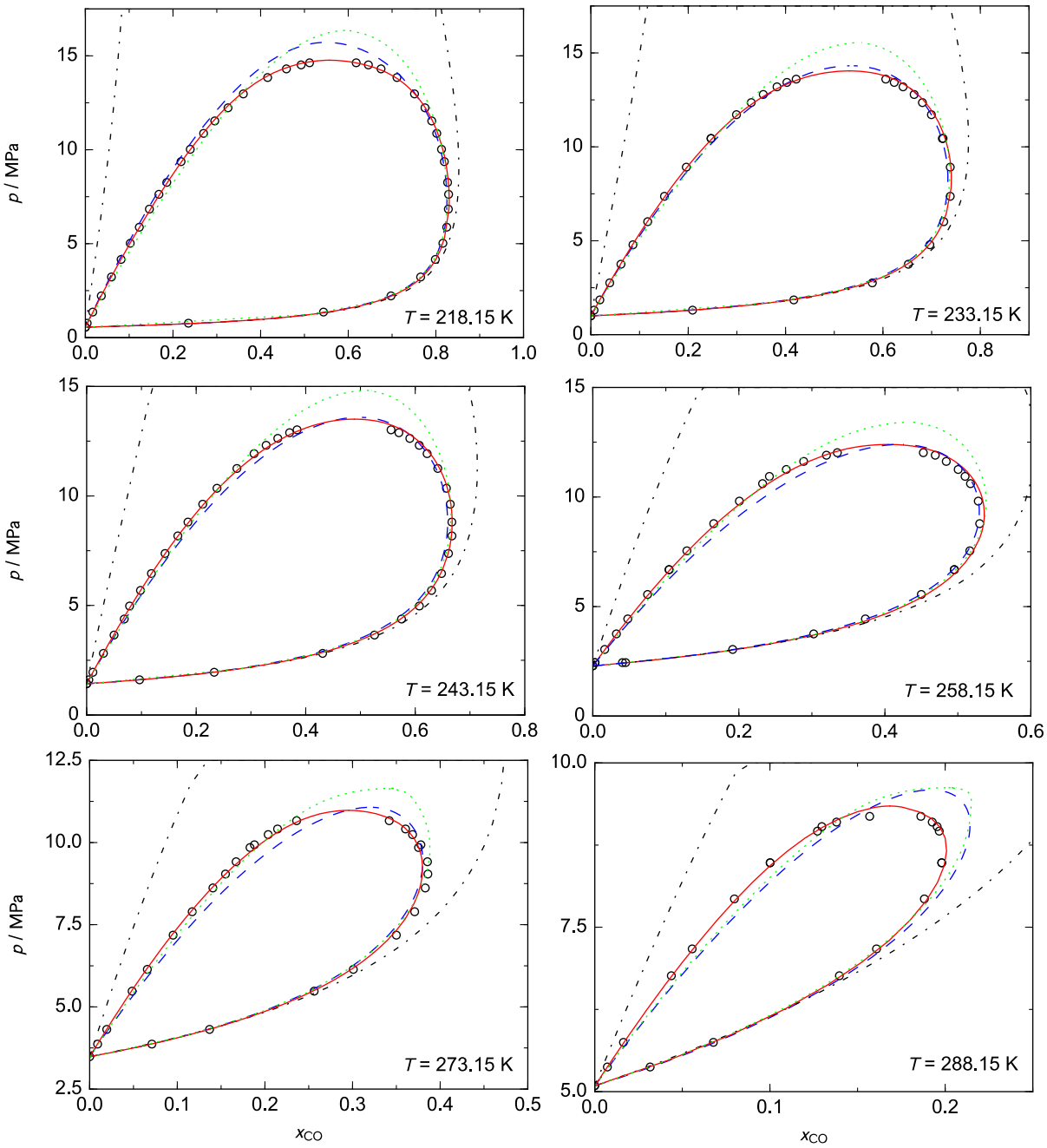


Figure 6.9 Pressure-composition diagrams of the (CO_2 + CO) system: ○, this work, published by Souza et al. [76] and models: – – –, EOS-CG; – ·– ·, GERG-2008 ——, New model and ·····, Peng-Robinson EOS fitted with recommended binary parameters.

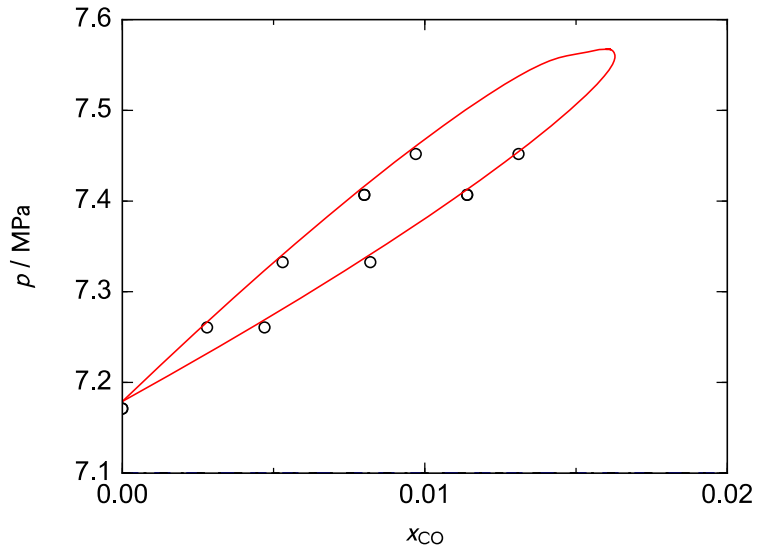


Figure 6.10 Pressure-composition diagram of the (CO_2 + CO) system at T = 302.94 K: ○, this work; ——, new mixture model.

It is apparent that the new mixture model represents a considerable improvement compared with both models, especially in the critical region. In the critical region, EOS-CG shows increasing deviations from the new mixture model as the critical point is approached. For example, at T = 288.15 K, the two models differ by about 3% in the estimated critical pressure and 13% in the estimated critical composition. Even at lower pressures, values calculated from EOS-CG deviate significantly from the measurements and the new model. For instance, when calculating liquid mole fraction of CO from EOS-CG at T = 273.15 K and p = 6.1 MPa, the deviations are more than 10 mol% for the data sets of Kaminishi et al. [83], Souza et al. [76] and Westman et al. [75]. Considerably higher deviations, some more than 40 mol%, are observed with GERG-2008. The new mixture model represent the same data sets with average deviation of 0.7 mol% even at the highest temperature of T = 302.94 K (See Figure 6.10).

Figure 6.11 presents the relative volatility for the (CO_2 + CO) system at four temperature studied. It shows both the experimental data from this work and for the results from the new mixture model.

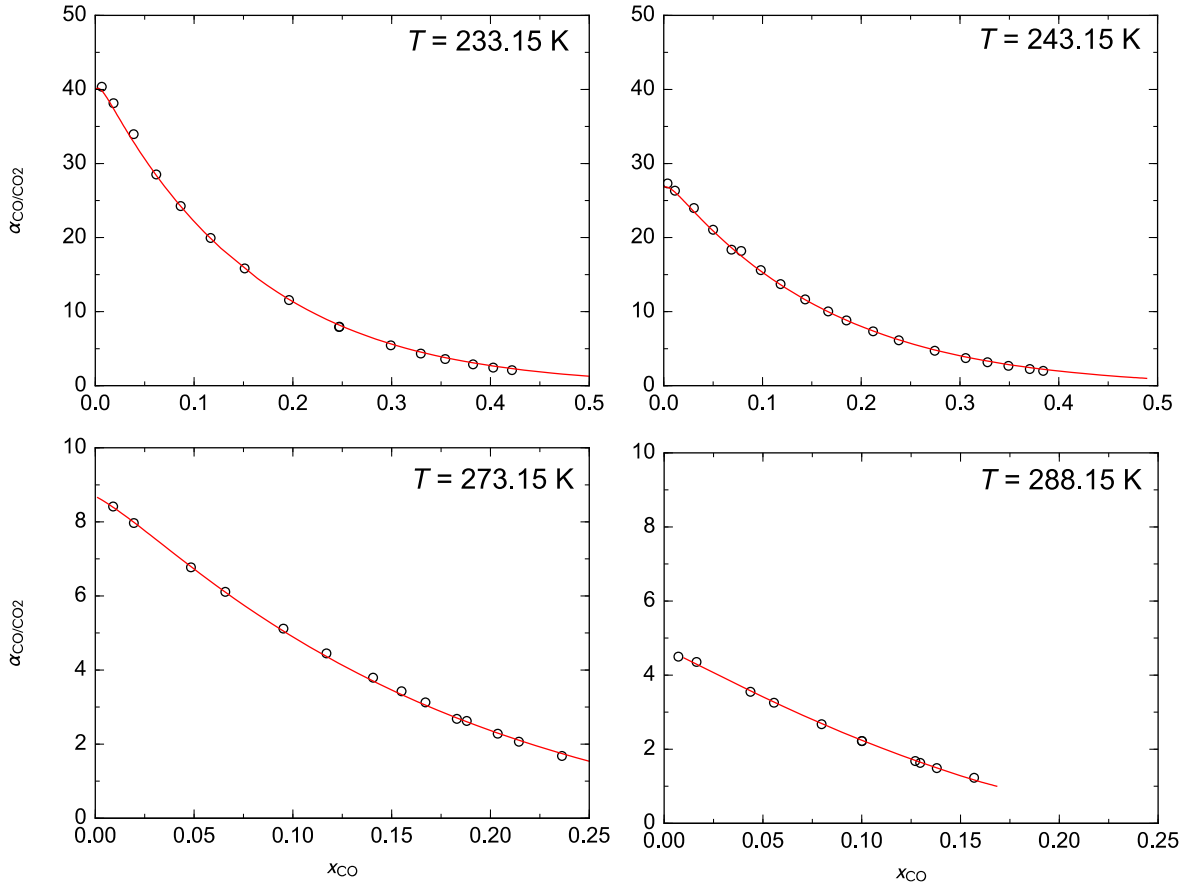


Figure 6.11 Relative volatility diagrams of the (CO_2 + CO) system at T = (233.15, 243.15, 273.15 and 288.15) K: ○, this work; ——, new mixture model.

Considering that the new mixture model was almost exclusively fitted to the VLE data from this work, published at Souza et al. [76] and the density data from this work, the overall good representation of experimental data from all literature sources underlines the high quality of the new mixture model, which certainly represents a major advance over the earlier models.

All this reflects the extent to which each model was optimised for the (CO_2 + CO) system. While the new mixture model comprises both a binary-specific departure function and re-optimised values of the binary reducing parameters (β_T, γ_T, β_v, and γ_v), EOS-CG includes only adjusted binary reducing parameters, and GERG-2008 includes no fitted binary parameters or departure function.

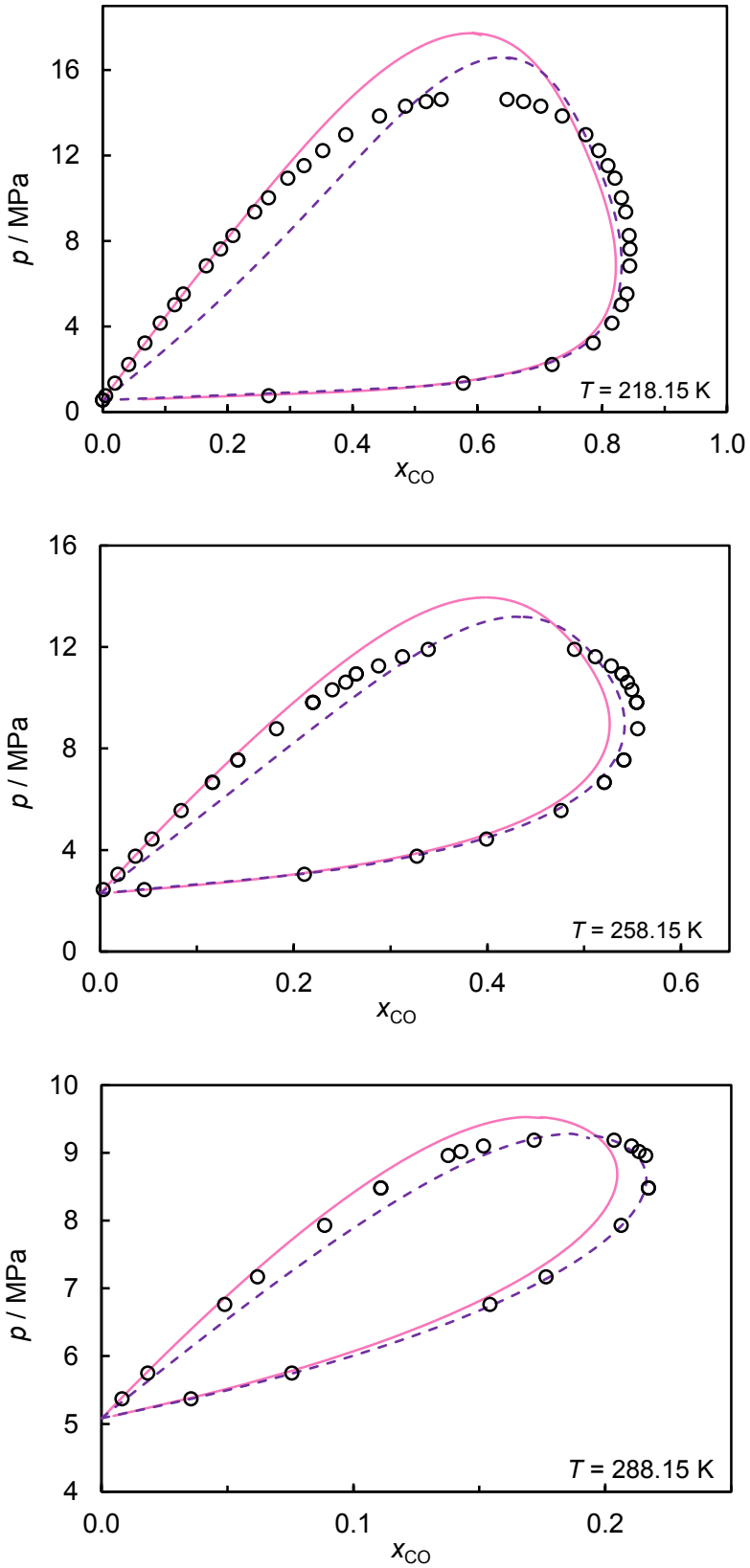


Figure 6.12 Pressure-composition diagrams of the (CO_2 + CO) system: ○, this work; ——, SAFT-γ Mie with original parameters values; - - -, SAFT-γ Mie fitted.

Furthermore, the binary parameters ε and λ^r of SAFT-γ Mie was preliminarily fitted to the VLE data from this work, published at Souza et al. [76] and the density data from this work. Results are shown in Figure 6.12, together with VLE data from this work and the values calculated from the SAFT-γ Mie with original parameters values. The SAFT-γ Mie fitted exhibits a considerable improvement on the description of measurements on the dew point curve but large deviations along the bubble curve, even at low pressures. Further improvement could be achieved with more intense optimization of the parameters.

6.3 Homogeneous Density Results

The densities of four mixtures of (CO_2 + CO) with compositions ranging from (5 to 50) mol% CO were measured at T = (283.15, 293.15, 303.15, 313.15, 333.15, 353.15, and 373.15) K at pressures up to 48 MPa. In total, 720 states points were measured, including validation points. The experimental results are summarised in Tables 6.5 – 6.8.

As explained in section 5, validation measurements were carried out for all isotherms with decreasing pressure to values between (10 and 28) MPa. The validation points measured verify the reproducibility of the measurements as they presented similar deviations from the new mixture model developed in this work than the corresponding first measurements. For all comparisons, the deviations are found to be ≤ 0.4 kg·m^{-3}, corresponding to relative differences of ≤ 0.2 %.

Comparisons of the measured densities with literature data and the new mixture model developed in this work and other models are presented in sections 6.3.1 and 6.3.2

Table 6.5 Density ρ for (CO_2 + CO) mixture x of 0.05031 at temperatures T and pressure p.[a]

p/MPa	ρ/(kg·m^{-3})	p/MPa	ρ/(kg·m^{-3})	p/MPa	ρ/(kg·m^{-3})	p/MPa	ρ/(kg·m^{-3})
			T = 283.15 K				
4.11	106.71	11.69	872.17	19.96	930.16	36.06	999.32
7.96	823.41	12.06	873.38	22.02	941.44	40.12	1012.25
9.03	838.98	14.08	891.10	23.92	950.97	43.94	1023.43
10.02	851.85	15.99	905.52	27.93	969.01	48.12	1034.82
10.07	852.40	18.20	919.40	32.35	986.25	48.15	1034.82

p/MPa	ρ/(kg·m^{-3})	p/MPa	ρ/(kg·m^{-3})	p/MPa	ρ/(kg·m^{-3})	p/MPa	ρ/(kg·m^{-3})
11.02	863.02	19.93	932.14				
			T = 293.15 K				
2.10	41.90	10.01	771.09	14.02	831.74	28.31	932.95
2.15	43.22	10.22	779.12	15.87	850.10	32.13	950.25
3.50	77.59	11.07	791.48	18.23	870.94	36.15	966.52
5.02	131.37	12.05	806.84	20.30	886.39	40.16	980.97
6.41	232.18	13.80	828.25	22.12	898.56	44.35	994.85
9.07	746.02	13.96	831.20	24.13	910.82	47.75	1005.09
			T = 303.15 K				
2.20	42.09	11.06	692.85	18.29	819.42	32.15	914.50
2.26	43.40	11.07	692.60	20.09	836.63	32.16	914.14
3.37	69.38	12.10	725.73	21.96	852.35	35.85	930.28
5.06	119.56	12.19	725.52	24.15	868.64	40.23	948.06
8.05	344.66	12.39	730.91	27.75	889.43	43.80	961.27
9.06	566.43	13.98	762.72	28.08	892.87	47.76	974.63
10.06	650.89	15.99	792.49	31.99	912.39		
			T = 313.15 K				
1.96	35.34	8.97	312.04	16.07	726.10	27.94	851.87
2.08	37.87	9.93	425.83	18.07	758.13	31.82	876.08
3.44	67.16	11.02	541.84	20.06	783.39	35.85	897.29
4.94	106.39	11.80	595.09	22.26	806.32	40.34	917.50
6.51	159.49	11.88	599.12	23.97	821.55	43.96	932.41
7.93	230.21	14.12	683.15	24.80	828.69	47.90	946.89
			T = 333.15 K				
2.08	34.96	10.16	265.59	19.92	660.58	32.13	801.10
2.11	35.33	11.19	317.87	19.93	660.82	36.01	827.53
3.55	63.24	12.05	366.53	22.17	698.57	37.93	839.24
4.98	94.51	13.90	469.40	24.05	723.94	39.92	850.00
6.52	133.54	16.06	561.35	28.04	767.05	44.31	872.24
7.96	177.78	17.97	617.94	32.09	800.71	48.21	889.41
9.01	215.79						
			T =353.15 K				
2.20	34.33	9.02	179.73	18.04	483.29	35.93	755.88
2.27	33.63	10.03	208.52	19.81	534.55	39.82	783.81

p/MPa	ρ/(kg·m^{-3})	p/MPa	ρ/(kg·m^{-3})	p/MPa	ρ/(kg·m^{-3})	p/MPa	ρ/(kg·m^{-3})
2.28	35.73	11.21	245.87	22.08	586.24	44.41	811.69
3.48	56.97	12.10	276.21	24.03	617.22	47.69	829.36
5.01	85.81	14.21	352.16	28.02	679.13	48.05	831.00
6.57	118.94	16.04	419.30	32.21	723.98	48.65	833.90
8.02	153.31						
			T = 373.15 K				
2.38	35.25	10.12	182.33	18.34	400.06	32.05	646.82
3.54	53.73	11.12	206.03	20.36	450.15	35.82	685.28
5.01	78.64	12.18	233.45	22.00	488.41	40.23	722.28
6.53	106.72	14.14	285.23	24.27	534.02	43.78	747.72
7.98	135.59	15.93	334.28	27.84	592.95	48.54	777.08
9.00	157.32	18.01	390.90				

[a] Expanded uncertainties are $U(T)$ = 0.05 K and $U(p)$ = 0.0175 MPa with a coverage factor k = 2.

Table 6.6 Density ρ for (CO_2 + CO) mixture x of 0.101073 at temperatures T and pressure p.[a]

p/MPa	ρ/(kg·m^{-3})	p/MPa	ρ/(kg·m^{-3})	p/MPa	ρ/(kg·m^{-3})	p/MPa	ρ/(kg·m^{-3})
			T =283.15 K				
2.16	44.28	11.60	799.34	17.96	862.93	31.98	940.35
2.97	64.83	11.62	800.04	19.93	877.01	36.14	956.63
3.10	69.33	13.01	817.09	22.12	891.16	39.96	970.11
4.48	120.41	13.72	828.55	24.01	902.13	43.93	983.02
5.00	138.40	14.00	827.73	28.02	922.70	48.06	995.32
11.36	796.20	15.98	846.61				
			T = 293.15 K				
2.60	52.05	6.16	176.02	11.24	689.75	27.89	881.60
2.65	53.18	6.94	221.35	12.82	732.02	31.86	902.50
2.69	54.17	8.94	583.14	13.88	752.40	35.95	921.09
2.82	57.23	8.99	581.06	15.89	782.15	40.01	937.37
2.93	59.87	10.82	682.64	18.14	808.27	44.03	951.95
4.31	98.17	10.86	683.48	20.05	826.58	47.82	964.85
5.24	131.97	11.24	689.75	24.20	858.77		
			T = 303.15 K				

p/MPa	ρ/(kg·m^{-3})	p/MPa	ρ/(kg·m^{-3})	p/MPa	ρ/(kg·m^{-3})	p/MPa	ρ/(kg·m^{-3})
1.97	36.17	8.96	351.03	17.93	750.44	32.03	869.95
3.33	65.98	9.99	475.27	19.94	775.38	32.08	868.79
3.33	66.03	11.01	561.29	22.04	796.80	35.90	888.04
4.94	109.71	12.00	614.44	22.22	798.58	39.89	906.13
6.50	166.44	14.03	680.73	24.13	815.25	40.28	908.25
6.50	166.58	15.92	719.92	27.67	841.45	43.96	922.56
7.96	250.43	16.00	720.61	32.03	868.04	47.79	936.62
			T = 313.15 K				
2.08	36.64	9.06	265.92	15.87	643.32	28.01	803.12
3.09	57.39	10.09	338.44	18.05	689.35	31.91	830.60
3.25	60.72	11.13	419.35	19.88	718.87	35.99	854.70
4.95	101.94	12.06	486.99	21.94	745.79	39.87	874.44
6.49	148.39	13.11	546.25	23.96	767.63	44.05	893.20
7.98	208.54	14.05	587.06	23.98	768.13	48.09	909.34
			T = 333.15 K				
1.90	30.90	9.99	235.01	19.94	599.22	28.05	718.10
3.17	53.85	11.05	276.74	19.94	599.12	32.09	755.27
3.26	55.53	12.04	319.13	19.95	598.87	35.87	783.76
5.09	93.66	12.98	362.93	19.95	599.41	40.08	810.41
6.59	129.39	14.06	411.25	21.96	637.75	43.93	831.46
8.06	170.20	15.99	488.89	23.97	668.86	48.20	852.04
9.02	200.45	17.91	549.61				
			T =353.15 K				
2.34	35.91	10.11	198.44	17.96	435.33	31.96	677.32
3.35	53.10	11.06	224.53	20.11	491.73	35.91	713.80
5.04	83.70	12.16	256.89	21.98	533.67	39.87	744.11
6.45	111.91	13.09	285.30	23.92	570.57	43.98	770.94
7.98	145.68	14.01	314.40	27.96	631.48	48.00	793.82
9.05	171.09	16.01	377.24				
			T = 373.15 K				
1.93	27.48	9.92	169.82	18.33	368.09	32.08	606.44
3.04	44.50	12.08	216.45	20.17	410.50	36.05	648.08
5.04	76.86	14.20	267.24	22.10	451.83	40.00	682.74
6.49	102.28	15.99	310.74	24.07	489.76	44.04	712.95

p/MPa	ρ/(kg·m^{-3})	p/MPa	ρ/(kg·m^{-3})	p/MPa	ρ/(kg·m^{-3})	p/MPa	ρ/(kg·m^{-3})
7.99	130.24	18.26	367.38	28.02	553.97	48.07	738.99

[a] Expanded uncertainties are $U(T)$ = 0.05 K and $U(p)$ = 0.0175 MPa with a coverage factor k = 2.

Table 6.7 Density ρ for (CO_2 + CO) mixture x of 0.25254 at temperatures T and pressure p.[a]

p/MPa	ρ/(kg·m^{-3})	p/MPa	ρ/(kg·m^{-3})	p/MPa	ρ/(kg·m^{-3})	p/MPa	ρ/(kg·m^{-3})
			T =283.15 K				
2.12	39.75	9.95	420.63	18.13	687.35	27.98	785.37
2.15	40.51	11.02	477.23	20.12	714.11	31.78	809.97
3.23	64.44	11.35	493.96	21.99	734.94	35.88	832.40
5.09	115.75	12.02	526.03	24.00	754.03	39.91	851.44
6.53	170.61	13.06	571.22	25.89	769.61	43.94	868.34
8.03	256.39	14.06	604.19	25.91	770.05	47.92	883.30
9.00	339.35	15.97	650.39				
			T = 293.15 K				
2.14	38.18	8.98	257.36	13.99	519.04	31.90	776.12
2.60	47.57	10.00	316.32	16.03	580.65	31.95	774.07
3.46	66.01	11.03	378.57	18.00	624.15	34.73	791.57
4.13	81.56	12.00	431.64	19.99	658.13	35.97	800.66
5.09	106.54	12.97	479.06	22.01	685.27	39.99	821.39
6.53	150.88	12.98	478.66	24.02	708.24	44.02	839.58
8.01	209.34	13.97	517.87	27.96	744.61	48.06	856.07
			T = 303.15 K				
2.16	37.00	9.01	221.33	17.94	559.85	34.38	754.19
2.18	37.37	10.03	263.80	19.92	599.96	35.99	764.61
3.44	62.00	11.04	310.26	22.19	637.23	36.08	765.29
5.04	98.19	12.05	357.33	24.21	664.03	39.93	787.50
6.55	138.06	14.06	443.40	28.16	705.19	43.97	808.36
6.58	139.01	16.02	510.81	28.18	705.44	47.99	826.45
7.99	183.39	16.17	516.37	32.08	737.80		
			T = 313.15 K				
2.20	36.20	9.07	199.47	15.92	444.46	31.96	700.45
3.40	58.40	10.00	230.43	18.10	505.04	32.04	701.43

p/MPa	ρ/(kg·m^{-3})	p/MPa	ρ/(kg·m^{-3})	p/MPa	ρ/(kg·m^{-3})	p/MPa	ρ/(kg·m^{-3})
3.56	61.44	11.11	270.26	19.96	547.17	33.19	710.66
5.03	92.34	12.05	304.76	19.99	547.56	35.93	730.95
6.52	126.96	12.10	307.64	22.02	584.75	39.94	756.78
6.55	128.04	13.06	344.79	24.00	614.95	43.98	779.20
8.08	169.26	14.07	382.04	27.93	662.61	47.98	798.82
			T = 333.15 K				
2.13	32.33	9.99	191.63	18.09	408.79	34.70	655.48
3.25	51.03	10.02	192.38	20.06	454.72	34.72	655.48
3.36	52.80	11.14	221.01	20.23	457.47	34.73	655.38
5.07	83.83	12.09	246.43	22.08	495.11	35.98	666.30
6.53	112.65	13.05	272.96	24.01	528.76	40.09	697.08
7.98	143.85	13.99	299.25	27.89	584.32	43.98	722.07
9.04	168.35	15.99	362.85	32.03	630.40	47.97	744.61
			T =353.15 K				
2.06	29.17	10.02	168.36	17.97	340.67	29.91	541.35
2.13	30.14	11.02	188.99	20.05	383.92	32.11	566.93
3.32	48.43	12.09	211.69	22.06	422.60	36.05	606.15
5.07	76.77	13.07	237.57	24.10	458.40	40.04	639.60
6.53	101.91	14.01	253.63	28.05	517.34	44.01	668.26
8.02	129.26	16.04	298.88	29.89	541.45	48.02	693.59
9.05	149.12						
			T = 373.15 K				
2.14	28.53	10.20	153.82	20.03	335.03	31.94	507.35
3.27	44.66	12.12	187.64	21.99	368.47	32.06	508.25
5.02	70.32	14.03	223.68	21.99	367.61	36.06	550.70
5.10	71.11	14.16	225.74	24.07	402.30	40.09	586.89
6.48	92.88	16.19	264.48	27.86	456.48	44.05	617.60
8.14	118.93	17.97	297.23	28.20	461.78	47.93	644.32
10.03	151.63	18.04	299.02				

[a] Expanded uncertainties are $U(T)$ = 0.05 K and $U(p)$ = 0.0175 MPa with a coverage factor k = 2.

Table 6.8 Density ρ for (CO_2 + CO) mixture x of 0.50183 at temperatures T and pressure p.[a]

p/MPa	ρ/(kg·m^{-3})	p/MPa	ρ/(kg·m^{-3})	p/MPa	ρ/(kg·m^{-3})	p/MPa	ρ/(kg·m^{-3})
			T =283.15 K				
2.03	32.82	9.06	185.86	18.00	420.82	31.99	605.59
2.04	32.96	10.01	211.81	20.00	459.45	35.95	635.95
3.65	62.04	11.07	241.89	22.06	493.34	40.03	662.48
4.98	88.55	12.02	268.91	24.00	521.33	44.04	685.04
6.50	122.14	13.96	323.53	26.21	548.36	48.12	705.28
8.02	158.83	15.97	375.31	27.88	567.08		
			T = 293.15 K				
2.12	32.90	6.16	107.26	14.01	292.95	27.99	534.96
3.11	49.56	7.53	136.24	16.01	340.55	32.13	575.86
4.17	68.60	9.09	171.57	18.11	386.00	35.91	606.91
4.99	83.86	9.99	192.91	19.97	421.56	40.02	635.46
5.00	84.00	11.11	220.49	23.88	484.04	44.05	659.67
5.98	103.39	11.99	242.54	27.98	534.91	47.89	679.62
			T = 303.15 K				
2.03	30.23	4.67	73.94	7.51	127.21	19.98	388.07
2.06	30.56	4.99	79.58	8.99	157.51	22.16	423.63
2.07	30.70	5.16	82.68	10.03	179.45	24.04	452.36
3.04	46.25	5.18	83.20	10.07	179.78	28.03	502.88
3.09	47.19	6.10	100.05	11.04	201.43	31.93	543.31
3.13	47.61	6.15	101.08	12.05	223.73	36.08	578.80
4.00	62.34	6.17	101.56	14.01	267.50	40.01	607.41
4.20	65.62	6.18	101.74	16.07	311.89	43.98	632.42
4.51	70.93	7.02	117.68	18.11	353.29	47.99	654.75
			T = 313.15 K				
2.08	29.83	9.06	149.25	16.06	288.43	27.94	473.45
2.09	29.92	10.11	169.52	17.93	324.03	32.09	517.40
3.45	50.78	10.17	170.65	20.42	367.92	36.07	552.63
4.54	68.67	11.15	190.20	22.03	393.89	40.02	582.61
5.15	78.99	12.22	211.63	22.19	395.81	44.34	610.88
6.37	99.93	14.01	247.45	24.04	423.65	48.11	632.62
8.01	129.58						

p/MPa	ρ/(kg·m^{-3})	p/MPa	ρ/(kg·m^{-3})	p/MPa	ρ/(kg·m^{-3})	p/MPa	ρ/(kg·m^{-3})
			T = 333.15 K				
2.04	27.19	9.06	134.03	18.00	284.41	28.09	425.50
2.09	27.84	10.06	150.62	20.03	316.35	31.96	466.88
3.59	49.12	10.11	151.50	20.04	316.60	35.99	503.90
4.59	64.13	11.05	167.22	22.03	346.47	40.37	538.58
5.07	71.24	12.03	183.95	24.11	375.82	44.07	564.25
6.49	92.93	14.01	217.65	26.02	400.52	48.15	589.37
8.01	116.95	16.00	251.39				
			T =353.15 K				
2.15	26.97	10.05	136.69	18.01	254.61	40.06	494.61
2.24	28.04	10.08	137.16	20.13	284.46	40.07	494.71
3.53	45.24	11.07	151.81	22.16	311.76	40.07	494.75
4.97	64.61	12.05	166.52	24.22	338.25	40.08	494.60
5.03	65.40	14.04	196.13	27.90	381.79	40.10	494.50
6.47	85.36	16.04	225.72	31.97	424.61	43.97	522.69
8.04	107.55	17.96	253.67	36.22	463.53	47.82	547.58
9.07	122.44						
			T = 373.15 K				
2.04	23.99	9.08	113.19	16.10	206.30	27.81	347.48
2.10	24.72	10.08	126.44	17.89	230.01	31.97	389.26
3.60	43.34	11.11	140.04	18.07	232.26	35.93	424.99
5.01	60.86	11.23	141.67	20.06	257.56	40.18	459.25
6.53	80.09	12.05	152.67	22.12	282.90	44.10	487.59
8.01	99.25	14.05	179.27	23.98	304.84	48.17	514.18

[a] Expanded uncertainties are $U(T)$ = 0.05 K and $U(p)$ = 0.0175 MPa with a coverage factor k = 2.

Figure 6.13 illustrates comparisons between the densities calculated from the new mixture model and experimental data from this work, as given in Tables 6.5 – 6.8. Each plot presents the four investigated mixtures at a specific temperature by means of relative percentage deviations in density against measured density. Error bars represent the relative combined expanded uncertainty (k = 2), as discussed in section 5.6. In all of the following deviation plots, symbols plotted on the upper or lower limits of the graph indicate points that are off scale. The baseline is the new mixture model.

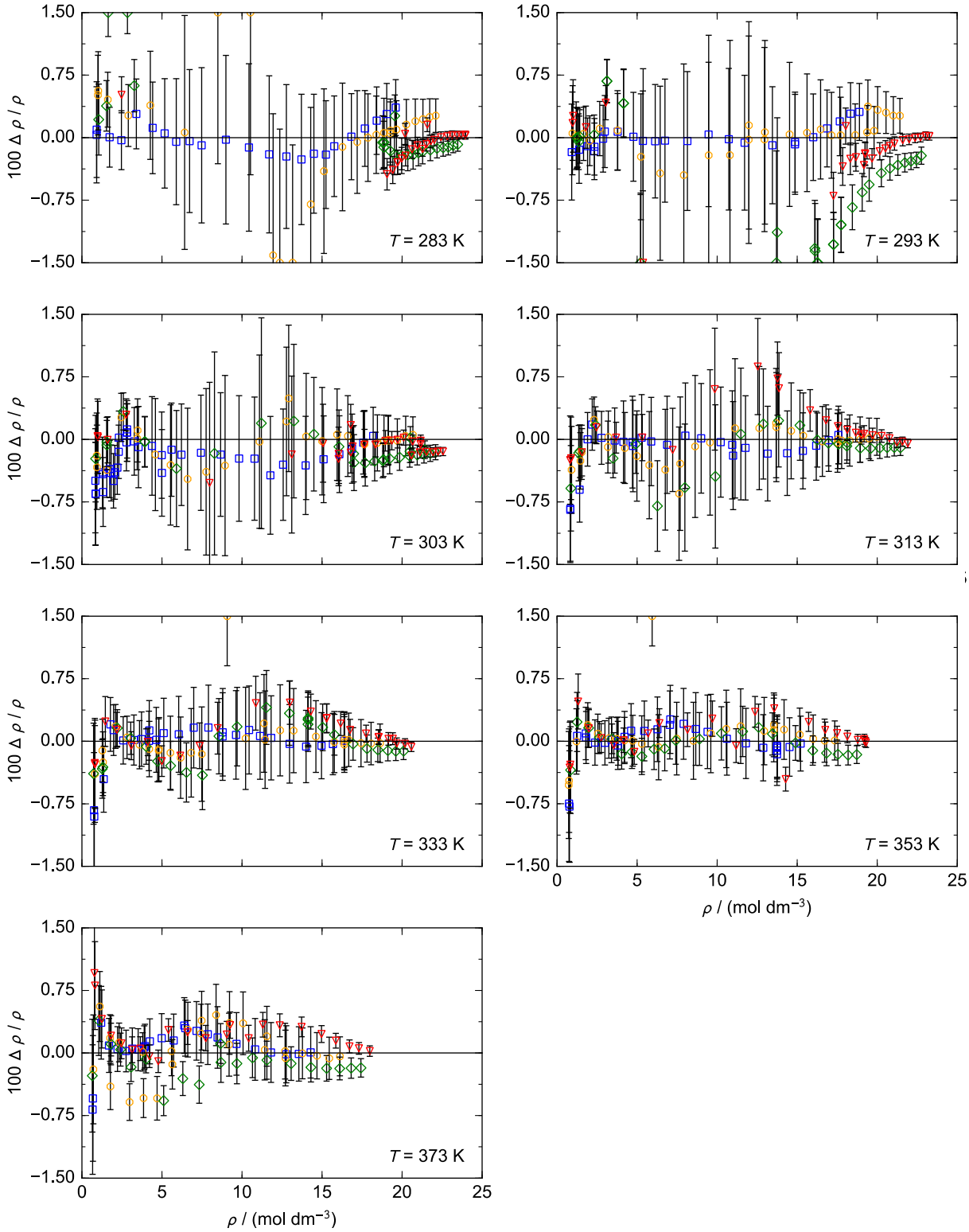


Figure 6.13 Relative percentage deviations $\Delta\rho/\rho = (\rho_{exp} - \rho_{calc})/\rho_{exp}$ between the experimental density ρ_{exp} of (CO_2 + CO) and values ρ_{calc} calculated from the new mixture model as a function of the measured density. ▽, $x_{CO} = 0.05031$; ◇, $x_{CO} = 0.10107$; ○, $x_{CO} = 0.25254$; and □, $x_{CO} = 0.50183$.

The deviation plots clearly demonstrate that the new mixture model represents the majority of the density data within their experimental uncertainty. The new model describes the measured densities within ±0.5% in general and within ±0.2% at pressures above 30 MPa. The main exception is the mixture with x = 0.1 at T = 293.15 K, where more than half of the measured densities deviate from the model by between -0.5% and -1.5%. In general, the data at lower densities (below about 2 mol dm^{-3}) present slightly higher deviations; nevertheless, all are within ±1.8% and most are within ±1.0%.

6.3.1 Comparison of Homogeneous Density Data with Literature Data

A comparison between the measured densities from this work and the literature data from Mallu et al. [85, 86], Cipollina et al. [84], Blanco et al. [21], and Tsankova et al. [77] is shown in Figure 6.14 for different isotherms. Blanco et al. [21] present over 40000 density points and considering all of them would make both the fitting process and result assessment impracticable. For that reason, the data set of Blanco et al. [21] was reduced to around 1000 representative points covering the whole range of temperature, pressure and mixture composition measured.

It is worth noting that, although densities from different sources are shown in the same plot, they can represent substantially different state points because the compositions are not generally the same. For instance, while the work of Blanco et al. [21] covers wide ranges of temperature and pressure, it has been carried out in a very narrow composition range from (0.4 to 3.0) mol% CO. Meanwhile, the work of Mallu et al. [85, 86] includes mixtures containing (20, 43 and 70) mol% CO at temperatures from (322 to 423) K and pressures up to 8 MPa.

The new model represents most of the measured densities within ±1.0% generally and within ±0.5% at pressures above 30 MPa. The work of Mallu et al. [85, 86] exhibits systematic deviations along lines of constant composition that increase with pressure. For most temperatures, the data from this work and Blanco et al. [21] exhibit slightly higher deviations from the new mixture model at lower pressures (below 10 MPa) than at higher pressures. This is probably a result of the decreasing relative uncertainty with increasing pressure. However, for all data sources at low pressures most

deviations are within ±1.8%. At high pressures, the work of Blanco et al. [21] exhibits good agreement with the new mixture model at temperatures below T = 300 K but significantly deviations of larger magnitude (up to 1.5%) at higher temperatures.

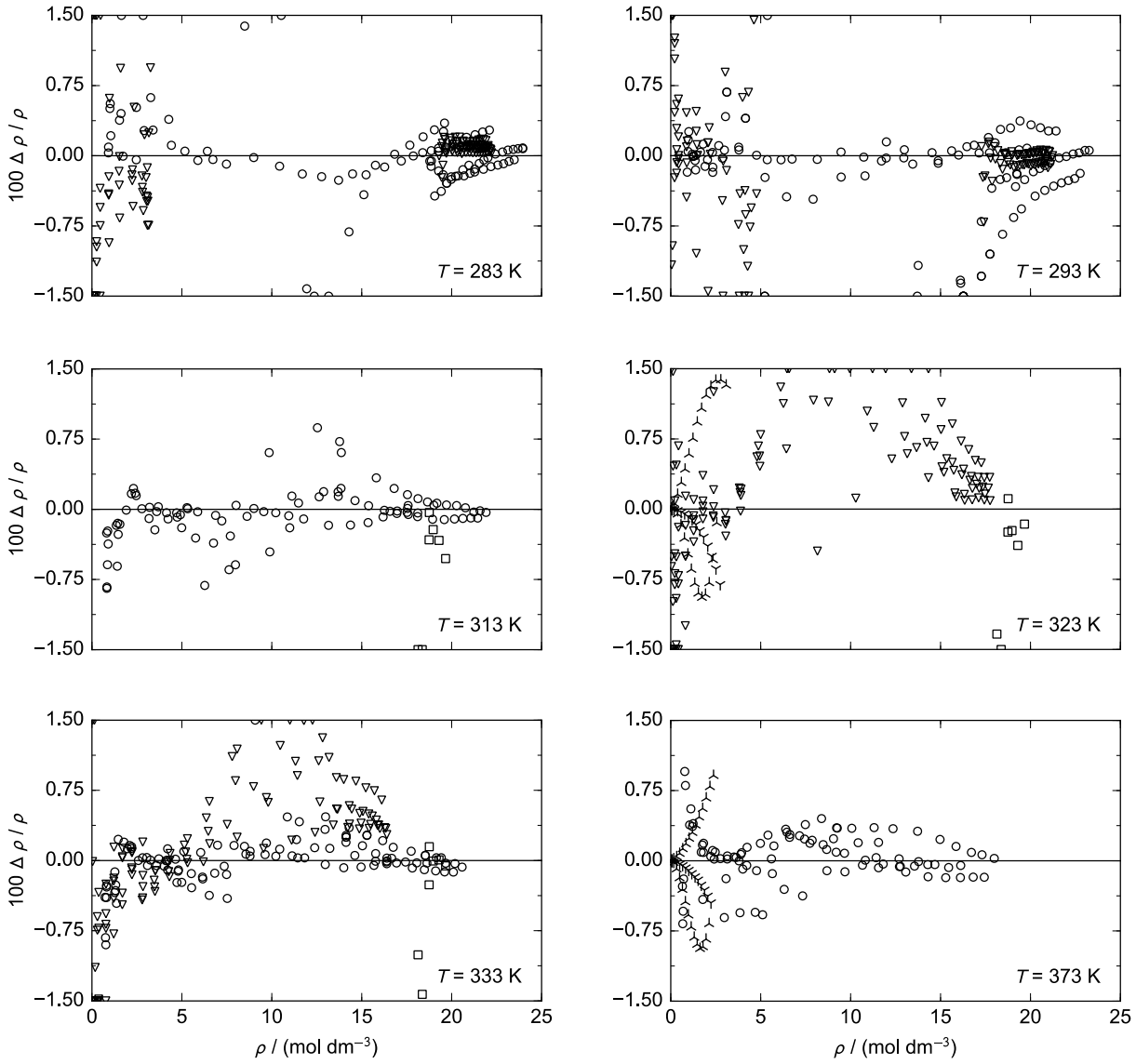


Figure 6.14 Relative percentage deviations $\Delta\rho/\rho = (\rho_{exp} - \rho_{calc})/\rho_{exp}$ between the experimental density ρ_{exp} of (CO_2 + CO) and values ρ_{calc} calculated from the new mixture model as a function of the measured density. ▽, Blanco et al., 2014; ⋎, Mallu et al., 1987; ⅄, Mallu et al., 1989; □, Cipollina et al., 2007; ○, this work.

6.3.2 Comparison of Homogeneous Density Data with Equations of State

Figure 6.15 compares densities calculated from GERG-2008 and EOS-CG, together with selected experimental data [77, 84-86], as deviations from the new mixture model. The measurements of Tsankova et al. [77] and Mallu et al. [85, 86] were carried out at pressures below 8 MPa, while both the present work and Cipollina et al. [84] cover pressures up to about 50 MPa. The new mixture model represents most of the data within ±1.0%. Densities obtained from GERG-2008 deviate significantly from the new mixture model, even at low densities. Although EOG-CG is in reasonable agreement with the new mixture model at low densities, namely within deviations of less than 2%, at high pressures the density deviations exceed 20%. This reflects the extent to which each model was optimised for the (CO_2 + CO) system. While the new mixture model comprises both a binary-specific departure function and re-optimised values of the binary reducing parameters (β_T, γ_T, β_v, and γ_v), EOS-CG includes only adjusted binary reducing parameters, and GERG-2008 includes no fitted binary parameters or departure function.

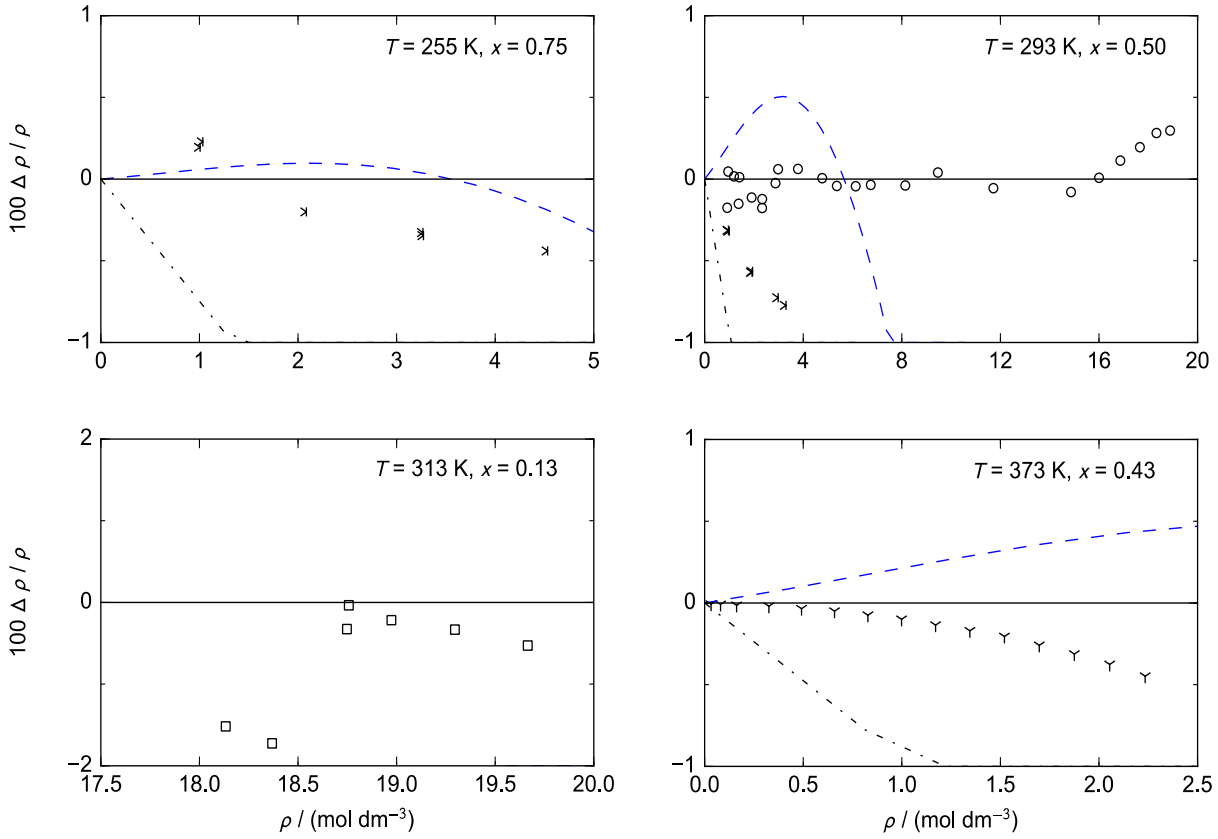


Figure 6.15 Relative percentage deviations $\Delta\rho/\rho = (\rho_{exp} - \rho_{calc})/\rho_{exp}$ between the experimental density ρ_{exp} of (CO_2 + CO) and values ρ_{calc} calculated from the new mixture model as a function of the measured density, ⋎, Mallu et al., 1987; □, Cipollina et al., 2007; ⋊, Tsankova et al., 2018; ○, this work. For further comparisons, deviations from values calculated with the – – –, EOS-CG; – ·– ·, GERG-2008.

Figure 6.16 presents compressibility factor as a function of pressure using the experimental data measured in this work compared with the new mixture model, also developed in this work. Results were assessed for the (CO_2 + CO) mixture of mole fraction equal to 0.5 at all measured temperatures, ranging from (283.15 to 383.15) K. The new mixture model describes the of the data within ±1.0%.

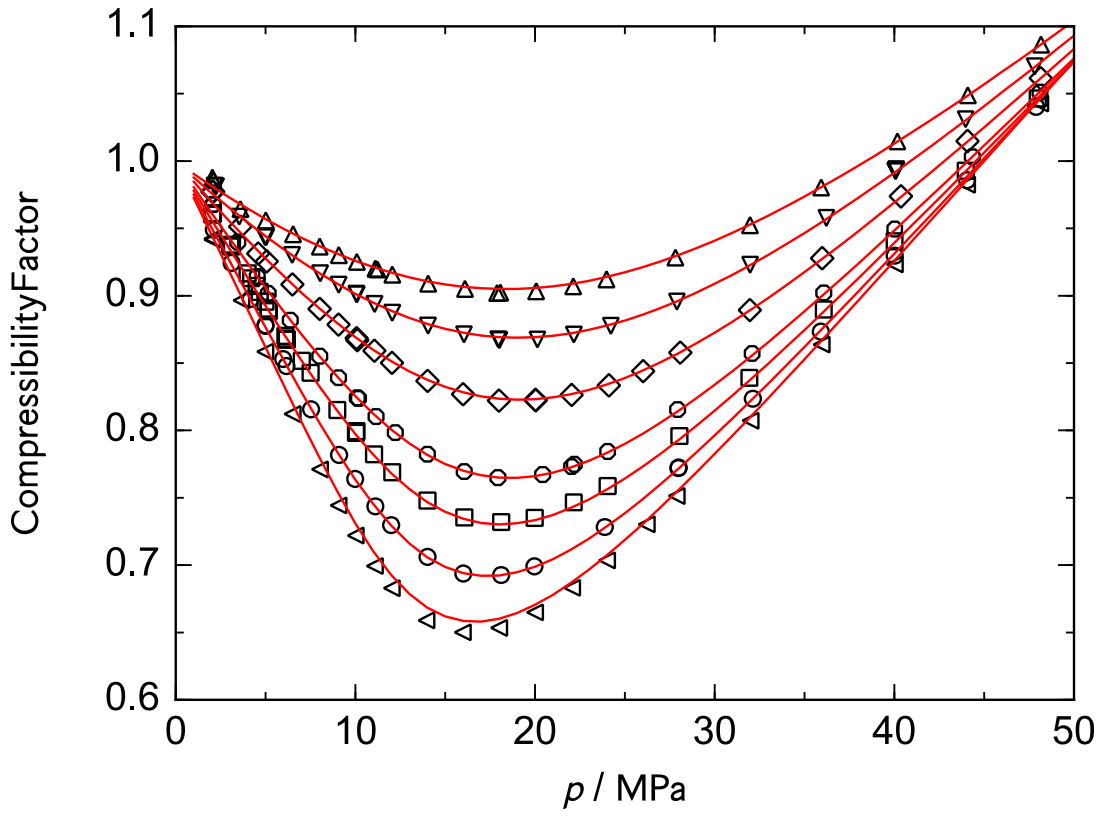


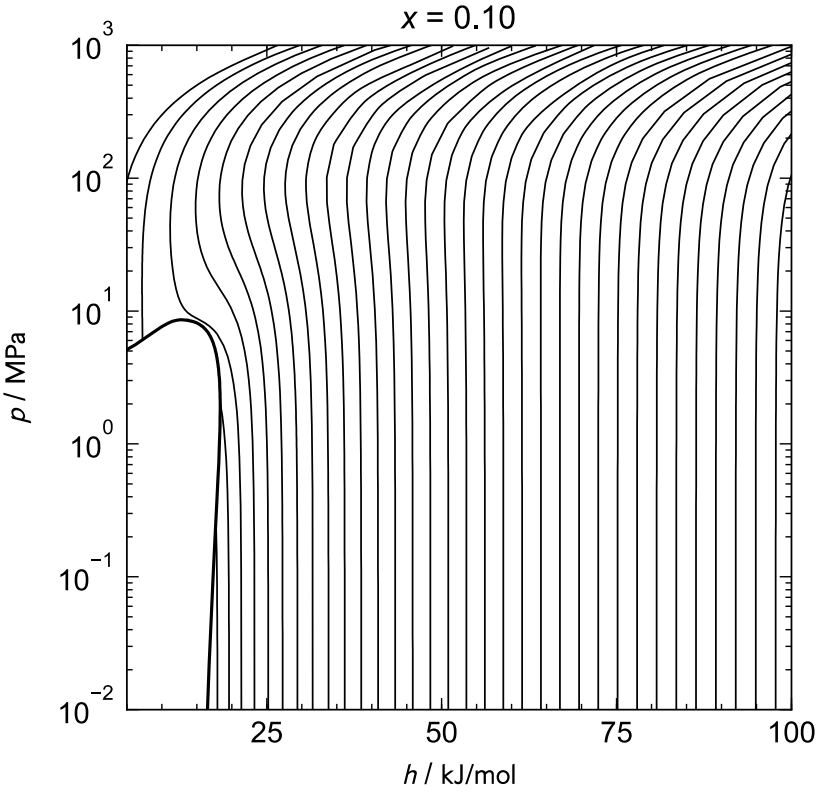
Figure 6.16 Compressibility factor as a function of pressure of the (CO_2 + CO) mixture with mole fraction equal to 0.5. Temperatures ranging from (283.15 to 383.15) K.: symbols, this work; ——, new mixture model.

6.4 Extrapolation Behaviour of the New Mixture Model

The extrapolation behaviour of a model outside the range of the experimental data can be problematic, for example with unphysical behaviour predicted. Reasonable

extrapolation behaviour of the predicted thermodynamic properties can be considered as a fundamental criterion for assessing the performance and consistency of the model during the fitting process [55].

Plots of pressure versus enthalpy, density, and temperature, shown in Figure 6.17, were generated from the new mixture model. Here, pressures were extrapolated up to 1 GPa. Isotherms up to 2000 K and 6000 K were included in the *p*,*h*-diagram and the *p*,*ρ*-diagram, respectively, while the *p*,*T*-diagram includes isochors up to 26 mol·dm^{-3}. These plots show reasonable behavior of the new mixture model in describing the respective thermodynamic properties not only over the temperature and pressure region in which the model was optimised but also at much higher temperatures and pressures. As expected in a qualitatively correct extrapolation behavior of an EOS, the isolines are smoothly shaped with no bumps or crossing points in any plot.



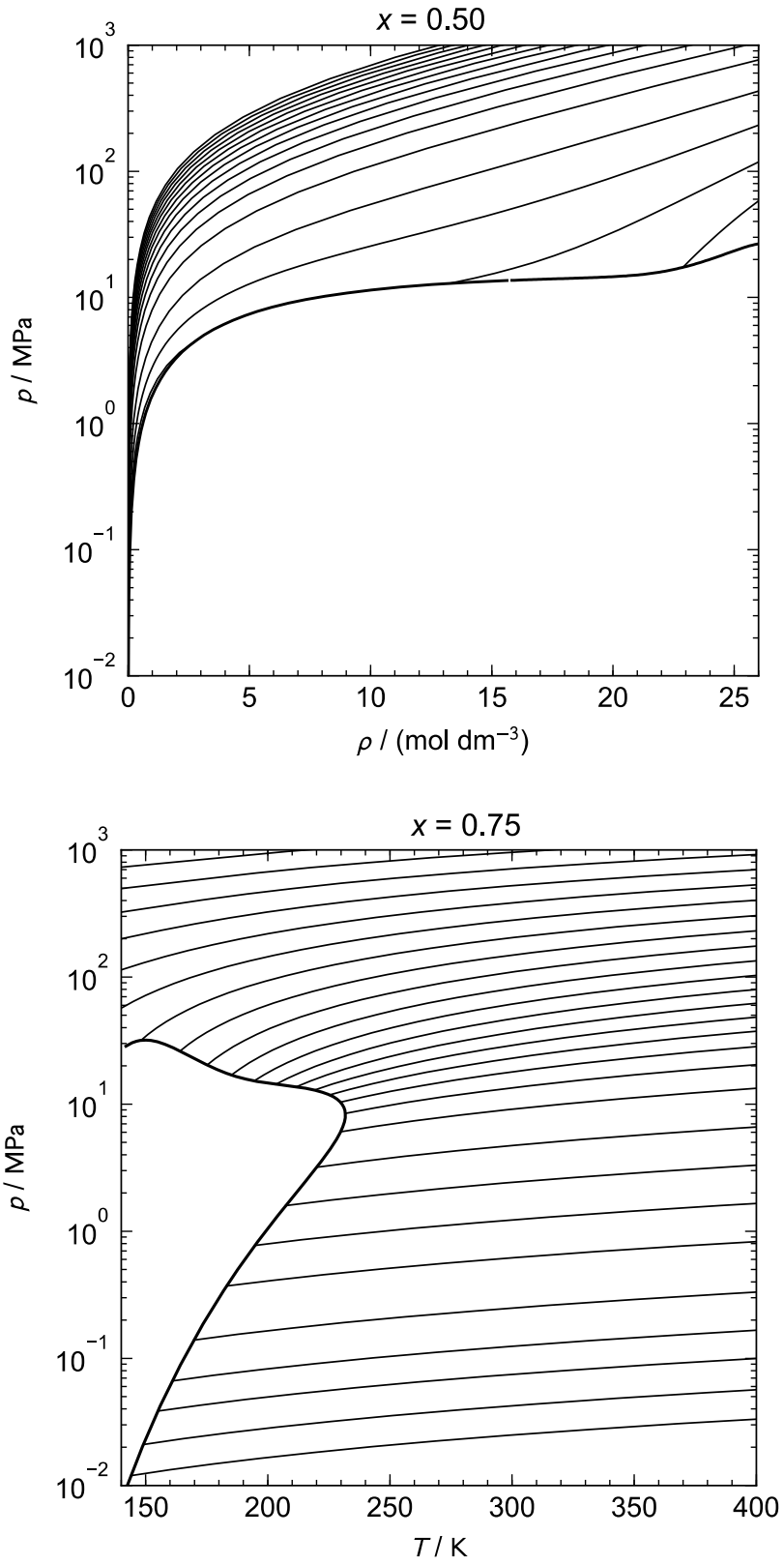


Figure 6.17 Top to bottom: p,h-, p,ρ-, and p,T-diagrams calculated with the new mixture model for three different compositions (10, 50, 75) mol% CO at extreme conditions. Isotherms up to 2000 K and 6000 K were included in the p,h-diagram and the p,ρ-diagram, respectively, while the p,T-diagram includes isochors up to 26 mol·dm^{-3}.

6.5 Estimated Uncertainty of Calculated Properties for the New Mixture Model

The new mixture model for (CO_2 + CO) describes the *pρT* surface with an uncertainty in homogeneous density of 0.5% at temperatures from (255 to 373) K and pressures up to 30 MPa, and with an uncertainty of 0.3% at pressures between 30 MPa and 50 MPa. At temperatures between (303 and 373) K and pressures below 5 MPa, the uncertainty in density increases to 1%. These estimations are based on the most reliable available density data, which cover a composition range up to 75 mol% CO. It is worth mentioning that the estimated uncertainties in density for mixtures are generally higher than for pure fluids, when comparing the same measuring techniques due to the significant contribution of the uncertainty in the mixture composition, as shown in section 5.6.

The estimated uncertainties in calculated dew- and bubble-point pressures are generally within 1% to 2% at temperatures from just above the triple point of CO_2 to just below the critical point of CO_2. This estimation was based mainly in comparison with the data of Kaminishi et al. [83], Souza et al. [76] and Westman at al. [75].

In this work, the consistency was experimentally established by using the same GC calibration and conditions to analyse both the compositions of VLE and the four samples provided by BOC for the density measurements. Due to this consistency, the new mixture model developed in this work represents with quality the VLE and density data.

6.6 Conclusions

New and low-uncertainty experimental VLE data for the (CO_2 + CO) system were reported along seven isotherms spanning almost the entire region of vapor-liquid coexistence and new density data for the (CO_2 + CO) system along seven isotherms, at temperatures from (283 to 373) K, and pressures up to 48 MPa for four different mixtures, with compositions ranging from (5 to 50) mol% CO. Critical points were estimated from the data by means of analysis with asymptotic behaviour approaching

the critical point. The new data help to fill a significant gap in VLE and density data of the (CO_2 + CO) system and will be important for the design and operation of a number of processes, especially those of relevance in CCS and flue gas applications. Careful evaluation of the uncertainties of VLE and density measurements is presented. The expanded relative uncertainties (k = 2) in mole fractions are $0.011 \cdot x \cdot (x\text{-}1)$ and in densities are between (0.2 and 1.8) %.

The VLE data from this work, published by Souza et al. [24], together with the densities measured in this work were used to develop an improved Helmholtz-energy-explicit mixture model. The new mixture model combines the mathematical approach of the GERG-2008 and EOS-CG models with refitted reducing parameters and a new binary-specific departure function. As a result, the new mixture model is significantly more accurate in describing the thermodynamic properties of the (CO_2 + CO) mixture than the GERG-2008 and the EOS-CG models. The new model has been already implemented in the software package REFPROP (version 10) [87]. Detailed comparisons between VLE and densities calculated from the different mixture models and experimental data available in the literature were presented. Density data of this work are mostly described by the new mixture model within their experimental uncertainty.

The new mixture model will contribute to the update of the multi-fluid mixture model for humid gases, combustion gases and CO_2-rich mixtures, mainly focus on CO_2 with impurities relevant to CCS and flue gas applications, which is under development at Ruhr-Universität Bochum.

Chapter 7 The (CO_2 + CH_4) System

This section presents the results and discussion of the measurements of VLE of the (CO_2 + CH_4) system and comparison with literature data, in addition to result and performance of existing models.

7.1 Literature Review on Vapour-Liquid Equilibrium and Density

In the pre-combustion CO_2 capture process, CH_4 is formed in the first stage during the gasification of the fuel in lower concentration, generally between 0.4 to 4 mol% [14, 15, 113]. The (CO_2 + CH_4) system is also important on the natural gas industry, as natural gas is a multi-component mixture of varying composition with methane as the main component and other components such as nitrogen, carbon dioxide, ethane, propane, and heavier hydrocarbons [13]. As a result, VLE and density data for binary system comprising of CO_2 and CH_4 are not as scarce as the (CO_2 + CO) system. In fact, the (CO_2 + CH_4) system has more experimental data available than most binaries comprised of (CO_2 + diluent) relevant to CCS processes, with focus on pre-combustion carbon capture and pipeline transportation. Nevertheless, the quality and extend of the data over the relevant temperature, pressure and composition ranges are limited. A detailed comparison between the VLE and SLVE data from this work and literature is found in section 6.2.3.

Figure 7.1 shows a graphic overview of the available literature VLE data of the (CO_2 + CH_4) system together with the present work, which range from temperatures just above the triple point of CO_2 to just below the critical point of CO_2. Additionally, available solid-liquid-vapor equilibrium (SLVE) data are presented together with the vapor pressure of CO_2 from Span and Wagner and vapour pressure of CH_4 from Setzmann and Wagner EOS.

Experimental VLE data for the (CO_2 + CH_4) system were first reported by Tsiklis et al., a few points at a single temperature of 255 K. A more complete work was later published by Donnelly et al. [117], who used an analytical method and reported data points covering the temperature range between (200 and 271) K, including

measurements close to the critical locus. Somait and Kidnay [118] used an analytical method with phase composition analysis by gas chromatography to measure VLE of the (CO_2 + CH_4) and other binary systems comprised of CO_2, N_2 and CH_4 at T = 270 K. Years later, work from the same group were published extending the measurements of Somait and Kidnay [118]. With data reported by Wei et al. at temperatures of (230, 250 and 270) K and pressure up to 8.4 MPa and by Webster and Kidnay [119] at temperatures of (230 and 250) K and pressure up to 8.4 MPa. Blanco et al. [21], who used a synthetic method to study five different mixtures with CO_2 mole fractions ranging from 0.970 to 0.996 at temperatures between (253.15 and 293.15) K. The most-recent VLE data for this system were reported by Nasir et al. [108] at temperature ranging from (240 and 293) K and pressures up to 9 MPa; and Petropoulou et al. [75] at limited temperature range between (293 and 303) K. Table 7.1 summarises the literature data available for the vapor-liquid equilibria of the (CO_2 + CO) system.

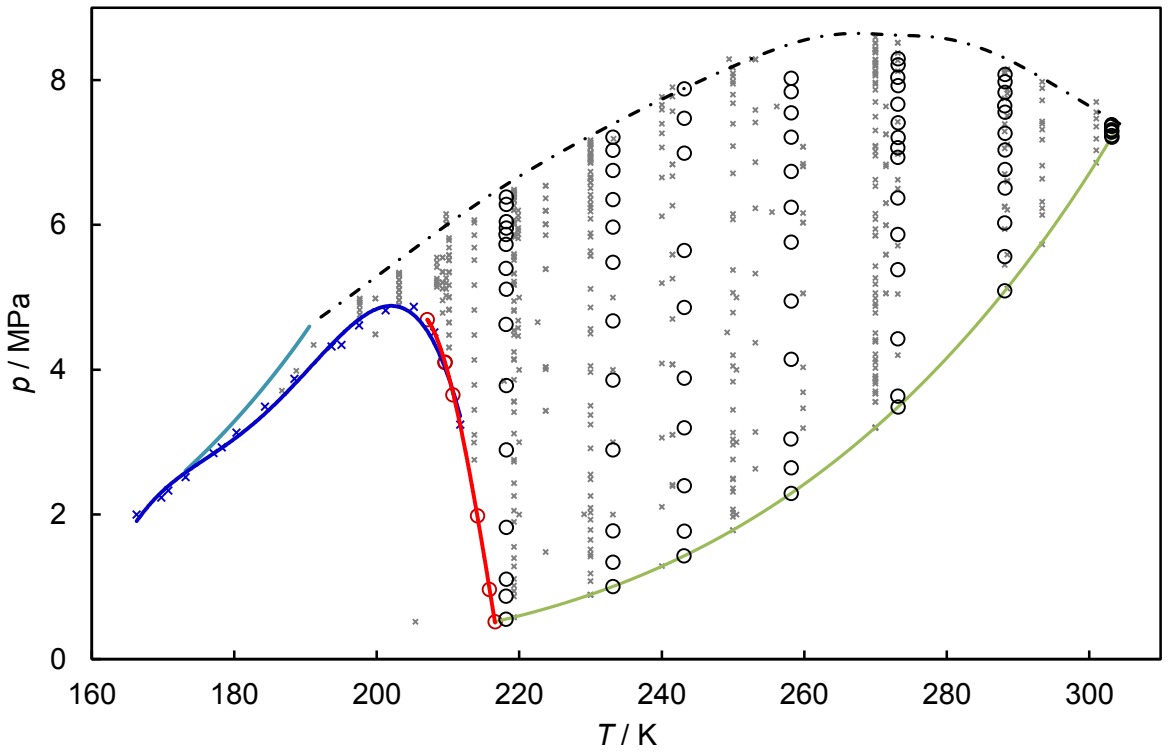


Figure 7.1 Temperature-pressure diagram of the (CO_2 + CH_4) system: x or x, available literature data; O, SVLE data from our group (unpublished); O, this work; – ·– ·, critical locus calculated from GERG-2008; ____, vapor pressure of CO_2 from Span and Wagner EOS [70]; ____, vapor pressure of CH_4 from Setzmann and Wagner EOS [71], ____, trend line of available solid-liquid-vapor equilibrium (SLVE) data and ____, trend line of solid-liquid-vapor equilibrium (SLVE) data from our group [120].

Table 7.1 Summary of the literature data available for the vapor-liquid equilibria and solid-liquid-vapor equilibria of the (CO_2 + CH_4) system.

Authors	T_{min}/K	T_{max}/K	p_{max}/MPa	Reference
VLE				
Al-Sahhaf et al. -1983	219	270	8.5	[121]
Arai et al. -1971	253	288	8.5	[122]
Bian et al. -1993	301		7.7	[123]
Blanco et al. -2014	253	293		[21]
Davalos et al. -1976	230	270	8.5	[124]
DeVaney et al. -1978	222		6.9	[125]
Donnelly et al. 1954	200	271	8.1	[117]
Hwang et al. 1976	153	219	6.5	[126]
Joffe et al. -1976	209	271	7.3	[127]
Kaminishi et al. 1968	233	283	8.2	[83]
Knapp et al. 1990	220	270	5	[128]
Mraw et al. 1978	153	219	6.5	[129]
Nasir et al. 2015	240	293	9.0	[108]
Neumann and Walch -1968	173	220	6.2	[130]
Somait and Kidnay 1978	270		8.4	[118]
Tsiklis 1946	255		6.9	[131]
Vrabec and Fischer 1996	230	270	7.8	[132]
Webster and Kidnay 2001	230	270	8.4	[119]
Wei et al. -1995	230	270	8.4	[133]
Petropoulou et al. - 2018	293	303	8.4	[134]
Xu et al. -1992	288	293	8.2	[135]
Yorizane et al. 1968	143		3.9	[136]
SVLE				
Davis et al. 1962	166	211	4.7	[137]
Our Group (2014)	204	217	4.8	[120][a]

[a] Unpublished data.

In order to check the consistency and reliability of these reported measurements experimental data available at similar conditions of mole fraction, pressure and temperature have been compared. Unfortunately, as detailed further below in section

6.2.2, the different data sources are scattered and do not agree at the whole range of temperature measured. Significant inconsistencies between the measurements of the different authors occur, especially at the retrograde and critical regions.

As mentioned before, density data are a valuable addition to VLE data because homogeneous density measurements are subject to an additional degree of freedom (mixture composition can also be varied). Similar to the (CO_2 + CO) system, most of the available data come from the work of Blanco et al. [21] which, despite the large number of data, covers an important temperature range between (253 to 333) K but only a limited composition range of (0.4 to 15) mol% CH_4. Other available data are those of Wöll and El Hawary , for mixtures containing (85 and 92) mol% CH_4 at temperatures from (233 to 373) K and pressures up to 18 MPa (equivalent to densities up to 15 mol·dm^{-3}) and represent, according to Kunz and Wagner [13], the only available accurate experimental information for the considered mixture compositions at these extended temperature and pressure conditions. Because they are located near the critical region, these data provide valuable information on the strong curvature in this region. The most-recent measurement for this system were reported by Liu et al. [102] for six compositions from (10 to 90) mol% CH_4 at limited temperatures (300 to 308) K and pressures up to 18 MPa. Table 7.2 summarises the literature data available for the density of the (CO_2 + CH_4) system.

Table 7.2 Summary of the literature data available for the density of the (CO_2 + CH_4) system.

Authors	T_{min}/K	T_{max}/K	p_{max}/MPa	x range	Reference
Blanco et al. -2012	253	333	20	0.04-0.15	[138]
Liu et al. -2017	300	308	18	0.10-0.90	[102]
Reamer et al. -1944	311	478	68.9	0.2	[139]
Ruhrgas -1990	270	350	28.4	0.69	[140]
Seitz and Blencoe -1996	673		99.9	0.10-0.90	[141]
Seitz et al. -1996	323	573	100.9	0.10-0.90	[142]
Simon et al. -1977	283	322	20.7	0.09	[143]
Wöll and El hawary -2003	233	373	18.3	0.85-0.92	[144]

Clearly from the relatively high average of the mol% CH_4 from the different data sources, most studies are of more relevance to natural gas industry then CCS processes and pipeline transportation of CO_2 rich mixtures.

Further measurements of additional thermodynamic properties, such as speed of sound, were reported by Estela-Uribe for a mixture containing 80 mol% CH_4 at temperatures from (200 to 450) K and pressures up to 17 MPa, and by Younglove et al. for mixtures containing (85 and 95) mol% CH_4 at temperatures from (250 to 350) K and pressures up to 11 MPa.

In summary, there is no single VLE study for the (CO_2 + CH_4) system that span the temperature from just above the triple point of CO_2 to just below the critical point of CO_2. This system presents gaps on VLE and density data among the pressure, temperature and composition range relevant to CCS, besides discrepancies between different data sources.

7.2 Vapour-Liquid Equilibrium Results

The VLE of the (CO_2 + CH_4) system was measured along seven isotherms at temperatures varying from (218.15 to 303.15) K at pressures from the vapor pressure of pure CO_2 to just below the mixture critical pressure. The experimental results obtained for both the vapor and the liquid phases are given in Table 7.3 in which the temperature T, pressure p and compositions x and y represent the average of temperature, pressure and liquid or vapor mole fraction of CH_4 at each state point, based on replicated measurements. The corresponding uncertainties for each series, which was obtain as described in Section 4.6, are also given in Table 7.3. The same set of measured data are shown in Figure 6.2 on a pressure-composition diagrams for all seven temperatures measured (218.15, 233.15, 243.15, 258.15, 273.15, 288.15, 303.15) K. There is an slightly increase in the uncertainty in the mole fractions with increase in pressure. The highest values of uncertainty are on the proximity to the critical point of each isotherm as a consequence of the increase of contribution of the uncertainty in pressure in the total uncertainty in the mole fractions.

Table 7.3 Experimental VLE data for the (CO_2 + CH_4) system at temperature T, pressure p, vapor mole fraction of CH_4 y, and liquid mole fraction of CH_4 x.[a]

T/K	p/MPa	x	y	$u_c(x)$	$u_c(y)$
218.124	0.5532	0.0000	0.0000	-	-
218.145	0.8732	0.0132	0.3468	1.07×10^{-3}	2.72×10^{-3}
218.180	1.1058	0.0237	0.4696	7.15×10^{-4}	2.83×10^{-3}
218.171	1.8213	0.0582	0.6546	6.55×10^{-3}	2.51×10^{-3}
218.169	2.8929	0.1218	0.7576	1.19×10^{-3}	2.03×10^{-3}
218.172	3.7838	0.1917	0.7963	1.71×10^{-3}	1.79×10^{-3}
218.160	4.6286	0.2919	0.8115	2.28×10^{-3}	1.69×10^{-3}
218.163	5.1122	0.3740	0.8162	2.59×10^{-3}	1.66×10^{-3}
218.151	5.3996	0.4287	0.8174	2.71×10^{-3}	1.65×10^{-3}
218.161	5.7312	0.5209	0.8157	2.76×10^{-3}	1.66×10^{-3}
218.161	5.8674	0.5588	0.8142	2.72×10^{-3}	1.67×10^{-3}
218.165	5.9578	0.5848	0.8126	2.68×10^{-3}	1.68×10^{-3}
218.162	6.0455	0.6099	0.8105	2.63×10^{-3}	1.70×10^{-3}
218.170	6.2832	0.6811	0.7970	2.40×10^{-3}	1.79×10^{-3}
218.162	6.3845	0.7245	0.7738	2.21×10^{-3}	1.94×10^{-3}
233.154	1.0040	0.0000	0.0000	-	-
233.160	1.3425	0.0141	0.2286	7.95×10^{-4}	2.10×10^{-3}
233.156	1.7737	0.0314	0.3955	5.67×10^{-4}	2.68×10^{-3}
233.156	2.8909	0.0862	0.5898	8.88×10^{-4}	2.68×10^{-3}
233.156	3.8581	0.1431	0.6639	1.36×10^{-3}	2.47×10^{-3}
233.158	4.6773	0.2028	0.6993	1.79×10^{-3}	2.32×10^{-3}
233.158	5.4856	0.2763	0.7180	2.21×10^{-3}	2.24×10^{-3}
233.160	5.9690	0.3314	0.7236	2.45×10^{-3}	2.21×10^{-3}
233.162	6.3499	0.3824	0.7245	2.61×10^{-3}	2.21×10^{-3}
233.163	6.7550	0.4449	0.7198	2.73×10^{-3}	2.23×10^{-3}
233.161	7.0343	0.4977	0.7104	2.76×10^{-3}	2.27×10^{-3}
233.159	7.2113	0.5360	0.6982	2.75×10^{-3}	2.33×10^{-3}
243.123	1.4287	0.0000	0.0000	-	-
243.160	1.7687	0.0133	0.1713	6.35×10^{-4}	1.69×10^{-3}

T/K	p/MPa	x	y	$u_c(x)$	$u_c(y)$
243.152	2.3978	0.0392	0.3552	5.43×10^{-4}	2.55×10^{-3}
243.152	3.1965	0.0760	0.4836	8.02×10^{-4}	2.77×10^{-3}
243.155	3.8823	0.1111	0.5495	1.10×10^{-3}	2.74×10^{-3}
243.154	4.8616	0.1694	0.6077	1.56×10^{-3}	2.63×10^{-3}
243.157	5.6499	0.2260	0.6348	1.93×10^{-3}	2.56×10^{-3}
243.150	6.9907	0.3551	0.6488	2.53×10^{-3}	2.52×10^{-3}
243.157	7.4730	0.4208	0.6376	2.69×10^{-3}	2.55×10^{-3}
243.158	7.8819	0.5101	0.5948	2.76×10^{-3}	2.66×10^{-3}
258.159	2.2923	0.0000	0.0000	-	-
258.157	2.6446	0.0162	0.1117	4.56×10^{-4}	1.17×10^{-3}
258.142	3.0422	0.0291	0.2047	4.50×10^{-4}	1.83×10^{-3}
258.151	4.1449	0.0769	0.3667	8.06×10^{-4}	2.57×10^{-3}
258.149	4.9488	0.1161	0.4363	1.14×10^{-3}	2.72×10^{-3}
258.148	5.7641	0.1613	0.4807	1.50×10^{-3}	2.76×10^{-3}
258.153	6.2466	0.1914	0.5003	1.71×10^{-3}	2.76×10^{-3}
258.154	6.7410	0.2240	0.5133	1.92×10^{-3}	2.76×10^{-3}
258.158	7.2125	0.2597	0.5205	2.12×10^{-3}	2.76×10^{-3}
258.152	7.5498	0.2922	0.5203	2.29×10^{-3}	2.76×10^{-3}
258.152	7.8400	0.3207	0.5156	2.41×10^{-3}	2.76×10^{-3}
258.157	8.0253	0.3511	0.5084	2.52×10^{-3}	2.76×10^{-3}
273.154	3.4840	0.0000	0.0000	-	-
273.145	3.6338	0.0056	0.0318	3.23×10^{-4}	4.65×10^{-4}
273.150	4.4255	0.0361	0.1606	4.42×10^{-4}	1.51×10^{-3}
273.146	5.3830	0.0769	0.2615	7.99×10^{-4}	2.14×10^{-3}
273.143	5.8701	0.0992	0.2980	9.95×10^{-4}	2.31×10^{-3}
273.145	6.3753	0.1245	0.3271	1.21×10^{-3}	2.43×10^{-3}
273.145	6.9351	0.1554	0.3506	1.45×10^{-3}	2.52×10^{-3}
273.149	7.0664	0.1625	0.3555	1.51×10^{-3}	2.53×10^{-3}
273.151	7.2102	0.1709	0.3590	1.57×10^{-3}	2.54×10^{-3}
273.153	7.4111	0.1845	0.3632	1.66×10^{-3}	2.56×10^{-3}
273.150	7.6710	0.2017	0.3668	1.78×10^{-3}	2.57×10^{-3}

T/K	p/MPa	x	y	$u_c(x)$	$u_c(y)$
273.156	7.9234	0.2210	0.3664	1.90×10^{-3}	2.57×10^{-3}
273.146	8.0407	0.2324	0.3636	1.97×10^{-3}	2.56×10^{-3}
273.152	8.2135	0.2495	0.3587	2.07×10^{-3}	2.54×10^{-3}
273.154	8.2957	0.2601	0.3526	2.13×10^{-3}	2.52×10^{-3}
288.155	5.0910	0.0000	0.0000	-	-
288.151	5.5641	0.0181	0.0563	2.67×10^{-4}	6.14×10^{-4}
288.137	6.0279	0.0367	0.1017	4.19×10^{-4}	1.02×10^{-3}
288.168	6.5109	0.0565	0.1389	6.04×10^{-4}	1.33×10^{-3}
288.156	6.7690	0.0684	0.1548	7.14×10^{-4}	1.45×10^{-3}
288.160	7.0385	0.0811	0.1694	8.31×10^{-4}	1.56×10^{-3}
288.161	7.2644	0.0922	0.1806	9.30×10^{-4}	1.64×10^{-3}
288.166	7.5583	0.1089	0.1899	1.08×10^{-3}	1.70×10^{-3}
288.153	7.6479	0.1146	0.1920	1.12×10^{-3}	1.72×10^{-3}
288.157	7.8325	0.1270	0.1944	1.23×10^{-3}	1.73×10^{-3}
288.158	7.9790	0.1395	0.1932	1.33×10^{-3}	1.72×10^{-3}
288.158	8.0795	0.1534	0.1874	1.44×10^{-3}	1.68×10^{-3}
303.166	7.2123	0.0000	0.0000	-	-
303.147	7.2363	0.0010	0.0017	1.17×10^{-5}	1.90×10^{-5}
303.147	7.2858	0.0034	0.0049	3.70×10^{-5}	5.36×10^{-5}
303.157	7.2925	0.0036	0.0052	3.98×10^{-5}	5.69×10^{-5}
303.156	7.3165	0.0047	0.0065	1.84×10^{-4}	1.90×10^{-4}
303.156	7.3649	0.0069	0.0091	1.77×10^{-4}	1.88×10^{-4}
303.157	7.3845	0.0080	0.0101	1.86×10^{-4}	1.98×10^{-4}

[a] Standard uncertainties (k = 1.73) are $u(T)$ = 0.006 K, $u(p)$ = 0.009 MPa.

[b] CO_2 vapor pressure measurement.

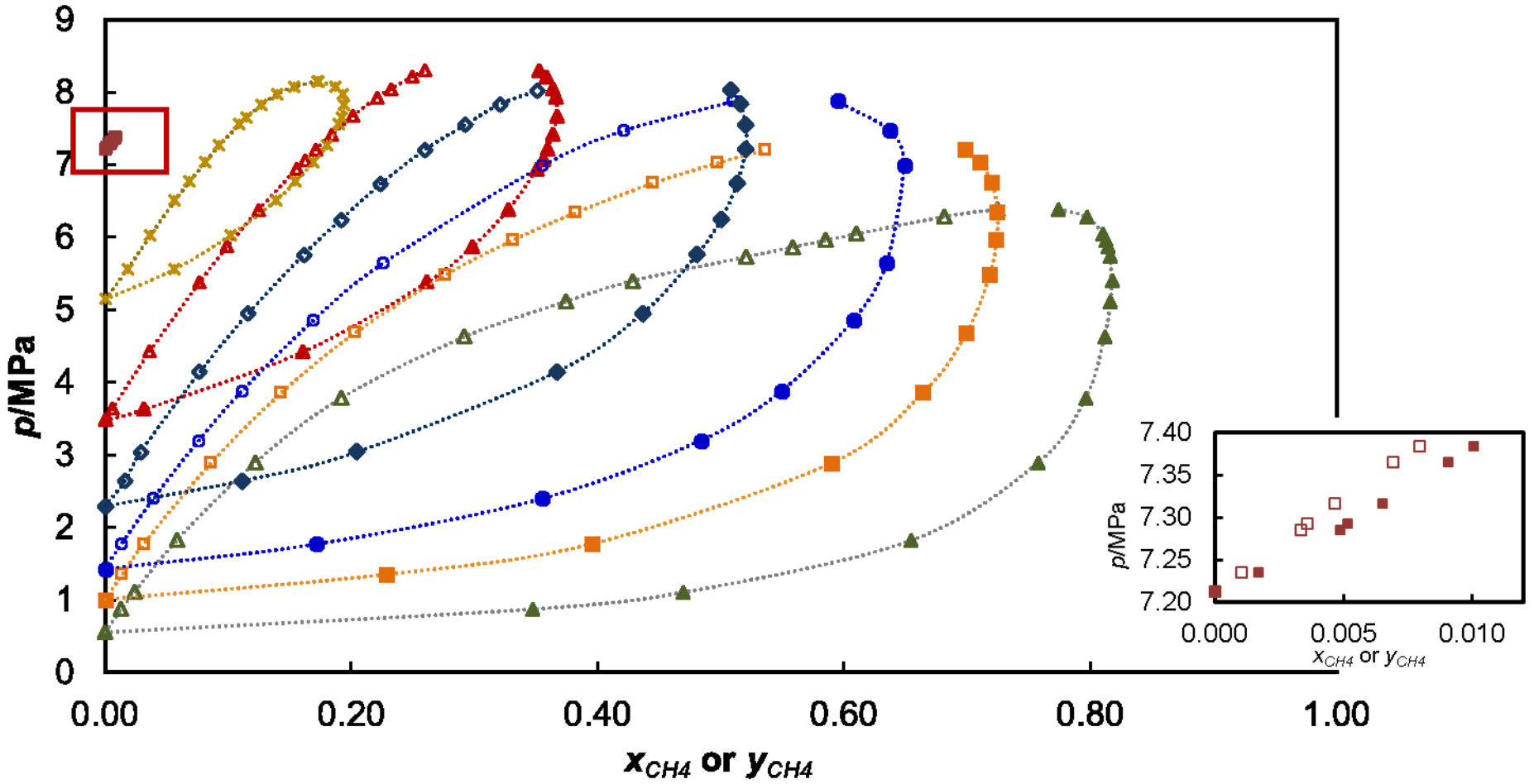


Figure 7.2 Pressure-composition diagrams for (CO_2 + CH_4) : (▲ and △), 218.15 K; (■ and □), 233.15 K; (● and ○), 243.15 K; (◆ and ◇), 258.15 K; (▲ and △), 273.15 K; (∗ and ∗); 288.15 K, (■ and □) 303.15 K, and ----, trend line.

7.2.1 Critical Point Estimation

As for the (CO_2 + CO) system, the critical point of (CO_2 + CH_4) were determined by analysing near-critical data in terms of the asymptotic behaviour approaching the critical point [116]. The optimization of the parameters were fully explained at section 6.2.1. Figure 7.3 presents the bubble and dew pressures against z/z_c, which illustrates the high quality of the fit in the critical region. It can be seen that, apart from T = 258.15 K, there is a good agreement between the experimental data and the prediction of the asymptotic behaviour approaching the critical locus, described by Eqs. (47) and (49).

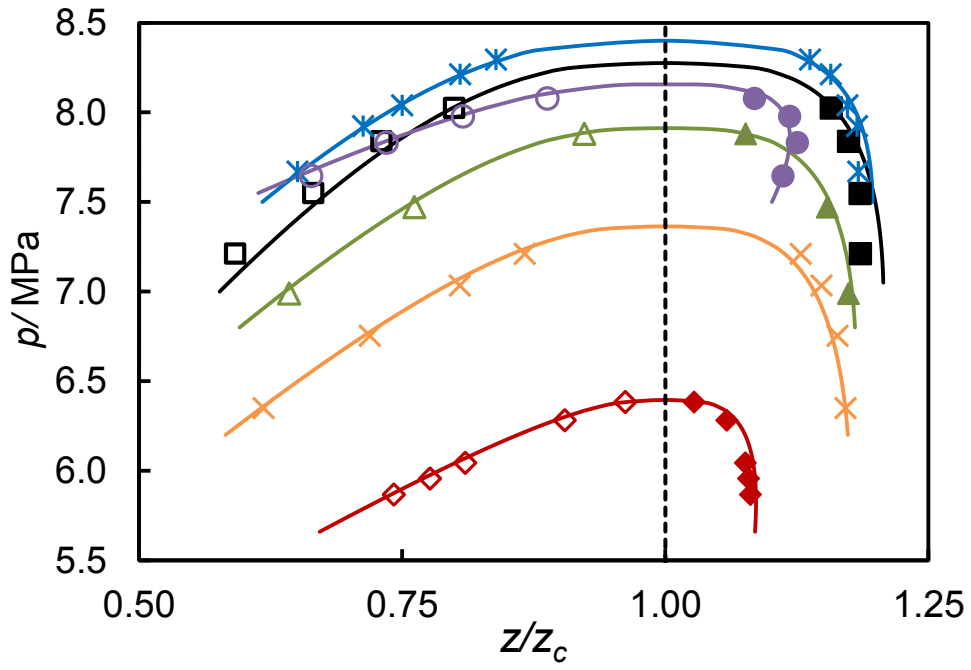


Figure 7.3 Critical point estimation by regression analysis of asymptotic behaviour approaching the critical point in Eq. (47). Pressure p vs. mole fraction z of CH_4 divided by critical mole fraction z_c for the (CO_2 + CH_4) system: ◇, T = 218.15 K; x, T = 233.15 K; △, T = 243.15 K; ○, T = 258.15 K; □, T = 273.15 K; ✳, T = 288.15 K, ——, asymptotic behaviour approaching the critical point in Eq. (47) at each temperature.

The optimized parameters are given in Table 6.4 and shown in Figure 6.3. The parameters were found to result in a good description of the critical region. Parameter z_c was found to be represented adequately as linear function, so that a_3 was zero in those cases. Parameters λ_1, λ_2, μ and p_c were found to be better represented as a quadratic function.

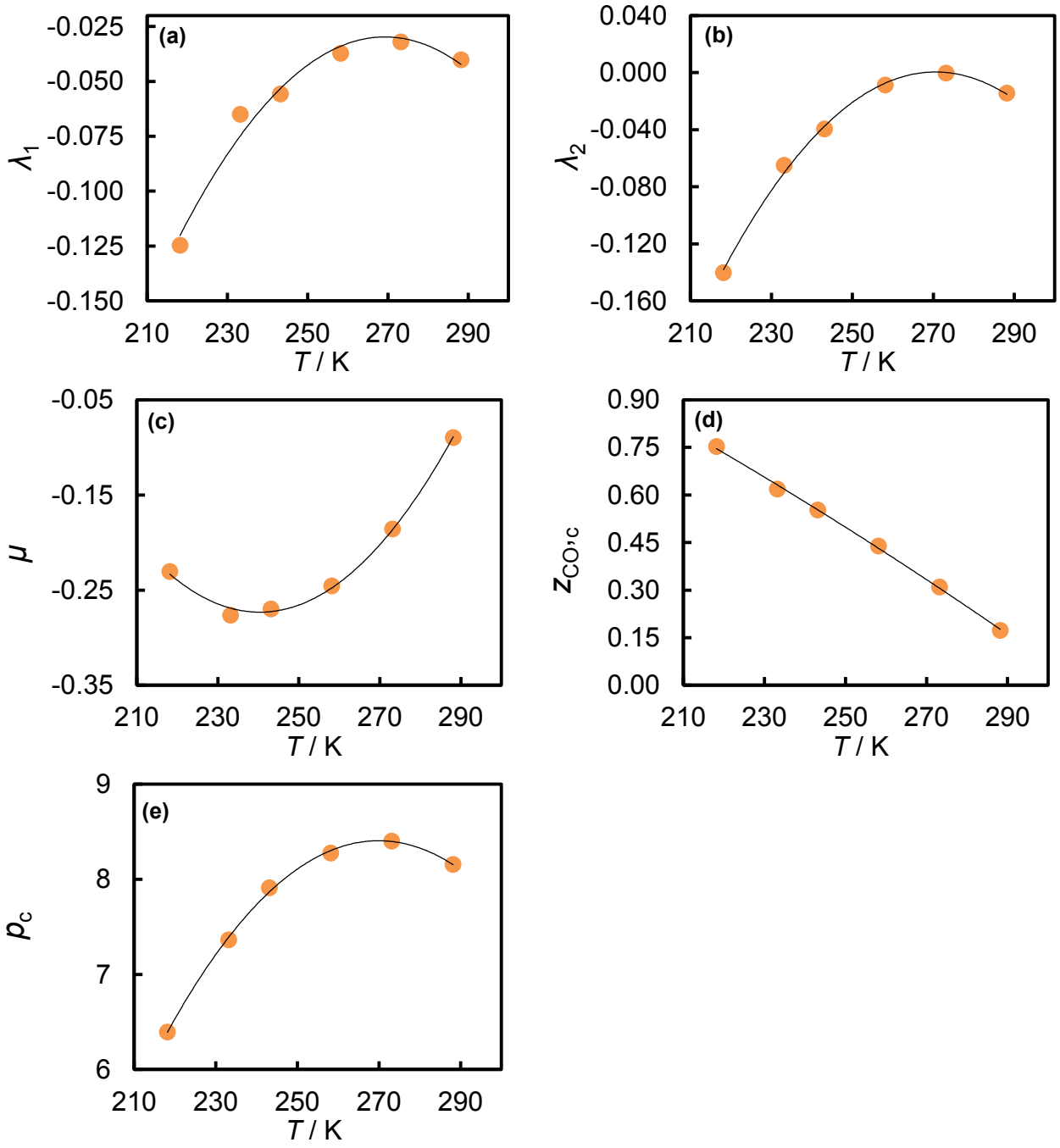


Figure 7.4 Optimized parameters from asymptotic behaviour approaching the critical point applied to the binary system (CO_2 + CH_4): λ_1 (a), λ_2 (b), μ (c), z_c (d) and p_c (e) against temperature. ——, Eq. (49).

Table 7.4 Coefficients of Eqs. (47) and (49) for the critical locus.

Parameter	a_1	a_2	a_3
$\lambda_1(T)$/MPa^{-1}	-2.55×10^{0}	1.87×10^{-2}	-3.47×10^{-5}
$\lambda_2(T)$/MPa^{-1}	-3.69×10^{0}	2.73×10^{-2}	-5.05×10^{-5}
$\mu(T)$/MPa$^{-\beta}$	4.44×10^{0}	-3.89×10^{-2}	8.08×10^{-5}
$z_{CO,c}(T)$	2.53×10^{0}	-8.14×10^{-3}	-
$p_c(T)$/MPa	-46.35×10^{0}	4.05×10^{-1}	-7.516×10^{-4}

The critical loci are plotted in Figure 6.5 over the temperature and pressure range of critical compositions investigated; also shown is the critical point of CO_2 [70].

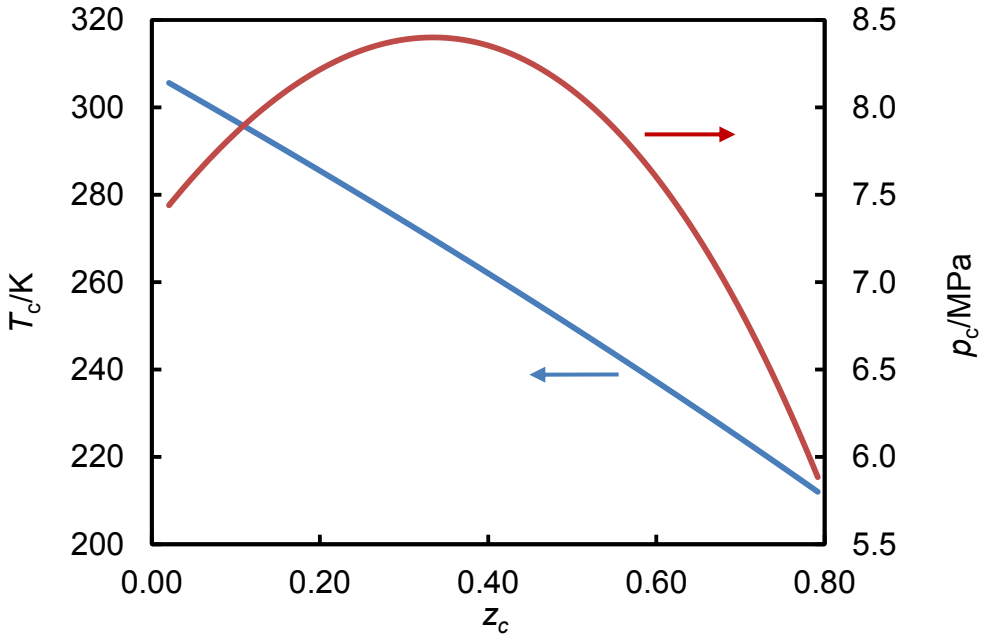


Figure 7.5 Critical loci for (CO_2 + CH_4) system predicted by Eq. (47). Critical temperature T_c (left) and critical pressure p_c (right) plotted against the critical mole fraction z_c of CH_4.

7.2.2 Comparison of VLE Literature Data

As mention before, the available data cover almost the full temperature range possible from just above the triple point temperature of CO_2 to just below the critical temperature of CO_2 (Figure 7.1). Nevertheless, no single work before ours, covers the full temperature spectrum of VLE. For example, the work of Davalos et al. [124], Webster and Kidnay [119] and Wei et al. [133] presented two isotherms 230 and 270 K of the (CO_2 + CH_4) system. While Al-Sahhaf et al. [121] work seems to cover a wide temperature range for the same system, the measurements were limited to low pressures; the isotherm of T = 220 K is measured until p = 4 MPa, way below the critical pressure of around p = 6.5 MPa.

Figure 7.6, Figure 7.7 and Figure 7.8 present comparisons between the available VLE data in the literature [117, 119, 121, 124, 126-128, 130, 133] and the GERG-2008 for the selected isotherms at temperatures of T = 220 K, 230 K and 270 K. The deviations among different authors are more evident when assessing pressure-composition diagrams than pressure temperature diagrams.

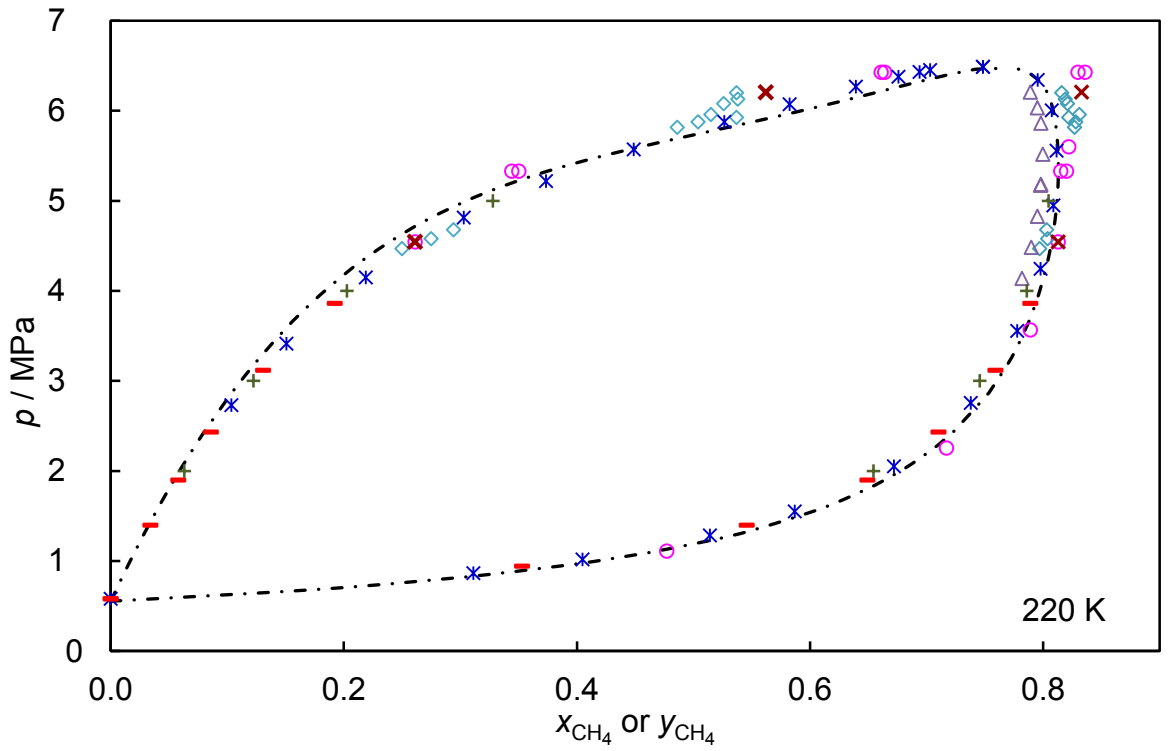


Figure 7.6 Pressure-composition diagrams of the (CO_2 + CH_4) system at 220 K as calculated from the GERG-2008. Experimental VLE data from different sources: ○, Donnelly et al. [117]; ◇, Neumann and Walch [130]; ∗, Mraw et al. [129]; △, Hwang et al. [126]; x, Joffe et al. [127]; –, Al-Sahhaf et al. [121]; +, Knapp et al. [128]; and – ·– ·, GERG-2008.

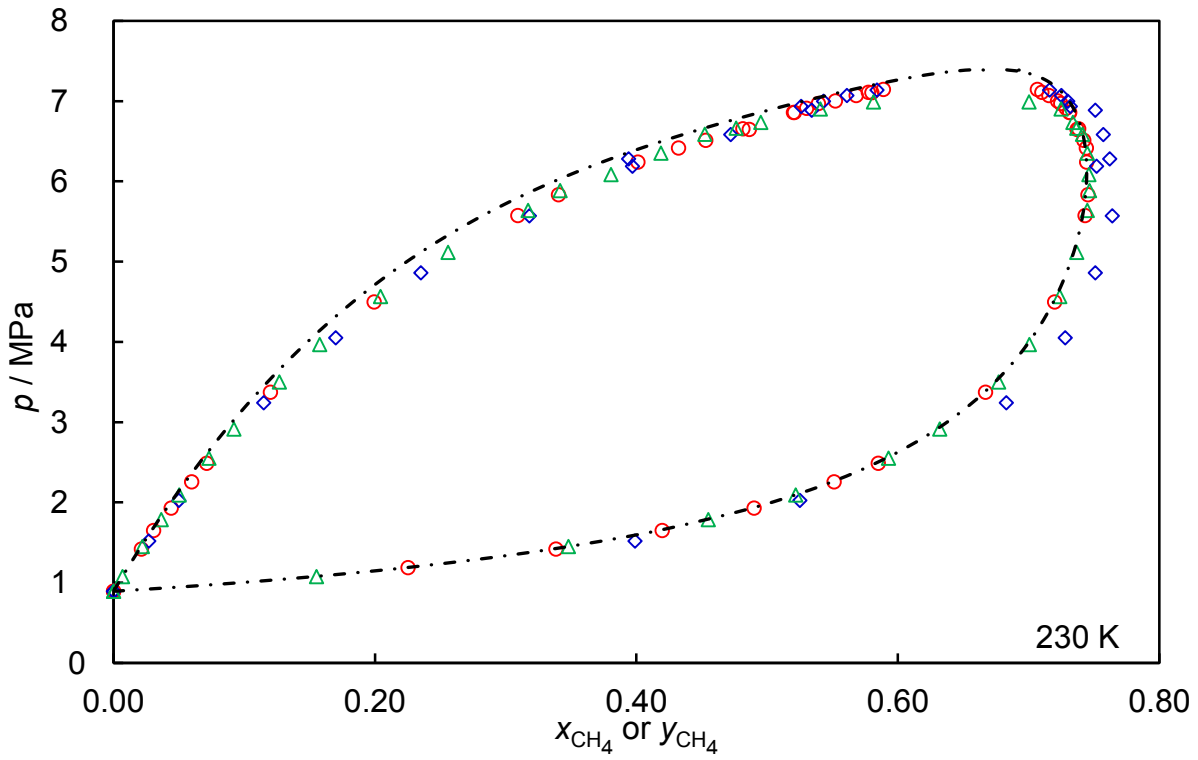


Figure 7.7 Pressure-composition diagrams of the (CO_2 + CH_4) system at 220 K as calculated from the GERG-2008. Experimental VLE data from different sources: ○, Webster and Kidnay [119]; ◇, Davalos et al. [124]; △, Wei et al. [133]; and – ·– ·, GERG-2008.

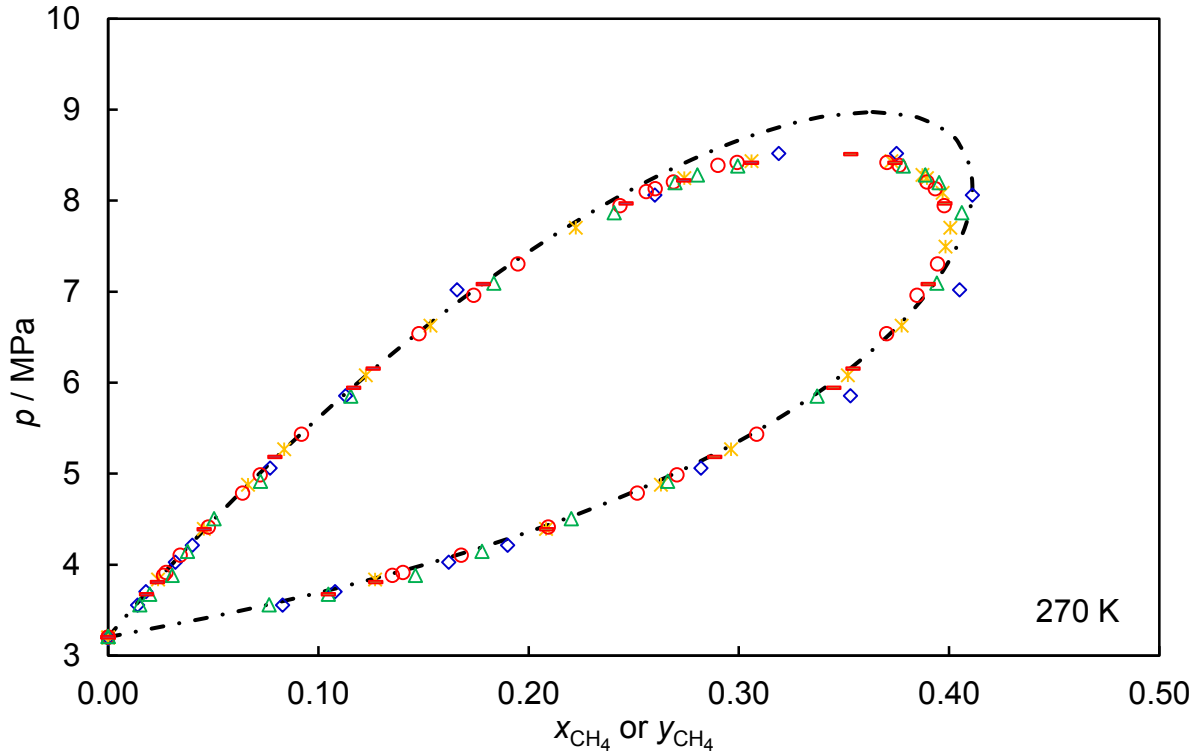


Figure 7.8 Pressure-composition diagrams of the (CO_2 + CH_4) system at 270 K as calculated from the GERG-2008. Experimental VLE data from different sources: ○, Webster and Kidnay[119]; ◇, Davalos et al. [124]; △, Wei et al. [133]; ✳, Somait and Kidnay[118]; –, Al-Sahhaf et al. [121]; and – ·– ·, GERG-2008.

It is clear from the plots that the data has better agreement in the vapour than the liquid measurements with significant disagreement in the critical region, as expected. The most significant disagreements are presented in the retrograde region. Data from different sources deviate among one another on average less than 4% in pressure at similar conditions of composition in the bubble line and on average less than 5% in composition at similar conditions of pressure in the dew line.

At T = 220 K isotherm, the VLE data from Al-Sahhaf et al. [121], which are limited to 4 MPa, agree well with the VLE data from Mraw et al. [129] on both dew and bubble lines. The VLE data from Neumann and Walch [130], which range from 4.5 to 6.2 MPa, present significantly scatter of ±(1 to 3)% in pressure at similar conditions of composition. In the critical region, at pressures around 6 MPa, the available VLE data from Mraw et al. [129] deviate from Hwang et al. [126] and Donnelly et al. [117] to within about 5%.

At T = 230 K isotherm, the available VLE data from Webster and Kidnay [119] agree well with the VLE data from Wei et al. [133] at pressures ranging from vapor pressure of pure CO_2 to the critical region while deviate considerably from Davalos et al. [124] to within 4% in the retrograde region.

At T = 270 K isotherm, similarly to T = 230 K isotherm, the available VLE data from Webster and Kidnay [119] agree well with the VLE data from Wei et al. [133], besides data from Somait and Kidnay [118] and Al-Sahhaf et al. [121] while deviate considerably from Davalos et al. [124] to within 4% in the retrograde region.

Figure 7.9 illustrates the available VLE data in the literature at same temperatures as this work was carried out, T = 233.15 K, 273.15 K, 288.15 K and 303.15 K. It also includes values calculated from GERG-2008 PR-EOS with the recommended binary parameters from Table 3.4, section 3.2.2 and SAFT-γ Mie and further comparisons with those models are discussed at section 6.2.3.

It is clear from the plots that the VLE data from this work agree with the VLE data from the literature: Knapp et al. [128], Arai et al. [122] and Xu et al. [145] except in the retrograde region of the isotherm T = 273.15 K, in which data from different sources deviate among one another up to 4% in composition at similar conditions of pressure.

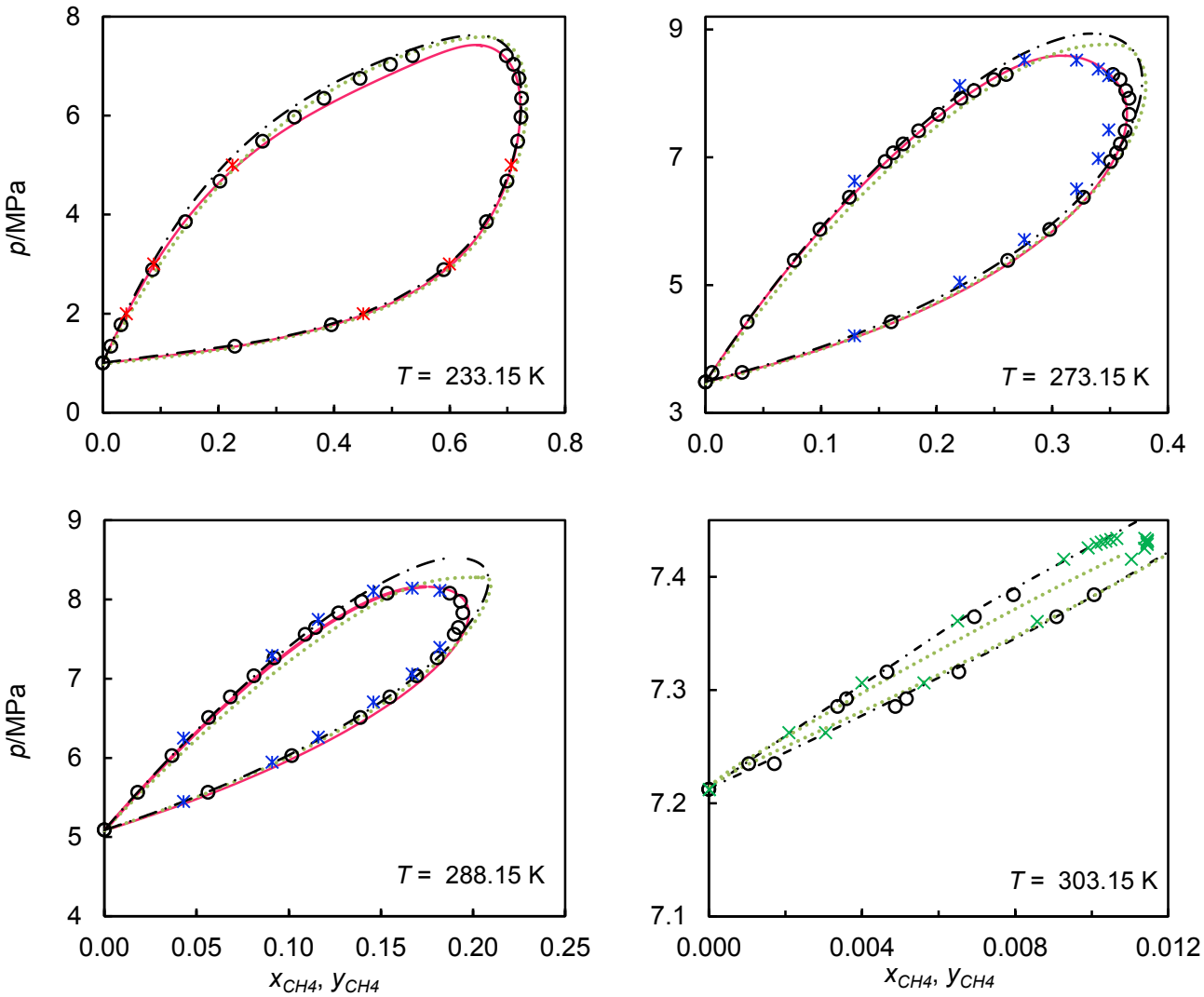


Figure 7.9 Pressure-composition diagrams of the (CO_2 + CH_4) system. Experimental VLE data from different sources: ✳, Knapp et al. [128]; ✳, Arai et al. [122]; x, Xu et al. [145]; O, this work; and model: ……, Peng-Robinson EOS fitted with recommended binary parameters from Table 3.4; – ·– ·, GERG-2008 _____, SAFT-γ Mie.

7.2.3 Comparison of VLE Data with Equations of State

Figure 7.10 illustrates the experimental pressure-composition data on six of the seven isotherms studied. Also plotted are the values calculated from the PR-EOS, with the optimized binary parameters presented in Table 3.4, section 3.2.2; GERG-2008 [26] and SAFT-γ Mie with original parameters values [30].

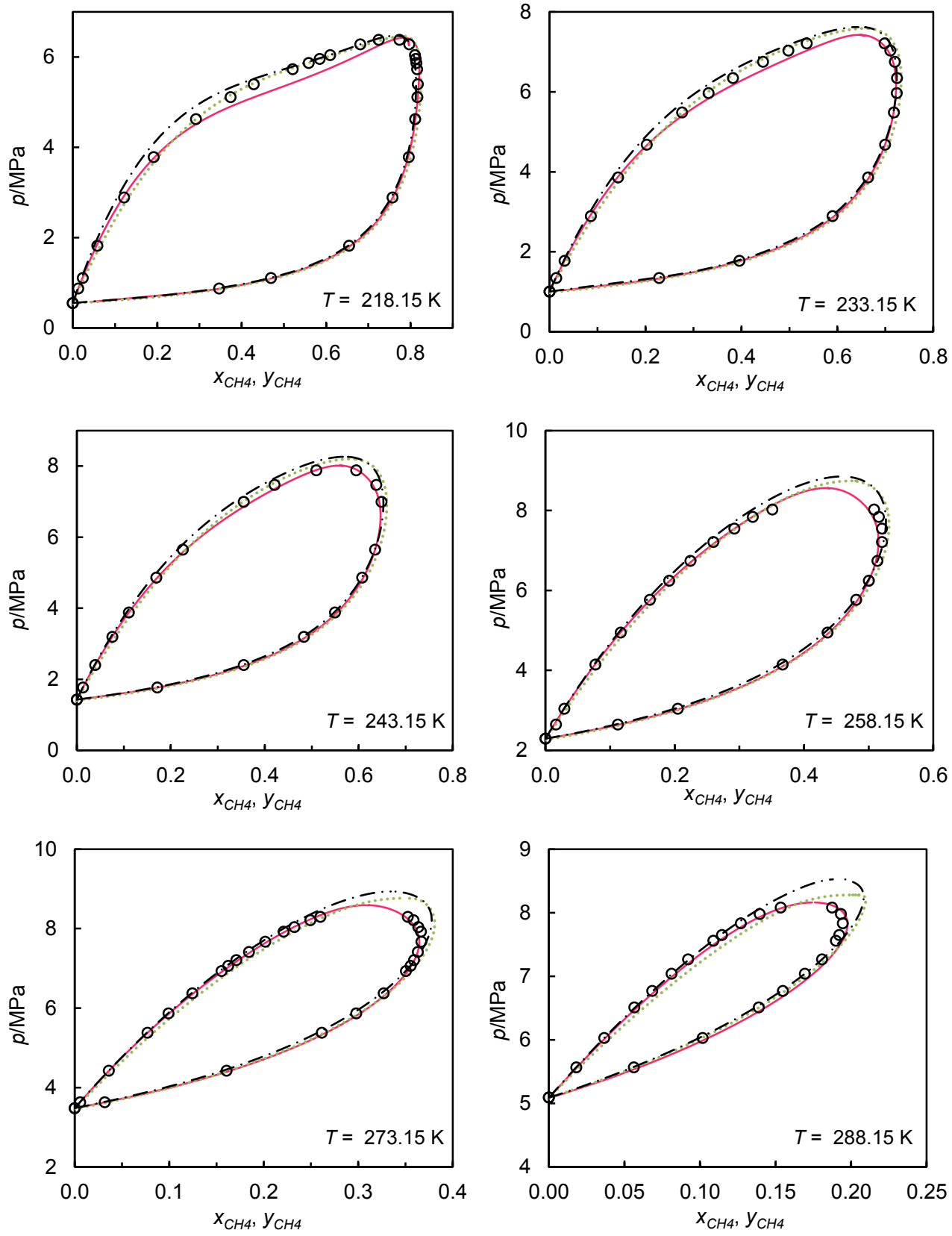


Figure 7.10 Pressure-composition diagrams of the (CO_2 + CH_4) system: O, this work; ·····, Peng-Robinson EOS fitted with recommended binary parameters from Table 3.4; – ·– ·, GERG-2008; _____, SAFT-γ Mie.

It is apparent from the plots that all three model: PR-EOS, GERG-2008 and SAFT-γ Mie give a reasonable-good representation of the data from this work.

The PR-EOS gives a good representation of our data in both vapor- and liquid-phase composition, except in the critical region. As expected, the PR-EOS overestimates the mole fractions in both liquid and vapor phases at pressures close to the critical point of all isotherms of the (CO_2 + CH_4) system except at the temperature of T = 218.15 K. GERG-2008 shows physically correct behavior on the phase boundary but presents significant representation of the data than PR-EOS. It similarly over predicts the mole fractions in both liquid and vapor phases at pressures close to the critical point. However, as described by Kunz and Wagner [13], the departure function for of the (CO_2 + CH_4) system was developed in order to allow for a very accurate description of the density along with an accurate and physically reasonable description of the mixture phase behavior.

It is obvious that SAFT-γ Mie presents a significant improvement in the estimation of mole fractions in both liquid and vapor phases at pressures close to the critical point of all isotherms of the (CO_2 + CH_4) system, except the two lower temperatures of 218.15 K and 233.15 K, when compared with PR-EOS and GERG-2008. As described by Papaioannou et al. [30], for the (CO_2 + CH_4) system, the unlike dispersion energy ε_{kl}, and repulsive Mie exponent λ_{kl} are estimated using the VLE data from Al-Sahhaf et al. [121] at T = 240K and 270 K. Including VLE data at lower temperature could have a direct result in the improvement of the estimation of the unlike parameters. However, attempts of estimating ε_{kl} and λ_{kl} using the VLE data from this work were carried out and the results showed no improving in the fitting.

In the critical region, both PR-EOS and GERG-2008 show increasing deviations from the SAFT-γ Mie approach as the critical point is approached. For example, at T = 273.15 K, the two models differ by about (3 to 5)% in the estimated critical pressure.

Figure 7.11 presents the relative volatility for the (CO_2 + CH_4) system at four temperature studied. It shows both the experimental data from this work and for the results from the new mixture model.

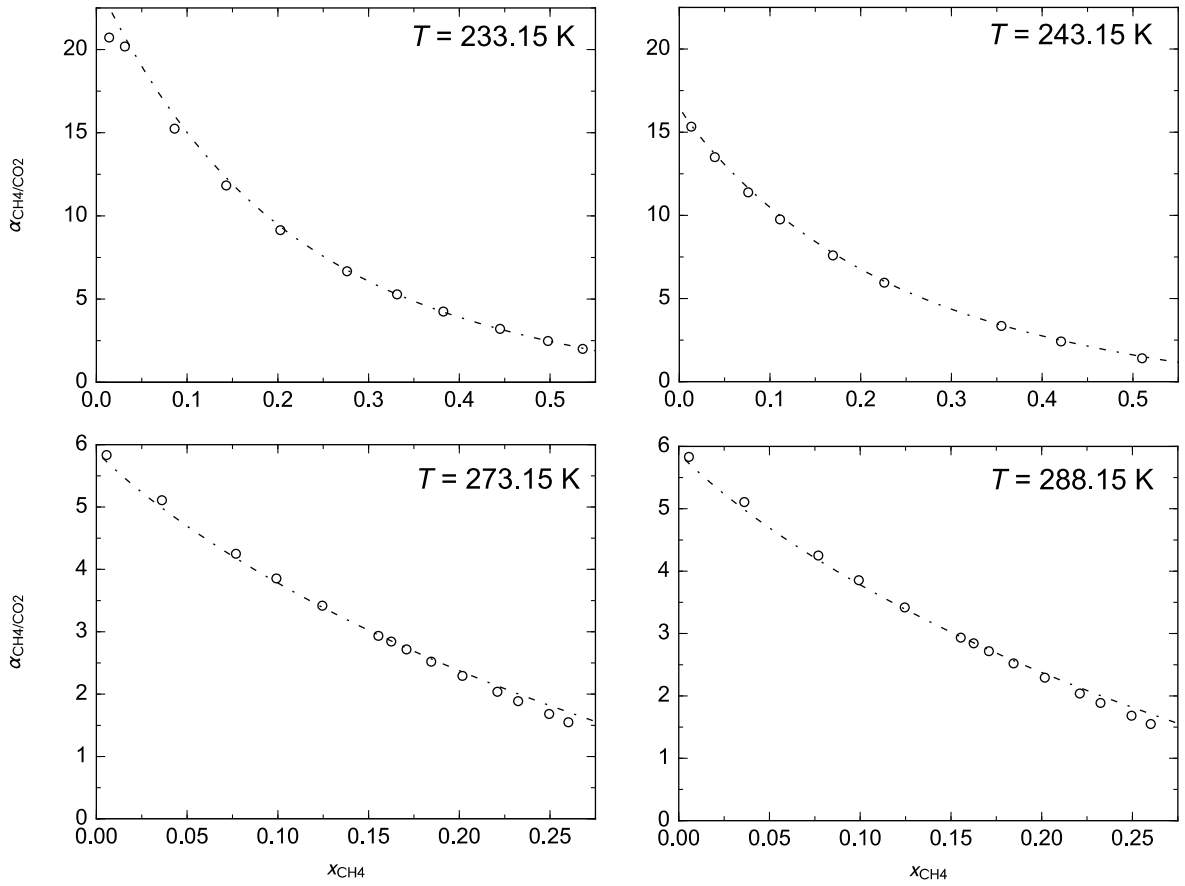


Figure 7.11 Relative volatility diagrams of the (CO_2 + CO) system at T = (233.15, 243.15, 273.15 and 288.15) K: ○, this work; – ·– ·, GERG-2008.

7.3 Conclusions

New and low-uncertainty experimental VLE data for the (CO_2 + CH_4) system were reported along seven isotherms spanning almost the entire region of vapor-liquid coexistence at temperatures from (218.15 to 303.15) K and pressures up to 9 MPa. Critical points were estimated from the data by means of analysis with asymptotic behaviour approaching the critical point. The new data help to fill a significant gap in VLE data of the (CO_2 + CH_4) system and, similarly to the data of the (CO_2 + CO) system, will be important for the design and operation of a number of processes, especially those of relevance in CCS and flue gas applications. Careful evaluation of the uncertainties of VLE measurements is presented, together with the expanded relative uncertainties (k = 2) in mole fractions, which are $0.011 \cdot x \cdot (x\text{-}1)$.

Detailed comparisons between the VLE data measured in this work and data available in the literature were presented. Besides, comparisons between experimental data and VLE calculated from the different mixture models: PR-EOS with the optimized binary parameters, GERG-2008 [26], and SAFT-γ Mie with original parameters values.

Chapter 8 H_2S Trace Analysis: (CO_2 + CH_4 + H_2S) and (CO_2 + CO + H_2S) Systems

This section presents the results and discussion of H_2S trace analysis, generally with concentrations lower than 200 ppm. The distribution of H_2S between the liquid and gas phases depends on the VLE, which is defined by the gas−liquid partition coefficient k: $k = (y_{H_2S}/x_{H_2S})$. The measurements of VLE of (CO_2 + CH_4 + H_2S) and (CO_2 + CO + H_2S) systems and comparison with literature data, in addition to result and performance of PR-EOS are reported.

8.1 Literature Review on Vapour-Liquid Equilibrium

In the pre-combustion processes, the sulfur presented in the fuel mainly yields H_2S, though other compounds such as carbonyl sulfide (COS) can be also formed. H_2S could be removed together with CO_2 or during pre-treatment, which involves an acid-gas removal stages prior to combustion. It is possible to add a selective process of H_2S removal by physical solvents if a purer CO_2 stream is required. Nonetheless, H_2S will remain an inevitable part of the CO_2 stream, typically in concentrations of 200 ppm or less [15].

A number of recent investigations reported VLE data for binary systems of H_2S with gases relevant to CCS, such as (CO_2 + H_2S) and (CH_4 + H_2S). Moreover, further investigations on the VLE of ternary systems of (CO_2 + diluent + H_2S) relevant to CCS processes were reported. In this work, two ternaries systems were assessed: (CO_2 + CH_4 + H_2S) and (CO_2 + CO + H_2S).

8.1.1 Binary Systems Relevant to the H_2S Trace Analysis

As discussed before in section 3.2, the binary interaction parameter from PR-EOS is commonly obtained by fitting experimental VLE data of the related binary systems. The binary systems relevant to the H_2S trace analysis assessed in this work are: (CO_2 + CO), (CO_2 + CH_4), (CO_2 + H_2S), (CH_4 + H_2S) and (CO + H_2S). The literature review on VLE data of the (CO_2 + CO) system were already presented in section 6.1, while

the (CO_2 + CH_4) system can be found in section 7.1. Table 8.1 summarises the VLE data available for (CO_2 + H_2S), (CH_4 + H_2S) and (CO + H_2S) systems.

Table 8.1 - Summary of the literature data available for the vapor-liquid equilibria of (CO_2 + H_2S), (CH_4 + H_2S) and (CO + H_2S) systems.

Authors	T_{min}/K	T_{max}/K	p_{max}/MPa	Reference
	(CO_2 + H_2S)			
Steckel -1945	252	273	-	[146]
Bierlein and Kay -1953	254	366	-	[147]
Sobocinski and Kurata -1959	225	364	8.3	[148]
Hirata et al. - 1975	273		3.5	[149]
Ferrell et al. - 1979	277	293	5.2	[150]
Chapoy et al. -2013	258	312	5.5	[66]
	(CH_4 + H_2S)			
Reamer et al. - 1951	277.6	344	13.5	[151]
Hirata et al. - 1975	278	-	13.3	[149]
Kohn and Kurata - 1958	173	273	13.8	[152]
Yarym-Agaev et al. - 1991				[153]
Coquelet et al. - 2014	186	313	14	[154]
	(CO + H_2S)			
Fredenslund and Mollerup	203.15	293.15	23.4	[155]

The (CO_2 + H_2S) system were first reported by Steckel [146] but no data were tabulated. Experimental VLE data for this system were first published by Bierlein and Kay [147] at temperature ranging from (254 to 366.44) K followed by the work of Sobocinski and Kurata [148] at similar temperature range from (224 to 363.44) K and pressures up to 8.3 MPa. The work of Hirata et al. [149] and Ferrell et al. [150] report data on temperatures above 273 K, ranging from (273.15 to 293) K. More recently, Chapoy et al. [66] reported VLE data at T = 258.41 K, 273.15 K, 293.47 K and 313.02 K and pressures up to 5.5 MPa.

Experimental VLE data for the (CH_4 + H_2S) system were first reported by Reamer et al. [151] at temperature ranging from (277.59 to 344.26) K and pressures up to 13.5

MPa, including the critical locus. A more comprehensive investigation was carried out by Kohn and Kurata [152], followed by Yarym-Agaev et al. [153].

The only available data for the ($CO + H_2S$) system were reported by Fredenslund and Mollerup [155] at T = 203.15 K, 233.15 K, 263.15 K and 293.15 K.

8.1.2 ($CO_2 + CH_4 + H_2S$) Ternary System

A number of VLE investigations has been carried out regarding the ($CO_2 + CH_4 + H_2S$) system, as a result of its importance in the oil and natural gas industry. All three components are present in many natural petroleum reservoir. Table 8.2 summarises the VLE data available for the ($CO_2 + CH_4 + H_2S$) system.

Table 8.2 - VLE data of the ($CO_2 + CH_4 + H_2S$) system.

Authors	T_{min}/K	T_{max}/K	p_{max}/MPa	Reference
Robinson and Bailey -1957	311	-	12.4	[156]
Robinson et al. -1981	277	344	12.4	[157]
Hensel and Massoth -1964	222	239		[158]
Ng et al. - 1985	273		3.5	[159]

The available VLE data of the ($CO_2 + CH_4 + H_2S$) system comprise the measurements at temperatures ranging from (222 to 344) K, pressures up to 12.4 MPa and concentration of H_2S greater than 0.1. On the other hand, this work studied the ternary system ($CH_4 + H_2S + CO_2$) with low concentration of H_2S (< 200 ppm) over similar ranges of temperature and pressure to assess the effect of this impurity on the phase behaviour. This means that no direct comparison between our data and the literature data were presented.

8.1.3 ($CO_2 + CO + H_2S$) Ternary System

No available data for the ($CO_2 + CO + H_2S$) system were found.

8.2 The Partition Coefficient of H_2S

The partition coefficient of H_2S *k* between liquid and vapor phases of the (CO_2 + CH_4 + H_2S) system was measured along four isotherms at temperatures of 218.15 K, 243.15 K, 273.15 K and 288.15 K and pressures up to 8 MPa. The experimental results obtained for the partition coefficient of H_2S *k* are given in Table 8.3, in which the temperature *T*, pressure *p* and partition coefficient of H_2S *k* represent the average of temperature, pressure and partition coefficient of H_2S *k* at each state point, based on replicated measurements. The corresponding relative uncertainties for each series, which was obtain as described in Section 4.6, are also given in Table 8.3.

Table 8.3 - Experimental partition coefficient of H_2S *k* of the (CO_2 + CH_4 + H_2S) system at temperature *T*, pressure *p*.[a]

T/K	*p*/MPa	*k*	$U_c(k)$	$100 \cdot \Delta k/k$
218.14	1.2294	0.481	0.022	4.53
218.14	2.4912	0.224	0.009	4.18
218.14	3.6964	0.224	0.009	4.18
218.14	4.9657	0.206	0.009	4.19
218.14	5.7826	0.448	0.019	4.15
218.14	6.2285	0.537	0.022	4.15
243.15	2.1546	0.702	0.032	4.52
243.15	2.9674	0.498	0.021	4.22
243.15	4.0887	0.395	0.016	4.16
243.15	4.3376	0.423	0.018	4.16
243.15	5.1673	0.623	0.026	4.14
243.15	6.0802	0.745	0.031	4.13
243.15	6.9366	0.829	0.034	4.12
243.15	7.5689	0.910	0.037	4.12
273.15	4.1553	0.782	0.043	5.46
273.15	5.3837	0.658	0.028	4.24
273.15	6.5935	0.667	0.028	4.15
273.15	7.2173	0.704	0.029	4.14

T/K	*p*/MPa	*k*	$U_c(k)$	$100 \cdot \Delta k/k$
273.15	8.0060	0.777	0.032	4.13
288.16	5.4826	0.843	0.066	7.86
288.16	6.4449	0.881	0.040	4.54
288.16	6.8314	0.874	0.038	4.34
288.16	7.5736	0.892	0.038	4.23
288.16	7.6197	0.865	0.036	4.20
288.16	8.0132	0.936	0.039	4.18

[a] Standard uncertainties (k = 1.73) are $u(T)$ = 0.006 K, $u(p)$ = 0.009 MPa.

The relative uncertainty in H_2S distribution *k* is roughly constant around 4.2%, except for slight higher values for the first points of each isotherm.

The partition coefficient of H_2S *k* between liquid and vapor phases of the (CO_2 + CO + H_2S) system was measured along the same four isotherms at temperatures of 218 K, 243.15 K, 273.15 K and 288.15 K and pressures up to 13 MPa. The experimental results obtained for the partition coefficient of H_2S *k* are given in Table 8.4, in which the temperature *T*, pressure *p* and partition coefficient of H_2S *k* represent the average of temperature, pressure and partition coefficient of H_2S *k* at each state point, based on replicated measurements. The corresponding uncertainties for each series, which was obtain as described in Section 4.6, are also given inTable 8.4.

Table 8.4 - Experimental partition coefficient of H_2S *k* of the (CO_2 + CO + H_2S) system at temperature *T*, pressure *p*.[a]

T/K	*p*/MPa	*k*	$U_c(k)$	$100 \cdot \Delta k/k$
218.13	0.7833	0.615	0.026	4.17
218.13	2.0928	0.321	0.013	4.16
218.13	3.4165	0.288	0.012	4.17
218.13	4.9724	0.259	0.011	4.16
218.12	6.5770	0.247	0.010	4.16
218.13	7.9474	0.233	0.010	4.15
218.10	9.3335	0.227	0.009	4.14

T/K	p/MPa	k	$U_c(k)$	$100 \cdot \Delta k/k$
218.15	10.6208	0.249	0.010	4.14
218.17	12.1105	0.314	0.013	4.13
218.16	12.1113	0.312	0.013	4.13
243.15	1.6893	0.660	0.028	4.18
243.15	2.4474	0.490	0.020	4.16
243.16	1.6876	0.653	0.027	4.19
243.15	1.6875	0.657	0.027	4.19
243.16	3.3346	0.390	0.016	4.15
243.15	4.8916	0.330	0.014	4.15
243.15	6.5319	0.310	0.013	4.14
243.15	8.1808	0.350	0.014	4.14
243.15	9.5023	0.370	0.015	4.13
243.15	11.0250	0.399	0.016	4.12
243.15	12.4874	0.466	0.019	4.12
273.15	6.0055	0.660	0.027	4.16
273.16	7.1626	0.663	0.027	4.15
273.14	7.7872	0.655	0.027	4.14
273.16	8.5487	0.667	0.028	4.14
273.16	9.2196	0.681	0.028	4.13
273.15	9.6255	0.694	0.029	4.13
273.16	9.8197	0.707	0.029	4.13
273.16	10.0234	0.714	0.029	4.13
273.16	10.3083	0.733	0.030	4.13
288.16	6.9368	0.818	0.034	4.18
288.17	7.9394	0.820	0.034	4.16
288.17	8.2416	0.832	0.035	4.16
288.17	8.7012	0.861	0.036	4.16
288.17	9.1951	0.906	0.038	4.15
288.16	5.3268	0.797	0.034	4.21
288.17	5.8775	0.779	0.033	4.19

T/K	p/MPa	k	$U_c(k)$	$100 \cdot \Delta k/k$
288.17	6.0828	0.770	0.032	4.19

[a] Standard uncertainties (k = 1.73) are $u(T)$ = 0.006 K, $u(p)$ = 0.009 MPa.

8.3 Comparison with Thermodynamic Models

The phase behaviour of (CO_2 + CH_4 + H_2S) and (CO_2 + CO + H_2S) systems were estimated using PR-EOS with one-classical mixing rules as described in section 3.2.1. The relevant binary parameters for these systems, which are (CO_2 + CH_4), (CO_2 + CO), (CO_2 + H_2S), (CH_4 + H_2S) and (CO + H_2S), were optimized as described in section 3.2.2. The results for the (CO_2 + CH_4) and (CO_2 + CO) are presented in Tables 3.3 and 3.4.

The VLE data of the (CO_2 + H_2S) system reported by Hirata et al. [149], Ferrell et al. [150] and Chapoy et al. [66] were considered to fit the binary parameter of PR-EOS and results are shown in Table 8.1. Figure 8.1 illustrates the selected literature experimental pressure-composition data on six isotherms with temperature ranging from (258.4 to 313) K. Also plotted are the values calculated from the PR-EOS, with the optimized binary parameters presented in Table 8.5.

The VLE data of the (CH_4 + H_2S) system reported by Reamer et al. [151], Kohn and Kurata [152] and Yarym-Agaev et al. [153] were considered to fit the binary parameter of PR-EOS and results are also shown in Table 8.1. Figure 8.2 illustrates the selected literature experimental pressure-composition data on six isotherms with temperature ranging from (220 to 344.3) K. Also plotted are the values calculated from the PR-EOS, with the optimized binary parameters presented in Table 8.5.

Finally, the VLE data of the (CO + H_2S) system reported by Fredenslund and Mollerup [155] was considered to fit the binary parameter of PR-EOS and results are also shown in Table 8.1. Figure 8.3 illustrates the selected literature experimental pressure-composition data on four isotherms with temperature ranging from (203.15 to 293.15) K. Also plotted are the values calculated from the PR-EOS, with the optimized binary parameters presented in Table 8.5

The PR-EOS gives a good representation of the literature data in both vapor- and liquid-phase composition over the whole temperature range fitted, except in the critical region with slightly overestimation of the critical point.

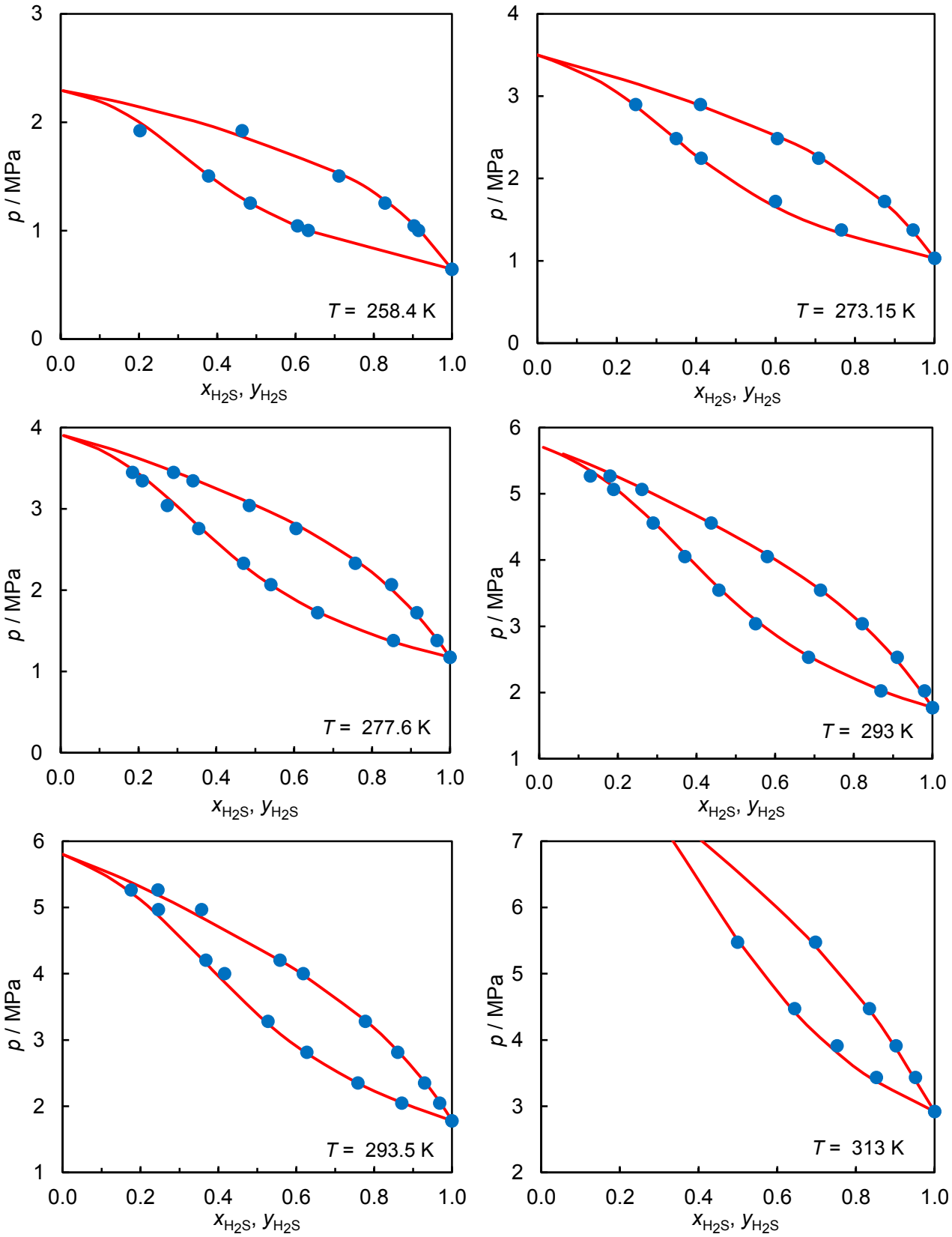


Figure 8.1 Pressure-composition diagrams of the (CO_2 + H_2S) system: ●, literature data; ----, Peng-Robinson EOS fitted with recommended binary parameters from Table 8.5.

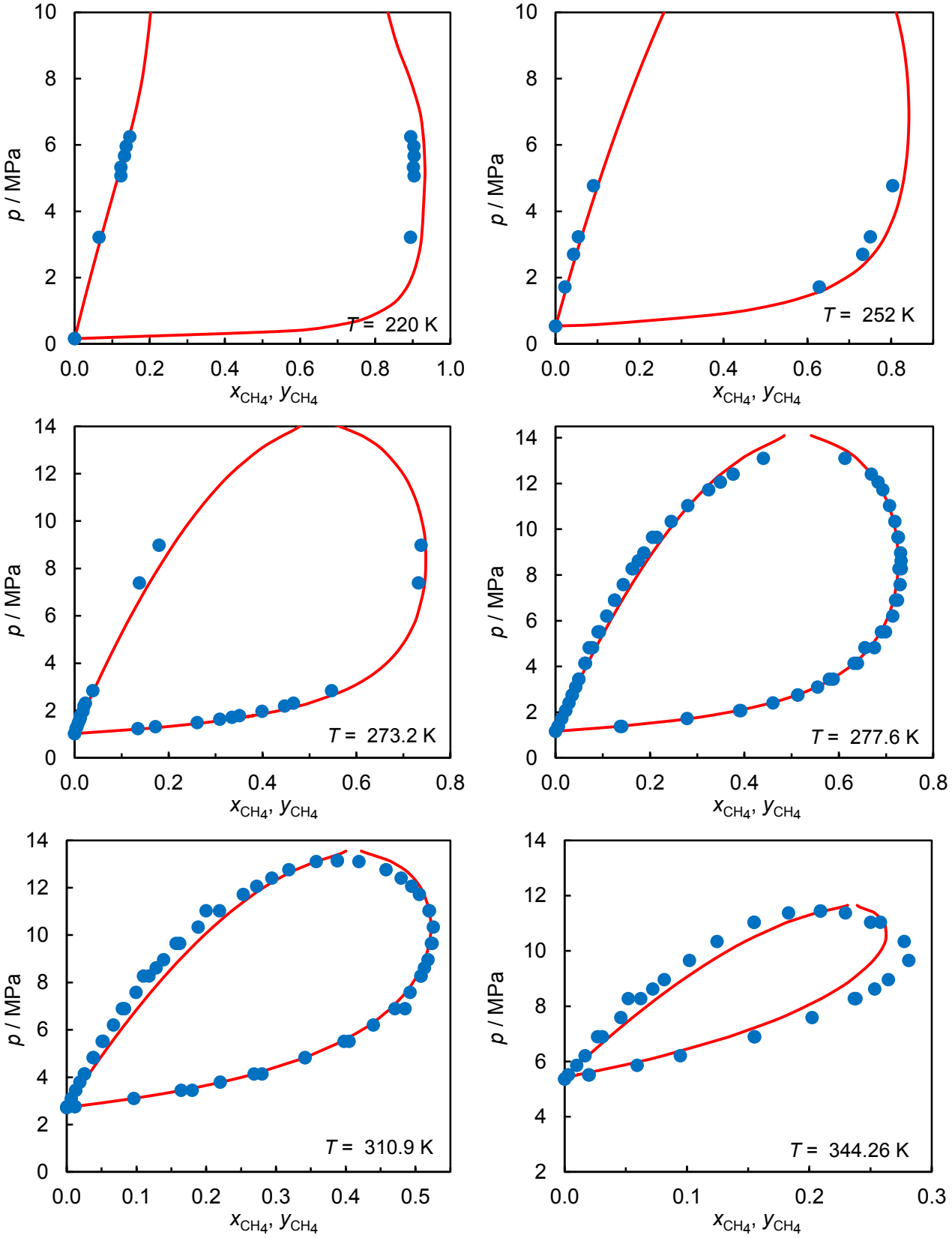


Figure 8.2 Pressure-composition diagrams of the (CH_4 + H_2S) system: ●, literature data; ----, Peng-Robinson EOS fitted with recommended binary parameters from Table 8.5.

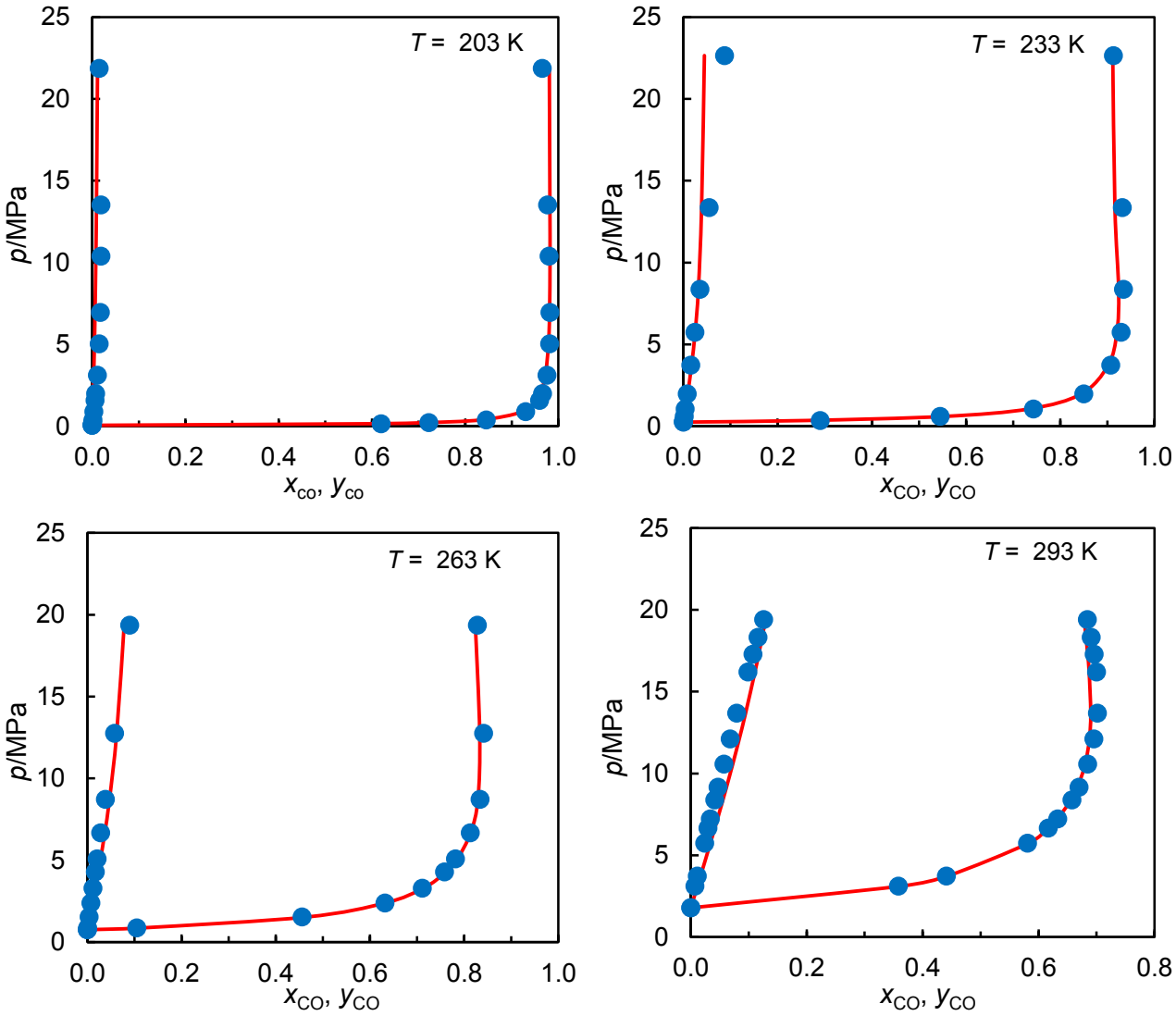


Figure 8.3 Pressure-composition diagrams of the (CO + H_2S) system: ●, literature data; ----, Peng-Robinson EOS fitted with recommended binary parameters from Table 8.5.

Table 8.5 Coefficients $k_{12,1}$ and $k_{12,2}$ and objective function S for the (CO_2 + CO) system fitted in this work.

System	Fitted range		$k_{12,0}$	$k_{12,1}$/K	l_{12}	S	Note
	T_{min}/K	T_{max}/K					
(CO_2 + H_2S)	258.4	313	0.1091	-3.2712	0.0000	0.1159	(a)
	258.4	313	0.0878	0.000	-0.0141	0.1168	
(CH_4 + H_2S)	222.2	344.3	-0.0143	22.2798	0.0000	0.0126	(a)
	222.2	344.3	0.0448	0.0000	-0.0365	0.0121	
(CO + H_2S)	203.2	293.2	0.2648	0.0000	0.0000	0.0099	(a)
	203.2	293.2	0.3199	-15.8828	0.0000	0.0098	

[a] recommended parameters.

Figure 8.4 illustrates the experimental results of the *k*-factor between liquid and vapor phases of the (CO_2 + CH_4 + H_2S) system measured for x_{H_2S} ≤ 200 ppm for four isotherms at temperatures of 218 K, 243.15 K, 273.15 K and 288.15 K and pressures up to 8 MPa. Also plotted are the values calculated from the PR-EOS, with the optimized binary parameters presented in Table 3.4, section 3.2.2, and Table 3.3. The corresponding uncertainties for each series, which was obtain as described in section 4.6, are also given in Table 8.3.

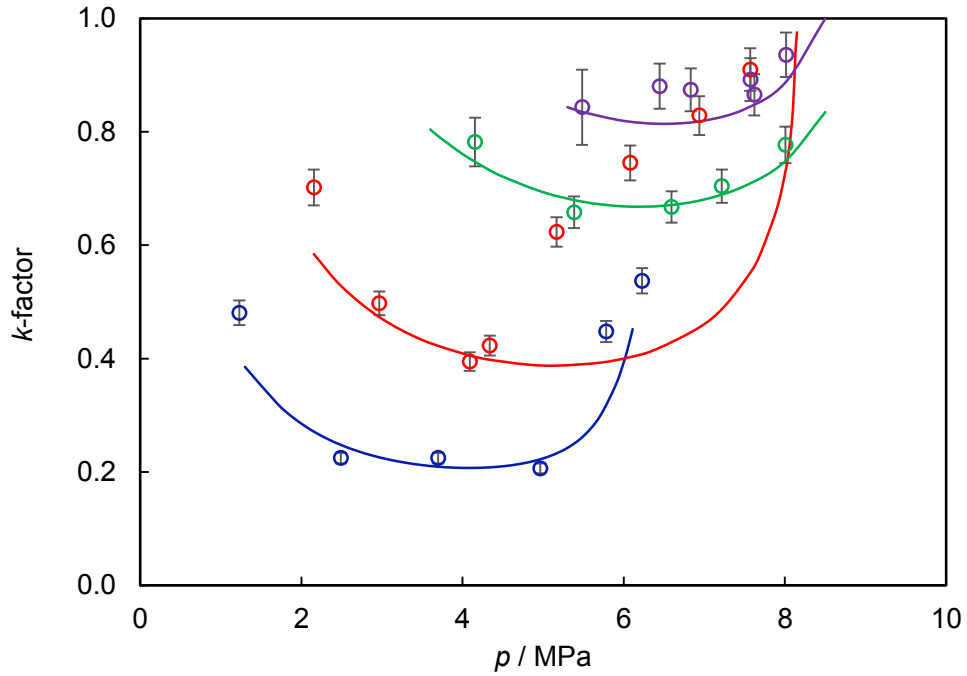


Figure 8.4 *k*-factor for H_2S: $k = (y_{H_2S}/x_{H_2S})$ measured for x_{H_2S} ≤ 200 ppm (CO_2 + CH_4 + H_2S) system: O, 218.15 K; O, 243.15 K; O, 273.15 K; O, 288.15 K; ____, Peng-Robinson EOS fitted with recommended binary parameters from Table 3.4 and Table 3.3.

The values obtained for the partition coefficient of H_2S *k* of the (CO_2 + CH_4 + H_2S) system vary from (0.2062 to 0.9359). At most temperatures measured, values of the partition coefficient of H_2S *k* first decrease with pressure until a minimum close to the retrograde region of the (CO_2 + CH_4) system than increase with pressure. A *k* value equal to 1 would be expected at the critical point. At the highest temperature measured at *T* = 288.15 K, the *k* values may not vary at the different pressures considering that the average uncertainty in the measurement is 4.2%. It is clear from the plot that there

is an increase of the partition coefficient k as usual with increase in temperature, meaning that H_2S favour the vapour phase at higher temperature.

Figure 8.5 compares the experimental k values from this work as deviations from the PR-EOS fitted with recommended binary parameters from Table 3.4 and Table 8.5 as a function of pressure and temperature. Although PR-EOG is in reasonable agreement with the measured data from temperatures of T = 273.15 K and above, namely within deviations of less than 7%, at lower temperatures the k-factor deviations exceed 45%. The PR-EOS represents the data of temperature T = 273.15 K to within ±4.5% and temperature T = 288.15 K within ±7.5%.

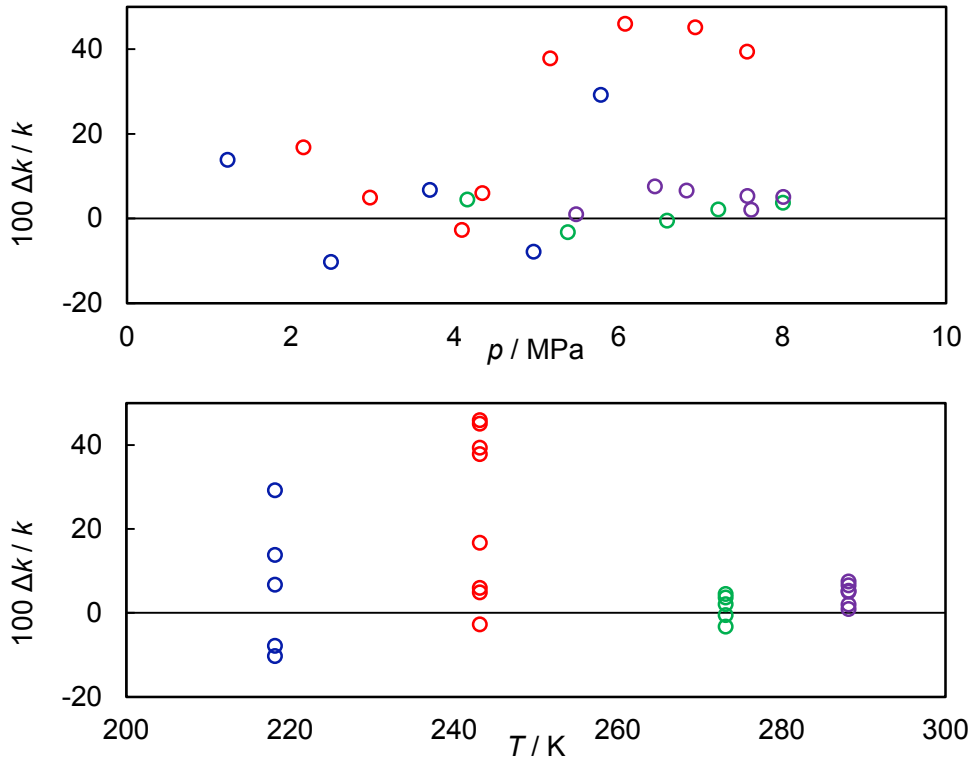


Figure 8.5 Relative deviations $\Delta k/k = (k_{exp} - k_{calc})/k_{exp}$ between the experimental H_2S distribution k_{exp} of (CO_2 + CH_4 + H_2S) and values k_{calc} calculated from the PR-EOS with the optimized binary parameters were presented as a function of pressure (top) and temperature (bottom). O, 218.15 K; O, 243.15 K; O, 273.15 K; O, 288.15 K; ___, PR-EOS fitted with recommended binary parameters from Table 3.4 and Table 3.3.

Figure 8.6 illustrates the experimental results of the k-factor between liquid and vapor phases of the (CO_2 + CO + H_2S) system measured for $x_{H_2S} \leq 200$ ppm for four isotherms at temperatures of 218 K, 243.15 K, 273.15 K and 288.15 K and pressures

up to 13 MPa. Also plotted are the values calculated from the PR-EOS, with the optimized binary parameters presented in Table 3.3, section 3.2.2, and Table 3.3. The corresponding uncertainties for each series, which was obtain as described in section 4.6, are also given in Table 8.3.

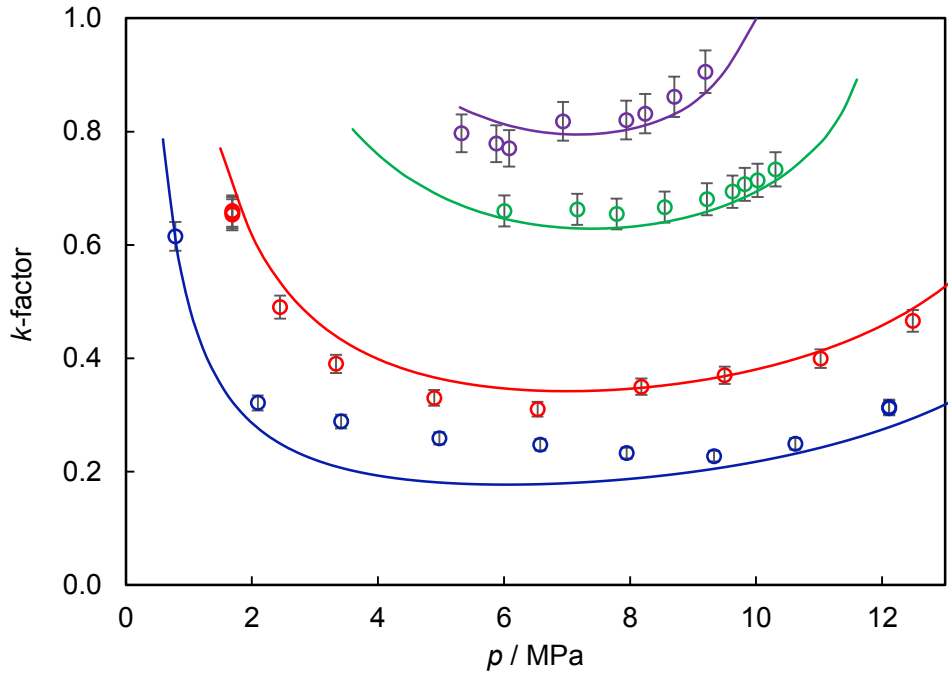


Figure 8.6 *K*-factor for H_2S: $k = (y_{H_2S}/x_{H_2S})$ measured for $x_{H_2S} \leq 200$ ppm (CO_2 + CO + H_2S) system: O, 218.15 K; O, 243.15 K; O, 273.15 K; O, 288.15 K; ____, Peng-Robinson EOS fitted with recommended binary parameters from Table 3.3 and Table 3.3.

The values obtained for the partition coefficient of H_2S *k* of the (CO_2 + CO + H_2S) system vary from (0.2271 to 0.9055). At all temperatures measured, values of the partition coefficient of H_2S *k* first decrease with pressure until a minimum close to the retrograde region of the (CO_2 + CO) system than slightly increase with pressure. A *k* value equal to 1 would be expected at the critical point. Here, as for the (CO_2 + CH_4 + H_2S) system It is clear from the plot that there is an increase of the partition coefficient *k* as usual with increase in temperature, meaning that H_2S favour the vapour phase at higher temperature.

Figure 8.7 compares the experimental *K* values from this work as deviations from the PR-EOS fitted with recommended binary parameters from Table 3.3 and Table 8.5 as a function of pressure and temperature. Although PR-EOG is in reasonable agreement with the measured data from temperatures of *T* = 273.15 K and above, namely within

deviations of less than 7%, at lower temperatures the *k*-factor deviations exceed 45%. The PR-EOS represents the data of temperature T = 273.15 K to within ±4.5% and temperature T = 288.15 K within ±7.5%.

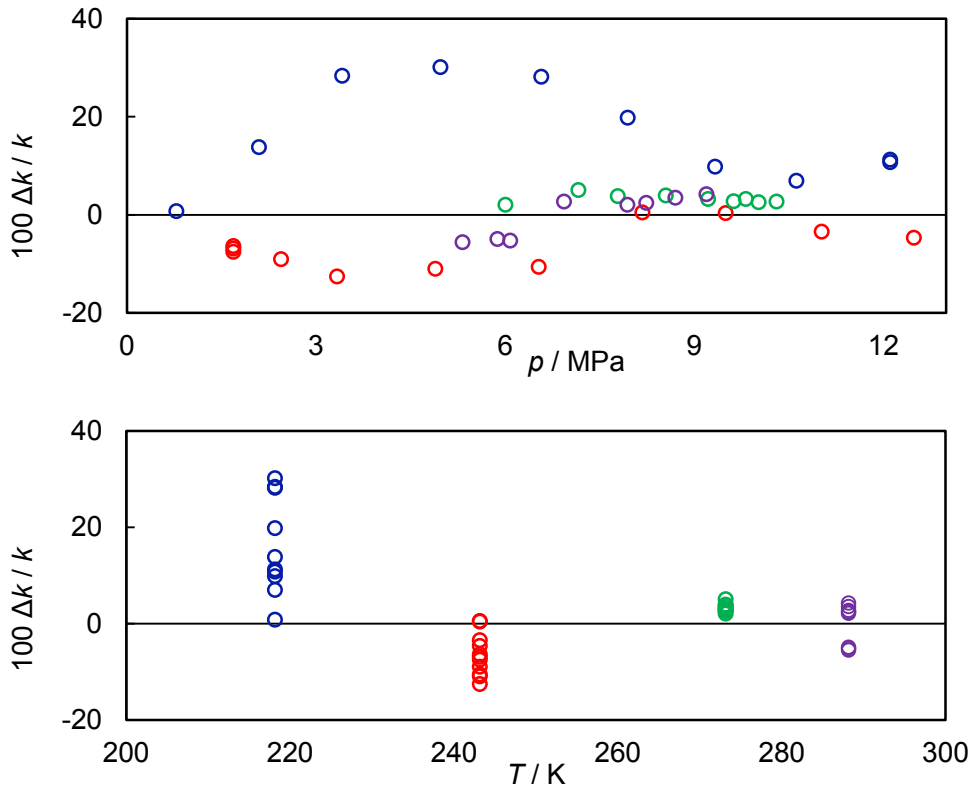


Figure 8.7 Relative deviations $\Delta k/k = (k_{exp} - k_{calc})/k_{exp}$ between the experimental H_2S distribution k_{exp} of (CO_2 + CO + H_2S) and values k_{calc} calculated from the PR-EOS with the optimized binary parameters were presented as a function of pressure (top) and temperature (bottom). O, 218.15 K; O, 243.15 K; O, 273.15 K; O, 288.15 K; ____, PR-EOS fitted with recommended binary parameters from Table 3.3 and Table 3.3.

8.4 Conclusions

New data of H_2S distribution (*k*-factor) between liquid and vapor phases of the (CO_2 + CH_4 + H_2S) and (CO_2 + CO + H_2S) systems measured for $x_{H_2S} \leq 200$ ppm were reported on four isotherms at temperatures of 218 K, 243.15 K, 273.15 K and 288.15 K and pressures up to 13 MPa. Careful evaluation of the uncertainties of the H_2S mole fraction measurements is presented, together with the expanded relative uncertainties (k = 2) in *k*-factor, which are around 4.2% for most points measured.

Comparisons between experimental data and *k*-factor calculated from the PR-EOS with the optimized binary parameters were presented.

Chapter 9 Conclusions and Recommendations for Future Work

9.1 Conclusions

In this work, the goal was to fill important gaps on VLE and homogeneous density relating to the thermodynamic properties of mixtures of CO_2 with substances relevant to pre-combustion CO_2 capture and pipeline transportation. This knowledge can ultimately lead to feasible design, optimization and safe operation of a wide range of high-pressure processes involving CO_2, in particular, processes such as separation of gas mixtures and pipeline transportation of CO_2-rich mixtures in CCS processes.

The thermodynamic study of this work involved experimental measurements of low-temperature and high-pressure VLE and high- pressure density of mixtures containing CO_2 and other components present as impurities in pre-combustion CO_2 capture processes. The VLE experimental work was carried out using a state-of-the-art computer-controlled apparatus in a wide temperature range from T = (218.15 to 303) K and pressures up to 15 MPa. The density work was carried out using a vibrating-tube densimeter (Anton-Paar model DMA HP) combined with a piston-driven pump (Teledyne Isco Series D single-pump, 100DM) from temperatures between (283.15 to 373.15) K and pressures up to 50 MPa. The temperature and pressure conditions of the VLE and density measurements were extended to higher conditions than typical processes in the pre-combustion CO_2 capture and pipeline transportation, useful in the development of new EOS as shown in Chapter 6. Data points at high temperature and pressure conditions, especially on density measurements, were extremely helpful in the development of the new mixture model for the (CO_2 + CO) based on the multi-fluid Helmholtz-energy approach. In fact, it was noted when the extrapolation behaviour of the new mixture model was carried out (see section 6.4) that the data measured at high pressures helped to define the shape of the new mixture model at extrapolated conditions.

The VLE data measured (CO_2 + CH_4) and (CO_2 + CO) systems were also used to fit the PR-EOS with one-classical mixing rule, which means to up to three adjustable parameters per binary mixture: $k_{ij,0}$, $k_{ij,1}$ and l_{ij}. As shown in chapter 3, no improvement

on the EOS was gain with the use of l_{ij}. In fact, the recommend parameters for both models are a single $k_{ij,0}$ without temperature dependence. However, in previous work from our group, Fandiño et al. [54] fitted the same three adjustable parameters for (CO_2 + H_2) and (CO_2 + N_2) systems in which better description of the experimental data was seen with the use of l_{ij}.

When assessing the (CO_2 + CO) system, among the Helmholtz-energy explicit mixture models used in this work, the new mixture model presented considerable improvement in the description of phase behaviour and density. The new mixture model combines the mathematical approach of the GERG-2008 and EOS-CG models with refitted reducing parameters - $\beta_{T,ij}$, $\beta_{v,ij}$, $\gamma_{T,ij}$ and $\gamma_{v,ij}$, and a new binary-specific departure function. As a result, the new mixture model is significantly more accurate in describing the thermodynamic properties of the (CO_2 + CO) mixture than the GERG-2008 and the EOS-CG models. The new model has been already implemented in the software package REFPROP (version 10) [87].

While SAFT-γ Mie with original values presented an reasonably good description of the (CO_2 + CH_4) system, it presented deviations on the prediction of the (CO_2 + CO) system. Further improvement of the two adjustable parameters: ε_{kl} and $\lambda^r_{kl,}$ was attempted for both systems. The results showed no improvement in the fitting for the (CO_2 + CH_4) system. The SAFT-γ Mie fitted for the (CO_2 + CO) system exhibited a considerable improvement on the description of measurements on the dew point curve but larger deviations along the bubble curve, even at low pressures. It is likely that further improvement could be achieved with more intense optimization of the parameters.

The distribution of H_2S between the liquid and gas phases depends on the VLE systems studied: (CO_2 + CH_4 + H_2S) and (CO_2 + CO + H_2S), are reasonably represented by PR-EOS with fitted binary parameters from this work. Most experimental points were described by the PR-EOS within the uncertainty of the experimental measurements of around 4.2%.

9.2 Contribution of This Work

The experimental data will be used to optimise parameters in suitable thermodynamic models for the mixtures investigated.

This work has provided a significant step forward in filling important gaps on VLE and homogeneous density relating to the thermodynamic properties of mixtures of CO_2 with substances relevant to pre-combustion CO_2 capture and pipeline transportation. The collected experimental data and derived parameters of thermodynamic models offer valuable inputs to process design and optimization concerning field of gas separation and transportation, and for potential uses in flue gas applications. The main outputs from this research are as follows:

- New and low-uncertainty experimental VLE data for the (CO_2 + CO) system along seven isotherms spanning almost the entire region of vapor-liquid coexistence at temperatures from (218.15 to 302.98) K and pressures up to 9 MPa.
- New density data for the (CO_2 + CO) system along seven isotherms, at temperatures from (283 to 373) K, and pressures up to 48 MPa for four different mixtures, with compositions ranging from (5 to 50) mol% CO.
- New and low-uncertainty experimental VLE data for the (CO_2 + CH_4) system along seven isotherms spanning almost the entire region of vapor-liquid coexistence at temperatures from (218.15 to 303.15) K and pressures up to 9 MPa.
- New data of H_2S distribution (*k*-factor) between liquid and vapor phases of (CO_2 + CH_4 + H_2S) and (CO_2 + CO + H_2S) systems measured for $x_{H_2S} \leq 200$ ppm on four isotherms at temperatures of 218 K, 243.15 K, 273.15 K and 288.15 K and pressures up to 13 MPa.
- Critical points of both systems: (CO_2 + CO) and (CO_2 + CH_4) were estimated from the experimental data by means of analysis with the asymptotic behaviour approaching the critical point.
- New fitted parameters for PR-EOS with van der Waals mixing rules for (CO_2 + CO) and (CO_2 + CH_4) systems.
- New mixture model for the (CO_2 + CO) system. The VLE data of the (CO_2 + CO) system from this work, published by Souza et al. [24], together with the densities measured in this work were used to develop an improved Helmholtz-energy-explicit mixture model. This work was develop in collaboration with Ruhr-Universität Bochum and the new model has been already implemented in the software package REFPROP (version 10) [87].

9.3 Recommendation for Future Work

9.3.1 Further Experimental Investigations

This work was focused on the measurement of VLE of relevant systems in pre-combustion CO_2 capture and pipeline transportation, mainly the (CO_2 + diluent), in which the diluents of interest are H_2, N_2, CH_4, CO, Ar, O_2 and H_2S. Results from this work, together with previous work by Fandiño et al. [54], [75, 160-162] and Chapoy et al. [66] have filled this gap in the literature. Nevertheless, other reliable and accurate experimental thermodynamic properties such as density and speed of sound are important in order to adjust the interaction parameters in EOS.

The remaining gaps in the binary systems relevant to pre-combustion CO_2 capture and pipeline transportation include:

- New VLE for binary systems comprised of the major and minor components of the pre-combustion CO_2 capture: H_2, N_2, CH_4, CO, Ar, O_2 and H_2S. It is worth mentioned that the existing phase enveloped for most of this systems would involve extremely low-temperatures, below the capability of our equipment.
- New density data for most binary systems. Even the systems with available density data, such as (CO_2 + CH_4), (CO_2 + N_2) and (CO_2 + H_2) could benefit from new data, especially at high pressure and different concentrations.
- New speed of sound for most binary systems. Experimental speed-of-sound data relevant to the CCS processes in general are scarce. Perhaps, except for the (CO_2 + Ar) system. Nevertheless, these data are extremely valuable for the fitting process of the Helmholtz-energy explicit mixture models.; that is because speed of sound are included in various derivatives of the Helmholtz-energy function.
- Besides, further investigation on the distribution of H_2S between the liquid and gas phases depends on other relevant VLE systems, such as (CO_2 + H_2 + H_2S) and (CO + H_2 + H_2S).

There are also many remaining gaps in the binary systems relevant to different CO_2 capture technologies, with possible impurities including SO_2, H_2O and Amines (MEA or DEA). For example, while there are reasonable density data available for the (SO_2

+ CO_2) system, the VLE data could be much improved. In fact, the only reliable values on this system come from the work of Lachet et al. [163] and comprises of two isotherms 263 K and 333 K. Binary systems comprised of (H_2O + diluent) are extremely hard to measured due to the low solubility of the diluent in H_2O and the H_2O in the diluent.

As CO_2 separation with amine (solvent) is the most well-established of the methods available for CO_2 capture. It presents the advantage of achieving high rates of CO_2 recovery, up to 98%, and also high purity product, over 99%. However, the amount of energy required for regeneration and the degradation rate of most solvents used in oxidising environment are limitations to be concerned.

New measurements of the ternary system (CO_2 + H_2O + Amines) is important for CCS separation process as CO_2 separation with amine (solvent) is the most well-established of the methods available for CO_2 capture. Binary systems such as (CO_2 + H_2O), (H_2O + MEA) and (H_2O + DEA) are fundamental to describe this ternary system. While the (CO_2 + H_2O) system had enough experimental data for a fully development of the EOS-CG by Gernert [58, 80], (H_2O + MEA) and (H_2O + DEA) present no enough data and only had the reducing parameters - $\beta_{T,ij}$, $\beta_{v,ij}$, $\gamma_{T,ij}$ and $\gamma_{v,ij}$ fitted by Ruhr-Universität Bochum (data unpublished). Unfortunately, there is the need for both density and VLE measurements of (CO_2 + MEA) and (CO_2 + DEA) systems. This system present an additional challenge as reactions can happen depending on the temperature and pressure conditions studied.

9.3.2 Further Apparatus Improvements

VLE apparatus

The current low-temperature and high-pressure VLE apparatus was carefully designed to measure bubble and dew points of (CO_2 + diluent), with possible diluents of interest are H_2, N_2, CH_4, CO, Ar, O_2, H_2S (the last in small concentration). As a result, the apparatus is capable of performing measurements at wide ranges of temperature, pressure and phase composition and include the critical region of most systems. A limitation of the current apparatus is the lack of compressor to introduce liquid or gas at high pressure. The current experimental procedure relays on the secondary gas cylinder to be at high pressure to increase the equilibrium cell pressure

and does not allow the introduction of liquids. So, a pump or compressor would allowed for the introduction of liquid or liquefied gases.

Density Apparatus

The current status of the density apparatus used in this work is satisfactory for the measurement of pure or mixtures of liquefied gases and liquids. However, the improvement of the data acquisition would decrease the amount of time needed to collect the data from the operator. For that, both the VTD DMA HP and the ISCO pump need to be linked to a dataflow programming software (implemented in Keysight VEE), similarly to the VLE apparatus, thereby permitting full automation of the measurements.

References

[1] Climate change 2014: contribution of working groups I, II and III to the fifth assessment report of the intergovernmental panel on climate change. Intergov Panel Climate Change. 2014.

[2] IPCC. Climate Change 2007: Impacts, Adaptation and Vulnerability. Cambridge University Press2007.

[3] NOAA. Earth System Research Laboratory, Global Monitoring Division.

[4] COP21 Paris Agreement, European Commission.

[5] Energy Technology Prospectives, Scenarios and Strategies to 2050. In: IEA IEA-, editor.2008.

[6] Organisation for Economic Co-Operation Development, Energy Technology Perspectives 2017: Catalysing Energy Technology Transformations: OECD; 2017.

[7] Shell Energy Scenarios to 2050. 2018.

[8] CO_2 Capture Technologies Pre-combustion Capture. Global CCS Institute; 2012.

[9] Bui M, Adjiman CS, Bardow A, Anthony EJ, Boston A, Brown S, et al. Carbon capture and storage (CCS): the way forward. Energy & Environmental Science. 2018;11:1062-176.

[10] EU Zero Emissions Platform, The costs of CO_2 capture, transport and storage. 2011.

[11] Mohammed A-J, Adam W. Realistic Costs of Carbon Capture'. Discussion Paper 2009-08. Energy Technology Innovation Research Group, Belfer Center for Science and International Affairs,. 2009.

[12] Maitland GC. Carbon capture and storage: The way ahead. Sustainable Technologies, Systems & Policies. 2012:9.

[13] Kunz O, Klimeck R, Wagner W, Jaeschke M. The GERG-2004 Wide-Range Equation of State for Natural Gases and Other Mixtures. GERG TM15. 2007.

[14] de Visser E, Hendriks C, Barrio M, Mølnvik MJ, de Koeijer G, Liljemark S, et al. Dynamis CO_2 quality recommendations. International Journal of Greenhouse Gas Control. 2008;2:478-84.

[15] Li H, Jakobsen JP, Wilhelmsen Ø, Yan J. PVTxy properties of CO_2 mixtures relevant for CO_2 capture, transport and storage: Review of available experimental data and theoretical models. Applied Energy. 2011;88:3567-79.

[16] Munkejord ST, Hammer M, Løvseth SW. CO_2 transport: Data and models – A review. Applied Energy. 2016;169:499-523.

[17] Porter RTJ, Fairweather M, Pourkashanian M, Woolley RM. The range and level of impurities in CO_2 streams from different carbon capture sources. International Journal of Greenhouse Gas Control. 2015;36:161-74.

[18] Tan Y, Nookuea W, Li H, Thorin E, Zhao L, Yan J. Property Impacts on Performance of CO_2 Pipeline Transport. Energy Procedia. 2015;75:2261-7.

[19] Lovseth SW, Skaugen G, Jacob Stang HG, Jakobsen JP, Wilhelmsen Ø, Span R, et al. CO_2Mix Project: Experimental Determination of Thermo Physical Properties of CO_2-Rich Mixtures. Energy Procedia. 2013;37:2888-96.

[20] Tan Y, Nookuea W, Li H, Thorin E, Yan J. Property impacts on Carbon Capture and Storage (CCS) processes: A review. Energy Conversion and Management. 2016;118:204-22.

[21] Blanco ST, Rivas C, Bravo R, Fernandez J, Artal M, Velasco I. Discussion of the influence of CO and CH_4 in CO_2 transport, injection, and storage for CCS technology. Environ Sci Technol. 2014;48:10984-92.

[22] Ahmad M, Gernert J, Wilbers E. Effect of impurities in captured CO_2 on liquid–vapor equilibrium. Fluid Phase Equilibria. 2014;363:149-55.

[23] Chapoy A, Nazeri M, Kapateh M, Burgass R, Coquelet C, Tohidi B. Effect of impurities on thermophysical properties and phase behaviour of a CO_2-rich system in CCS. International Journal of Greenhouse Gas Control. 2013;19:92-100.

[24] Peng D-Y, Robinson DB. A new two-constant equation of state. Ind Eng Chem Fundamentals. 1976;15:59−64.

[25] Kontogeorgis GM, Voutsas EC, Yakoumis IV, Tassios DP. An Equation of State for Associating Fluids. Ind Eng Chem Res 1996;35:4310-8.

[26] Kunz O, Wagner W. The GERG-2008 Wide-Range Equation of State for Natural Gases and Other Mixtures: An Expansion of GERG-2004. Journal of Chemical & Engineering Data. 2012;57:3032-91.

[27] Span R. Multivariate Equations of State: An Accurate Source of Thermodynamic Property Data. Berlin-Heidelberg, Germany: Springer 2000.

[28] Span R, Wagner W, Lemmon EW, Jacobsen RT. Multiparameter equations of state — recent trends and future challenges. Fluid Phase Equilibria 183. 2001;183–184: 1–20.

[29] Papaioannou V, Lafitte T, Avendaño C, Adjiman CS, Jackson G, Müller EA, et al. Group contribution methodology based on the statistical associating fluid theory for heteronuclear molecules formed from Mie segments. J Chem Phys. 2014;140:054107.

[30] Papaioannou V, Calado F, Lafitte T, Dufal S, Sadeqzadeh M, Jackson G, et al. Application of the SAFT-γ Mie group contribution equation of state to fluids of relevance to the oil and gas industry. Fluid Phase Equilibria. 2016;416:104-19.

[31] Mac Dowell N, Fennell PS, Shah N, Maitland GC. The role of CO2 capture and utilization in mitigating climate change. Nature Climate Change. 2017;7:243-9.

[32] Jackson SR, Corden C, Howells PW. Process and apparatus for the separtion of carbon dioxide and hydrogen. In: Application UP, editor. Uk Patent Application2011.

[33] Trusler JPM. Thermophysical Properties and Phase Behavior of Fluids for Application in Carbon Capture and Storage Processes. Annual review of chemical and biomolecular engineering. 2017;8:381-402.

[34] Mansouri Majoumerd M, De S, Assadi M, Breuhaus P. An EU initiative for future generation of IGCC power plants using hydrogen-rich syngas: Simulation results for the baseline configuration. Applied Energy. 2012;99:280-90.

[35] Chen S, Xiang W, Wang D, Xue Z. Incorporating IGCC and CaO sorption-enhanced process for power generation with CO_2 capture. Applied Energy. 2012;95:285-94.

[36] Kunze C, Spliethoff H. Assessment of oxy-fuel, pre- and post-combustion-based carbon capture for future IGCC plants. Applied Energy. 2012;94:109-16.

[37] Jansen D, Gazzani M, Manzolini G, Dijk Ev, Carbo M. Pre-combustion CO_2 capture. International Journal of Greenhouse Gas Control. 2015;40:167-87.

[38] Sudiro M, Bertucco A, Ruggeri F, Fontana M. Improving process performances in coal gasification for power and synfuel production. Energy Fuels. 2008;22:3894–901.

[39] Huh C, Cho M-I, Hong S, Kang S-G. Effect of Impurities on Depressurization of CO_2 Pipeline Transport. Energy Procedia. 2014;63:2583-8.

[40] Wang Z, Fang M, Pan Y, Yan S, Luo Z. Amine-based absorbents selection for CO_2 membrane vacuum regeneration technology by combined absorption–desorption analysis. Chemical Engineering Science. 2013;93:238-49.

[41] Diamantonis NI, Boulougouris GC, Mansoor E, Tsangaris DM, Economou IG. Evaluation of Cubic, SAFT, and PC-SAFT Equations of State for the Vapor–Liquid Equilibrium Modeling of CO2Mixtures with Other Gases. Industrial & Engineering Chemistry Research. 2013:130227083947003.

[42] Scholes CA, Smith KH, Kentish SE, Stevens GW. CO_2 capture from pre-combustion processes—Strategies for membrane gas separation. International Journal of Greenhouse Gas Control. 2010;4:739-55.

[43] Coquelet C, Stringari P, Hajiw M, Gonzalez A, Pereira L, Nazeri M, et al. Transport of CO 2 : Presentation of New Thermophysical Property Measurements and Phase Diagrams. Energy Procedia. 2017;114:6844-59.

[44] Coquelet C, Valtz A, Arpentinier P. Thermodynamic study of binary and ternary systems containing CO_2+impurities in the context of CO_2 transportation. Fluid Phase Equilibria. 2014;382:205-11.

[45] Zhang ZX, Wang GX, P M, V. R. Optimization of pipeline transport for CO_2 sequestration. . Energy Convers Manag 2006;47:702–15.

[46] JW J, JJ N, KG. K. Reactive Transport Modelling of CO_2 Storage in Saline Aquifers to Elucidate Fundamental Processes, Trapping Mechanisms and Sequestration Partitioning. . Geol Soc Lond. 2004.

[47] Institute GC. CO2 Capture Technologies - Pre combustion capture. Global CCS Institute; 2012.

[48] Carbon Dioxide Capture and Storage. Intergovernmental Panel on Climate Change (IPCC); 2005.

[49] Martynov SB, Daud NK, Mahgerefteh H, Brown S, Porter RTJ. Impact of stream impurities on compressor power requirements for CO_2 pipeline transportation. International Journal of Greenhouse Gas Control. 2016;54:652-61.

[50] Najafi-Marghmaleki A, Barati-Harooni A, Mohammadi AH. Impact of gas impurities on CO 2 mole fraction: Application in carbon capture and storage (CCS) processes. International Journal of Greenhouse Gas Control. 2017;57:173-84.

[51] Pipitone G, Bolland O. Power generation with CO2 capture: Technology for CO2 purification. International Journal of Greenhouse Gas Control. 2009;3:528-34.

[52] EC. Implementation of Directive 2009/31/EC on the Geological Storage of Carbon Dioxide Guidance Document 2: Characterisation of the Storage Complex, CO_2 Stream-Composition, Monitoring and Corrective Measures. 2011.

[53] Kather A, Kownatzki S. Assessment of the different parameters affecting the CO_2 purity from coal fired oxyfuel process. Int J Greenh Gas Control. 2011;55:S204–S9.

[54] Fandiño O, Trusler JPM, Vega-Maza D. Phase behavior of (CO_2+H_2) and (CO_2+N_2) at temperatures between (218.15 and 303.15)K at pressures up to 15MPa. International Journal of Greenhouse Gas Control. 2015;36:78-92.

[55] Span R, Wagner W. On the Extrapolation Behavior of Empirical Equations of State. International Journal of Thermophysics. 1997;18.

[56] Lemmon EW, Jacobsen RT. A New Functional Form and New Fitting Techniques for Equations of State with Application to Pentafluoroethane (HFC-125). Journal of Physical and Chemical Reference Data. 2005;34:69-108.

[57] Scott RL, van Konynenburg PH. Static properties of solutions. Van der Waals and related models for hydrocarbon mixtures. Discussions of the Faraday Society. 1970;49:87-97.

[58] Gernert J, Span R. EOS–CG: A Helmholtz energy mixture model for humid gases and CCS mixtures. The Journal of Chemical Thermodynamics. 2016;93:274-93.

[59] van der Waals JD. On the continuity of the gas and liquid state [PhD]. The Netherlands, Leiden1873.

[60] (11) Soave GEcfaMR, Kwong Equation of State. Chem. Eng. Sci. 1972, 1197−1203.

[61] Valderrama JO. The State of the Cubic Equations of State. Industrial & Engineering Chemistry Research. 2003;42:1603-18.

[62] Redlich O, Kwong JNS. On the Thermodynamics of Solutions. V. An Equation of State. Fugacities of Gaseous Solutions. Chemical Reviews. 1949;44:233-44.

[63] Patel NC, Teja AS. A new cubic equation of state for fluids and fluid mixtures. Chemical Engineering Science. 1982;37:463-73.

[64] Lopez-Echeverry JS, Reif-Acherman S, Araujo-Lopez E. Peng-Robinson equation of state: 40 years through cubics. Fluid Phase Equilibria. 2017;447:39-71.

[65] Paul M. Mathias TWC. Extension of the Peng-Robinson equation of state to complex mixtures: Evaluation of the various forms of the local composition concept. Fluid Phase Equilibria. 1983;13:91-108.

[66] Chapoy A, Coquelet C, Liu H, Valtz A, Tohidi B. Vapour–liquid equilibrium data for the hydrogen sulphide (H2S)+carbon dioxide (CO2) system at temperatures from 258 to 313K. Fluid Phase Equilibria. 2013;356:223-8.

[67] van der Waals JD. Continuity of the Gaseous and liquid state of mater. 1873.

[68] Kwak TY, Mansoori GA. Van der waals mixing rules for cubic equations of state. Applications for supercritical fluid extraction modelling. Chemical Engineering Science. 1986;41:1303-9.

[69] Jaubert J-N, Mutelet F. VLE predictions with the Peng–Robinson equation of state and temperature dependent kij calculated through a group contribution method. Fluid Phase Equilibria. 2004;224:285-304.

[70] Span R, Wagner W. A New Equation of State for Carbon Dioxide Covering the Fluid Region from the Triple-Point Temperature to 1100 K at Pressures up to 800 MPa. Journal of Physical and Chemical Reference Data. 1996;25:1509.

[71] U. Setzmann WW. A New Equation of State and Tables of Thermodynamic Properties for Methane Covering the Range from the Melting Line to 625 K at Pressures up to 1000 MPa. The Journal of Physical and Chemical Reference Data. 1991;20: 1061-155.

[72] Lemmon EW, Span R. Short Fundamental Equations of State for 20 Industrial Fluids. Journal of Chemical & Engineering Data. 2006;51:785-850.

[73] Gernert J, Jäger A, Span R. Calculation of phase equilibria for multi-component mixtures using highly accurate Helmholtz energy equations of state. Fluid Phase Equilibria. 2014;375:209-18.

[74] Span R, Gernert J, Jäger A. Accurate Thermodynamic - Property Models for CO_2-Rich Mixtures. Energy Procedia. 2013;37:2914-22.

[75] Westman SF, Austegard A, Stang HGJ, Løvseth SW. Vapor-liquid equilibrium data for the carbon dioxide and carbon monoxide (CO_2 + CO) system at the temperatures 253, 273, 283 and 298 K and pressures up to 13 MPa. Fluid Phase Equilibria. 2018;473:37-49.

[76] Souza LFS, Al Ghafri SZS, Trusler JPM. Measurement and modelling of the vapor–liquid equilibrium of (CO_2 + CO) at temperatures between (218.15 and 302.93) K at pressures up to 15 MPa. The Journal of Chemical Thermodynamics. 2018;126:63-73.

[77] Tsankova G, Richter M, Stanwix P, May EF. Densities and dielectric permittivities for (carbon monoxide + carbon dioxide) mixtures determined with a microwave re-entrant cavity resonator. The Journal of Chemical Thermodynamics. 2019.

[78] I.H. Bell KG, J. Wu, and E.W. Lemmon. A Helmholtz energy equation of state for ammonia/water. Journal of Physical and Chemical Reference Data. 2018.

[79] Lemmon EW. Latest Techniques of using constraints to fit equations of state.

[80] Gernert GJ. A New Helmholtz Energy Model for Humid Gases and CCS Mixtures. [Ph.D.]: Ruhr-Universitat Bochum; 2013.

[81] Christiansen LJ, Fredenslund A, Gardner N. Gas-Liquid Equilibria of the CO_2-CO and CO_2-CH_4-CO Systems. Adv Cryog Eng. 1974;19:309-19.

[82] Huamin S. Solubility of Carbon Monoxide in Methanol and Carbon Dioxide under High Pressure. Huaxue Gongcheng China. 1991;19:61-9.

[83] Kaminishi GI, Arai Y, Saito S, Maeda S. Vapor-Liquid Equilibria for Binary and Ternary Systems Containing Carbon Dioxide. J Chem Eng Jpn. 1968;1:109-16.

[84] Cipollina A, Anselmo R, Scialdone O, Filardo G, Galia A. Experimental P-T-G Measurements of Supercritical Mixtures of Carbon Dioxide, Carbon Monoxide, and Hydrogen and Semiquantitative Estimation of Their Solvent Power Using the Solubility Parameter Concept. J Chem Eng Data. 2007; 52:2291-7.

[85] Mallu BVN, G.; Viswantah, D. S. Compression Factors and Second Virial Coefficients of CO_2, CO, and {xCO+(1-x)CO_2}. Journal of Chemical Thermodynamics. 1987;19:549–54.

[86] B.V.Mallu GN, D.S.Viswanath. (p, Vm, T, x) and virial coefficients of {xCO_2 + (1 − x)CO}. Journal of Chemical Thermodynamics. 1989;21:989-96.

[87] Lemmon EW, Bell IH, Huber ML, McLinden MO. NIST Standard Reference Database 23: Reference Fluid Thermodynamic and Transport Properties-REFPROP, Version 10.0, National Institute of Standards and Technology. Standard Reference Data Program. 2018.

[88] R. Span TE, S. Herrig, S. Hielscher, A. Jäger, M. Thol. TREND. Thermodynamic Reference and Engineering Data 3.0, Lehrstuhl für Thermodynamik, Ruhr-Universität Bochum. 2016.

[89] Chapman WG, Gubbins KE, Jackson G, Radosz M. SAFT: Equation-of-state solution model for associating fluids. Fluid Phase Equilibria. 1989;52:31-8.

[90] Wertheim MS. Fluids with highly directional attractive forces. I. Statistical thermodynamics. J Stat Phys. 1984;35:19-34.

[91] Wertheim MS. Fluids with highly directional attractive forces. II. Thermodynamic perturbation theory and integral equations. . J Stat Phys. 1984;35:35-47.

[92] Wertheim MS. Fluids with highly directional attractive forces. III. Multiple attraction sites. J Stat Phys. 1986;42:459-76.

[93] Wertheim MS. Fluids with highly directional attractive forces. IV. Equilibrium polymerization. J Stat Phys. 1986;42:477-92.

[94] Wertheim MS. Thermodynamic perturbation theory of polymerization. J Chem Phys. 1987;87:7323-31.

[95] Adidharma H, Radosz M. Square-well SAFT equation of state for homopolymeric and heteropolymeric fluids. Fluid Phase Equilibria. 1999;158-160:165-74.

[96] McCabe C, Gil-Villegas A, Jackson G, Río Fd. The thermodynamics of heteronuclear molecules formed from bonded square-well (BSW) segments using the SAFT-VR approach. Molecular Physics. 1999;97:551-8.

[97] Felipe J B, Lourdes F V. Thermodynamic behaviour of homonuclear and heteronuclear Lennard-Jones chains with association sites from simulation and theory. Molecular Physics. 1997;92:135-50.

[98] Gil-Villegas A, Galindo A, Whitehead P, Mills S, Jackson G, Burgess A. Statistical associating fluid theory for chain molecules with attractive potentials of variable range. The Journal of Chemical Physics. 1997;106:4168-86.

[99] Kontogeorgis GM. Thermodynamic models for industrial applications : from classical and advanced mixing rules to association theories. Chichester: Wiley; 2010.

[100] Müller EA, Gubbins KE. Molecular-Based Equations of State for Associating Fluids: A Review of SAFT and Related Approaches. Industrial & Engineering Chemistry Research. 2001;40:2193-211.

[101] McCabe C, Galindo A. Chapter 8 - SAFT Associating Fluids and Fluid Mixtures. Applied Thermodynamics of Fluids: The Royal Society of Chemistry; 2010. p. 215-79.

[102] Liu S, Zhang Y, Chi Y, Song Y, Yang M, Liu Y, et al. Density characteristics of CO_2–CH_4 binary mixtures at temperatures from (300 to 308.15)K and pressures from (2 to 18)MPa. The Journal of Chemical Thermodynamics. 2017;106:1-9.

[103] Lorentz HA. Ueber die Anwendung des Satzes vom Virial in der kinetischen Theorie der Gase. Annalen der Physik. 1881;248:127-36.

[104] Al Ghafri SZ, Forte E, Maitland GC, Rodriguez-Henríquez JJ, Trusler JPM. Experimental and modeling study of the phase behavior of (methane + CO_2 + water) mixtures. J Phys Chem B. 2014;118:14461-78.

[105] Sanchez-Vicente Y, Tay WJ, Al Ghafri SZ, Trusler JPM. Thermodynamics of carbon dioxide-hydrocarbon systems. Applied Energy. 2018;220:629-42.

[106] Process Systems Enterprise g. 1997-2018.

[107] JCGM. Evaluation of measurement data - Guide to the expression of of uncertainty in measurement - JCGM 100:2008. 2008.

[108] Nasir Q, Sabil KM, Lau KK. Measurement of isothermal (vapor + liquid) equilibria, (VLE) for binary (CH 4 + CO 2) from T = (240.35 to 293.15) K and CO 2 rich synthetic natural gas systems from T = (248.15 to 279.15) K. Journal of Natural Gas Science and Engineering. 2015;27:158-67.

[109] Richter M, Kleinrahm R, Lentner R, Span R. Development of a special single-sinker densimeter for cryogenic liquid mixtures and first results for a liquefied natural gas (LNG). The Journal of Chemical Thermodynamics. 2016;93:205-21.

[110] Lentner R, Richter M, Kleinrahm R, Span R. Density measurements of liquefied natural gas (LNG) over the temperature range from (105 to 135) K at pressures up to 8.9 MPa. The Journal of Chemical Thermodynamics. 2017;112:68-76.

[111] Tay WJ, Trusler JPM. Density, Sound Speed and Derived Thermophysical Properties of n-Nonane at Temperatures Between (283.15 and 473.15) K and at Pressures up to 390 MPa. J Chem Thermodynamics. 2018.

[112] McLinden MO, Splett JD. A Liquid Density Standard Over Wide Ranges of Temperature and Pressure Based on Toluene. J Res Natl Inst Stand Technol 2008;113:29-67.

[113] Li H, Jakobsen JP, Wilhelmsen Ø, Yan, J. PVTxy properties of CO_2 mixtures relevant for CO_2 capture, transport and storage: Review of available experimental data and theoretical models. Applied Energy. 2011;88:3567-79.

[114] Christiansen LJ, Fredenslund A, Gardner N. Gas-Liquid Equilibria of the CO2 - CO and CO2 - CH4 - CO Systems

OF MONOGRAPH Proceedings of the 1973 Cryogenic Engineering Conference. Adv Cryog Eng. 1974;19:309-19.

[115] Tsankova G, Richter M, Stanwix PL, May EF, Span R. Accurate High-Pressure Measurements of Carbon Monoxide's Electrical Properties. Chemphyschem. 2018;19:784-92.

[116] Green MS, Vicentini-Missoni M, Sengers JMHL. Scaling-Law Equation of State for Gases in the Critical Region. Physical Review Letters. 1967;18:1113-7.

[117] Donnelly HG, Katz DL. Phase equilibria in the carbon dioxide - methane system. Ind Eng Chem. 1954;46:511-7.

[118] Somait FA, Kidnay AJ. Liquid-Vapor Equilibria at 270.00 K for Systems Containing Nitrogen, Methane, and Carbon Dioxide. J Chem Eng Data. 1978;23:301-5.

[119] Webster LA, Kidnay AJ. Vapor-Liquid Equilibria for the Methane - Propane - Carbon Dioxide Systems at 230 K and 270 K. J Chem Eng Data. 2001;46:759-64.

[120] Olivia Fandiño JPMT. SVLE data for the (CO_2 + CH_4) system. Unpublished. 2012.

[121] Al-Sahhaf TA, Kidnay AJ, Sloan ED. Vapor-liquid equilibria in the N2 - CO2 - CH4 system. Ind Eng Chem Fundamentals. 1983;22:372-80.

[122] Arai Y, Kaminishi GI, Saito S. The experimental determination of the p-v-T-x relations for the carbon dioxide - nitrogen and the carbon dioxide - methane systems. J Chem Eng Jpn. 1971;4:113-22.

[123] Bian B, Wang Y, Shi J. Simultaneous determination of vapor-liquid equilibrium and molar volumes for coexisting phases up to the critical temperature with a static method. Fluid Phase Equilib. 1993;90:177-87.

[124] Davalos J, Anderson WR, Phelps RE, Kidnay AJ. Liquid-Vapor Equilibria at 250.00 K for Systems Containing Methane, Ethane, and Carbon Dioxide. J Chem Eng Data. 1976;21:81-4.

[125] DeVaney W, Berryman JM, Kao P-L, Eakin B. High temperature V-L-E measurements for substitute gas components. Gas Processors Association, Research Report RR-30, Project 735-A, Tulsa. 1978.

[126] Hwang SC, Lin HM, Chappelear PS, Kobayashi R. Dew-Point Values for the Methane - Carbon Dioxide System. GPA Research Report. 1976:1-14.

[127] Joffe J. Vapor-Liquid Equilibria by the Pseudocritical Method. Ind Eng Chem Fundamentals. 1976;15:298-303.

[128] Knapp H, Yang X, Zhang Z. Vapor-Liquid Equilibria in Ternary Mixtures Containing Nitrogen, Methane, Ethane and Carbon Dioxide at Low Temperatures and High Pressures. Fluid Phase Equilib. 1990;54:1-18.

[129] Mraw SC, Hwang SC, Kobayashi R. Vapor-Liquid Equilibrium of the CH_4 - CO_2 System at Low Temperatures. J Chem Eng Data. 1978;23:135-9.

[130] Neumann A, Walch W. Vapor-Liquid equilibrium CO_2 - CH_4 in the Range of low Temperatures and small Mole Fractions of CO_2. Chem Ing Tech. 1968;40:241-4.

[131] Tsiklis DS. Heterogeneous equilibria in binary systems (in Russian) Zhur Fiz Khim 1946;20.

[132] Vrabec JF, J. Vapor-liquid equilibria of binary mixtures containing methane, ethane, and carbon dioxide from molecular simulation. J Int J Thermophys. 1996;17.

[133] Wei MSW, Brown TS, Kidnay AJ, Sloan ED. Vapor + Liquid Equilibria for the Ternary System Methane + Ethane + Carbon Dioxide at 230 K and Its Constituent Binaries at Temperatures from 207 to 270 K. J Chem Eng Data. 1995;40:726-31.

[134] Petropoulou E, Voutsas E, Westman SF, Austegard A, Stang HGJ, Løvseth SW. Vapor - liquid equilibrium of the carbon dioxide/methane mixture at three isotherms. Fluid Phase Equilibria. 2018;462:44-58.

[135] Xu N, Dong J, Wang Y, Shi J. Vapor Liquid Equilibria for N_2 - CH_4 - CO_2 System Near Critical Region. Huagong Xuebao. 1992;43:640-4.

[136] Yorizane M, Yoshimura S, Masuoka H, Toyama A. Low Temperature Vapor-Liquid Equilibria of Hydrogen - Containing Binaries. Proc Int Cryog Eng Conf ICEC. 1968;1:57-62.

[137] Davis JA, Rodewald N, Kurata F. Solid-liquid-vapor phase behavior of the methane-carbon dioxide system. AIChE Journal. 1962;8:537-9.

[138] Blanco ST, Rivas C, Fernández J, Artal M, Velasco I. Influence of Methane in CO2 Transport and Storage for CCS Technology. Environmental Science & Technology. 2012;46:13016-23.

[139] Reamer HH, Olds RH, Sage BH, Lacey WN. Phase Equilibrium in Hydrocarbon Systems.Methane–Carbon Dioxide System in the Gaseous Region. Industrial & Engineering Chemistry. 1944;36:88-90.

[140] Jaeschke MH, A. E. The GERG databank of high accuracy compressibility factor measurements. GERG Technical Monograph 4 Fortschr.-Ber. VDI, Reihe 6, Nr. 251, VDI-Verlag, Düsseldorf. 1991.

[141] Seitz JC, Blencoe JG. Volumetric properties for $\{(1 - x)CO_2 + xCH_4\}$, $\{(1 - x)CO_2 + xN_2\}$, and $\{(1 - x)CH_4 + xN_2\}$ at the pressures (19.94, 29.94, 39.94, 59.93, 79.93,

and 99.93) MPa and the temperature 673.15 K. . J Chem Thermodynamics. 1996;28:1207–13.

[142] Seitz JC, Blencoe JG, Bodnar RJ. Volumetric properties for {(1 − x)CO_2 + xCH_4}, {(1 − x)CO_2 + xN_2}, and {(1 − x)CH_4 + xN_2} at the pressures (9.94, 19.94, 29.94, 39.94, 59.93, 79.93, and 99.93) MPa and temperatures (323.15, 373.15, 473.15, and 573.15) K. J Chem Thermodynamics. 1996;28:521–38.

[143] Simon RF, C. J.; Dicharry, R. M.; Vorhis, F. H. Compressibility factors for carbon dioxide–methane mixtures. J Pet Technol. 1977;29:81–5.

[144] Wöll OEH, T. Messung der dynamischen Viskosität und der Dichte von vier Erdgasgemischen für Drücke bis 15 MPa und Temperaturen bis 373 K in einer kombinierten Viskositäts-Dichte-Messaparatur. Lehrstuhl für Thermodynamik, Ruhr-Universität Bochum. 2003.

[145] Xu N, Dong J, Wang Y, Shi J. High Pressure Vapor Liquid Equilibria at 293 K for Systems Containing Nitrogen, Methane and Carbon Dioxide. Fluid Phase Equilib. 1992;81:175-86.

[146] Steckel F. Dampf-Flussigkeits-Gleichgewichte einiger binarer, schwefelwasserstoffhaltiger systeme unter Druck. Sven Kem Tidskr. 1945;57:209-16.

[147] Bierlein JA, Kay WB. Phase-Equilibrium Properties of System Carbon Dioxide-Hydrogen Sulfide. Industrial & Engineering Chemistry. 1953;45:618-24.

[148] Sobocinski DP, Kurata F. Heterogeneous phase equilibria of the hydrogen sulfide–carbon dioxide system. AIChE Journal. 1959;5:545-51.

[149] M. Hirata SO, and K. Nagahama. Computer aided data book of vapor-liquid equilibria. Copublished by Kodansha limited, Tokyo, and Elsevier scientific Publishing Company. AIChE Journal. 1975;22:957-.

[150] Ferrell JKR, R.W.; Bass,D.G. The Solubility of Acid Gases in Methanol. Report EPA 600/7-79/097, PB-296707, North Carolina State Univ. 1979.

[151] Reamer HH, Sage BH, Lacey WN. Phase Equilibria in Hydrocarbon Systems - Volumetric and Phase Behavior of the Methane-Hydrogen Sulfide System. Industrial & Engineering Chemistry. 1951;43:976-81.

[152] Kohn JPK, F. Heterogeneous Phase Equilibria of the Methane - Hydrogen Sulfide System. AIChE J. 1958;4:211-7.

[153] Yarym-Agaev NLA, L.D.; Matvienko,V.G.; Ryabkin,Yu.Ya.; Tolmacheva,G.B. Vapor-Liquid Equilibrium in the System Methane - Hydrogen Sulfide at Temperatures below 273 K. Ukr Khim Zh Russ Ed. 1991;57:701-4.

[154] Coquelet C, Valtz A, Stringari P, Popovic M, Richon D, Mougin P. Phase equilibrium data for the hydrogen sulphide + methane system at temperatures from 186 to 313 K and pressures up to about 14 MPa. Fluid Phase Equilibria. 2014;383:94-9.

[155] Fredenslund A, Mollerup J. Gas-liquid equilibrium of hydrogen sulphide + carbon monoxide. The Journal of Chemical Thermodynamics. 1975;7:677-82.

[156] Robinson DB, Bailey JA. The carbon dioxide - hydrogen sulfide - methane system. Part I. Phase behavior at 100 degrees F. Can J Chem Eng. 1957;35:151-8.

[157] Robinson DB, Ng HJ, Leu AD. The Behavior of CH4 - CO2 - H2S Mixtures at Sub-Ambient Temperatures. GPA Research Report. 1981:Jan-38.

[158] Hensel WE, Massoth FE. Phase equilibria for the ternary system: CH4 - CO2 - H2S at low temperatures. J Chem Eng Data. 1964;9:352-6.

[159] Ng HJ, Robinson DB, Leu AD. Critical Phenomena in a Mixture of Methane, Carbon Dioxide and Hydrogen Sulfide. Fluid Phase Equilib. 1985;19:273-86.

[160] Westman SF, Stang HGJ, Løvseth SW, Austegard A, Snustad I, Størset SØ, et al. Vapor–liquid equilibrium data for the carbon dioxide and nitrogen (CO_2 + N_2) system at the temperatures 223, 270, 298 and 303 K and pressures up to 18 MPa. Fluid Phase Equilibria. 2016;409:207-41.

[161] Westman SF, Stang HGJ, Løvseth SW, Austegard A, Snustad I, Ertesvåg IS. Vapor-liquid equilibrium data for the carbon dioxide and oxygen (CO_2 + O_2) system at the temperatures 218, 233, 253, 273, 288 and 298 K and pressures up to 14 MPa. Fluid Phase Equilibria. 2016;421:67-87.

[162] Løvseth SW, Austegard A, Westman SF, Stang HGJ, Herrig S, Neumann T, et al. Thermodynamics of the carbon dioxide plus argon (CO_2 + Ar) system: An improved reference mixture model and measurements of vapor-liquid, vapor-solid, liquid-solid

and vapor-liquid-solid phase equilibrium data at the temperatures 213–299 K and pressures up to 16 MPa. Fluid Phase Equilibria. 2018;466:48-78.

[163] Lachet V, de Bruin T, Ungerer P, Coquelet C, Valtz A, Hasanov V, et al. Thermodynamic behavior of the CO_2+SO_2 mixture: Experimental and Monte Carlo simulation studies. Energy Procedia. 2009;1:1641-7.

Appendices

Appendix A Toxicology

Table A1 Hazard Evaluation and Risk Determination matrix.

List each of the chemical substances used in the activity or procedure in the table below and use this matrix to determine the risk level for each one.

(A) Health Hazard	(B) Dustiness or *Volatility	(C) **Quantity	Score
Low ***Hazard Statements:*** H303; 305 H313; 315; 316 H320 H336 EUH066	**Low** ***Solids:*** Pellet-like solids that do not break up. Little or no dust observed during use. Solids forming large crystals ***Liquids:*** Boiling point > 150°C	**Small** <1g (ml)	1
Medium ***Hazard Statements:*** H301; H302; H304 H311; H312; H314; H317 H318; H319 H332; H335 H371; H372; H373	**Medium** ***Solids:*** Smaller crystalline or granular solids. Minimal dust, or if any dust is seen it settles out quickly. ***Liquids:*** Boiling point between 50 and 150°C	**Medium** 1 to 100g (ml)	2
High ***Hazard Statements:*** H300 H310 H330; H331; H334 H340; H341 H350; H351 H360; H361; H362 H370; H372 EUH070	**High** ***Solids:*** Fine, light powders. Dust can be seen during use and possibly remains airborne for several minutes. ***Liquids:*** Boiling point < 50°C	**Large** > 100g (ml)	3

Multiply (A)x(B)x(C) to estimate overall risk level: ≤ 7 Low; 8-11 Medium; ≥ 12 High

* For purposes of calculation, if a chemical has more than one risk phrase, use the one(s) with the highest health hazard score
** When stating quantity, this should consider the quantity in the stock bottle as well as the quantity of the aliquots, since loss of containment from the entire stock bottle whilst removing aliquots may represent the greatest risk.

Table A2 CO concentrations, effects, inhalation time and toxic symptoms developed.

Concentration of CO in the air (*ppm*)	Inhalation Time	Toxic Symptoms
9	Short term exposure	ASHRAE recommended maximum allowable concentration in living area.
35	8 hours	The maximum exposure allowed by OSHA in the workplace over an eight hour period.
200	2-3 hours	Slight headache, tiredness, fatigue, nausea and dizziness.
400	1-2 hours	Serious headache-other symptoms intensify. Life threatening after 3 hours.
800	45 minutes	Dizziness, nausea and convulsions. Unconscious within 2 hours. Death after 2-3 hours.
1,600	20 minutes	Headache, dizziness and nausea. Death within 1 hour.
3,200	5-10 minutes	Headache, dizziness, nausea. Death within 1 hour.
6,400	1-2 minutes	Headache, dizziness, nausea. Death within 25-30 minutes.
12,800	1-3 minutes	Death within 1-3 minutes

Table A3 H_2S concentrations, effects, inhalation time and toxic symptoms developed.

Worker Exposure Limits
NIOSH REL (10-min. ceiling): 10 ppm
OSHA PELs: General Industry Ceiling Limit: 20 ppm General Industry Peak Limit: 50 ppm (up to 10 minutes if no other exposure during shift) Construction 8-hour Limit: 10 ppm Shipyard 8-hour limit: 10 ppm
NIOSH IDLH: 100 ppm
IDLH: immediately dangerous to life and health (level that interferes with the ability to escape) (NIOSH)
PEL: permissible exposure limit (enforceable) (OSHA)
ppm: parts per million
REL: recommended exposure limit (NIOSH)

Concentration (ppm)	**Symptoms/Effects**
0.00011-0.00033	Typical background concentrations
0.01-1.5	Odor threshold (when rotten egg smell is first noticeable to some). Odor becomes more offensive at 3-5 ppm. Above 30 ppm, odor described as sweet or sickeningly sweet.
2-5	Prolonged exposure may cause nausea, tearing of the eyes, headaches or loss of sleep. Airway problems (bronchial constriction) in some asthma patients.
20	Possible fatigue, loss of appetite, headache, irritability, poor memory, dizziness.
50-100	Slight conjunctivitis ("gas eye") and respiratory tract irritation after 1 hour. May cause digestive upset and loss of appetite.
100	Coughing, eye irritation, loss of smell after 2-15 minutes (olfactory fatigue). Altered breathing, drowsiness after 15-30 minutes. Throat irritation after 1 hour. Gradual increase in severity of symptoms over several hours. Death may occur after 48 hours.
100-150	Loss of smell (olfactory fatigue or paralysis).
200-300	Marked conjunctivitis and respiratory tract irritation after 1 hour. Pulmonary edema may occur from prolonged exposure.
500-700	Staggering, collapse in 5 minutes. Serious damage to the eyes in 30 minutes. Death after 30-60 minutes.
700-1000	Rapid unconsciousness, "knockdown" or immediate collapse within 1 to 2 breaths, breathing stops, death within minutes.
1000-2000	Nearly instant death

Appendix B Pictures and Engineering drawings of the VLE cell

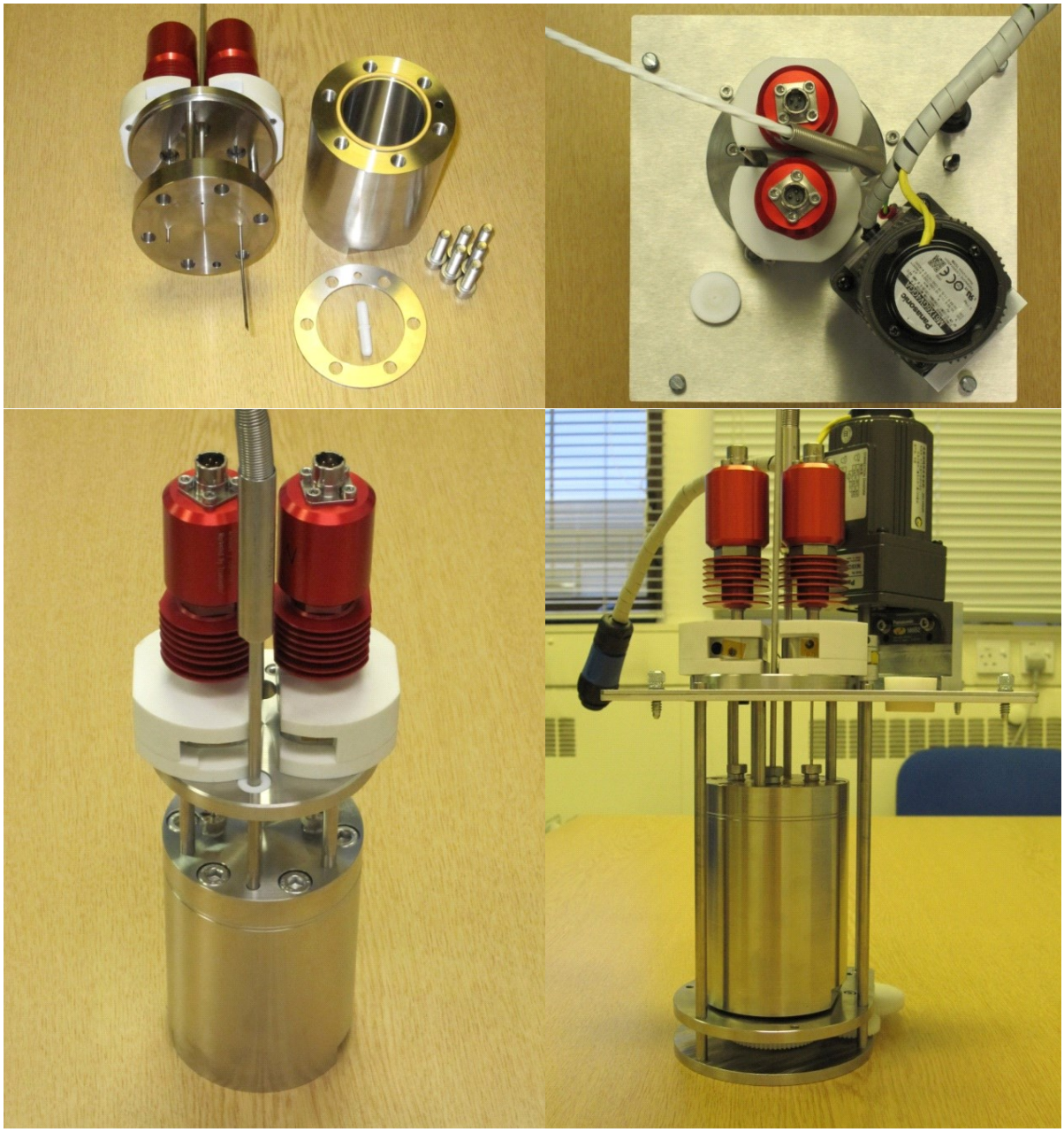


Figure B1 VLE cell. Counter clockwise from the top left: (a) components prior to assembly; (b) assembled vessel with support rods and disc, sampling valves atop and Pt100 temperature sensor inserted (foreground); (c) cell mounted in bath lid fitted with stirrer motor, drive shaft and gears; (d) plan view of bath lid with vessel inserted.

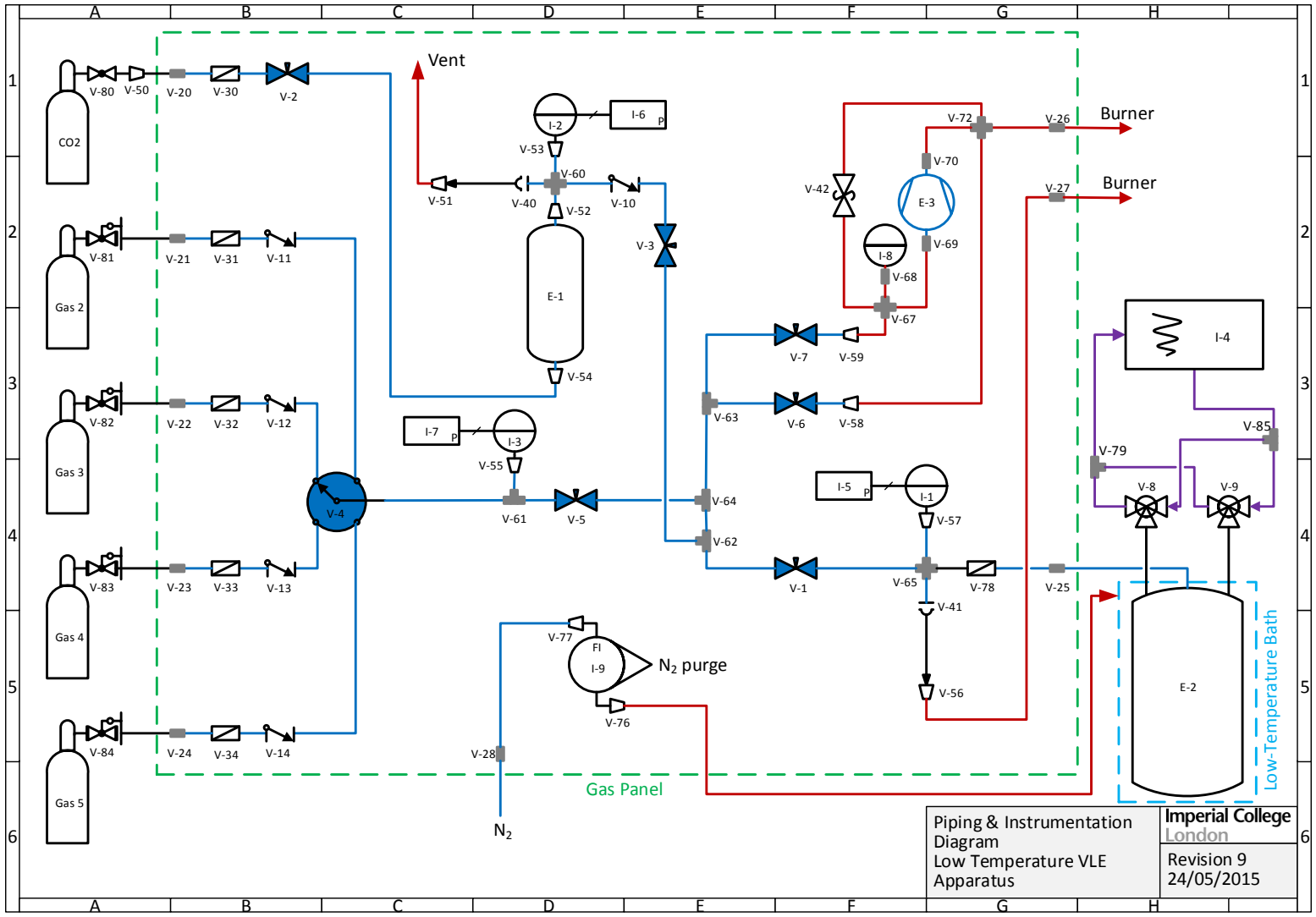


Figure B2 P&ID of the low-temperature high-pressure VLE apparatus as-built.

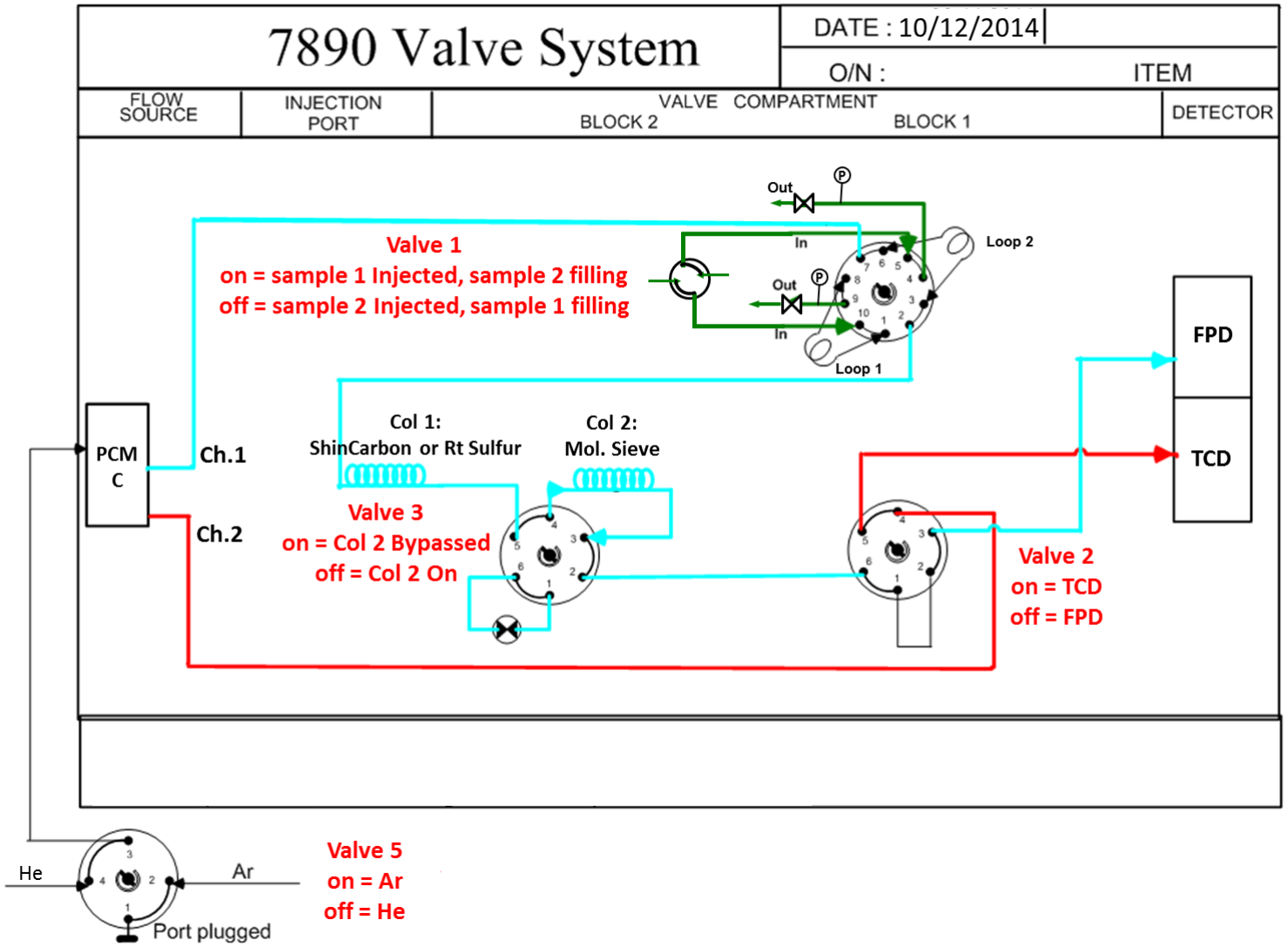


Figure B3 P&ID of the GC valve system.